Numerical methods and applications in many fermion systems

Dissertation zur Erlangung
des naturwissenschaftlichen Doktorgrades
der *Julius-Maximilians-Universität Würzburg*

David J. Luitz

Würzburg, 5. November 2012

vorgelegt von *Dipl.-Phys. David J. Luitz* aus Schongau.

revision: `261a90b6b18149e93805b31644ae661ca3ec6dc3`
typeset using XƎLATEX

Eingereicht am *5. November 2012* bei der Fakultät für Physik und Astronomie

1. Gutachter: *Prof. Dr. Fakher F. Assaad* (Universität Würzburg)
2. Gutachter: *Prof. Dr. Giorgio Sangiovanni* (Universität Würzburg)
3. Gutachter: *Prof. Dr. Emanuel Gull* (University of Michigan)
der Dissertation.

Vorsitzender: *Prof. Dr. Karl Brunner* (Universität Würzburg)

1. Prüfer: *Prof. Dr. Fakher F. Assaad* (Universität Würzburg)
2. Prüfer: *Prof. Dr. Giorgio Sangiovanni* (Universität Würzburg)
3. Prüfer: *Prof. Dr. Hartmut Buhmann* (Universität Würzburg)
im Promotionskolloquium.

Tag des Promotionskolloquiums: *7. Februar 2013*
Doktorurkunde ausgehändigt am:

Abstract

This thesis presents results covering several topics in correlated many fermion systems. A Monte Carlo technique (CT-INT) that has been implemented, used and extended by the author is discussed in great detail in chapter 3. The following chapter discusses how CT-INT can be used to calculate the two particle Green's function and explains how exact frequency summations can be obtained. A benchmark against exact diagonalization is presented. The link to the dynamical cluster approximation is made in the end of chapter 4, where these techniques are of immense importance.

In chapter 5 an extensive CT-INT study of a strongly correlated Josephson junction is shown. In particular, the signature of the first order quantum phase transition between a Kondo and a local moment regime in the Josephson current is discussed.

The connection to an experimental system is made with great care by developing a parameter extraction strategy. As a final result, we show that it is possible to reproduce experimental data from a numerically exact CT-INT model-calculation.

The last topic is a study of graphene edge magnetism. We introduce a general effective model for the edge states, incorporating a complicated interaction Hamiltonian and perform an exact diagonalization study for different parameter regimes. This yields a strong argument for the importance of forbidden umklapp processes and of the strongly momentum dependent interaction vertex for the formation of edge magnetism.

Additional fragments concerning the use of a Legendre polynomial basis for the representation of the two particle Green's function, the analytic continuation of the self energy for the Anderson Kane Mele Model as well as the generation of test data with a given covariance matrix are documented in the appendix.

A final appendix provides some very important matrix identities that are used for the discussion of technical details of CT-INT.

Zusammenfassung

In der vorliegenden Dissertation werden verschiedene Themen aus dem Feld der stark korrelierten Viel-Fermionensysteme präsentiert. Zunächst wird in Kapitel 3 eine Monte Carlo Methode (CT-INT), welche der Autor implementiert, angewandt und erweitert hat, auf detaillierte Weise eingeführt. Das nachfolgende Kapitel diskutiert wie die Zweiteilchen Greensche Funktion in CT-INT berechnet werden kann und wie exakte Frequenzsummen ausgewertet werden können. Dies wird in einem Vergleich mit Daten aus exakter Diagonalisierung demonstriert. Abschließend wird die Verbindung zur dynamischen Cluster Näherung am Ende von Kapitel 4 aufgezeigt, wo diese Methoden von außerordentlicher Bedeutung sind.

In Kapitel 5 wird eine umfangreiche CT-INT Studie eines stark korrelierten Josephson Kontakts vorgestellt. Insbesondere wird die Verbindung zwischen dem Phasenübergang erster Ordnung von einem Kondoregime zu einem Regime mit lokalem magnetischem Moment mit der Phasenverschiebung um π des Josephson-Stroms herausgearbeitet.

Es wird gezeigt, wie der Übergang zu einem realen experimentellen System durchgeführt werden kann, wobei besondere Sorgfalt auf die Entwicklung einer Strategie zur Extraktion der Modellparameter aus den experimentellen Daten gelegt wurde. Als Endergebnis demonstrieren wir, dass es es möglich ist, experimentelle Daten mit Hilfe einer numerisch exakten Modellrechnung zu reproduzieren.

Als letztes Projekt wird eine Untersuchung des Randmagnetismus von Graphen vorgestellt. Dazu wird ein allgemeines effektives Modell eingeführt, welches einen komplizierten Wechselwirkungshamiltonian enthält. Hierfür wird eine Studie mit Hilfe von exakter Diagonalisierung des Hamiltonians in verschiedenen Parameterbereichen erarbeitet, wodurch wir argumentieren können, dass das Verbot von Umklappprozessen und die starke Impulsabhängigkeit der Wechselwirkung für die Bildung des Randmagnetismus verantwortlich sind.

Zusätzlich dokumentieren einige Fragmente im Anhang theoretische Arbeiten zur Benutzung einer Basis von Legendre Polynomen zur Darstellung der Zweiteilchen Greenschen Funktion, zur analytischen Fortsetzung der Selbstenergie für das Anderson Kane Mele Modell sowie zur Erstellung von Testdaten mit einer analytisch bestimmbaren Kovarianzmatrix.

Ein Anhang mit einigen Matrix Identitäten die wichtig für die Diskussion der technischen Details von CT-INT sind schließt diese Arbeit ab.

Contents

1. Introduction

The field of solid state physics is today divided in three parts: Experimental physics providing the fundamental and ultimate foundation of scientific research by empirical studies of real materials, analytic theoretical physics searching for a fundamental understanding of phenomena through a huge apparatus of mathematical concepts and computational theoretical physics making use of modern computers in order to treat numerically mathematical problems that appear to be unsolvable analytically.

All three disciplines are strongly entangled, and from today's perspective, neither of them can solve the riddles of strongly correlated systems individually, and only a collective effort will eventually lead to a breakthrough for a deeper understanding of phenomena in strongly interacting systems. These systems can show fascinating physics, such as magnetic phenomena (one fascinating example of which is presented in chapter 6), the Kondo effect [1], high temperature superconductivity [2] and other exotic states of matter such as spin liquids [3, 4].

Researchers in the field of computational solid state theory set out to solve problems that cannot be solved or that can only be partially solved (for example only for special points in the parameter space) by analytical methods. Various methods have been proposed and used for different problems, such as NRG [5], fRG [6], exact diagonalization, Monte Carlo Methods [7–12] , DMRG [13], tensor network methods [14], DMFT [15] and cluster extensions [16], the dual fermion method [17], DΓA [18] and many others. Every method has its shortcomings and drawbacks, whether it be applicability to low temperatures or for groundstate properties, finite size limitations, applicability to interaction strength or controlled and uncontrolled approximations as well as practical applicability and computer time or memory restrictions.

This has led to the necessity of studying in detail available methods and the class of problems they are suited for, culminating in the importance of the development and improvement of new and existing algorithms.

Even though experience shows that an algorithmic improvement is always preferable, code optimization has shown amazing breakthroughs in recent applications [4, 19] and the performance enhancement can be by orders of magnitude in some cases. Examples for outstanding algorithmic improvements can be found for example in the domain of Quantum Monte Carlo methods: The loop algorithm applicable e.g. to the stochastic series expansion [20] introducing global updates that reduce autocorrelation times by orders of magnitude or the segment picture for the hybridization expansion continuous time Monte Carlo method (CT-HYB)[21] to name only two examples. Another even more impressive example is the introduction of the Lanczos method [22] for the exact calculation of ground state properties for finite size systems.

The present thesis is in this sense a detailed showcase of the field of a computational approach to strongly correlated fermion systems, as a numerically exact continuous time quantum Monte Carlo method CT-INT and its optimization is presented in chapter 3. The goal in this chapter is to provide a pedagogical introduction to the method, including the matrix theoretical background which is the foundation of an efficient implementation with so called *fast updates*. Chapter 4 goes in even deeper algorithmic detail and presents a method for the calculation of two particle quantities using CT-INT, a procedure that is crucial for accurate computations of for example susceptibilities within the framework of the dynamical cluster approximation (DCA), which is a method that has been used successfully in the past for the calculation of properties of systems in the thermodynamic limit (cf. e.g. [23]). We will clearly place the focus on the development, description and verification of the mathematical and numerical toolbox and will only present some illustrative results obtained by the method.

In chapter 5, we trace the methodological way from a method to the study of physical properties of a model system: An interacting quantum dot embedded between two superconducting leads. This system shows the fascinating phenomenon of the Josephson current including a first order transition reflected by a sign change of the supercurrent. The CT-INT is ideally suited for the study of this system and we present detailed results describing the mechanism of this phase transition and the connection between the π-phase shift of the

Josephson current and the transition from local moment behaviour to the formation of a Kondo singlet on the quantum dot is discussed in detail. The work presented in chapter 5 is a reproduction of reference [24]. After the study of the physics in this model, we go one step beyond and calculate quantities observable in a real experimental sample. We demonstrate in detail, how a model calculation can be compared with experimental data, including a very careful treatment of the determination of the experimental parameters. Also here, some methodological details are presented, focussing on the presentation of an accurate calculation of the linear conductance from a CT-INT calculation.

Finally, we show in chapter 6 how analytical and numerical work can be used in synergy and present a study of the edge magnetism in graphene. For this problem, the CT-INT method is not applicable in an easy way and we use the Lanczos method for the exact calculation of ground state properties. This is an illustrative example of how one can treat the finite size limitations of the exact diagonalization method and how meaningful results can be obtained.

This collection of interesting physical problems that are tackled with different methods should give a nice view on the importance of numerical algorithms suited particularly for specific problems at hand, a property extraordinarily prominent in this field.

2. General matter

2.1. Abbreviations

In the field of computational many body physics, a large number of abbreviations is used especially in order to refer to different numerical methods. Here, the most important acronyms used in the text are listed.

DCA Dynamical Cluster Approximation
CT-INT Interaction Expansion Continuous Time Quantum Monte Carlo method
CTQMC Continuous Time Quantum Monte Carlo method
QMC Quantum Monte Carlo method
DΓA Dynamical vertex approximation
DMFT Dynamical mean field theory

2.2. System of units

For convenience, brevity and elegance, we employ the system of *natural units* — which is widely used in theoretical physics — throughout this work. Some exceptions are made in chapter 5 where we show how theoretical and experimental unit systems are synchronized. This example is particularly instructive and should convince a sceptic reader of the usability of the theoretical unit system even in practical applications as from a comparison of the theoretical result with the experimental measurement data the translation to laboratory units (in this case meV) can be deduced.

The *natural unit* system is defined by setting various universal constants to the value of 1. Of particular importance are the definitions

$$\hbar = k_\mathrm{B} = 1 \tag{2.1}$$

in the present work. They imply that energies and inverse temperatures have the same units.

2.3. General notation

In table 2.1 the most important special symbols used in this work are introduced. Note that standard mathematical notation as well as notation used widely in theoretical physics is not introduced here with some exceptions which may be defined differently in different references — such as for example the Heavyside function $\Theta(x)$ or the Green's functions $G(\tau)$.

2.4. Fourier transforms of Grassmann numbers

Let us fix the Fourier transforms between imaginary time and Matsubara frequencies as well as between real space and momentum space in terms of *Grassmann numbers* (cf. [25–27]). We make use of Grassmann numbers here, as they provide a more general and flexible formulation of fermionic quantum thermodynamics in terms of a field theory. However — in the following — we will mix operator and Grassmann language freely wherever appropriate, always choosing the conceptually simplest formulation.

$$c_{\mathbf{k},\sigma}(\mathrm{i}\omega_n) = \frac{1}{\sqrt{\beta N}} \sum_{\mathbf{x}} \int\limits_0^\beta \mathrm{d}\tau\, \mathrm{e}^{-\mathrm{i}\left(\omega_n \tau - \mathbf{k}^T \mathbf{x}\right)} c_{\mathbf{x},\sigma}(\tau). \tag{2.2}$$

Symbol	Meaning
β	Inverse temperature, $\beta = 1/T$.
$\mathrm{ind}\,(\mathbf{k})$	Maps a cluster momentum vector $\mathbf{k}$ to an index.
$\Theta(x)$	Heaviside step function: $\Theta(x) = \begin{cases} 1 \text{ if } x \geq 0 \\ 0 \text{ if } x < 0 \end{cases}$.
$c_{\mathbf{x},\sigma}$	Annihilation operator for particle on site $\mathbf{x}$ with spin z component σ or its eigenvalue which is a Grassmann number depending on context.
$c^\dagger_{\mathbf{x},\sigma}$	Creation operator for particle on site $\mathbf{x}$ with spin z component σ.
$\bar{c}_{\mathbf{x},\sigma}$	Grassmann number corresponding to $c^\dagger_{\mathbf{x},\sigma}$.
$\mathrm{i}\omega_n$	Fermionic Matsubara frequency, $\mathrm{i}\omega_n = (2n+1)\pi/\beta$, $n \in \mathbb{Z}$.
$\mathrm{i}\nu$	Bosonic Matsubara frequency, $\mathrm{i}\nu = (2n)\pi/\beta$, $n \in \mathbb{Z}$.
$n_{\mathrm{F}}(z)$	Fermi function $n_{\mathrm{F}}(z) = \frac{1}{1+\mathrm{e}^{\beta z}}$.
K	Combined fermionic frequency and momentum $K = (\mathbf{K}, \mathrm{i}\omega_n)$
P	Combined fermionic frequency and momentum $P = (\mathbf{P}, \mathrm{i}\omega'_n)$
Q	Combined bosonic frequency and momentum $Q = (\mathbf{Q}, \mathrm{i}\nu)$
k	Combined fermionic frequency and momentum $k = (\mathbf{k}, \mathrm{i}\omega_n)$
p	Combined fermionic frequency and momentum $p = (\mathbf{p}, \mathrm{i}\omega'_n)$
q	Combined bosonic frequency and momentum $q = (\mathbf{q}, \mathrm{i}\nu)$
Z	Grand canonical partition function

Table 2.1.: Important notation used throughout this document.

$$\bar{c}_{\mathbf{k},\sigma}(\mathrm{i}\omega_n) = \frac{1}{\sqrt{\beta N}} \sum_{\mathbf{x}} \int_0^\beta \mathrm{d}\tau\, \mathrm{e}^{\mathrm{i}\left(\omega_n \tau - \mathbf{k}^T \mathbf{x}\right)} \bar{c}_{\mathbf{x},\sigma}(\tau). \tag{2.3}$$

2.5. Single particle Green's function

For the single particle Green's function, we will use the convention common in the CT-INT literature (cf. e.g. [9, 10, 21, 24, 28])

$$G(\tau) = \langle T c^\dagger(\tau) c \rangle \tag{2.4}$$

together with the Fourier transform to Matsubara frequencies

$$G(\mathrm{i}\omega_n) = \int_0^\beta \mathrm{d}\tau\, \mathrm{e}^{\mathrm{i}\omega_n \tau} G(\tau) \quad \text{and} \quad G(\tau) = \frac{1}{\beta} \sum_{\mathrm{i}\omega_n} \mathrm{e}^{-\mathrm{i}\omega_n \tau} G(\mathrm{i}\omega_n). \tag{2.5}$$

It should be brought to the reader's attention that this definition also has an impact on equations of motion and – in particular – to the form of the resolvent operator $\mathbf{G}(\mathrm{i}\omega_n)$:

$$\mathbf{G}(\mathrm{i}\omega_n) = \frac{1}{-\mathrm{i}\omega_n - \mathbf{H}^\dagger}, \tag{2.6}$$

which deviates by complex conjugation and transposition order from the form prevalent in the literature. In other words, we could also write

$$\mathbf{G}(\mathrm{i}\omega_n) = \mathbf{G}_{\text{literature}}(\mathrm{i}\omega_n)^\dagger. \tag{2.7}$$

3. CT-INT

One of the most recent developments in quantum Monte Carlo methods, applicable to strongly interacting systems, is the research in continuous time algorithms, a class of algorithms stemming historically from an algorithm presented by Rombouts et al [12]. The main advantage of continuous time quantum Monte Carlo methods over traditional approaches is the fact that they do not rely on a Trotter decomposition of the interacting Hamiltonian and thus abstain from the introduction of a discrete imaginary time grid such as methods introduced previously, e.g. the BSS algorithm [7] or the impurity solver given by Hirsch and Fye [8]. A discrete imaginary time grid with a time spacing $\Delta\tau$ introduces a systematic error which can only be overcome by the tedious procedure of performing calculations for different values of $\Delta\tau$ (which become more and more expensive for small values of $\Delta\tau$) and eventually extrapolate to the exact result for $\Delta\tau = 0$. While this procedure is viable and has been used successfully in the past, continuous time Monte Carlo algorithms provide — at least for impurity or cluster type problems as presented in this thesis[1] — a numerically exact and more efficient path for the solution of strongly interacting systems.

Today, we have three major continuous time Quantum Monte Carlo algorithms, classified according to reference [21]:

- CT-AUX: Auxiliary field algorithm which is related to the Hirsch-Fye algorithm and has first been proposed by Rombouts et al in [12] and further developed and reformulated by Gull et al in [11].

- CT-INT: Interaction expansion algorithm first proposed by Rubtsov et al in [9]. This method is amazingly flexible and has been extended to imaginary time and space displaced interactions (cf. [10]) as well as to Nambu type Green's functions (cf. [24]). It is also the method of choice for the solution of cluster problems as demonstrated in chapter 4 of this thesis. This method is presented in depth below.

- CT-HYB: Hybridization expansion algorithm first presented by Werner and Millis in [30]. It is a powerful method for the solution of multi orbital problems, although the application to clusters is strongly hindered by the occurance of a trace over an operator product of cluster operators, the dimensionality of which grows of course exponentially with the cluster size.

We will focus on CT-INT throughout the rest of the present thesis.

3.1. Density-density type interaction

The interaction expansion continuous time quantum Monte Carlo method (CT-INT) [9, 21] is a general method for the solution of a system described by an action

$$\begin{aligned}\mathcal{S} = &\sum_{\sigma,\sigma',i,j} \int_0^\beta \mathrm{d}\tau \mathrm{d}\tau'\, \bar{c}_{\sigma,i}(\tau) G^{0\;-1}_{\sigma,\sigma'}(i,\tau;j,\tau') c_{\sigma',j}(\tau') + \\ &+ \sum_{i,j,\sigma,\sigma'} \sum_{s_i} \int_0^\beta \mathrm{d}\tau \mathrm{d}\tau'\; V^0_{\sigma,\sigma'}(i,\tau;j,\tau') \left[\bar{c}_{\sigma,i}(\tau) c_{\sigma,i}(\tau) - \alpha_\sigma(s_i)\right] \left[\bar{c}_{\sigma',j}(\tau') c_{\sigma',j}(\tau') - \alpha_{\sigma'}(s_i)\right],\end{aligned} \tag{3.1}$$

---

[1] The story is different for lattice type problems as the BSS algorithm scales linearly in β and the lattice size, leading to studies of huge 2 dimensional systems of up to 2592 sites in the example of a honeycomb Hubbard model [4, 29]. Although the actual presence of a spin liquid is still under debate, this example shows the enormous power of the BSS method for fermionic lattice problems.

including imaginary time and space displaced interactions as well as non spin diagonal Green's functions. We have already incorporated an additional c-number $\alpha_\sigma(s)$ which is used for the reduction of the sign problem in the Monte Carlo algorithm[2]. The additional variables s that are introduced here are Ising spins and take the values ± 1 [10, 31]. Possible choices for the case of the Hubbard model and a problem having Nambu Green's functions will be given below. In principle, the action may even be more complicated and include non density-density interactions but it is at present unknown how severe the sign problem for these cases is, therefore we restrict the discussion of CT-INT to an action of the form (3.1). We will present the algorithm following the lines of references [9, 10, 24] and will include implementation details about more general moves and improved estimators, aiming for a comprehensive review enabling the reader to understand, use and implement the algorithm.

3.2. Perturbation expansion of the partition function

The starting point for the derivation of CT-INT is a perturbation expansion around the noninteracting limit of the grand canonical partition function Z which can be written in the field theoretical language of Grassmann numbers (cf. e.g. [25, 26])

$$\begin{aligned} Z &= \int D\left[\bar{c}_{\sigma,i,\tau} c_{\sigma,i,\tau}\right] \mathrm{e}^{-\mathcal{S}} \\ &= Z_0 \left\langle \mathrm{e}^{-\sum_{i,j,\sigma,\sigma',s_i} \int_0^\beta \mathrm{d}\tau \mathrm{d}\tau' V^0_{\sigma,\sigma'}(i,\tau;j,\tau')[\bar{c}_{\sigma,i}(\tau) c_{\sigma,i}(\tau) - \alpha_\sigma(s_i)]\left[\bar{c}_{\sigma',j}(\tau') c_{\sigma',j}(\tau') - \alpha_{\sigma'}(s_i)\right]} \right\rangle_0 . \end{aligned} \tag{3.2}$$

Here, $\langle \bullet \rangle_0$ denotes a thermal average with respect to the bare action (the gaussian part of the action (3.1) containing the bare Green's function G^0). The actual perturbation expansion is then given by

$$\begin{aligned} \frac{Z}{Z_0} = \sum_{n=0}^{\infty} \frac{(-1)^n}{n!} \int_0^\beta \mathrm{d}\tau_1 \mathrm{d}\tau_1' \ldots \mathrm{d}\tau_n \mathrm{d}\tau_n' \sum_{\substack{i_1,\ldots,i_n \\ j_1,\ldots,j_n}} \sum_{\substack{\sigma_1,\ldots,\sigma_n \\ \sigma_1',\ldots,\sigma_n' \\ s_1,\ldots,s_n}} V^0_{\sigma_1,\sigma_1'}(i_1,\tau_1;j_1,\tau_1') \cdot \cdots \cdot V^0_{\sigma_n,\sigma_n'}(i_n,\tau_n;j_n,\tau_n') \times \\ \times \left\langle T \left[n_{\sigma_1}(i_1,\tau_1) - \alpha_1\right] \left[n_{\sigma_1'}(j_1,\tau_1') - \alpha_1'\right] \ldots \left[n_{\sigma_n}(i_n,\tau_n) - \alpha_n\right] \left[n_{\sigma_n'}(j_n,\tau_n') - \alpha_n'\right] \right\rangle_0 . \end{aligned} \tag{3.3}$$

Here, we have used the shorthand notation $\alpha_l = \alpha_{\sigma_l}(s_l)$ and $\alpha_l' = \alpha_{\sigma_l'}(s_l)$. This expression can be cast in diagrammatic language by collecting the indices i, τ, σ, s, j, τ', σ' and s' into *vertices*[3]:

$$v = \{i, \tau, \sigma; j, \tau', \sigma'; s\} . \tag{3.4}$$

It should be noted that this choice is strongly dependent on the form of the interacting action and we will show that a vertex in the case of a Hubbard interaction reduces to a simpler form. Additional complexity can however be acquired by an even more general form of the interaction[4] , which is deliberately not discussed here, as the behaviour of the sign problem for this case as well as a good ansatz for the choice of the α parameters are not known at the moment.

Let us define a left (x) and a right (y) end of the vertex and keep the artificial variable s separately $v = \{x; y; s\}$, collecting first indices of $V^0(x;y)$ in $x = [i, \tau, \sigma]$ and second indices in $y = [j, \tau', \sigma']$. The next

---

[2] Potentially, α could also depend on τ and i but we suppress this complexity for readability.

[3] This is rather natural, as we see that the bare interaction vertex V^0 carries all these indices. The indices s and s' are appended for technical reasons to the vertex and in principle additional degrees of freedom might be added.

[4] The most general form of a two particle interaction can be written as

$$H_{\text{int}} = \sum_{ijkl} \sum_{\substack{\sigma_1,\sigma_2 \\ \sigma_3,\sigma_4}} \int_0^\beta \mathrm{d}\tau_1 \tau_2 \tau_3 \tau_4 \, V(1,2;3,4) \bar{c}_{i,\sigma_1}(\tau_1) c_{j,\sigma_2}(\tau_2) \bar{c}_{k,\sigma_3}(\tau_3) c_{l,\sigma_4}(\tau_4). \tag{3.5}$$

step is the introduction of a *configuration* C_n of vertices as an *unordered* set of vertices:

$$C_n = \{v_1, v_2, \dots, v_n\}\,. \tag{3.6}$$

Our goal is to rewrite sums and integrals in equation (3.3) in terms of a sum (which contains of course integrals in continuous variables) over *all* configurations of vertices. We have to be cautious at this step, because we do not impose any order on the vertices in C_n and therefore

$$C_n = \widetilde{C_n} \quad \Leftrightarrow \quad C_n \subset \widetilde{C_n} \wedge C_n \supset \widetilde{C_n}. \tag{3.7}$$

As every integral and sum in equation (3.3) carries an index, order matters in this formulation, and it is easy to see that this can be corrected for by the number $n!$ of permutations of an ordered set each of which is identified with the same unordered set C_n. We therefore get:

$$\sum_{n=0}^{\infty} \int_0^{\beta} \mathrm{d}\tau_1 \mathrm{d}\tau_1' \dots \mathrm{d}\tau_n \mathrm{d}\tau_n' \sum_{\substack{i_1,\dots,i_n \\ j_1,\dots,j_n}} \sum_{\substack{\sigma_1,\dots,\sigma_n \\ \sigma_1',\dots,\sigma_n'}} \sum_{s_1,\dots,s_n} = \sum_{C_n}, \tag{3.8}$$

where $\sum_{C_n}$ really visits every single distinct configuration of n vertices v as well as every possible perturbation order n. Thus, equation (3.3) can be cast in much simpler language:

$$\begin{aligned} \frac{Z}{Z_0} = \sum_{C_n} (-1)^n \, V^0(x_1; y_1) \cdot \dots \cdot V^0(x_n; y_n) \times \\ \times \left\langle T \left[n(x_1) - \alpha(x_1; s)\right] \left[n(y_1) - \alpha(y_1; s)\right] \dots \left[n(x_n) - \alpha(x_n; s)\right] \left[n(y_n) - \alpha(y_n; s)\right] \right\rangle_0 . \end{aligned} \tag{3.9}$$

Note that we write $\alpha(x; s)$ and $\alpha(y; s)$ in a very general form here for elegance, even though an extremely simple form is used in practice, as e.g.

$$\alpha(x; s) = \frac{\langle n \rangle}{2} + s\delta, \quad \text{and} \quad \alpha(y; s) = \frac{\langle n \rangle}{2} - s\delta \tag{3.10}$$

with $\frac{\langle n \rangle}{2} + \delta > 1$ for $V^0(x; y) > 0$ has been found to be beneficial [31].

The expectation value with respect to the gaussian action can be cast into a determinant by virtue of Wick's theorem and takes the form

$$\begin{aligned} &\left\langle T \left[n(x_1) - \alpha(x_1; s_1)\right] \dots \left[n(y_n) - \alpha(y_n; s_n)\right] \right\rangle_0 \\ &= \det \begin{pmatrix} G^0(x_1, x_1) - \alpha(x_1; s_1) & G^0(x_1, y_1) & \dots & G^0(x_1, y_n) \\ G^0(y_1, x_1) & G^0(y_1, y_1) - \alpha(y_1; s_1) & \dots & G^0(y_1, y_n) \\ \dots & \dots & \ddots & \dots \\ G^0(y_n, x_1) & & \dots & G^0(y_n, y_n) - \alpha(y_n; s_n) \end{pmatrix} \\ &=: \det \mathbf{M}_{C_n} . \end{aligned} \tag{3.11}$$

Through the definition

$$W(C_n) = (-1)^n V^0(x_1; y_1) \dots V^0(x_n; y_n) \det \mathbf{M}_{C_n}, \tag{3.12}$$

we finally have a very compact form for the perturbation expansion of $\frac{Z}{Z_0}$, collecting terms by the number of vertices given through the perturbation order n:

$$\frac{Z}{Z_0} = \sum_{C_n} W(C_n). \tag{3.13}$$

This equation is the starting point for the development of a Monte Carlo method that samples configurations of vertices — each of which corresponds to a whole class of diagrams with fixed labels and n vertices. The relative phases between individual diagrams are already incorporated partly by means of the determinant. However, in principle, the terms $W(C_n)$ may carry a complex phase factor which corresponds to the fermionic sign problem. Formally, this problem can be overcome by moving the sign from the weight to the observable[5], a technique that is also referred to as *reweighting*. Let us ignore this problem for now and come back to it later, as the equations can be adapted to the case of a system afflicted by the fermionic sign problem rather easily. We will assume that $W(C_n) > 0$ for all C_n from now on, an assumption that is indeed true in some special cases.

3.3. Markov chain

We present here the fundamental concept of standard Markov chain Monte Carlo methods as it can also be found for example in [32] and show, how the Markov chain should be generated specifically in the case of CT-INT.

As we will see in section 3.4, it is necessary to devise an ergodic stochastic process that generates configurations of vertices C_n such that they are distributed according to the weight $W(C_n)$ or in other words, we want to employ an importance sampling method that allows us to pull a configuration of vertices C_n with probability[6]

$$P(C_n) = \frac{W(C_n)}{\sum_{C_n} W(C_n)}. \tag{3.14}$$

In general, such a stochastic process is defined by a proposal probability matrix $T_{C_n \to C'_n}$ which can be chosen arbitrarily. In order to achieve the correct probability distribution $W(C_n)$, the acceptance probability $P_{C_n \to C'_n}$ has to be chosen accordingly. If we add a "Monte Carlo" time scale to the stochastic process (which evolves with every *move* $C_n \to C'_n$), a *Master equation* describes the time evolution of the probability distribution $W_{C_n}(t)$:

$$\mathrm{d}_t W_{C_n}(t) = \sum_{C'_n} T_{C'_n \to C_n} P_{C'_n \to C_n} W_{C'_n}(t) - \sum_{C'_n} T_{C_n \to C'_n} P_{C_n \to C'_n} W_{C_n}(t). \tag{3.15}$$

We design our algorithm such that the probability distribution $W_{C_n}(t)$ becomes stationary (after a thermalization period) and reaches the distribution given by the CT-INT weights $W(C_n)$ from equation (3.12). Then, the acceptance probability matrix $P_{C_n \to C'_n}$ can be extracted from the *stationary* Master equation with $\mathrm{d}_t W_{C_n}(t) = 0$:

$$\begin{aligned} 0 &= \sum_{C'_n} T_{C'_n \to C_n} P_{C'_n \to C_n} W(C'_n) - \sum_{C'_n} T_{C_n \to C'_n} P_{C_n \to C'_n} W(C_n) \\ &= \sum_{C'_n} \left[T_{C'_n \to C_n} P_{C'_n \to C_n} W(C'_n) - T_{C_n \to C'_n} P_{C_n \to C'_n} W(C_n) \right]. \end{aligned} \tag{3.16}$$

This equation can be fulfilled in many ways and the most common and easiest choice is the *detailed balance*, where we require for every two configurations C_n and C'_n to hold

$$0 = T_{C'_n \to C_n} P_{C'_n \to C_n} W(C'_n) - T_{C_n \to C'_n} P_{C_n \to C'_n} W(C_n) \tag{3.17}$$

One possible way of obeying equation (3.17) is the *Metropolis algorithm* (cf. [33]):

$$P_{C_n \to C'_n} = \min\left(1, \frac{T_{C'_n \to C_n} W(C'_n)}{T_{C_n \to C'_n} W(C_n)}\right). \tag{3.18}$$

---

[5] This leads, however, to an increase of the statistical noise and upgrades the computational complexity from polynomial to exponential. For this reason, the sign problem is considered to be a severe drawback of QMC methods in the case of frustrated systems.

[6] This implies that the weights must be normalizable. Further note that actually $P(C_n)$ is a probability density, as it depends on continuous variables. This implies that also $T_{C_n \to C'_n}$ introduced below is a probability density. Keeping this in mind, we will call them still probabilities.

3.3.1. Multi vertex updates

In a practical calculation, the probability matrix will be a *sparse* matrix, as the calculation of the weight for the new configuration $W(C_n')$ is very expensive. We therefore will only use "local" updates that correspond to small changes to the configuration C_n. It is sufficient to use only two moves:

- Addition of 1 vertex: $C_n \to C_{n+1} = C_n \cup \{v_{n+1}\}$
- Removal of 1 vertex: $C_n \to C_n \setminus \{v_x\}$ with $x \in \mathbb{N}$ and $1 \leq x \leq n$.

Obviously these two moves allow for visiting *every* possible configuration of vertices and are therefore *ergodic*.

However, it turns out that the operations required for this kind of updates do not exploit modern computer hardware as much as we would like, as outer products of vectors have a very bad floating point operations per memory access ratio. In addition to that, we prefer to perform slightly bigger changes in configurations in one step in order to move through the configuration space more quickly and obtain *independent* configurations in less moves by reducing autocorrelation times. This can be achieved with a generalized set of updates:

- Addition of m vertices: $C_n \to C_{n+m} = C_n \cup \{v_{n+1}, \dots, v_{n+m}\}$.
- Removal of $m \leq n$ vertices: $C_n \to C_{n-m} = C_n \setminus \{v_{x_1}, \dots, v_{x_m}\}$ with $x_i \in \mathbb{N}$ and $1 \leq x_i \leq n$ in addition to $x_i \neq x_j$ if $i \neq j$.

An ergodic set of moves is then achieved by using these updates with $m = 1$ and in addition to that any set of moves with $m > 1$. Note that using only $m > 1$ is not sufficient and can only be justified in very rare and special cases (cf. [9] where $m = 2$ is used for a half filled Hubbard cluster).

We will study in detail how to design the stochastic process with a set of multiple updates at the example of multi vertex addition and removal. Further updates — such as delayed spin flips shown later — can be incorporated easily.

Let us break the stochastic process T into several steps:

- Add vertices with probability p_{add}.
- Remove vertices with probability p_{del}.
- If addition is requested, add m vertices with probability $p_{\text{add}}(m)$, $m \in \{1, 2, \dots, N_{\text{add}}\}$.
- If removal is requested, remove m vertices with probability $p_{\text{del}}(m)$, $m \in \{1, 2, \dots, N_{\text{del}}\}$.

All other processes in the probability matrix $T_{C_n \to C_n'}$ are set to zero:

$$T_{C_n \to C_{n+k}} = 0, \quad \text{if} \quad k < -\min(n, N_{\text{del}}) \vee k > N_{\text{add}}. \tag{3.19}$$

For the nonzero matrix elements of T, we still have to find the probability density for the proposal of new vertices in the case of a vertex addition as well as the probability for selecting m specific vertices for deletion.

- Generation of m random vertices $v_l = [i_l, \tau_l, \sigma_l, s_l, j_l, \tau_l', \sigma_l']$ with all variables equally distributed yields:
  $$p_{\text{new}}(m) = p_{\text{new}}^m = \left(\frac{1}{16N^2\beta^2}\right)^m, \tag{3.20}$$
  as the variables s, s', σ and σ' each have two possibilities, i and j are chosen from 1 to the number of interacting lattice sites N. In addition to this τ and τ' are continuous random numbers taken from the interval $[0, \beta]$.
- Removal of m vertices leaves us with $n!/(n-m)!$ possible choices and the corresponding probability is therefore:
  $$\frac{(n-m)!}{n!}. \tag{3.21}$$

Putting everything together, we obtain:

- Vertex addition:
$$T_{C_n \to C_{n+m}} = p_{\text{add}}\, p_{\text{add}}(m) \left(\frac{1}{16N^2\beta^2}\right)^m , \quad m > 0. \tag{3.22}$$
- Vertex removal:
$$T_{C_n \to C_{n-m}} = p_{\text{del}}\, p_{\text{del}}(m) \frac{(n-m)!}{n!}. \tag{3.23}$$

Using equation (3.18), we can specify the acceptance probability for the addition of the set of m vertices, with $C_{n+m} = C_n \cup \{v_{n+1}, \dots, v_{n+m}\}$:

$$\begin{aligned} P_{C_n \to C_{n+m}} &= \min\left(1, \frac{p_{\text{del}} p_{\text{del}}(m)\,(n-m)!\,\left(16\beta^2N^2\right)^m W(C_{n+m})}{p_{\text{add}} p_{\text{add}}(m)\, n!\, W(C_n)}\right) \\ &= \min\left(1, \frac{p_{\text{del}} p_{\text{del}}(m)\,(n-m)!\,\left(16\beta^2N^2\right)^m (-1)^m V^0(v_{n+1}) \dots V^0(v_{n+m}) \det \mathbf{M}_{C_{n+m}}}{p_{\text{add}} p_{\text{add}}(m)\, n!\, \det \mathbf{M}_{C_n}}\right). \end{aligned} \tag{3.24}$$

For the removal of the $m \leq n$ vertices $\{v_{\bar{1}}, \dots, v_{\bar{m}}\} \subseteq C_n$, with the new configuration $C_{n-m} = C_n \setminus \{v_{\bar{1}}, \dots, v_{\bar{m}}\}$ we obtain similarly:

$$P_{C_n \to C_{n-m}} = \min\left(1, \frac{p_{\text{add}} p_{\text{add}}(m)\, n!\, \det \mathbf{M}_{C_{n-m}}}{p_{\text{del}} p_{\text{del}}(m)\,(n-m)!\,(16\beta^2N^2)^m V^0(v_{\bar{1}}) \dots V^0(v_{\bar{m}}) \det \mathbf{M}_{C_n}}\right). \tag{3.25}$$

It is apparent that for the generation of the Markov chain, the ratios of the determinants $\det \mathbf{M}_{C_n}$ and $\det \mathbf{M}_{C_{n+m}}$ or $\det \mathbf{M}_{C_{n-m}}$ have to be determined. The direct calculation of matrix determinants is extremely expensive and should therefore be avoided. Additionally, the direct calculation of huge matrices is easily afflicted by the numerical overflow of double precision floating point numbers, a problem that has to be treated in a naive implementation by the transition to $\log \det \mathbf{M}_{C_n}$. A far better way of calculating the acceptance probabilities is given by the so called *fast updates* presented in section 3.3.2.

Note that because of the condition

$$\sum_{C'_n} T_{C'_n \to C_n} = 1 \quad \text{and} \quad T_{C_n \to C'_n} \geq 0, \tag{3.26}$$

we must have

$$p_{\text{add}} + p_{\text{del}} = 1, \quad \sum_{m=1}^{N_{\text{add}}} p_{\text{add}}(m) = 1, \quad \sum_{m=1}^{N_{\text{del}}} p_{\text{del}}(m) = 1 \tag{3.27}$$

and all probabilities must of course be ≥ 0.

3.3.2. Fast updates

The idea of fast updates is based on the fact that the configuration C_n is not totally changed by the removal or addition of m vertices and therefore already known information should be used. The foundation of fast updates lies certainly in matrix and determinant theory and we will make heavy use of *Sylvester's determinant theorem* for two matrices $\mathbf{A} \in \mathbb{C}^{n\times m}$ and $\mathbf{B} \in \mathbb{C}^{m\times n}$ and appropriately sized identity matrices $\mathbf{1}$:

$$\det(\mathbf{1} + \mathbf{AB}) = \det(\mathbf{1} + \mathbf{BA}). \tag{3.28}$$

A collection of proofs for this identity can be found in [34]. We will also need standard block matrix notation and manipulation in addition to the inversion of block matrices presented in B.1.1. These ingredients can be condensed into the central block determinant identity used for fast updates:

$$\det \begin{pmatrix} \mathbf{M} & \mathbf{u} \\ \mathbf{v}^T & \boldsymbol{\alpha} \end{pmatrix} = \det \mathbf{M} \det\left(\boldsymbol{\alpha} - \mathbf{v}^T \mathbf{M}^{-1} \mathbf{u}\right), \tag{3.29}$$

with the matrices $\mathbf{M} \in \mathbb{C}^{n\times n}$, $\mathbf{u}, \mathbf{v} \in \mathbb{C}^{n\times m}$ and $\boldsymbol{\alpha} \in \mathbb{C}^{m\times m}$. We present a simple proof for equation (3.29) in section B.1.2, exploiting Sylvester's theorem. Note that in numerical calculations, the matrix $\boldsymbol{\alpha}$ is usually *much* smaller than $\mathbf{M}$, i.e. $n \gg m$ and therefore only a small determinant has to be calculated, which is beneficial, as the determinant has a computational complexity of $\mathcal{O}(N^3)$ for a $N \times N$ matrix.

Vertex addition

As already mentioned, for the calculation of the acceptance probability of the move $C_n \to C_{n+m}$, i.e. the addition of m vertices, the most expensive part is the calculation of the determinant ratio

$$\frac{\det \mathbf{M}_{C_{n+m}}}{\det \mathbf{M}_{C_n}}. \tag{3.30}$$

However, as the configurations C_n and C_{n+m} are very similar, because of $C_n \subset C_{n+m}$, we note that the matrices $\mathbf{M}_{C_n}$ and $\mathbf{M}_{C_{n+m}}$ are also very similar, in fact, $\mathbf{M}_{C_{n+m}}$ is just an extension of M_{C_n} by $2m$ rows and columns:

$$\mathbf{M}_{C_{n+m}} = \begin{pmatrix} & & & G^0(x_1, x_{n+1}) & \dots & G^0(x_1, y_{n+m}) \\ & \mathbf{M}_{C_n} & & G^0(y_1, x_{n+1}) & \dots & G^0(y_1, y_{n+m}) \\ & & & \vdots & & \vdots \\ G^0(x_{n+1}, x_1) & G^0(x_{n+1}, y_1) & \dots & G^0(x_{n+1}, x_{n+1}) - \alpha(x_{n+1}) & \dots & G^0(x_{n+1}, y_{n+m}) \\ \vdots & \vdots & & \vdots & \ddots & \dots \\ G^0(y_{n+m}, x_1) & G^0(y_{n+m}, y_1) & \dots & G^0(y_{n+m}, x_{n+1}) & \dots & G^0(y_{n+m}, y_{n+m}) - \alpha(y_{n+m}) \end{pmatrix}. \tag{3.31}$$

This form allows of course for an easy application of equation (3.29) and the determinant ratio (3.30) can be easily calculated thus requiring only the determination of the determinant of a small $2m \times 2m$ matrix.

Note that in equation (3.29) the inverse matrix $\mathbf{M}_{C_n}^{-1}$ is needed. This may seem to be a problem at first sight but can be overcome by keeping *only* the inverse Green's function matrix $\mathbf{M}_{C_n}^{-1}$ in memory. Once a move is accepted, this matrix can be updated easily by the block matrix inversion technique detailed in section B.1.1. We will see that the knowledge of $\mathbf{M}_{C_n}^{-1}$ is also sufficient for the calculation of observables and the direct matrix is in fact never needed. Usually, a robust code contains a mechanism to check the quality of the inverse matrix after a certain number of updates, but it has been found that the reconditioning, i.e. the recalculation of $\mathbf{M}_{C_n}^{-1}$ from scratch is necessary only very rarely, making this algorithm numerically extremely stable.

Vertex removal

The case of the removal of m vertices $\{v_{\bar{1}}, \dots, v_{\bar{m}}\} \subset C_n$ is very similar to the addition of vertices and the same strategy for the calculation of the determinant ratio is employed. The reason for this is that the matrix $\mathbf{M}_{C_n}$ has exactly the same structure as in equation (3.31), except that $\mathbf{M}_{C_{n-m}}$ is now in the upper left corner. This is achieved by the trick of changing *all* rows and columns in $\mathbf{M}_{C_n}$ that contain Green's functions with the deleted vertices to the end. An operation leaving the value of the determinant trivially invariant if rows and columns are exchanged by the same permutation matrix $\mathbf{P}$ in the way $\mathbf{P}\mathbf{M}_{C_n}\mathbf{P}^T$. Because of $\mathbf{P}^T = \mathbf{P}^{-1}$, this operation has to be applied equally to $\mathbf{M}_{C_n}^{-1}$. This is of course clearly legal as C_n has an *unordered* set structure. Let us write $\mathbf{M}_{C_n}$ in a corresponding block form to clarify this:

$$\mathbf{M}_{C_n} = \begin{pmatrix} \mathbf{M}_{C_{n-m}} & \mathbf{u} \\ \mathbf{v}^T & \boldsymbol{\alpha} \end{pmatrix}. \tag{3.32}$$

Together with equation (3.29), the determinant ratio required in equation (3.25) can be calculated:

$$\frac{\det \mathbf{M}_{C_{n-m}}}{\det \mathbf{M}_{C_n}} = \det \left[\left(\boldsymbol{\alpha} - \mathbf{v}^T \mathbf{M}_{C_{n-m}}^{-1} \mathbf{u} \right)^{-1} \right]. \tag{3.33}$$

The reader might object that we do not yet know $\mathbf{M}^{-1}_{C_{n-m}}$ in contrary to the known $\mathbf{M}^{-1}_{C_n}$ in the case of vertex addition and that this may be expensive to calculate but the contrary is the case! As we only store inverse matrices in memory, we have

$$\mathbf{M}^{-1}_{C_n} = \begin{pmatrix} \mathbf{E} & \mathbf{F} \\ \mathbf{G} & \mathbf{H} \end{pmatrix} \tag{3.34}$$

in memory[7]. However, as we detail in section B.1.1, $\mathbf{H}$ is given by:

$$\mathbf{H} = \left(\boldsymbol{\alpha} - \mathbf{v}^T \mathbf{M}^{-1}_{C_{n-m}} \mathbf{u}\right)^{-1}. \tag{3.35}$$

This is really remarkable, as we have this quantity already in memory and are left with the calculation of a *small* $2m \times 2m$ determinant without further matrix-vector or matrix-(slender matrix) products as in the case of vertex addition. This leads to an *asymmetric* computational cost of vertex addition and vertex removal, and can be corrected for by a choice of $p_{\text{del}} > p_{\text{add}}$. This leads to more trials of vertex deletion, where the acceptance probability can be calculated at extremely low cost and the new inverse matrix is subsequently calculated only in the (rare) case of acceptance of this move by means of the toolbox presented in section B.1.1.

Vertex addition is in consequence proposed on rare occasions but accepted very often, so the hard work for the acceptance probability calculation is not wasted as it would be in the case $p_{\text{add}} = p_{\text{del}}$.

Efficient treatment of $G_0(x, y)$

During the calculation of updates, the auxiliary matrices $\mathbf{u}$ and $\mathbf{v}^T$ as well as $\boldsymbol{\alpha}$ have to be generated. While this is in principle no problem, as they only contain the noninteracting Green's function $G_0(x, y)$ for different combinations of vertices, it should be noted that considerable amounts of computer time can be wasted by recalculating $G_0(x, y)$ again and again. A commonly used technique to avoid this problem is the discretization of the imaginary time axis into a fine grid. Then, $G_0(x, y)$ can be stored in a table and the calculation is replaced by a table lookup. This introduces a small systematic error which can usually be kept smaller than the statistical error by increasing the table size.

However, for very high precision benchmark calculations, it can be observed that quantities are affected by this discretization error. The table lookup procedure can be improved by a simple linear interpolation method that makes use of an additional table for the first derivative of the Green's function. Let us for simplicity show this in reduced notation, suppressing all indices except the imaginary time difference τ:

$$G(\tau) = G(\tau_i) + (\tau - \tau_i)\mathrm{d}_\tau G(\tau_i), \tag{3.36}$$

with the tabelized time τ_i that is closest to τ. This method allows for a considerable reduction of the table size, sometimes leading even to a situation where the tables fit in the CPU cache, while still yielding extremely accurate results and pushing the discretization error one order higher in $\Delta\tau$.

3.4. Observables

In CT-INT, accessible observables are thermal averages of products of creation and annihilation operators. We will see that the central observable is the single particle Green's function and all other observables (which are higher Green's functions) can be constructed from it by virtue of a special Wick's theorem (cf. [9, 24]).

3.4.1. Single particle Green's function

Imaginary time formulation

Let us begin the discussion with the description of the calculation of the single particle Green's function in imaginary time

$$G(x, y) = \langle T c^\dagger_x c_y \rangle = \frac{1}{Z} \int \mathrm{D}\left[\bar{c}_{x_i} c_{y_i}\right] \mathrm{e}^{-\mathcal{S}} \bar{c}_x c_y \tag{3.37}$$

---

[7] Here, the blocksizes are chosen such that they match the convention in equation (3.32), i.e. $\mathbf{E} \in \mathbb{C}^{(n-m)\times(n-m)}$.

where $x = [i, \tau, \sigma]$ and $y = [j, \tau', \sigma']$ as defined for the density density vertex formulation of the Markov chain in the previous section. For the calculation of this quantity, we can again write down a perturbation expansion as in the case of the partition function, the equations being exactly the same as in section 3.3 with the exception that the Grassmann numbers $\bar{c}_x$ and c_y have to be inserted at the end of the operator chain. This is finally reflected after the application of Wick's theorem by the insertion of one additional row and one column in the determinant and we obtain:

$$\begin{aligned} G(x,y) &= \frac{Z_0}{Z} \sum_{C_n} (-1)^n \, V^0(x_1;y_1) \dots V^0(x_n;y_n) \, \langle T\, [n(x_1) - \alpha(x_1;s)] \dots [n(y_n) - \alpha(y_n;s)] \, c_x^\dagger c_y \, \rangle_0 \\ &= \frac{Z_0}{Z} \sum_{C_n} (-1)^n \, V^0(x_1;y_1) \dots V^0(x_n;y_n) \det \begin{pmatrix} & & & G^0(x_1,y) \\ & \mathbf{M}_{C_n} & & G^0(y_1,y) \\ & & & \vdots \\ G^0(x,x_1) & G^0(x,y_1) & \dots & G^0(x,y) \end{pmatrix} . \end{aligned} \tag{3.38}$$

This is nearly the form that we need for the sampling of the observable. Unfortunately, the determinant does not match $\det \mathbf{M}_{C_n}$ which we need for the identification of $W(C_n)$ to make use of the Markov chain of configurations of vertices distributed according to $W(C_n)$. This can be corrected easily by multiplying and dividing by the correct determinant:

$$\begin{aligned} G(x,y) &= \\ &= \frac{Z_0}{Z} \sum_{C_n} (-1)^n V^0(x_1;y_1) \dots V^0(x_n;y_n) \det \mathbf{M}_{C_n} \frac{\det \begin{pmatrix} & & & G^0(x_1,y) \\ & \mathbf{M}_{C_n} & & G^0(y_1,y) \\ & & & \vdots \\ G^0(x,x_1) & G^0(x,y_1) & \dots & G^0(x,y) \end{pmatrix}}{\det \mathbf{M}_{C_n}} \\ &= \frac{\sum_{C_n} W(C_n) \frac{\det \begin{pmatrix} & & & G^0(x_1,y) \\ & \mathbf{M}_{C_n} & & G^0(y_1,y) \\ & & & \vdots \\ G^0(x,x_1) & G^0(x,y_1) & \dots & G^0(x,y) \end{pmatrix}}{\det \mathbf{M}_{C_n}}}{\sum_{C_n} W(C_n)} . \end{aligned} \tag{3.39}$$

Thus, we only have to sample the *contribution* of a configuration C_n of vertices in our Markov chain to the observable $G(x,y)$:

$$\langle\langle G(x,y) \rangle\rangle_{C_n} = \frac{\det \begin{pmatrix} & & & G^0(x_1,y) \\ & \mathbf{M}_{C_n} & & G^0(y_1,y) \\ & & & \vdots \\ G^0(x,x_1) & G^0(x,y_1) & \dots & G^0(x,y) \end{pmatrix}}{\det \mathbf{M}_{C_n}} . \tag{3.40}$$

Fortunately, this equation can be reduced again using equation (B.4) to reduce the computational complexity of the determinant and we obtain the simple equation

$$\langle\langle G(x,y) \rangle\rangle_{C_n} = G^0(x,y) - \sum_{r,s=1}^{2n} G^0(x,z_r) \left(\mathbf{M}_{C_n}^{-1} \right)_{rs} G^0(z_s,y), \tag{3.41}$$

leaving only a vector matrix vector product with complexity proportional to the square of the perturbation order. Here, z_r denotes either x or y parts of the specific vertex v, depending on the index r

Note that we only need to know the inverse matrix $\mathbf{M}_{C_n}^{-1}$, which we already have in memory from the generation of the Markov chain by means of fast updates.

Direct calculation in Matsubara frequencies

For systems that are translation invariant in space and imaginary time, we can introduce a Fourier transformation to lattice momenta $\mathbf{k}$ and fermionic Matsubara frequencies $\mathrm{i}\omega_n$. As time and space translation invariance are broken by the fixed positions i, j and times τ, τ', the symmetry has to be restored stochastically in principle. However, as we know that $G(x, y)$ will only depend on $\tau - \tau'$ and $i - j$, we can also construct an improved estimator, incorporating translational invariance before performing the Fourier transformation

$$\langle\langle G(\tau, i, \sigma, \sigma')\rangle\rangle_{C_n} = \frac{1}{\beta N} \int\limits_0^\beta \mathrm{d}\tau' \sum_j \langle\langle G(\tau + \tau', i + j, \sigma; \tau', j, \sigma')\rangle\rangle_{C_n}. \tag{3.42}$$

This improved estimator can be understood as averaging over all *equivalent* configurations C_n at once, where we understand configurations to be equivalent if they can be transformed into each other by moving *all* imaginary times τ by the same time difference τ' (while taking care of mapping the resulting time back to the interval $[0, \beta]$ with the correct fermionic rule $G(\beta - \tau) = -G(-\tau)$ and $G(\tau) = G(\tau + 2\beta)$) as well as moving all lattice position vectors i by the same distance j. These operations leave the matrix $\mathbf{M}_{C_n}$ invariant because $G^0(x, y)$ is translation invariant in time and space. Therefore, all equivalent configurations have the same weight $W(C_n)$ and averaging over them allows for faster sampling in the configuration space. Any such operation reduces the variance of the observable and we obtain the estimator for the Matsubara Green's function $G(\mathrm{i}\omega_n, \mathbf{k}, \sigma, \sigma')$ in momentum space (cf. also [9]):

$$\begin{aligned} &\langle\langle G(\mathrm{i}\omega_n, \mathbf{k}, \sigma, \sigma')\rangle\rangle_{C_n} = \\ &G^0(\mathrm{i}\omega_n, \mathbf{k}, \sigma, \sigma') - \frac{1}{\beta N} \sum_{r,s=1}^{2n} G^0(\mathrm{i}\omega_n, \mathbf{k}, \sigma, \sigma_r) \mathrm{e}^{\mathrm{i}\omega_n(\tau_r - \tau_s) - \mathrm{i}\mathbf{k}^T(\mathbf{s}-\mathbf{r})} \left(\mathbf{M}_{C_n}^{-1}\right)_{r,s} G^0(\mathrm{i}\omega_n, \mathbf{k}, \sigma_s, \sigma'). \end{aligned} \tag{3.43}$$

Here the vectors $\mathbf{r}$ and $\mathbf{s}$ denote the corresponding lattice positions i and j of the specific vertex depending on the summation indices.

Note that this equation has the form of a reducible Dyson equation and gives consequently direct access to the reducible self energy.

Using this method for the calculation of the Green's function massively reduces the noise and is therefore the method of choice.

3.4.2. Wick's theorem per Monte Carlo configuration $W(C_n)$ for higher Green's functions

The equations for the calculation of the single particle Green's function $G(x, y)$ presented in section 3.4.1 can be easily generalized to higher Green's functions

$$G_m(\xi_1, \gamma_1, \ldots, \xi_m, \gamma_m) = \langle T c^\dagger_{\xi_1} c_{\gamma_1} \ldots c^\dagger_{\xi_m} c_{\gamma_m} \rangle\,. \tag{3.44}$$

The indices ξ_i and γ_i shall again denote a multiindex $[\tau, i, \sigma]$.

It is found, that this quantity can be calculated from the Markov chain of configurations of vertices through a perturbation expansion in the interaction:

$$G_m(\xi_1, \gamma_1, \ldots, \xi_m, \gamma_m) = \frac{\sum_{C_n} W(C_n) \langle\langle G_m(\xi_1, \gamma_1, \ldots, \xi_m, \gamma_m)\rangle\rangle_{C_n}}{\sum_{C_n} W(C_n)}. \tag{3.45}$$

The direct calculation of the contribution $\langle\langle G_m(\xi_1, \gamma_1, \ldots, \xi_m, \gamma_m)\rangle\rangle_{C_n}$ is tedious and time consuming. Luckily for every configuration C_n a relation similar to Wick's theorem can be found, which greatly simplifies the calculation of higher Green's functions. It is closely connected to the determinant identity (B.15) proven in section B.1.4. As in the case of the single particle Green's function, the application of Wick's theorem for the noninteracting thermal expectation values yields

$$\langle\langle T c^\dagger_{\xi_1} c_{\gamma_1} \ldots c^\dagger_{\xi_m} c_{\gamma_m} \rangle\rangle_{C_n} = \frac{\det \mathbf{B}_{C_n}}{\det \mathbf{M}_{C_n}}, \tag{3.46}$$

where we have defined the matrix $\mathbf{B}_{C_n} \in \mathbb{C}^{(2n+m)\times(2n+m)}$ as

$$\mathbf{B}_{C_n} = \begin{pmatrix} & & & G_0(x_1,\gamma_1) & \dots & G_0(x_1,\gamma_m) \\ & \mathbf{M}_{C_n} & & \vdots & \ddots & \vdots \\ & & & G_0(y_n,\gamma_1) & \dots & G_0(y_n,\gamma_m) \\ G_0(\xi_1,x_1) & \dots & G_0(\xi_1,y_n) & G_0(\xi_1,\gamma_1) & \dots & G_0(\xi_1,\gamma_m) \\ \vdots & \ddots & \vdots & \vdots & \ddots & \vdots \\ G_0(\xi_m,x_1) & \dots & G_0(\xi_m,y_n) & G_0(\xi_m,\gamma_1) & \dots & G_0(\xi_m,\gamma_m) \end{pmatrix}. \tag{3.47}$$

Defining the matrices $\mathbf{B}^{\mathbf{ij}}_{C_n} \in \mathbb{C}^{(2n+1)\times(2n+1)}$, we can make use of the determinant identity (B.15)

$$\mathbf{B}^{\mathbf{ij}}_{C_n} = \begin{pmatrix} & & & G_0(x_1,\gamma_j) \\ & \mathbf{M}_{C_n} & & \vdots \\ & & & G_0(y_m,\gamma_j) \\ G_0(\xi_i,x_1) & \dots & G_0(\xi_i,y_n) & G_0(\xi_i,\gamma_j) \end{pmatrix}, \tag{3.48}$$

yielding

$$\frac{\det \mathbf{B}_{C_n}}{\det \mathbf{M}_{C_n}} = \frac{1}{(\det \mathbf{M}_{C_n})^n} \det \begin{pmatrix} \det \mathbf{B}^{\mathbf{11}}_{C_n} & \dots & \det \mathbf{B}^{\mathbf{1m}}_{C_n} \\ \vdots & \ddots & \vdots \\ \det \mathbf{B}^{\mathbf{m1}}_{C_n} & \dots & \det \mathbf{B}^{\mathbf{mm}}_{C_n} \end{pmatrix}. \tag{3.49}$$

From equation 3.38 it is obvious, that $\det \mathbf{B}^{\mathbf{ij}}_{C_n} / \det \mathbf{M}_{C_n}$ is identical to the contribution of the configuration C_n to the one particle Green's function $\langle T c^\dagger_{\xi_i} c_{\gamma_j} \rangle$. Hence, Wick's theorem holds for every configuration C_n and is given by

$$\begin{aligned} &\langle\langle G_m(\xi_1,\gamma_1,\dots,\xi_m,\gamma_m)\rangle\rangle_{C_n} = \\ &\det \begin{pmatrix} \langle\langle G_0(\xi_1,\gamma_1)\rangle\rangle_{C_n} & \dots & \langle\langle G_0(\xi_1,\gamma_m)\rangle\rangle_{C_n} \\ \vdots & \ddots & \vdots \\ \langle\langle G_0(\xi_m,\gamma_1)\rangle\rangle_{C_n} & \dots & \langle\langle G_0(\xi_m,\gamma_m)\rangle\rangle_{C_n} \end{pmatrix}. \end{aligned} \tag{3.50}$$

This relation is particularly useful in a simulation measuring multiple physical observables as measurements of single particle Green's functions can be reused in an economic way.

Note that this is a higher order Wick's theorem, as the basic quantities are not bare Green's functions but configuration contributions to the fully interacting Green's functions, however, this identity is of course a direct consequence of Wick's theorem in it's standard form expressed in terms of bare Green's functions.

3.4.3. Perturbation order

An interesting feature that CT-INT shares with other Monte Carlo methods, such as for example the stochastic series expansion [35], is the fact that the average perturbation order is directly linked to a physical observable, i.e. the potential energy, providing an internal consistency check of the method. This is found easily following the discussion in [9, 10]

$$\langle n \rangle = - \int_0^\beta \mathrm{d}\tau \mathrm{d}\tau' \sum_{\sigma,\sigma'} \sum_{i,j} \sum_s V^0_{\sigma,\sigma'}(i,\tau;j,\tau') \, \langle [n_\sigma(i,\tau) - \alpha_\sigma(s)] \, [n_{\sigma'}(j,\tau') - \alpha_{\sigma'}(s)] \rangle \, . \tag{3.51}$$

The perturbation order can be measured very easily and is usually determined with great accuracy. Higher moments of the distribution can in principle be derived in the same way.

For an interaction local in space and time, i.e. $V^0_{\sigma,\sigma'}(i,\tau;j,\tau') = U\delta(\tau-\tau')\delta_{i,j}$, it is easy to see that

$$\langle n \rangle \propto UN\beta. \tag{3.52}$$

We have already seen that one update move of a configuration C_n to $C_{n\pm m}$ by vertex addition involves only (generalized) vector-matrix-vector products with a computational complexity proportional to the matrix size $(2n)^2 \propto (UN\beta)^2$. As we have to perform on average n moves to obtain an independent configuration C_n' by touching every vertex in the configuration, we need n moves and thus can estimate the overall complexity for an effective move between two *independent* configurations of vertices as

$$\mathcal{O}\left((UN\beta)^3\right). \tag{3.53}$$

Observe that the average expansion order diverges with growing lattice size N as well as at strong coupling $U \to \infty$ and equally for $\beta \to \infty$. This is in complete agreement with the intuition that we are dealing with a finite temperature perturbation expansion around the noninteracting case and need more and more diagrams to take into account the interaction with growing U.

3.4.4. Sign problem

Up to now, we did not discuss how to deal with the *fermionic sign problem*, which can lead to a negative (or even complex) weight $W(C_n)$. Clearly, in this case $W(C_n)$ cannot be interpreted as a statistical *weight* as the corresponding probabilities

$$P(C_n) = \frac{W(C_n)}{\sum_{C_n} W(C_n)} \tag{3.54}$$

would not satisfy the condition $P(C_n) \geq 0$. Does our whole derivation break down now? Fortunately not! We can still save the equations and rewrite them in a meaningful way by moving the phase factor of $W(C_n)$ to the observable:

$$\begin{aligned}\langle G_m(\xi_1, \dots, \gamma_m)\rangle &= \frac{\sum_{C_n} W(C_n)\langle\langle G_m(\xi_1, \dots, \gamma_m)\rangle\rangle_{C_n}}{\sum_{C_n} W(C_n)} = \\ &= \frac{\sum_{C_n} |W(C_n)|\,\mathrm{sgn}(W(C_n))\langle\langle G_m(\xi_1, \dots, \gamma_m)\rangle\rangle_{C_n}}{\sum_{C_n} |W(C_n)|\,\mathrm{sgn}(W(C_n))}.\end{aligned} \tag{3.55}$$

In order to have an importance sampling equation of the form

$$\langle O\rangle = \sum_{C_n} p(C_n) O(C_n) \tag{3.56}$$

with actual probabilities $p(C_n)$, we have to expand this equation by the normalization $\sum_{C_n} \|W(C_n)\|$:

$$\langle G_m(\xi_1, \dots, \gamma_m)\rangle = \frac{\sum_{C_n} |W(C_n)|\,\mathrm{sgn}(W(C_n))\langle\langle G_m(\xi_1, \dots, \gamma_m)\rangle\rangle_{C_n}}{\sum_{C_n} |W(C_n)|} \frac{\sum_{C_n} |W(C_n)|}{\sum_{C_n} |W(C_n)|\,\mathrm{sgn}(W(C_n))}. \tag{3.57}$$

This way, we can now write the observable as the ratio of two Monte Carlo expectation values

$$\langle G_m(\xi_1, \dots, \gamma_m)\rangle = \frac{\langle sG_m\rangle}{\langle s\rangle}, \tag{3.58}$$

where $s = \mathrm{sgn}(W(C_n))$ is the phase factor corresponding to the weight $W(C_n)$. This means that instead of one observable G_m, we now have to measure *two*, namely the phase s and the observable times the phase sG_m. The advantage is that we can again generate a Markov chain of configurations of vertices with real and positive weights $|W(C_n)|$. All the equations presented up to now can be easily changed by $W(C_n) \to |W(C_n)|$ and by keeping in mind that observables are replaced by their value *times the phase s of the weight.* Formally, this means that we can perform simulations even if the simplistic formulation given above would yield negative or complex weights. This does — unfortunately — not mean that the sign problem is solved. The severity can be seen following the discussion provided in reference [21]. Analogy to bosonic models can be used to argue that the average phase behaves as

$$\langle s \rangle = \mathrm{e}^{-\beta \Delta F}, \tag{3.59}$$

with the free energy difference ΔF between the fermionic system at hand and a corresponding bosonic system (which is constructed such that it has already the weights $W(C_n)$). Clearly, at low temperatures the average phase approaches 0, thus leading to the division by a very small number in equation (3.58). This alone would not be a big problem, however it is found (cf. [21]) that the variance of the sign approaches 1 at low temperatures

$$\sigma_s^2 = \langle s^2 \rangle - \langle s \rangle^2 = 1 - \mathrm{e}^{-2\beta\Delta F} \approx 1. \tag{3.60}$$

And thus we have a highly fluctuating sign observable with $\sigma_s \gg \langle s \rangle$. This is the essence of the fermionic sign problem and renders it impossible to extract reliable estimates for observables at very low temperatures in general as the noise of the final result grows exponentially with decreasing temperature.

It may — however — be possible to calculate quantities at intermediate temperatures if the average sign is not too small and this is the domain of applicability of Quantum Monte Carlo methods. In addition to that, special cases may exist, in which no sign problem exists at all [10]. One such problem is presented in chapter 5, where we study an impurity problem with even complex bath Green's functions, that does not have a sign problem.

3.5. Specific examples

Up to now, we have kept the discussion of CT-INT as general as possible, sticking to a density-density interacting action formulation. In order to make the further discussion in subsequent chapters more transparent, we will introduce here two instructive examples on how the complexity of the general form is reduced in simpler examples. We will only discuss interactions that are local in space and time and can therefore think in terms of Hamiltonians. The reader is pointed to [10] for an example including Holstein phonons that lead to a time delayed interaction term after integrating them out. An example for long range interactions can be found in reference [31].

3.5.1. Hubbard model

The Hamiltonian of the Hubbard model describes nearest neighbor hopping of electrons in addition to an onsite repulsion term in the case of double occupancy of a site. In an extended standard form already incorporating the α parameters for the reduction of the sign problem as proposed in reference [10], it reads:

$$H = -t \sum_{i,j,\sigma} c_{i,\sigma}^{\dagger} c_{j,\sigma} + \frac{U}{2} \sum_{i} \sum_{s=\pm 1} \left(n_{i,\uparrow} - \alpha_{\uparrow}(s)\right) \left(n_{i,\downarrow} - \alpha_{\downarrow}(s)\right). \tag{3.61}$$

A good choice of $\alpha_\sigma(s)$ for this case is

$$\alpha_\sigma(s) = \frac{1}{2} + \sigma s \delta, \tag{3.62}$$

with $\delta = \frac{1}{2} + 0^+$. Because of equation (3.51), the average expansion order is proportional to δ^2 and can thus be chosen within limits given by the sign problem.

A comparison of the Hubbard Hamiltonian to the general action (3.1) shows how to chose the vertices:

$$V^0_{\sigma\sigma'}(i,\tau;j,\tau') = \delta_{\sigma,\uparrow}\delta_{\sigma,\downarrow}\delta(\tau-\tau')\delta_{i,j}\frac{U}{2}. \tag{3.63}$$

Obviously, this means that many configurations C_n of vertices will have a weight of 0 according to equation (3.12). This means, that we can reduce the general vertex

$$v = \{i, \tau, \sigma, j, \tau', \sigma', s\} \tag{3.64}$$

to a form that is restricted to the subspace of configurations with nonvanishing weight[8]:

$$v_{\text{Hubbard}} = \{i, \tau, \uparrow, i, \tau, \downarrow, s\} =: [i, \tau, s] \,. \tag{3.65}$$

Proceeding further in this formulation, we notice that now every occurrence of a left end x of a density density vertex corresponds to spin $\uparrow$ and y corresponds to spin $\downarrow$. As we know that in the Hubbard model

$$G^0_{\uparrow\downarrow}(\tau, i) = 0, \tag{3.66}$$

This means that the matrix $\mathbf{M}_{C_n}$ will be block diagonal with one block $\mathbf{M}^{\uparrow}_{C_n}$ corresponding to spin up Green's functions and the other block $\mathbf{M}^{\downarrow}_{C_n}$ to spin down Green's functions. Using

$$\det \begin{pmatrix} \mathbf{M}^{\uparrow}_{C_n} & 0 \\ 0 & \mathbf{M}^{\downarrow}_{C_n} \end{pmatrix} = \det \mathbf{M}^{\uparrow}_{C_n} \det \mathbf{M}^{\downarrow}_{C_n}, \tag{3.67}$$

all $(2n) \times (2n)$ determinants presented in the general case can be reduced to 2 determinants of $n \times n$ matrices, thus greatly reducing the computational effort. For a more detailed description of this case, find the equations exploiting the separation of the spin blocks in reference [10].

Delayed updates

In the case of Hubbard type interactions, analogy to the Hirsch Fye algorithm [8, 36] teaches us that in addition to the standard CT-INT updates, a third move may be introduced, flipping one Ising spin s in on vertex of the configuration, i.e. the move

$$[\tau, i, s] \to [\tau, i, -s] \,. \tag{3.68}$$

The introduction of this kind of moves requires of course the extension of the stochastic process $T_{C_n \to C'_n}$ which can be easily accomplished.

Clearly, as in the case of vertex addition and removal, the expensive part of the calculation is again the determination of the determinant ratio for both spin blocks

$$\frac{\det \mathbf{M}^{\sigma}_{C'_n}}{\det \mathbf{M}^{\sigma}_{C_n}}, \tag{3.69}$$

where C'_n is the configuration with s_x flipped in vertex v_x.

Because of equation (3.62), it is obvious that

$$\mathbf{M}^{\sigma}_{C'_n} = \mathbf{M}^{\sigma}_{C_n} + \begin{pmatrix} 0 & 0 & 0 \\ 0 & 2\sigma s_x \delta & 0 \\ 0 & 0 & 0 \end{pmatrix} . \tag{3.70}$$

Here, the blocks are sized such that the only nonzero matrix element $2\sigma s_x \delta$ corresponds to the x, x element of the matrix. Using the matrix determinant lemma presented in section B.1.3, the required determinant ratio can be obtained without difficulty:

$$\det(\mathbf{M}^{\sigma}_{C'_n}) = \det(\mathbf{M}^{\sigma}_{C_n}) \det\left(1 + \mathbf{v}^T (\mathbf{M}^{\sigma}_{C_n})^{-1} \mathbf{u}\right) = \det(\mathbf{M}^{\sigma}_{C_n}) \left(1 + 2\sigma s_x \delta \left((\mathbf{M}^{\sigma}_{C_n})^{-1}\right)_{x,x}\right), \tag{3.71}$$

as $\mathbf{u}_i = \delta_{i,x}$ and $\mathbf{v}_i = 2\sigma s \delta \delta_{i,x}$. Apparently, we only have to look up the (x, x) element of the inverse matrix $\left(\mathbf{M}^{\sigma}_{C_n}\right)^{-1}$, which we *have in memory*. So the calculation of the acceptance probability of a single spin flip is extremely cheap!

---

[8] Actually, the weight can still vanish for some configurations, we only exclude configurations here, that would have weight 0 due to the bare vertex V^0.

Once the move is accepted, the inverse matrices has to be updated, what can be done easily using the well known *Sherman-Morrison* formula (cf. e.g. [37])

$$\left[\mathbf{M}^{\sigma}_{C'_n}\right]^{-1} = \left[\mathbf{M}_{C_n} + \mathbf{u}\mathbf{v}^T\right]^{-1} = \left[\mathbf{M}^{\sigma}_{C_n}\right]^{-1} - \frac{\left[\mathbf{M}^{\sigma}_{C_n}\right]^{-1} \mathbf{u}\mathbf{v}^T \left[\mathbf{M}^{\sigma}_{C_n}\right]^{-1}}{1 + \mathbf{v}^T \left[\mathbf{M}^{\sigma}_{C_n}\right]^{-1} \mathbf{u}}. \tag{3.72}$$

with the choices of $\mathbf{u}$ and $\mathbf{v}$ given above. As pointed out by Alvarez et. al. (cf. e.g. [19, 38]), this equation has the numerical drawback that we have to calculate an *outer product* of the column vector $\left[\mathbf{M}^{\sigma}_{C_n}\right]^{-1} \mathbf{u}$ with the row vector $\mathbf{v}^T \left[\mathbf{M}^{\sigma}_{C_n}\right]^{-1}$, an operation which has an extremely bad floating point operations per memory access ratio. This is hurtful because modern computers can perform floating point operations orders of magnitude faster than memory access and therefore a naive implementation of the spin flip move would waste a big part of the calculation time waiting for data stored in the memory.

The method that has been proposed to circumvent this problem e.g. in references [19, 38] is the following: Instead of proposing one single spin flip in the Markov chain and then allowing for the proposal of other moves subsequently, the stochastic process should be changed slightly such as to propose a certain number N_{flip} of single spin flip moves in a row before moving on to different moves. This is the only change in the stochastic process and the implementation details does not touch it any further.

As we have already seen, for the calculation of the acceptance probability of the flip of spin x, we only need *one* element of the inverse Green's function matrix. The trick is now to calculate the needed elements on the fly and to *delay* the full update of the inverse matrix for a number of N_{delay} spin flips. The calculation of intermediate matrix elements is then simply done by taking matrix elements of the Sherman Morrison formula. This way, the final update of the inverse matrix is a rank N update with N being the number of accepted spin flips. This kind of updates has a greatly improved floating point operations per memory access ratio and is therefore much more efficient. In our general code, performance gain claims of orders of magnitude [38] could not be reproduced completely but a speedup for $N_{\text{delay}} > 10$ of factors of $2 \ldots 8$ could be seen depending on the problem parameters as well as on cache sizes of the used CPUs.

Improved estimators

If we can identify configurations C_n and $\tilde{C}_n$ in the Markov chain that carry the same weight $W(C_n) = W(\tilde{C}_n)$, it is possible to construct an improved estimator that effectively integrates over all equivalent configurations. This idea has already been used in order to introduce an improved estimator for the single particle Green's function $G(\mathbf{k}, \mathrm{i}\omega_n)$ in Matsubara frequencies and momentum space and guarantees the reduction of the variance of the estimator, as more configurations of the configuration space are sampled synchronously.

It is easy to see that the transposition of the Green's function matrix M_{C_n} does not change the weight of a configuration, as the determinant in equation (3.12) is invariant under transposition of the matrix. However, the transposed matrix belongs to a different configuration of Hubbard vertices

$$\tilde{C}_n = \left\{(\beta - \tau_1, -x_1, s_1), \ldots, (\beta - \tau_n, -x_n, s_n)\right\}. \tag{3.73}$$

Exploiting this property, we obtain an improved estimator $\langle\langle O \rangle\rangle_{C_n, \tilde{C}_n}$ for the observable O:

$$\langle\langle O \rangle\rangle_{C_n, \tilde{C}_n} = \frac{1}{2}\left(\langle\langle O \rangle\rangle_{C_n} + \langle\langle O \rangle\rangle_{\tilde{C}_n}\right). \tag{3.74}$$

This method is especially intriguing as it improves data quality at virtually zero cost.

3.6. Impurity problem with superconducting leads

A very interesting class of problems for which CT-INT is extremely well suited are *impurity problems*. Here we present the form of the algorithm suited for an impurity problem with superconducting leads as discussed in chapter 5. We will closely follow and partly reproduce work published in reference [24]. This example shows that the method is indeed very well applicable to the case of a non spin diagonal Green's function, i.e. if $G_{\uparrow\downarrow}(\tau) \neq 0$.

For the numerically exact solution of the so called *BCS-Anderson-model* presented in detail in chapter 5, we use CT-INT boiled down to the impurity formulation.

As pointed out in [9, 10] the interacting Hamiltonian H_U in Eq. (5.4) can up to a constant be rewritten as

$$H_U = -\frac{U}{2} \sum_{s=\pm 1} \left(d_\uparrow^\dagger d_\uparrow - \alpha_\uparrow^s \right) \left(d_\downarrow^\dagger d_\downarrow - \alpha_\downarrow^s \right) \tag{3.75}$$

introducing the parameters α_σ^s to minimize the sign problem. For the present case, a choice of $\alpha_\uparrow^s = \alpha_\downarrow^s = \frac{1}{2} + s\delta$ with $\delta = \frac{1}{2} + 0^+$ was found to completely eliminate the sign problem at half filling, even after the complex phase factors $\exp(i\phi_\alpha)$ in the Hamiltonian were introduced.

This form of the interacting Hamiltonian is equivalent to the Hubbard interaction on a single site (the impurity) and the algorithm can be derived easily from the general form as before by noting that the interaction vertex now only depends on an imaginary time τ and the Ising spin s and is given by

$$V^0_{\sigma,\sigma'}(i,\tau;j,\tau') = \left(-\frac{U}{2}\right) \delta_{\sigma,\uparrow}\delta_{\sigma,\downarrow}\delta(\tau-\tau')\delta_{i,j}\delta_{i,d}, \tag{3.76}$$

where d represents the index of the impurity site. Let us however, reproduce the work published in [24] here to provide a more practical derivation of the algorithm for this simple case.

Using perturbation theory, the partition function Z of the full Hamiltonian (5.4) can be written as:

$$\begin{aligned} \frac{Z}{Z_0} &= \langle T \mathrm{e}^{-\int_0^\beta \mathrm{d}\tau H_U(\tau)} \rangle_0 = \\ &= \sum_{n=0}^{\infty} \left(\frac{U}{2}\right)^n \int_0^\beta \mathrm{d}\tau_1 \ldots \int_0^{\tau_{n-1}} \mathrm{d}\tau_n \sum_{s_1,\ldots,s_n} \times \\ &\times \langle T \left(\hat{n}_\uparrow(\tau_1) - \alpha_\uparrow^{s_1}\right) \ldots \left(\hat{n}_\downarrow(\tau_n) - \alpha_\downarrow^{s_n}\right) \rangle_0 , \end{aligned} \tag{3.77}$$

with the number operators $\hat{n}_\sigma = d_\sigma^\dagger d_\sigma$ and the thermal expectation value $\langle \bullet \rangle_0 = \frac{1}{Z_0} \operatorname{Tr}\left[\mathrm{e}^{-\beta H_0} \bullet\right]$. As H_0 is a noninteracting Hamiltonian, Wick's theorem holds, and the expectation value $\langle T(\hat{n}_\uparrow(\tau_1) - \alpha_\uparrow^1) \ldots (\hat{n}_\downarrow(\tau_n) - \alpha_\uparrow^n) \rangle_0$ can be cast in a determinant of a matrix $\mathbf{M}_{C_n}$ of size $2n \times 2n$, where C_n is a configuration of vertices $\{\tau_i, s_i\}$. In contrast to the formulation for the Hubbard model given in [10], we do not need to include an index for the lattice site as we only have one correlated site, the impurity. The Matrix $\mathbf{M}_{C_n}$ is not block diagonal for the two spin sectors in the case $\Delta \neq 0$, so we cannot factor the determinant in two determinants of $n \times n$ matrices. Finally, the partition function of the model is given by

$$\frac{Z}{Z_0} = \sum_{C_n} \left(\frac{U}{2}\right)^n \det \mathbf{M}_{C_n}, \tag{3.78}$$

where the sum runs over all possible configurations C_n of vertices as in [10]. The matrix $\mathbf{M}_{C_n}$ is defined by

$$\mathbf{M}_{C_n} = \begin{pmatrix} \mathbf{G}^0_{dd}(\tau_1,\tau_1) - \boldsymbol{\alpha}_1 & \ldots & \mathbf{G}^0_{dd}(\tau_n,\tau_1) \\ \vdots & \ddots & \vdots \\ \mathbf{G}^0_{dd}(\tau_1,\tau_n) & \ldots & \mathbf{G}^0_{dd}(\tau_n,\tau_n) - \boldsymbol{\alpha}_n \end{pmatrix} \tag{3.79}$$

using the 2×2 Green's function matrices $\mathbf{G}^0_{dd}(\tau,\tau') = \begin{pmatrix} \langle T d_\uparrow^\dagger(\tau) d_\uparrow(\tau') \rangle_0 & \langle T d_\downarrow^\dagger(\tau) d_\uparrow(\tau') \rangle_0 \\ \langle T d_\uparrow^\dagger(\tau) d_\downarrow(\tau') \rangle_0 & \langle T d_\downarrow^\dagger(\tau) d_\downarrow(\tau') \rangle_0 \end{pmatrix}$ and with $\boldsymbol{\alpha}_i = \begin{pmatrix} \alpha_\uparrow^i & 0 \\ 0 & \alpha_\downarrow^i \end{pmatrix}$.

A similar reasoning yields an expression for the thermal expectation value $\langle O(\tau) \rangle = \frac{1}{Z} \operatorname{Tr}\left[\mathrm{e}^{-\beta H} O(\tau)\right]$ of the full model:

$$\langle O(\tau) \rangle = \frac{\sum_{C_n} \left(\frac{U}{2}\right)^n \det \mathbf{M}_{C_n} \langle\langle O(\tau) \rangle\rangle_{C_n}}{\sum_{C_n} \left(\frac{U}{2}\right)^n \det \mathbf{M}_{C_n}}. \tag{3.80}$$

Here $\langle\langle O(\tau)\rangle\rangle_{C_n}$ is the contribution of the configuration C_n to the observable $O(\tau)$, which is given by

$$\langle\langle O(\tau)\rangle\rangle_{C_n} = \frac{\langle T(\hat{n}_\uparrow(\tau_1) - \alpha_\uparrow^1)\dots(\hat{n}_\downarrow(\tau_n) - \alpha_\downarrow^n)O(\tau)\rangle_0}{\langle T(\hat{n}_\uparrow(\tau_1) - \alpha_\uparrow^1)\dots(\hat{n}_\downarrow(\tau_n) - \alpha_\downarrow^n)\rangle_0}. \tag{3.81}$$

From this equation, we can easily use the concepts presented for the general case above and generate a Markov chain of configurations distributed according to $W(C_n)$ (note the absence of the sign problem.), as discussed above. It is important to realize that this is a concrete example, where the separation of the matrices $\mathbf{M}_{C_n}$ into two spin blocks does not occur.

3.7. Conclusion and Outlook

In this chapter, we have discussed various technical aspects of CT-INT in extensive detail. The reader should be able to make use of the information collected here and understand the method completely, enabling him or her to implement the method in a computer code and give an overview about the different tricks used in modern CT-INT codes.

In contrast to most other presentations of the algorithm, multi vertex updates have been discussed here, as the mathematical formulation can be provided elegantly by generalizing all matrix equations to block equations.

The actual benefit of multi-vertex updates is however extremely hard to quantify and would require a systematic and problem dependent study of the parameters of the stochastic process in combination with the actual CPU time needed to acquire a specific accuracy. This involves a complete and careful error analysis in order to be sure that autocorrelation times for the requested observable (!) are overcome by the simulation. General or even trustworthy claims can therefore not be made here but it should be noted that the author found that tuning proposal probabilities can bring a weak performance factor[9]. This is a really involved problem, though, that also depends on the computer architecture at hand as e.g. cache sizes in combination with the perturbation order matter. To get an idea of how much can be expected in an ideal case, it should be repeated that the introduction of delayed updates has been reported to bring an improvement in CPU time of about *one order of magnitude* (cf. [38]).

The reduction of the general formulation to two example cases has been given mostly for pedagogical reasons and gives an idea of the great variety of problems for which the method can be used. The most complicated forms of the interaction that have been studied so far are long range interactions [31] and imaginary time retarded interactions [10], however additional complexity may be introduced by the noninteracting part of the Hamiltonian as has been shown in reference [24] for a complex Nambu spinor Green's function also discussed in section 3.6 as well as in chapter 5, where the results are presented and the power of the method becomes apparent.

One fascinating example for the remarkable flexibility of the method that has not been mentioned here is the formulation on the generalized Keldysh contour, allowing for a real time evolution and the study of non equilibrium physics within the bounds of the domain accessible due to the complex phase problem that is rather severe in this case at long evolution times. This has been demonstrated by Florian Goth and Fakher F. Assaad in reference [39].

We also describe how configurations of equal weight can be identified and used for the creation of improved estimators. This is useful for the calculation of two particle quantities and allows to exploit a given configuration as much as possible while economizing CPU time.

---

[9] Think of something like 1.5 to get a feeling.

4. Two particle quantities

In recent years, the numerical interest in general two particle quantities given by a four point Green's function $G_4(q;k,p)$ has emerged mostly for technical reasons:

- Methods like the Dynamical mean field theory (DMFT) and its generalizations give access to two particle quantities in the thermodynamic limit — such as susceptibilities $\chi(\mathbf{q},\mathrm{i}\nu)$ — only via the corresponding irreducible vertex $\Gamma(q;k,p)$, which is obtained from $G_4(q;k,p)$ through the Bethe Salpeter equation as detailed in section 4.6.

- Methods like the Dynamical vertex approximation (DΓA)[18], the dual fermion method [17] or the Parquet formalism [40, 41] are formulated in terms of self consistency equations on the two particle level, i.e. through $\Gamma(q;k,p)$.

In this chapter, we will present a detailed theoretical study of two particle quantities in the particle hole channel. The focus lies clearly on the methodological part aiming for a proof of concept and the goal is to present a method to compute two particle quantities using the example of the dynamical spin susceptibility in DCA using CT-INT in a rigorous way. Special care is taken in the data analysis part in order to provide a reliable estimate of the covariance matrix $\mathrm{Cov}(\chi(\mathbf{q},\mathrm{i}\nu))$ which is needed for a meaningful analytic continuation of the imaginary frequency result to real frequencies using the stochastic maximum entropy method [42].

The difficulty of this task lies in the enormous amount of numerical data that has to be computed, stored and analyzed. This can already be understood by noting that the two particle Green's function $G_4(q;k,p)$ is a rank 6 tensor, as it depends on the three momenta $\mathbf{k}$, $\mathbf{p}$ and $\mathbf{q}$ as well as on two *internal*[1] fermionic Matsubara frequencies $\mathrm{i}\omega_n$ and $\mathrm{i}\omega'_n$ in addition to the *external* bosonic Matsubara frequency.

In order to provide sound and verified results, we will first study general properties of the two particle Green's functions and proceed with calculations on an exactly solvable system: The Hubbard model on a finite size 2×2 cluster. The comparison with exact results obtained by exact diagonalization will provide a line of argumentation for the method employed. In section 4.6 we will finally step up to the thermodynamic limit of the 2D Hubbard model and present DCA results for the dynamical spin susceptibility using a 2×2 cluster. While it is known from previous results (e.g. [43]) that finite size cluster DCA results are biased[2], this is nevertheless a first step in the reliable calculation of momentum resolved dynamical two particle quantities including nonlocal and vertex corrections. Future developments in the availability of computational resources will provide access to larger clusters including further nonlocal corrections. Note that the method discussed here is applicable without changes to larger clusters and limited only by the required CPU time and memory and — as will become clear in the data analysis part — the amount of fast permanent storage.

4.1. Channels

The most general two particle Green's function in a many electron system can be written down in the following way

$$G_4(1234) = \mathcal{N}\,\langle\, c^{\#_1}_{\sigma_1,k_1} c^{\#_2}_{\sigma_2,k_2} c^{\#_3}_{\sigma_3,k_3} c^{\#_4}_{\sigma_4,k_4} \,\rangle\,. \tag{4.1}$$

---

[1] The nomenclature will become more apparent later, when we remind ourselves that a physical *susceptibility* — which is in fact the real quantity of interest — is obtained by summing over the internal momenta and frequencies k and p and depends only on the external momentum and frequency q.

[2] For example in finite cluster DCA calculations a nonvanishing Neel temperature T_N for an antiferromagnetic phase transition can be found in 2D, which is a clear violation of the Mermin Wagner theorem. In systematic studies, however, it is found that for increasing cluster size T_N is found to extrapolate to 0 and the exact result is recovered for infinite cluster size.

In this general form, appearing operators $c^{\#}_{\sigma,k}$ can be either creation operators $c^{\dagger}_{\sigma,k}$ for a particle with spin σ and combined imaginary frequency and momentum $k = (\mathrm{i}\omega_n, \mathbf{k})$ or the corresponding annihilation operators $c_{\sigma,k}$. $\mathcal{N}$ is just a normalization factor.

It is clear that for special systems, the freedom in $G_4(1234)$ is rapidly reduced as we will impose a non-broken U(1) symmetry associated with charge conservation, which implies that only two operators may be creation operators, whereas the other two have to be annihilation operators in consequence. Let us use the convention $\#_1 = \#_3 = \dagger$.

Furthermore, in the thermodynamic limit or in a finite system by introduction of periodic boundary conditions, we have translation invariance on the lattice, which is linked to lattice momentum conservation up to a reciprocal lattice vector[3].

In addition to that, we also have conservation of frequency which stems from the fact that in imaginary time the two particle Green's function only depends on 3 imaginary time variables because of imaginary time translation invariance:

$$\begin{aligned}
\langle T c_1^{\#_1}(\tau_1) c_2^{\#_2}(\tau_2) c_3^{\#_3}(\tau_3) c_4^{\#_4}(\tau_4) \rangle &= \mathrm{sgn}(\pi)\, \langle c_{\pi(1)}^{\#_{\pi(1)}}(\tau_{\pi(1)}) c_{\pi(2)}^{\#_{\pi(2)}}(\tau_{\pi(2)}) c_{\pi(3)}^{\#_{\pi(3)}}(\tau_{\pi(3)}) c_{\pi(4)}^{\#_{\pi(4)}}(\tau_{\pi(4)}) \rangle \\
&= \mathrm{sgn}(\pi) \frac{1}{Z}\, \mathrm{Tr}\left(\mathrm{e}^{-\beta H} \mathrm{e}^{\tau_{\tilde{1}} H} c_{\tilde{1}}^{\#_{\tilde{1}}} \mathrm{e}^{(\tau_{\tilde{2}} - \tau_{\tilde{1}})H} c_{\tilde{2}}^{\#_{\tilde{2}}} \mathrm{e}^{(\tau_{\tilde{3}} - \tau_{\tilde{2}})H} c_{\tilde{3}}^{\#_{\tilde{3}}} \mathrm{e}^{(\tau_{\tilde{4}} - \tau_{\tilde{3}})H} c_{\tilde{4}}^{\#_{\tilde{4}}} \mathrm{e}^{-\tau_{\tilde{4}} H} \right) \\
&= \frac{1}{Z}\, \mathrm{sgn}(\pi)\, \langle c_{\tilde{1}}^{\#_{\tilde{1}}}(\tau_{\tilde{1}} - \tau_{\tilde{4}}) c_{\tilde{2}}^{\#_{\tilde{2}}}(\tau_{\tilde{2}} - \tau_{\tilde{4}}) c_{\tilde{3}}^{\#_{\tilde{3}}}(\tau_{\tilde{3}} - \tau_{\tilde{4}}) c_{\tilde{4}}^{\#_{\tilde{4}}}(0) \rangle\,,
\end{aligned} \tag{4.2}$$

because of the cyclic property of the trace. Here π is the permutation that brings $\{\tau_1, \tau_2, \tau_3, \tau_4\}$ in time order.

In order to implement our convention that momentum and frequency 1 and 3 should be associated with a creation operator, we will use the notation $\bar{1}$ and $\bar{3}$ for them. Finally, we will ensure the conditions

$$\mathbf{k_1} + \mathbf{k_3} = \mathbf{k_2} + \mathbf{k_4} \quad \text{and} \quad \mathrm{i}\omega_1 + \mathrm{i}\omega_3 = \mathrm{i}\omega_2 + \mathrm{i}\omega_4 \tag{4.3}$$

by defining

$$k_1 = k, \quad k_2 = k + q, \quad k_3 = p, \quad k_4 = p - q. \tag{4.4}$$

And thus limiting our discussion to the so called *particle hole* channel. Depending on how the transfer momentum $\mathbf{q}$ and its associated (bosonic) transfer frequency are defined, one can also study the particle particle or the vertical particle hole channel (cf e.g. [44]) but these will be unimportant to our further discussion. Note that the nomenclature stems from a diagrammatic way of thinking about two particle scattering processes and the way of labelling incoming and outgoing momenta. A complete and detailed analysis eventually leads to a set of diagrammatic equations, the *parquet* equations.

4.2. Symmetries of the two particle Greenfunction

In this section[4] we study the symmetries of the two particle Green's function $G_4(\bar{1}2\bar{3}4)$ defined by:

$$G_4(\bar{1}2\bar{3}4) = \langle \xi_1^{\dagger} \xi_2 \xi_3^{\dagger} \xi_4 \rangle = \mathcal{N} \int_0^{\beta} \mathrm{d}(1234) \mathrm{e}^{i\boldsymbol{\omega}_{\mathbf{n}} M \boldsymbol{\tau}} \mathrm{e}^{-i\mathbf{k} M \mathbf{x}} \langle T c_1^{\dagger} c_2 c_3^{\dagger} c_4 \rangle \tag{4.5}$$

with

$$c_i^{(\dagger)} := c^{(\dagger)}(\tau_i, x_i, \sigma_i) \quad \text{and} \quad \xi_i^{(\dagger)} := \xi^{(\dagger)}(i\omega_i, k_i, \sigma_i) \tag{4.6}$$

and[5]

$$M_{ij} = \delta_{ij} (-1)^{(j-1)} \quad i, j \in \{1, 2, 3, 4\} \tag{4.7}$$

---

[3] This will always be understood implicitly without further comment whenever we write equations containing lattice momenta. The equation $\mathbf{k_1} + \mathbf{k_3} = \mathbf{k_2} + \mathbf{k_4}$ has to be interpreted as an equality of left and right hand side *after mapping them to the first Brillouin zone.*

[4] The collection of symmetries of the two particle Green's function was done in collaboration with Jutta Ortloff and can also be found in her PhD thesis (ref. [45]). Information about symmetries in slightly different notation can also be found in ref. [46]

[5] This compact notation is literally only applicable for one spatial dimension, but may be generalized to higher dimensions.

4.2.1. General Symmetries

SU(2) Symmetry: Introduction of $G_4^{\perp}(\bar{1}2\bar{3}4)$

Because of SU(2) symmetry, we can restrict ourselves to the "S_+S_-"-spin susceptibility ($G_4^{\perp}$), i.e. the spin indices will be pinned to $\sigma_1 = \uparrow, \sigma_2 = \downarrow, \sigma_3 = \downarrow, \sigma_4 = \uparrow$. (Referring to this definition of $G_4^{\perp}$, we will neglect the spin indices in our further discussion)

A complete analysis of SU(2) symmetry would yield (cf. e.g. [45, 47]):

$$G_4^{\|}(\bar{1}2\bar{3}4) = G_4^{\perp}(\bar{1}2\bar{3}4) - G_4^{\perp}(\bar{3}2\bar{1}4). \tag{4.8}$$

with $\| = \sigma\sigma\sigma\sigma$ and $\perp = \sigma\sigma'\sigma'\sigma$.

RAS-Symmetry: Remainder of Antisymmetry $G_4^{\perp}(\bar{1}2\bar{3}4) = G_4^{\perp}(\bar{3}4\bar{1}2)$

The canonical fermionic anticommutation relations lead to the exchangability of creators ($\bar{1} \leftrightarrow \bar{3}$) and annihilators ($2 \leftrightarrow 4$) yielding the sign of the corresponding permutation. Note, that because of the pinning of the spin indices, in our case, we are not allowed to do this independently and we have to apply SU(2) symmetry to get:

$$G_4^{\perp}(\bar{1}2\bar{3}4) = G_4^{\perp}(\bar{3}4\bar{1}2). \tag{4.9}$$

Auxiliary symmetry $\langle T[c_1^\dagger c_2 c_3^\dagger c_4]\rangle^* = \langle T[c_{4_\beta}^\dagger c_{3_\beta} c_{2_\beta}^\dagger c_{1_\beta}]\rangle$

To prove this, we need to exchange a hermitian conjugation with the time ordering operator:

$$c(\tau, x)^\dagger = (\mathrm{e}^{\tau H} c_x \mathrm{e}^{-\tau H})^\dagger = \mathrm{e}^{-\tau H} c_x^\dagger \mathrm{e}^{\tau H} = c^\dagger(-\tau, x). \tag{4.10}$$

Using this, we have:

$$(T[c_1^\dagger c_2 c_3^\dagger c_4])^\dagger = T[(c_1^\dagger c_2 c_3^\dagger c_4)^\dagger]. \tag{4.11}$$

(Proof trivial, think of a time ordering permutation.) Now, using $\operatorname{Tr} O = \operatorname{Tr} O^T$ we have:

$$\begin{aligned} \langle T c_1^\dagger c_2 c_3^\dagger c_4 \rangle^* &= \frac{1}{Z} \operatorname{Tr} \left(T[\mathrm{e}^{-\beta H} c_1^\dagger c_2 c_3^\dagger c_4] \right)^* = \frac{1}{Z} \operatorname{Tr} \left(T[\mathrm{e}^{-\beta H} c_{4_\beta}^\dagger c_{3_\beta} c_{2_\beta}^\dagger c_{1_\beta}] \right) \\ &= \langle T[c_{4_\beta}^\dagger c_{3_\beta} c_{2_\beta}^\dagger c_{1_\beta}] \rangle \end{aligned} \tag{4.12}$$

Note, that

$$c_{i_\beta}^{(\dagger)} = c^{(\dagger)}(\beta - \tau_i, x_i) \tag{4.13}$$

and we also inserted $\mathbf{1} = \mathrm{e}^{-\beta H} \mathrm{e}^{\beta H}$ in between the c operators and used the cyclicity of the trace.

4.2.2. Symmetries for real Hamiltonians: $H = H^T$

r-Symmetry $G_4^{\perp}(\bar{1}2\bar{3}4)^* = G_4^{\perp}(\bar{1}_r 2_r \bar{3}_r 4_r)$ for real Hamiltonians

In the case of a real Hamiltonian, we have: $\langle T c_1^\dagger c_2 c_3^\dagger c_4 \rangle \in \mathbb{R}$, because everything can be written in terms of real matrices.

$$G_4^{\perp}(\bar{1}2\bar{3}4)^* = \int_0^\beta \mathrm{d}(1234) \mathrm{e}^{-i\boldsymbol{\omega}_\mathbf{n} M \boldsymbol{\tau}} \mathrm{e}^{+i\mathbf{k} M \mathbf{x}} \langle T c_1^\dagger c_2 c_3^\dagger c_4 \rangle = G_4^{\perp}(\bar{1}_r 2_r \bar{3}_r 4_r). \tag{4.14}$$

Here we use the notation

$$\xi_{i_r} = \xi(-i\omega_i, -k_i) \tag{4.15}$$

RAS-r-Symmetry $G_4^{\perp}(\bar{1}2\bar{3}4) = G_4^{\perp}(\bar{3}_r 4_r \bar{1}_r 2_r)^*$ for real Hamiltonians

Combining already derived symmetries, we get:

$$G_4^{\perp}(\bar{1}2\bar{3}4) \overset{(4.9)}{=} G_4^{\perp}(\bar{3}4\bar{1}2) \overset{(4.14)}{=} G_4^{\perp}(\bar{3}_r 4_r \bar{1}_r 2_r)^*. \tag{4.16}$$

κ-Symmetry $G_4^{\perp}(\bar{1}2\bar{3}4) = G_4^{\perp}(\bar{4}_\kappa 3_\kappa \bar{2}_\kappa 1_\kappa)$ for real Hamiltonians

Here we use that for real Hamiltonians, $\langle T c_1^\dagger c_2 c_3^\dagger c_4 \rangle \in \mathbb{R}$:

$$\begin{aligned}
G_4^{\perp}(\bar{1}2\bar{3}4) &= \int_0^\beta \mathrm{d}(1234) \mathrm{e}^{i\boldsymbol{\omega}_\mathbf{n}{}^T M \boldsymbol{\tau}} \mathrm{e}^{-i\mathbf{k}^T M \mathbf{x}} \langle T c_1^\dagger c_2 c_3^\dagger c_4 \rangle \\
&= \int_0^\beta \mathrm{d}(1234) \mathrm{e}^{i\boldsymbol{\omega}_\mathbf{n}{}^T M \boldsymbol{\tau}} \mathrm{e}^{-i\mathbf{k}^T M \mathbf{x}} \langle T c_{4_\beta}^\dagger c_{3_\beta} c_{2_\beta}^\dagger c_{1_\beta} \rangle \\
&\overset{\tau \leftarrow \beta - \tau}{=} \int_0^\beta (-1)^4 \mathrm{d}(1234) \mathrm{e}^{-i\boldsymbol{\omega}_\mathbf{n}{}^T M \boldsymbol{\tau}} (-1)^4 \mathrm{e}^{-i\mathbf{k}^T M \mathbf{x}} \langle T c_4^\dagger c_3 c_2^\dagger c_1 \rangle \\
&= \int_0^\beta \mathrm{d}(1234) \mathrm{e}^{i\boldsymbol{\omega}_\mathbf{n}{}^T (-M) \boldsymbol{\tau}} \mathrm{e}^{-i(-\mathbf{k})^T (-M) \mathbf{x}} \langle T c_4^\dagger c_3 c_2^\dagger c_1 \rangle \\
&= G_4^{\perp}(\bar{4}_\kappa 3_\kappa \bar{2}_\kappa 1_\kappa).
\end{aligned} \tag{4.17}$$

Note, that we need to change the sign matrix M to $-M$ in order to identify the term with the Fourier transform convention for $G_4^{\perp}$. Further, we used the notation:

$$\xi_{i_\kappa} = \xi(i\omega_i, -k_i). \tag{4.18}$$

RAS-κ-Symmetry $G_4^{\perp}(\bar{1}2\bar{3}4) = G_4^{\perp}(\bar{2}_\kappa 1_\kappa \bar{4}_\kappa 3_\kappa)$ for real Hamiltonians

Combining already derived symmetries, we get:

$$G_4^{\perp}(\bar{1}2\bar{3}4) \overset{(4.9)}{=} G_4^{\perp}(\bar{3}4\bar{1}2) \overset{(4.17)}{=} G_4^{\perp}(\bar{2}_\kappa 1_\kappa \bar{4}_\kappa 3_\kappa) \tag{4.19}$$

w-Symmetry $G_4^{\perp}(\bar{1}2\bar{3}4)^* = G_4^{\perp}(\bar{4}_w 3_w \bar{2}_w 1_w)$ for real Hamiltonians

Combining symmetries from subsubsection 4.2.2 , we get:

$$G_4^{\perp}(\bar{1}2\bar{3}4)^* = G_4^{\perp}(\bar{1}_r 2_r \bar{3}_r 4_r) = G_4^{\perp}((\bar{4}_r)_\kappa (3_r)_\kappa (\bar{2}_r)_\kappa (1_r)_\kappa) = G_4^{\perp}(\bar{4}_w 3_w \bar{2}_w 1_w). \tag{4.20}$$

with

$$(\xi_{i_r})_\kappa = \xi_{i_w} = \xi(-i\omega_i, k_i). \tag{4.21}$$

RAS-w-Symmetry $G_4^{\perp}(\bar{1}2\bar{3}4)^* = G_4^{\perp}(\bar{2}_w 1_w \bar{4}_w 3_w)$ for real Hamiltonians

Combining already derived symmetries, we get:

$$G_4^{\perp}(\bar{1}2\bar{3}4) \overset{(4.9)}{=} G_4^{\perp}(\bar{3}4\bar{1}2) \overset{(4.20)}{=} G_4^{\perp}(\bar{2}_w 1_w \bar{4}_w 3_w)^* \tag{4.22}$$

Efficient Parametrization

As noted in section 4.1, we only have 3 independent frequencies/momenta. Let us therefore define with a bosonic multiindex $Q = (i\nu, q)$:

$$\begin{aligned} &i\omega_2 = i(\omega_1 + \nu), \quad i\omega_4 = i(\omega_3 - \nu), \quad k_2 = k_1 + q, \quad k_4 = k_3 - q. \\ &G_4^{\perp}(Q; \bar{1}\bar{3}) = G_4^{\perp}(\bar{1}(1+Q)\bar{3}(3-Q)) \end{aligned} \tag{4.23}$$

The above symmetries have the following implications for $G_4^{\perp}(Q; \bar{1}\bar{3})$:

$$G_4^{\perp}(Q; \bar{1}\bar{3}) \overset{(4.9)}{=} G_4^{\perp}(Q_r; \bar{3}\bar{1}) \tag{4.24}$$

$$G_4^{\perp}(Q; \bar{1}\bar{3}) \overset{(4.14)}{=} G_4^{\perp}(Q_r; \bar{1}_r\bar{3}_r)^* \tag{4.25}$$

$$G_4^{\perp}(Q; \bar{1}\bar{3}) \overset{(4.16)}{=} G_4^{\perp}(Q; \bar{3}_r\bar{1}_r)^* \tag{4.26}$$

$$G_4^{\perp}(Q; \bar{1}\bar{3}) \overset{(4.17)}{=} G_4^{\perp}(Q_\kappa; (\bar{3}-Q)_\kappa(\bar{1}+Q)_\kappa) \tag{4.27}$$

$$G_4^{\perp}(Q; \bar{1}\bar{3}) \overset{(4.19)}{=} G_4^{\perp}(Q_w; (\bar{1}+Q)_\kappa(\bar{3}-Q)_\kappa) \tag{4.28}$$

$$G_4^{\perp}(Q; \bar{1}\bar{3}) \overset{(4.20)}{=} G_4^{\perp}(Q_w; (\bar{3}-Q)_w(\bar{1}+Q)_w)^* \tag{4.29}$$

$$G_4^{\perp}(Q; \bar{1}\bar{3}) \overset{(4.22)}{=} G_4^{\perp}(Q_\kappa; (\bar{1}+Q)_w(\bar{3}-Q)_w)^* \tag{4.30}$$

Frequency shift

From this summary of symmetries, it is clear that with nonvanishing Q the center of symmetry shifts. We can therefore redefine frequencies and momenta in the following way:

$$\bar{1}^- = \bar{1} - \frac{Q}{2}^- \quad \text{and} \quad \bar{3}^+ = \bar{3} + \frac{Q}{2}^+. \tag{4.31}$$

Note that bosonic[6] frequency-momenta $\frac{Q}{2}^\pm$ are defined such that

$$\frac{Q}{2}^+ + \frac{Q}{2}^- = Q. \tag{4.32}$$

Using these relations, equation (4.27) reduces to

$$G_4^{\perp}(Q; \bar{1}^-\bar{3}^+) = G_4^{\perp}(Q_\kappa; (\bar{3}^-)_\kappa(\bar{1}^+)_\kappa). \tag{4.33}$$

For $\mathbf{Q} = 0$ and $\mathrm{i}\nu = \frac{4n}{\beta}\pi$ with $n \in \mathbb{Z}$ it is obvious that the choice $\frac{Q}{2}^+ = \frac{Q}{2}^- = \left(\mathrm{i}\frac{\nu}{2}, 0\right)$ fullfills the requirement of bosonic Matsubara frequencies and equation (4.32) and makes it apparent that the center of symmetry under frequency exchange is really shifted by $(\frac{Q}{2}^-, \frac{Q}{2}^+)$. For nonzero $\mathbf{Q}$, the simplest choice is $\frac{Q}{2}^+ = (\mathrm{i}\frac{\nu}{2}^+, \mathbf{Q})$ and $\frac{Q}{2}^- = (\mathrm{i}\frac{\nu}{2}^-, \mathbf{0})$. We will not expand on the symmetry in the momentum domain as the actual treatment might depend on lattice properties and is not as general as the frequency domain.

The case of general bosonic Matsubara frequencies $\mathrm{i}\nu = \frac{2n}{\beta}\pi$ with $n \in \mathbb{Z}$ is treated such that we define $\mathrm{i}\frac{\nu}{2}^\pm = \mathrm{i}\frac{n^\pm}{\beta}\pi$ with $n^- \in \mathbb{Z}$ being the largest *even* number with $n^- < n$ and $n^+ = 2n - n^-$. Therefore, n^+ is also even and both $\mathrm{i}\frac{\nu}{2}^\pm$ are consequently legal bosonic Matsubara frequencies.

---

[6] $\frac{Q}{2}^\pm$ must be implemented such that the corresponding frequencies are *always* bosonic matsubara frequencies and the corresponding momenta are allowed lattice momenta.

4.3. $G_4(q;k,p)$ in the particle hole channel

As already discussed in section 4.1, a general susceptibility in the particle hole channel has the Grassmann number representation

$$G_{4,\mathrm{ph}}^{\sigma_1,\sigma_2,\sigma_3,\sigma_4}(q;k,p) = \frac{1}{\beta N}\left\langle c^\dagger_{\sigma_1,k} c_{\sigma_2,k+q} c^\dagger_{\sigma_3,p} c_{\sigma_4,p-q}\right\rangle, \tag{4.34}$$

We will restrict the following discussion to the case of conserved total spin. This leads to the restriction

$$\sigma_1 + \sigma_3 = \sigma_2 + \sigma_4. \tag{4.35}$$

Therefore, we obtain a 4×4 matrix representation of the general susceptibility in spin space (4.34) putting the spin indices σ_1 and σ_2 in the first index and the spin indices σ_3 and σ_4 in the second index using the ordering $\uparrow\uparrow\to 0$, $\downarrow\downarrow\to 1$, $\uparrow\downarrow\to 2$ and $\downarrow\uparrow\to 3$.

Let us introduce the following shorthand notation for the generalized susceptibility in order to write the matrix in a compact form:

$$\sigma_1\sigma_2\sigma_3\sigma_4 = G_{4,\mathrm{ph}}^{\sigma_1,\sigma_2,\sigma_3,\sigma_4}(q;k,p). \tag{4.36}$$

Thus, we obtain

$$G_{4,\mathrm{ph}}(q;k,p) = \begin{pmatrix} \uparrow\uparrow\uparrow\uparrow & \uparrow\uparrow\downarrow\downarrow & \uparrow\uparrow\uparrow\downarrow & \uparrow\uparrow\downarrow\uparrow \\ \downarrow\downarrow\uparrow\uparrow & \downarrow\downarrow\downarrow\downarrow & \downarrow\downarrow\uparrow\downarrow & \downarrow\downarrow\downarrow\uparrow \\ \uparrow\downarrow\uparrow\uparrow & \uparrow\downarrow\downarrow\downarrow & \uparrow\downarrow\uparrow\downarrow & \uparrow\downarrow\downarrow\uparrow \\ \downarrow\downarrow\uparrow\uparrow & \downarrow\downarrow\downarrow\downarrow & \downarrow\uparrow\uparrow\downarrow & \downarrow\uparrow\downarrow\uparrow \end{pmatrix} \tag{4.37}$$

Of course, not all entries fulfill the condition (4.35), it is obvious, that $\uparrow\uparrow\uparrow\downarrow = 0$, $\uparrow\uparrow\downarrow\uparrow = 0$, $\uparrow\downarrow\uparrow\uparrow = 0$, $\uparrow\downarrow\downarrow\downarrow = 0$, $\downarrow\uparrow\uparrow\uparrow = 0$, $\downarrow\uparrow\downarrow\downarrow = 0$, $\downarrow\downarrow\uparrow\downarrow = 0$, $\downarrow\downarrow\downarrow\uparrow = 0$. Also, $\uparrow\downarrow\uparrow\downarrow = \downarrow\uparrow\downarrow\uparrow = 0$, because the corresponding term contains two creation operators for spin ↑ (↓) but two annihilation operators for spin ↓ (↑), which would not conserve the total spin. Then, $G_{4,\mathrm{ph}}(q;k,p)$ gets the following form:

$$G_{4,\mathrm{ph}}(q;k,p) = \begin{pmatrix} \uparrow\uparrow\uparrow\uparrow & \uparrow\uparrow\downarrow\downarrow & 0 & 0 \\ \downarrow\downarrow\uparrow\uparrow & \downarrow\downarrow\downarrow\downarrow & 0 & 0 \\ 0 & 0 & 0 & \uparrow\downarrow\downarrow\uparrow \\ 0 & 0 & \downarrow\uparrow\uparrow\downarrow & 0 \end{pmatrix} \tag{4.38}$$

The Hamiltonian of the Hubbard model

$$H = -t \sum_{<i,j>,\sigma} c^\dagger_{i,\sigma} c_{j,\sigma} + U \sum_i \left(\hat{n}_{i,\uparrow} - \frac{1}{2}\right)\left(\hat{n}_{i,\downarrow} - \frac{1}{2}\right). \tag{4.39}$$

is naturally invariant under the transformation $\uparrow\leftrightarrow\downarrow$ because of SU(2)-symmetry.

This implies that observables will also obey this symmetry, therefore we directly obtain that $\downarrow\uparrow\uparrow\downarrow = \uparrow\downarrow\downarrow\uparrow$ and $\downarrow\downarrow\uparrow\uparrow = \uparrow\uparrow\downarrow\downarrow$ as well as $\uparrow\uparrow\uparrow\uparrow = \downarrow\downarrow\downarrow\downarrow$. This simplifies the particle-hole channel immensely:

$$G_{4,\mathrm{ph}}(q;k,p) = \begin{pmatrix} \uparrow\uparrow\uparrow\uparrow & \uparrow\uparrow\downarrow\downarrow & 0 & 0 \\ \uparrow\uparrow\downarrow\downarrow & \uparrow\uparrow\uparrow\uparrow & 0 & 0 \\ 0 & 0 & 0 & \uparrow\downarrow\downarrow\uparrow \\ 0 & 0 & \uparrow\downarrow\downarrow\uparrow & 0 \end{pmatrix} \tag{4.40}$$

Diagonalization of this matrix form yields of course the eigenvalues $\uparrow\uparrow\uparrow\uparrow + \uparrow\uparrow\downarrow\downarrow$, $\uparrow\uparrow\uparrow\uparrow - \uparrow\uparrow\downarrow\downarrow$, $\uparrow\downarrow\downarrow\uparrow$ and $\downarrow\uparrow\uparrow\downarrow$. The channel containing $\uparrow\uparrow\uparrow\uparrow + \uparrow\uparrow\downarrow\downarrow$ is called the *charge-channel*, while the other three eigenvalues form the *spin-channel* as the corresponding susceptibilities

$$\chi_{\sigma_1\sigma_2\sigma_3\sigma_4}(q) = \sum_{k,p} G_{4,\mathrm{ph}}^{\sigma_1\sigma_2\sigma_3\sigma_4}(q;k,p). \tag{4.41}$$

are the *charge* ($\chi_{\mathrm{c}}(q)$) and *spin* ($\chi_{\mathrm{s}}^{z}(q)$, $\chi_{\mathrm{s}}^{+-}(q)$ and $\chi_{\mathrm{s}}^{-+}(q)$) susceptibilities[7]. The huge advantage of using the susceptibility χ_{s}^{+-} is that for this quantity the Bethe-Salpeter equation does not have an additional spin structure, i.e. it can be written in terms of rank 6 tensors[8] instead of rank 8 tensors for the accomodation of 2 additional spin indices. This reduces the required complexity already by a factor of 4.

4.4. Calculation of two particle quantities in Matsubara frequencies

Here, we will only look at $G_4^{\perp}(Q;K,P)$ in the spin channel, as all the information of the particle-hole channel is contained in this quantity[9] for an SU(2) symmetric problem, in particular the Hubbard model, wich we will have in mind throughout this section. As we will be dealing with finite size clusters from now on, let us use capital letters K, P for fermionic Matsubara frequency-momenta and Q for a bosonic frequency momentum.

4.4.1. Calculation of $G_4(Q;K,P)$ in the spin channel in CT-INT

The calculation of $G_4(Q;K,P)$ in Matsubara frequencies is extremely expensive in terms of computer time, therefore we have to economize time wherever possible. However, it is instructive to study the direct approach, which makes direct use of Wick's theorem for CT-INT configurations according to equation (3.50) first, before we move on to a reduced approach, which economizes a substantial amount of multiplications by factoring out as many known quantities as possible.

Direct approach

In its Matsubara frequency variant, equation (3.50) for $G_4(Q;K,P)$ reads[10]:

$$\langle\langle G_4^{\perp}(Q;K,P)\rangle\rangle_{C_n} = \frac{1}{\beta N}\langle\langle c^{\dagger}_{\uparrow,K}c_{\downarrow,K+Q}c^{\dagger}_{\downarrow,P}c_{\uparrow,P-Q}\rangle\rangle_{C_n} = -\frac{1}{\beta N}\langle\langle c^{\dagger}_{\uparrow,K}c_{\uparrow,P-Q}\rangle\rangle_{C_n}\langle\langle c^{\dagger}_{\downarrow,P}c_{\downarrow,K+Q}\rangle\rangle_{C_n}. \tag{4.42}$$

with

$$\langle\langle \bar{c}_{\sigma,K}c_{\sigma,P}\rangle\rangle_{C_n} = \delta_{K,P}G^0_{\sigma}(K) - \frac{1}{\beta N}G^0_{\sigma}(K)G^0_{\sigma}(P)\sum_{r,s}\mathrm{e}^{\mathrm{i}(\omega_n\tau_r-\mathbf{K}^T\mathbf{X}_r)}\left(M^{-1}_{\sigma}\right)_{r,s}\mathrm{e}^{-\mathrm{i}(\omega'_n\tau_s-\mathbf{P}^T\mathbf{X}_s)}. \tag{4.43}$$

Clearly, $\langle\langle \bar{c}_{\sigma,K}c_{\sigma,P}\rangle\rangle_{C_n}$ can be easily tabelized for the required Matsubara frequency range and from this table, $\langle\langle G_4(Q;K,P)\rangle\rangle_{C_n}$ can be constructed by iterating over all frequencies and momenta.

This approach, however, has the drawback that we have to look up the bare one particle Green's function $G^0(K)$ for every combination of K and P and that we have to multiply the sum over vertices by two complex numbers during the calculation of table $\langle\langle \bar{c}_{\sigma,K}c_{\sigma,P}\rangle\rangle_{C_n}$. While the computational cost of this operation is not dominant, it is nevertheless preferable to calculate a reduced quantity. This is presented in the following paragraph.

Reduced approach

We will argue that it is possible to reduce the amount of multiplications neccessary in the calculation of the table $\langle\langle \bar{c}_{\sigma,K}c_{\sigma,P}\rangle\rangle_{C_n}$ by multiplying out equation (4.42) and directly measuring the vertex $T(Q;K,P)$

---

[7] The spin sector is built up by S_z, S_+ and S_-.

[8] 3 frequencies and 3 momenta

[9] This is of course only true theoretically, as a redefinition of Q and exploitation of symmetries is required, which can in practice not be done in order to obtain the full information on the same frequency window also in the charge channel.

[10] It is important to note that we only obtain one term because of the conservation of spin. In this case, $G^0_{2,\uparrow\downarrow}(\tau) = 0$ and therefore, the expanded matrix needed for the calculation of $\langle\langle \bar{c}_{\uparrow,K}c_{\downarrow,P}\rangle\rangle_{C_n}$ does not have full rank and its determinant is therefore 0. Thus, the second term from Wick's theorem involving mixed spin contributions vanishes.

instead of the two particle Green's function $G_4^{\perp}(Q;K,P)$. Before writing down the result, let us introduce the short hand notation

$$X_\sigma^{C_n}(K,P) = \sum_{r,s} \mathrm{e}^{\mathrm{i}\left(\omega_n \tau_r - \mathbf{K}^T \mathbf{X}_r\right)} \left(M_\sigma^{-1}\right)_{r,s} \mathrm{e}^{-\mathrm{i}\left(\omega_n' \tau_s - \mathbf{P}^T \mathbf{X}_s\right)}. \tag{4.44}$$

Hence, we obtain:

$$\begin{aligned}\langle\langle G_4^{\perp}(Q;K,P)\rangle\rangle_{C_n} = -\frac{1}{\beta N}\Big[&\delta_{K,P-Q} G_\uparrow^0(K) G_\downarrow^0(K+Q) \\ &- \frac{1}{\beta N}\delta_{P,K+Q} G_\downarrow^0(P) G_\uparrow^0(K) G_\uparrow^0(K) X_\uparrow^{C_n}(K,K) \\ &- \frac{1}{\beta N}\delta_{K,P-Q} G_\uparrow^0(K) G_\downarrow^0(P) G_\downarrow^0(P) X_\downarrow^{C_n}(P,P) \\ &+ \left(\frac{1}{\beta N}\right)^2 G_\uparrow^0(K) G_\downarrow^0(K+Q) G_\uparrow^0(P-Q) G_\downarrow^0(P) X_\uparrow^{C_n}(K,P-Q) X_\downarrow^{C_n}(P,K+Q)\Big]\end{aligned} \tag{4.45}$$

Detailed inspection of this result allows for further simplification, as we can use the fact that[11]

$$-\frac{1}{\beta N} G_\sigma^0(K) G_\sigma^0(K) \left\langle X_\sigma^{C_n}(K,K) \right\rangle = G_\sigma(K) - G_\sigma^0(K). \tag{4.46}$$

Here, the statistical average $\langle \bullet \rangle$ denotes a Monte Carlo average in CT-INT over all (weighted) configurations C_n of vertices as detailed in chapter 3. Note that in a practical calculation, the fully interacting one particle Green's function can be usually calculated to a much higher precision than the two particle Green's function and is — in the context of the DCA — basically already known at the moment when the two particle calculation is started.

Using this simplification and factoring out all vertex-independent quantities, we obtain:

$$\begin{aligned}G_4^{\perp}(Q;K,P) = -\frac{1}{\beta N}\Big[&\delta_{K,P-Q} G_\uparrow^0(K) G_\downarrow^0(K+Q) \\ &+ \delta_{P,K+Q} G_\downarrow^0(P) \left(G_\uparrow(K) - G_\uparrow^0(K)\right) \\ &+ \delta_{K,P-Q} G_\uparrow^0(K) \left(G_\downarrow(P) - G_\downarrow^0(P)\right) \\ &+ \left(\frac{1}{\beta N}\right)^2 G_\uparrow^0(K) G_\downarrow^0(K+Q) G_\uparrow^0(P-Q) G_\downarrow^0(P) \left\langle X_\uparrow^{C_n}(K,P-Q) X_\downarrow^{C_n}(P,K+Q) \right\rangle\Big]\end{aligned} \tag{4.47}$$

At this point, it is already obvious that we only have to calculate the vertex

$$T(Q;K,P) = \left\langle X_\uparrow^{C_n}(K,P-Q) X_\downarrow^{C_n}(P,K+Q) \right\rangle \tag{4.48}$$

From this result, the two particle Green's function can easily be reconstructed via

$$\begin{aligned}G_4^{\perp}(Q;K,P) = &-\frac{1}{\beta N}\delta_{K,P-Q}\Big[-G_\downarrow^0(K) G_\uparrow^0(K+Q) + G_\downarrow^0(P) G_\uparrow(K) + G_\uparrow^0(K) G_\downarrow(P)\Big] \\ &- \left(\frac{1}{\beta N}\right)^3 G_\uparrow^0(K) G_\downarrow^0(K+Q) G_\uparrow^0(P-Q) G_\downarrow^0(P) T(Q;K,P).\end{aligned} \tag{4.49}$$

For a noninteracting system, the vertex $T(Q;K,P)$ vanishes and the two particle Green's function reduces nicely to the correct result.

---

[11] This is of course just the accumulation formula for $G(K)$ as already given in reference [9] and also in chapter 3.

4.4.2. Improved estimator for $T(Q;K,P)$

Following the recipe presented in section 3.5.1, we can enhance the statistics for the measurement of the vertex $T(Q;K,P)$. The configuration of vertices $\tilde{C_n}$ is obtained from C_n by applying the transformations $\tau \to \beta - \tau$ and $x \to -x$ to every vertex $[\tau, x, s]$ of the configuration C_n. This leads to

$$X_\sigma^{\tilde{C_n}}(K,P) = \sum_{r,s} \mathrm{e}^{\mathrm{i}\left(\omega_n[\beta-\tau_r]+\mathbf{K}^T\mathbf{X}_r\right)} \left(M_\sigma^{-1}\right)_{s,r} \mathrm{e}^{-\mathrm{i}\left(\omega_n'[\beta-\tau_s]+\mathbf{P}^T\mathbf{X}_\mathbf{s}\right)} = X_\sigma^{C_n}(P,K), \tag{4.50}$$

i.e. the X matrix is just transposed by the transformation $C_n \to \tilde{C_n}$, an operation that can virtually be performed at *no computational cost*. We use the fact that $W(C_n) = W(\tilde{C_n})$ in order to redefine the estimator $\langle\langle T(Q;K,P)\rangle\rangle_{C_n}$ in the following way:

$$\langle\langle T(Q;K,P)\rangle\rangle_{C_n} := \frac{1}{2}\Big(X_\uparrow^{C_n}(K,P-Q)X_\downarrow^{C_n}(P,K+Q) + X_\uparrow^{C_n}(P-Q,K)X_\downarrow^{C_n}(K+Q,P)\Big). \tag{4.51}$$

In addition to that, we will also will make use of SU(2) symmetry, as we have seen in section 4.3 that the ↑↓↓↑ variant of $G_4^{\perp}$ must by symmetry be equal to the ↓↑↑↓ version. Taking together equations (4.42), (4.43) and (4.44), we immediately see that the ↓↑↑↓ susceptibility can be obtained through the exchange

$$X_\uparrow^{C_n}(K,P) \leftrightarrow X_\downarrow^{C_n}(K,P). \tag{4.52}$$

As we know that by virtue of symmetry the two ↑↓↓↑ two particle Green's function must be equal to the ↓↑↑↓ variant, we will *enforce* this symmetry already on the level of Monte Carlo configurations rather than waiting for an automatic *stochastic* restoration of SU(2) symmetry. This leads to a second redefinition of the estimator $\langle\langle T(Q;K\ ,P)\rangle\rangle_{C_n}$:

$$\begin{aligned}\langle\langle T(Q;K,P)\rangle\rangle_{C_n} := \frac{1}{4}\Big[&X_\uparrow^{C_n}(K,P-Q)X_\downarrow^{C_n}(P,K+Q) + X_\uparrow^{C_n}(P-Q,K)X_\downarrow^{C_n}(K+Q,P)\\ &+ X_\downarrow^{C_n}(K,P-Q)X_\uparrow^{C_n}(P,K+Q) + X_\downarrow^{C_n}(P-Q,K)X_\uparrow^{C_n}(K+Q,P)\Big].\end{aligned} \tag{4.53}$$

This procedure allows for a more complete exploitation of a configuration C_n of vertices and makes the expensive transition through nested `for`-loops for the construction of $\langle\langle T(Q;K,P)\rangle\rangle_{C_n}$ in memory more worthwhile.

4.4.3. Frequency and momentum structure of $T(Q;K,P)$

Before moving on to the physically interesting quantities, we discuss shortly the frequency and momentum structure of $T(Q;K,P)$ as this is the basic quantity that we obtain from the Monte Carlo calculation. This study already gives us important hints on how to deal with $G_4^{\perp}(Q;K,P)$ as the frequency structure of this quantity is very similar.

We observe several features in the frequency structure that have also been identified by Jan Kuneš [48] for a related but of course different quantity in an impurity model: The irreducible vertex $\Gamma(\mathrm{i}\nu;\mathrm{i}\omega_n,\mathrm{i}\omega_n')$.

As it is impossible to visualize the whole quantity $T(Q;K,P)$, we provide two example graphs illustrating the momentum and frequency structure: One at vanishing bosonic transfer frequency $\mathrm{i}\nu$ in figure 4.1 and one for $\mathrm{i}\nu \neq 0$ in figure 4.2.

$T(Q;K,P)$ possesses a background that is constant in frequency and momentum on top of which structures emerge:

- a constant in terms of $\mathrm{i}\omega_n'$ for fixed $\mathrm{i}\omega_n$ at a small Matsubara frequency (dominant at $\mathrm{i}\omega_n \in \left[\frac{\pi}{\beta}, \frac{-\pi}{\beta}\right]$).
- a constant in terms of $\mathrm{i}\omega_n$ for fixed $\mathrm{i}\omega_n'$ at a small Matsubara frequency (dominant at $\mathrm{i}\omega_n' \in \left[\frac{\pi}{\beta}, \frac{-\pi}{\beta}\right]$).
- a constant on the diagonal ($\mathrm{i}\omega_n = \mathrm{i}\omega_n'$) and on the antidiagonal ($\mathrm{i}\omega_n = \mathrm{i}\omega_n'$) as well as on offdiagonals/antidiagonals immidiatelly adjacent to the diagonal and antidiagonal.

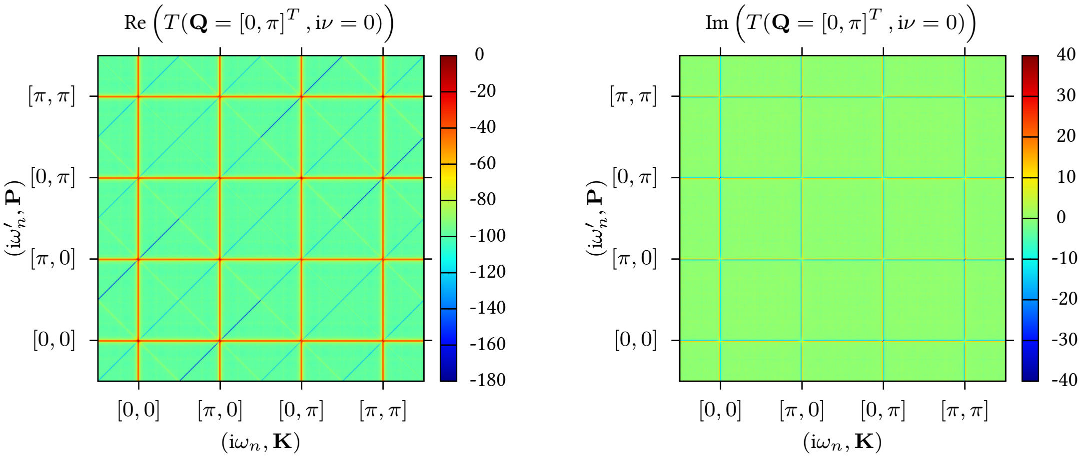

Figure 4.1.: Graphical representation of the vertex $T(Q, \mathrm{i}\nu)$ for fixed $\mathbf{Q} = [0, \pi]^T$ and $\mathrm{i}\nu = 0$ as a matrix. The multiindex $(\mathrm{i}\omega_n, \mathbf{K})$ is used as column index, while $(\mathrm{i}\omega'_n, \mathbf{P})$ serves as the row index. The tick position indicating the momenta $\mathbf{K}$ and $\mathbf{P}$ specifies the first nonzero fermionic Matsubara frequency $\mathrm{i}\frac{\pi}{\beta}$. This is example data calculated in CT-INT for the Hubbard model on a 2×2 lattice with $t = 1$, $U = 8$, $\beta = 1$ and $\mu = 0$.

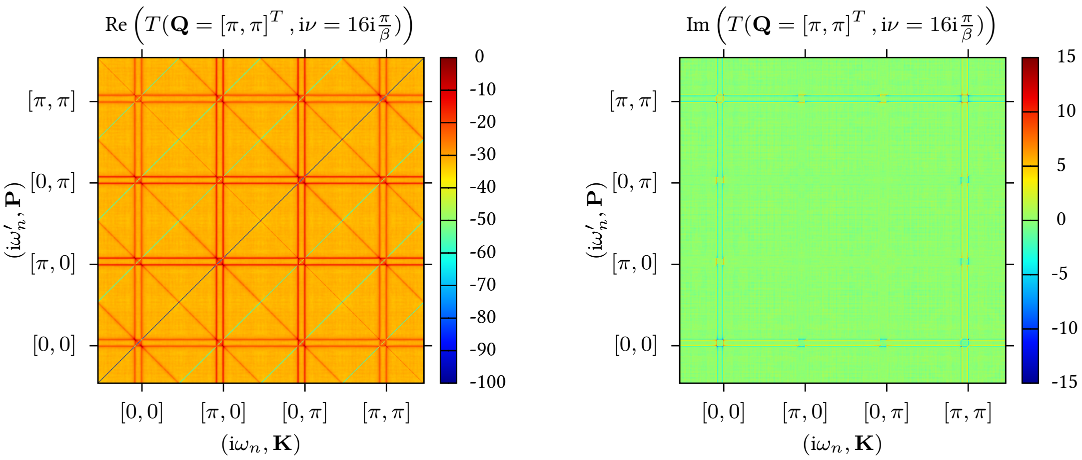

Figure 4.2.: Graphical representation of the vertex $T(Q, \mathrm{i}\nu)$ for fixed $\mathbf{Q} = [\pi, \pi]^T$ and $\mathrm{i}\nu = 16\mathrm{i}\frac{\pi}{\beta}$ as a matrix. The multiindex $(\mathrm{i}\omega_n, \mathbf{K})$ is used as column index, while $(\mathrm{i}\omega'_n, \mathbf{P})$ serves as the row index. The tick position indicating the momenta $\mathbf{K}$ and $\mathbf{P}$ specifies the first nonzero fermionic Matsubara frequency $\frac{\pi}{\beta}$. These results stem from the same calculation as figure 4.1.

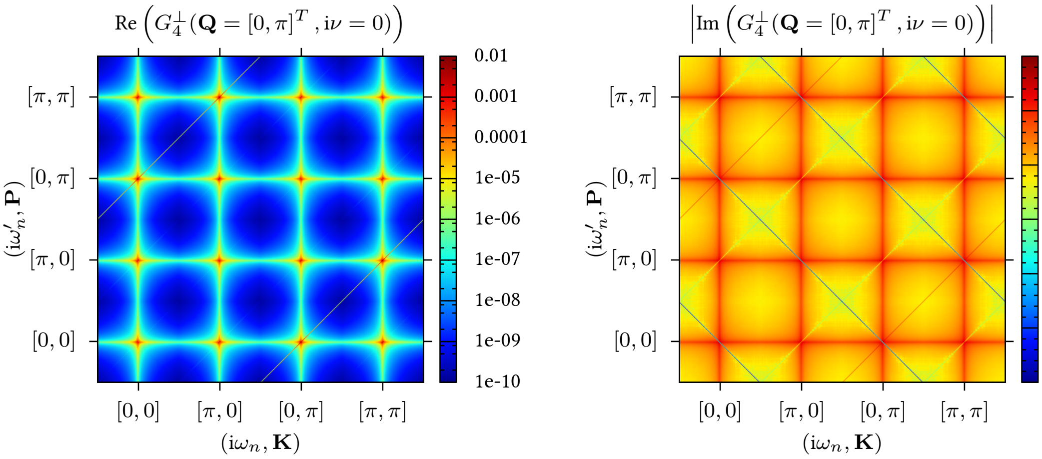

Figure 4.3.: Frequency and momentum structure of $G_4^{\perp}(Q)$ for the 2×2 Hubbard model at $U=8$, $\mu=0$, $t=1$ and $\beta=1$ plotted in logarithmic color scale for a better visibility of the features.

This frequency structure is repeated in every momentum sector and is exactly the same even for an impurity model without any momentum dependency. However, the important momentum structure emerges from the different weights of the individual terms of the frequency structure, depending on the momentum sector. Regarding every momentum sector, clearly the *center of mass* is located symmetrically in a Matsubara frequency window centered at $(0,0)$[12].

Additional complexity emerges at a nonvanishing bosonic transfer frequency $\mathrm{i}\nu$. It appears that the "cross" shaped structure with one frequency being constant is split into two and one cross is moved by $(-\mathrm{i}\nu, \mathrm{i}\nu)$ in frequency space. This is of course directly related with the shift of the symmetry centre discussed in section 4.2. We have already adjusted for this shift and moved the center of mass in the plot accordingly. While symmetries show that this choice is natural, we will argue in section 4.6.2 that this way of choosing the frequency window is mandatory for an efficient treatment of the Bethe Salpeter equation.

4.4.4. Frequency and momentum structure of $G_4^{\perp}(Q;K,P)$

The frequency and momentum features of the two particle Green's function are clearly inherited from $T(Q;K,P)$ as can be seen from the bulk term in equation (4.49) containing the vertex $T(Q;K,P)$. The term containing bare one particle Green's functions and the Kronecker delta $\delta_{K,P-Q}$ does not introduce additional structure but modifies the weight of the (shifted) diagonal.

For a visualization of the features, we provide CT-INT results for $G_4^{\perp}$ for the same parameters as depicted in figures 4.1 and 4.2. The results are shown in figures 4.3 and 4.4.

At 0 transfer frequency $\mathrm{i}\nu$, the center of mass of the frequency structure is in the $(0,0)$ point for each momentum sector. The diagonal lines emerging from the Kronecker delta term in equation (4.49) are clearly visible. It is also apparent that $G_4^{\perp}$ decays quickly in nearly all directions of the momentum space except the diagonal and on the "cross"-feature. The same picture is valid for nonvanishing bosonic transfer frequency in figure 4.4 with the generalization that the center of mass shifts in frequency and the "cross" feature is split into two parts shifted away from each other by $\mathrm{i}\nu$ exactly as in the case of the $T(Q)$ vertex. Again, momentum structure is manifested in different weights depending on the momentum sector which is probably most apparent in the frequency diagonal seen in figure 4.4.

---

[12] Even though, $\mathrm{i}\omega_n = 0$ is of course not an allowed fermionic Matsubara frequency

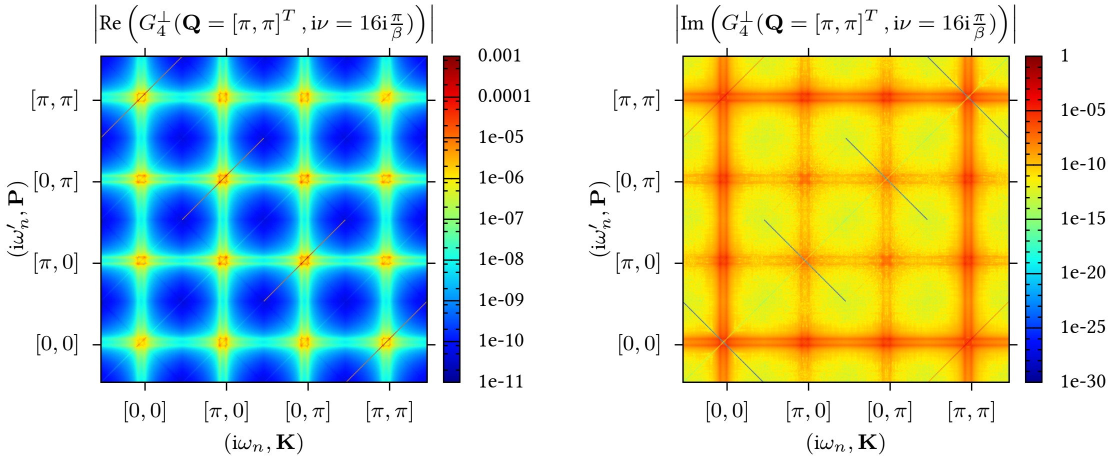

Figure 4.4.: Frequency and momentum structure of $G_4^{\perp}(Q)$ for the 2×2 Hubbard model at $U = 8$, $\mu = 0$, $t = 1$ and $\beta = 1$ plotted in logarithmic color scale after taking the absolute value for a better visibility of the features.

4.4.5. Matsubara summation

Two particle physical quantities of interest in a many fermion system are for instance susceptibilities, which can be obtained from the general two particle Green's functions by summation over *internal* frequencies and momenta. From $G_4^{\perp}(Q;K,P)$, the spin susceptibility $\chi_s^{+-}(Q)$ is thus obtained by

$$\chi_s^{+-}(Q) = \sum_{K,P} G_4^{\perp}(Q;K,P) \tag{4.54}$$

Naturally, the sum over K and P contains a sum over the momenta $\mathbf{K}$ and $\mathbf{P}$ as well as over the associated Matsubara frequencies $\mathrm{i}\omega_n$ and $\mathrm{i}\omega_n'$. The sum over momenta in the first Brillouin zone can be performed exactly as we are always dealing with finite clusters and these sums are therefore always finite. The problem, however, is the frequency sum, as it runs over an *infinite* number of Matsubara frequencies. Let us write this explicitly to make the matter more clear

$$\sum_{K} = \sum_{\mathbf{K}\in 1\mathrm{BZ}} \sum_{n=-\infty}^{\infty}, \quad \text{with} \quad \mathrm{i}\omega_n = \frac{(2n+1)\pi}{\beta}. \tag{4.55}$$

Clearly, the exact evaluation of equation (4.54) is impossible, as in a practical calculation we do not know $G_4^{\perp}(Q;K,P)$ for an infinite number of frequencies $\mathrm{i}\omega_n$ and $\mathrm{i}\omega_n'$.

The problem of evaluation of Matsubara sums has been studied in the past and an intriguing idea has been brought forward by Hartmut Monien in reference [49]. This idea transports the ansatz for Gaussian integration to discrete sums and proposes a set of frequency positions and weights at which the summand has to be evaluated in order to exponentially converge to the correct value of the sum. This application of this idea to our problem is hindered by an obstacle: It requires the knowledge of the two particle Green's function $G_4^{\perp}(Q;K,P)$ on a frequency grid *differing* from the Matsubara frequency grid. In particular, one needs to know $G_4^{\perp}$ at positions that are no legal Matsubara frequencies. This requires analytical continuation of a complex function of multiple variables and is per se a difficult problem. The sheer amount of data is frightening enough, so we did not pursue this approach any further.

Another very promising approach has been explained by Jan Kuneš in [48]. He makes use of the frequency structure of the irreducible vertex $\Gamma(Q;K,P)$ and attaches to the exactly known function $G_4(Q;K,P)$ on a small frequency window an asymptotic part constructed from the irreducible vertex. It is believed that this

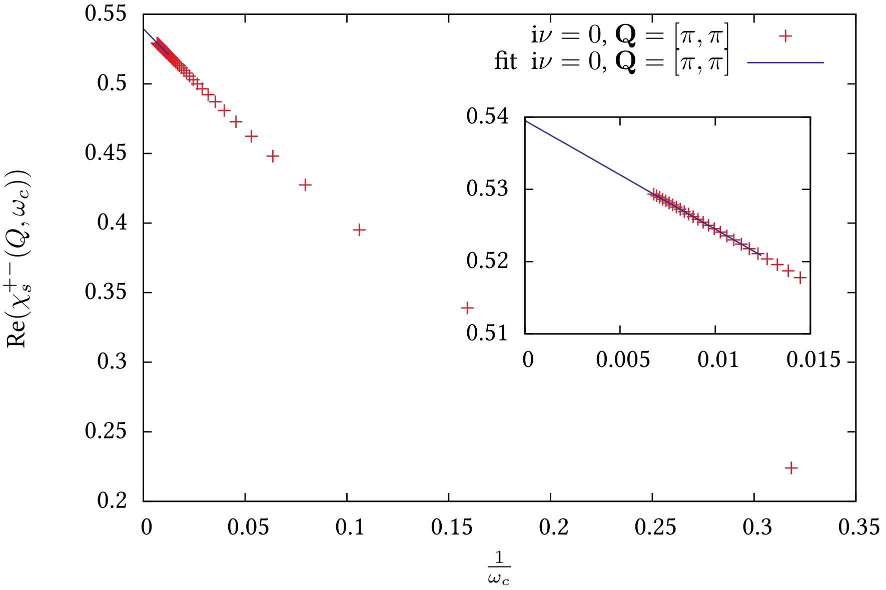

Figure 4.5.: Symmetric sum over Matsubara frequencies of $G_4(Q; K, P)$ as a function of the cutoff frequency for $\mathrm{i}\nu = 0$. At small cutoff frequency, the linear behaviour is dominant and can be fitted to a linear function.

approach can be adapted for a multisite cluster including momentum structure and in fact our results show that the frequency structure of $G_4^{\perp}(Q; K, P)$ does not become any more complicated with the introduction of momenta. However, the approach requires the use of even bigger amounts of data and the asymptotic part has to be cut at a (of course much higher) cutoff frequency. Also the frequency at which the numerically exactly known $G_4^{\perp}$ is replaced by the asymptotic part introduces some amount of approximation[13].

A third idea that has obtained particular interest is the introduction of a new basis. This idea has been brought forward by Lewin Boehnke et al. in [50]. Here, a mixed basis representation is used and the Matsubara frequencies $\mathrm{i}\omega_n$ and $\mathrm{i}\omega'_n$ are replaced by indices l and l' of Legendre indices through a unitary transformation, while the bosonic Matsubara frequency is kept. Although this has not been clear a priory, it has been shown that sums in the new basis converge exponentially and the truncation of the sum[14] at a particular order of Legendre polynomials l_{cutoff} is acceptable. This idea is particularly intriguing and has therefore been studied in the framework of this thesis. While it became apparent that it is possible to formulate the equations even when the impurity formulation is upgraded to lattice terms by the introduction of momenta, it turned out that an efficient method for the calculation of $G_4^{\perp}(Q; L, L')$ directly in the Legendre basis in CT-INT could not be developed. The reason for this is that Wick's theorem becomes entangled in the Legendre basis and this kills the performance of the algorithm. This problem is discussed in appendix A.1.

In order to find out how to deal with this problem, let us first look at the convergence of the frequency sum (4.54). We will introduce a cutoff frequency $\mathrm{i}\omega_c$ at which we will stop summations. Note however, that the cutoff frequency will *always* be measured with respect to the center of mass of $G_4^{\perp}(Q; K, P)$ such as to ensure symmetric summing. Failure to do so will lead to a biassed summation and slow down convergence.

We thus obtain

$$\chi_s^{+-}(Q; \omega_c) = \sum_{\mathbf{K},\mathbf{P}} \sum_{\mathrm{i}\omega_n^-, \mathrm{i}\omega_n'^+ = -\omega_c}^{\omega_c} G_4^{\perp}(Q; K, P) \tag{4.56}$$

---

[13] This method together with the idea discussed in the next paragraph is discussed systematically in great detail in Jutta Ortloffs PhD thesis [45].

[14] by virtue of the unitary transformation, sums over Matsubara frequencies translate into sums over Legendre indices

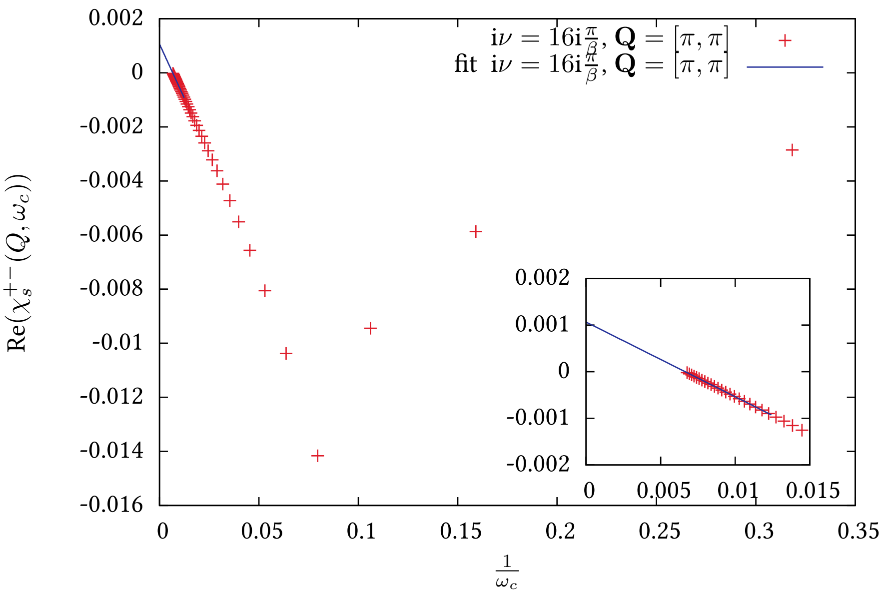

Figure 4.6.: Symmetric sum over Matsubara frequencies of $G_4(Q;K,P)$ as a function of the cutoff frequency. At small cutoff frequency, the linear behaviour is dominant and can be fitted to a linear function. Note the special feature appearing for $\mathrm{i}\nu \neq 0$: The sum only becomes monotonic if the frequency window is larger than the bosonic transfer frequency $\mathrm{i}\nu$. This can be understood nicely by considering that for too small cutoff frequency the summation window is inside of the "double-cross" feature of $G_4^{+}(Q)$ as depicted in figure 4.4.

It is clear that for $\omega_c \to \infty$, we obtain

$$\lim_{\omega_c \to \infty} \chi_s^{+-}(Q;\omega_c) = \chi_s^{+-}(Q). \tag{4.57}$$

If we introduce a new variable $x = \frac{1}{\omega_c}$, we can Taylor expand $\chi_s^{+-}(Q;\frac{1}{x})$ around $x = 0$ in terms of x and replace x afterwards:

$$\chi_s^{+-}(Q;\omega_c) = \chi_s^{+-}(Q) + \frac{a}{\omega_c} + \mathcal{O}\left(\frac{1}{\omega_c^2}\right) \tag{4.58}$$

with some constant $a \in \mathbb{C}$.

We can check the validity of this expansion by calculating $\chi_s^{+-}(Q,\omega_c)$ for different values of ω_c. We show two representative examples in figures 4.5 and 4.6. It is apparent that the linear approximation for small values of $\frac{1}{\omega_c}$ is valid, the linear fit to this region shows this very nicely. It is also very clear that the change of the sum even at the largest accessible cutoff frequency is still substantial and it is already from this picture questionable if the truncation of the sum is an acceptable approximation. We will argue here that it is indeed not, as the asymptotic behaviour of $\chi_s^{+-}(Q)$ in terms of bosonic frequencies will not be reproduced correctly.

Fortunately, the way out is already obvious now: We will use the asymptotic form (4.58) and perform a linear fit to $\chi_s^{+-}(Q;\omega_c)$ as a function of $\frac{1}{\omega_c}$ in the region of the largest cutoff frequencies. The constant term of the linear fit at $\frac{1}{\omega_c} = 0$ is then the extrapolated estimator for the exact value of $\chi_s^{+-}(Q)$.

4.5. Spin susceptibility on a 2×2 cluster: An instructive test case

4.5.1. Exact diagonalization

In order to test our approach, we introduce an exactly tractible system, namely the Hubbard model on a finite size system of small size. Here, we will restrict ourselves to a 2×2 Hubbard cluster with periodic boundary conditions. The Hamiltonian reads:

$$\mathcal{H}_{2\times 2} = -t \sum_{\langle i,j\rangle,\sigma} c^\dagger_{i,\sigma} c_{j,\sigma} + U \sum_i \left(n_{i,\uparrow} - \frac{1}{2}\right)\left(n_{i,\downarrow} - \frac{1}{2}\right) - \mu \sum_i n_i. \tag{4.59}$$

This system can be solved exactly by *exact diagonalization*[15] . In order to perform this, we construct a product basis of the Fock space, as every orbital of spin σ can either be empty or occupied. Therefore, we can write $|\,\alpha\,\rangle \in \{|\,0\,\rangle, |\,\sigma\,\rangle\}$. The product basis then has the dimension 2^{2N}, where N is the number of lattice sites and every lattice site corresponds to one spin up and one spin down orbital. Every state of the product basis can be written as

$$|\,\psi\,\rangle = |\,n_{\uparrow,i_1}, n_{\downarrow,i_1}, \dots, n_{\uparrow,i_N}, n_{\downarrow,i_N}\,\rangle \quad \text{with} \quad n_{\sigma,i} \in \{0,1\}\,\text{[16]}. \tag{4.60}$$

Clearly, in this basis, it is easy to construct matrix representations for the operators $c^\dagger_{i,\sigma}$ and $c_{i,\sigma}$ as they only operate on single orbitals (cf. e.g. [25, 26, 51]):

$$c^\dagger_{i,\sigma}\,|\,n_{\uparrow,i_1}, \dots, n_{\downarrow,i_N}\,\rangle = \begin{cases} (-1)^{\sum_{j\le i,\sigma'} n_{\sigma',j}}\,|\,n_{\uparrow,i_1}, \dots, n_{\sigma,i}+1, \dots, n_{\downarrow,i_N}\,\rangle \ \text{if}\ n_{\sigma,i} = 0 \\ 0 \quad \text{else.} \end{cases} \tag{4.61}$$

Using the standard matrix product of the matrix forms of the operators in equation (4.59), the Hamiltonian can subsequently be obtained in its matrix form H. In a second step, we use `numpy` (see e.g. [52]) to calculate eigenvectors $|\,n\,\rangle$ and eigenvalues E_n of H.

This enables us to calculate the spin susceptibility from the Lehmann representation given in equation (4.108). However, we have to be careful in the case $\mathrm{i}\nu = 0$, as for $E_n = E_m$, equation (4.108) would contain an undefined expression. It turns out that the term for this case yields:

$$\chi(\mathbf{q}, \mathrm{i}\nu = 0) = \frac{1}{Z} \sum_{\substack{n,m \\ E_n \neq E_m}} |\langle n\,|\,S_+(\mathbf{q})\,|\,m\rangle|^2\, \frac{\mathrm{e}^{-\beta E_m} - \mathrm{e}^{-\beta E_n}}{E_n - E_m} + \frac{1}{Z} \sum_{\substack{n,m \\ E_n = E_m}} |\langle n\,|\,S_+(\mathbf{q})\,|\,m\rangle|^2\, \beta \mathrm{e}^{-\beta E_n}. \tag{4.62}$$

In order to evaluate this expression on a computer, we make use of a standard trick in exact diagonalization, i.e. we transform the creation and annihilation operators into the eigenbasis $\{|\,n\,\rangle\}$ of the Hamiltonian in order to economize matrix-vector products[17]. We define

$$Q^{n,m}_{\mathbf{x},\sigma} = \langle\, n\,|\, c^\dagger_{\mathbf{x},\sigma}\,|\, m\,\rangle\,. \tag{4.63}$$

Thus, we can write

$$S_+(\mathbf{q}) = \frac{1}{\sqrt{N_s}} \sum_{\mathbf{k}} c_{\mathbf{k},\uparrow} c_{\mathbf{k}+\mathbf{q},\downarrow} = \frac{1}{\sqrt{N_s}} \sum_{\mathbf{x}} \mathrm{e}^{\mathrm{i}\mathbf{q}^T\mathbf{x}} c^\dagger_{\mathbf{x},\uparrow} c_{\mathbf{x},\downarrow}. \tag{4.64}$$

And therefore

$$\langle\, n\,|\, S_+(\mathbf{q})\,|\, m\,\rangle = \frac{1}{\sqrt{N_s}} \sum_{\mathbf{x}} \mathrm{e}^{\mathrm{i}\mathbf{q}^T\mathbf{x}} \left(Q_{\mathbf{x},\uparrow} Q^\dagger_{\mathbf{x},\downarrow}\right)_{n,m}. \tag{4.65}$$

---

[15] In the literature, this term is used ambiguously and often refers to methods extracting information about the ground state of a system, such as the Lanczos method that we use in chapter 6. Here, however, we mean a calculation of the *full* spectrum of the Hamiltonian, which gives us exact access to dynamical quantities at finite temperatures.

[16] This is of course Wolfgang Pauli's exlusion principle for identical fermions.

[17] A computer scientist would refer to this technique as *caching*.

4.5.2. Cross check at $U = 0$

It is often instructive to begin a study of a correlated many fermion system with the noninteracting case which can be studied exactly relatively easily in many cases. In the present case, the noninteracting limit is obtained by setting $U = 0$. This yields the Hamiltonian

$$\mathcal{H}^0_{2\times 2} = -t \sum_{\langle i,j\rangle,\sigma} c^\dagger_{i,\sigma} c_{j,\sigma} - \mu \sum_i n_i. \tag{4.66}$$

It can be diagonalized easily be making the transition to momentum space according to the momentum part of equations (2.2) and (2.3):

$$\begin{aligned} \mathcal{H}^0_{2\times 2} &= -t \sum_{\mathbf{x}} \sum_{\boldsymbol{\delta}\in\{(0,\pm1)^T,(\pm1,0)^T\}} \frac{1}{N} \sum_{\mathbf{k}} \sum_{\mathbf{p}} \mathrm{e}^{\mathrm{i}\left(\mathbf{k}^T\mathbf{x} - \mathbf{p}^T[\mathbf{x}+\boldsymbol{\delta}]\right)} c^\dagger_{\mathbf{k},\sigma} c_{\mathbf{p},\sigma} - \mu \sum_{\mathbf{k}} n_{\mathbf{k}} \\ &= \sum_{\mathbf{k}} \left[-2t\left(\cos(k_x) + \cos(k_y)\right) - \mu\right] c^\dagger_{\mathbf{k},\sigma} c_{\mathbf{k},\sigma} \\ &= \sum_{\mathbf{k}} \epsilon_{\mathbf{k}} c^\dagger_{\mathbf{k},\sigma} c_{\mathbf{k},\sigma}. \end{aligned} \tag{4.67}$$

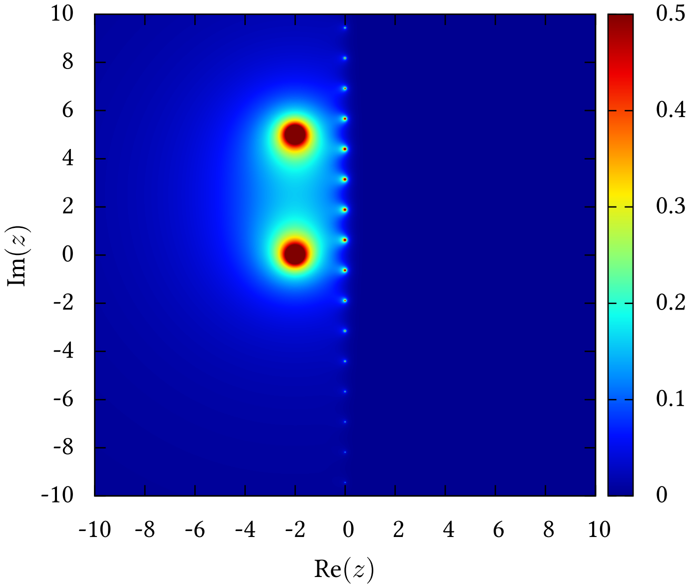

Figure 4.7.: Absolute value of the function $f_{\text{aux}}(z)$ in the complex plane for the parameters $\beta = 5$, $\epsilon_{\mathbf{k}} = -2$, $\epsilon_{\mathbf{k}+\mathbf{q}} = -2$, $\mathrm{i}\nu = \mathrm{i}8\frac{\pi}{\beta}$. The pole structure of $f_{\text{aux}}(z)$ is clearly illustrated. Note the poles on the imaginary axis correspond to fermionic Matsubara frequencies. The color axis has been truncated in order to make the structure more prominent.

The calculation of the spin susceptibility is now straightforward, as we can make use of *Wick's theorem* [18]

---

[18] Unfortunately, in the literature the term *Wick's theorem* refers to many identities who are eventually linked to Wick's original form first published in [53]. Here, we refer to the form reducing a higher order Gaussian integral to a determinant of two point Gaussian integrals, which are linked to Green's functions of a noninteracting system by quantum field theory.

for noninteracting many particle Green's functions (see e.g. [25, 26, 54])

$$\begin{aligned}
\chi(\mathbf{q}, \mathrm{i}\nu) &= \frac{1}{\beta N_s} \sum_{\mathbf{k},\mathbf{p},\mathrm{i}\omega_n,\mathrm{i}\omega_n'} \langle \bar{c}_{\mathbf{k},\uparrow}(\mathrm{i}\omega_n) c_{\mathbf{k}+\mathbf{q},\downarrow}(\mathrm{i}\omega_n + \mathrm{i}\nu) \bar{c}_{\mathbf{p},\downarrow}(\mathrm{i}\omega_n') c_{\mathbf{p}-\mathbf{q},\uparrow}(\mathrm{i}\omega_n' - \mathrm{i}\nu) \rangle_0 = \\
&= -\frac{1}{\beta N_s} \sum_{\mathbf{k},\mathbf{p},\mathrm{i}\omega_n,\mathrm{i}\omega_n'} \delta_{\mathbf{k},\mathbf{p}-\mathbf{q}} \delta_{\mathrm{i}\omega_n,\mathrm{i}\omega_n'-\mathrm{i}\nu} G^0_\uparrow(\mathbf{k}, \mathrm{i}\omega_n) G^0_\downarrow(\mathbf{k}+\mathbf{q}, \mathrm{i}\omega_n + \mathrm{i}\nu) = \\
&= -\frac{1}{\beta N_s} \sum_{\mathbf{k},\mathrm{i}\omega_n} G^0_\uparrow(\mathbf{k}, \mathrm{i}\omega_n) G^0_\downarrow(\mathbf{k}+\mathbf{q}, \mathrm{i}\omega_n + \mathrm{i}\nu).
\end{aligned} \tag{4.68}$$

Obviously, $SU(2)$ symmetry implies that the single particle Green's function is spin independent. Using the resolvent formalism (cf. e.g. [26, 54, 55]) [19], we obtain

$$\chi(\mathbf{q}, \mathrm{i}\nu) = -\frac{1}{\beta N_s} \sum_{\mathbf{k},\mathrm{i}\omega_n} \frac{1}{(\mathrm{i}\omega_n - \epsilon_{\mathbf{k}})} \frac{1}{(\mathrm{i}\omega_n - \mathrm{i}\nu - \epsilon_{\mathbf{k}+\mathbf{q}})}. \tag{4.70}$$

The sum over fermionic Matsubara fequencies may be carried out using a common trick in solid state physics (cf. e.g. [54, 55]): We introduce an auxiliary function $f_{\text{aux}}(z)$, which has poles at the positions of the fermionic Matsubara frequencies:

$$f_{\text{aux}}(z) = \frac{1}{1 + \mathrm{e}^{\beta z}} \frac{1}{z - \epsilon_{\mathbf{k}}} \frac{1}{z - \mathrm{i}\nu - \epsilon_{\mathbf{k}+\mathbf{q}}} \tag{4.71}$$

Figure 4.7 illustrates the pole structure of $f_{\text{aux}}(z)$ and shows that we have poles at $z \in \{\mathrm{i}\omega_n, \epsilon_{\mathbf{k}}, \epsilon_{\mathbf{k}+\mathbf{q}} + \mathrm{i}\nu\} = M_{\text{poles}}$. As $f_{\text{aux}}(z)$ decays more quickly than $\frac{1}{z}$ at the boundary of the complex plane which we denote by C_∞, we have

$$\oint_{C_\infty} \mathrm{d}z\, f_{\text{aux}}(z) = 0. \tag{4.72}$$

However, using the residue theorem, this integral can be evaluated in a different way:

$$\oint_{C_\infty} \mathrm{d}z\, f_{\text{aux}}(z) = 2\pi\mathrm{i} \sum_{z_i \in M_{\text{poles}}} \operatorname{Res}_{z_i} f_{\text{aux}}(z) \tag{4.73}$$

The function $f_{\text{aux}}(z)$ only has simple poles in the case of $\mathrm{i}\nu \neq 0 \vee \epsilon_{\mathbf{k}} \neq \epsilon_{\mathbf{k}+\mathbf{q}}$. Let us consider this case first and continue with the other case $\mathrm{i}\nu = 0 \wedge \epsilon_{\mathbf{k}} = \epsilon_{\mathbf{k}+\mathbf{q}}$ later. In the end, we will see that both results are indeed linked through the consideration of the first case in the limit of $\epsilon_{\mathbf{k}+\mathbf{q}} \to \epsilon_{\mathbf{k}}$.

Case $\mathrm{i}\nu \neq 0 \vee \epsilon_{\mathbf{k}} \neq \epsilon_{\mathbf{k}+\mathbf{q}}$ Here, all poles in M_{poles} are distinct and of order one. We therefore have:

$$\operatorname{Res}_{\epsilon_{\mathbf{k}}} f_{\text{aux}}(z) = \lim_{z \to \epsilon_{\mathbf{k}}} (z - \epsilon_{\mathbf{k}}) f_{\text{aux}}(z) = \frac{1}{1 + \mathrm{e}^{\beta \epsilon_{\mathbf{k}}}} \frac{1}{\epsilon_{\mathbf{k}} - \epsilon_{\mathbf{k}+\mathbf{q}} - \mathrm{i}\nu}. \tag{4.74}$$

$$\operatorname{Res}_{\epsilon_{\mathbf{k}+\mathbf{q}}+\mathrm{i}\nu} f_{\text{aux}}(z) = \lim_{z \to \epsilon_{\mathbf{k}+\mathbf{q}}+\mathrm{i}\nu} (z - \epsilon_{\mathbf{k}+\mathbf{q}} - \mathrm{i}\nu) f_{\text{aux}}(z) = \frac{1}{1 + \mathrm{e}^{\beta \epsilon_{\mathbf{k}+\mathbf{q}}}} \frac{1}{\epsilon_{\mathbf{k}+\mathbf{q}} - \epsilon_{\mathbf{k}} + \mathrm{i}\nu}. \tag{4.75}$$

$$\operatorname{Res}_{\mathrm{i}\omega_n} f_{\text{aux}}(z) = \lim_{z \to \mathrm{i}\omega_n} (z - \mathrm{i}\omega_n) f_{\text{aux}}(z) = -\frac{1}{\beta} \frac{1}{\mathrm{i}\omega_n - \epsilon_{\mathbf{k}}} \frac{1}{\mathrm{i}\omega_n - \mathrm{i}\nu - \epsilon_{\mathbf{k}+\mathbf{q}}}. \tag{4.76}$$

---

[19] Keep in mind that because of our non-standard definition of the single particle Green's function, the resolvent reads

$$G^0(\mathbf{k}, \mathrm{i}\omega_n) = \frac{1}{-\mathrm{i}\omega_n - \epsilon_{\mathbf{k}}}. \tag{4.69}$$

However, we can invert the sum over fermionic Matsubara frequencies in this case, as it runs over all frequencies, thus introducing the transformation $\mathrm{i}\omega_n \to -\mathrm{i}\omega_n$.

In total, we get

$$\frac{1}{\beta}\sum_{\mathrm{i}\omega_n}\frac{1}{\mathrm{i}\omega_n-\epsilon_{\mathbf{k}}}\frac{1}{\mathrm{i}\omega_n-\mathrm{i}\nu-\epsilon_{\mathbf{k+q}}}=\left(n_{\mathrm{F}}(\epsilon_{\mathbf{k}})-n_{\mathrm{F}}(\epsilon_{\mathbf{k+q}})\right)\frac{1}{\epsilon_{\mathbf{k}}-\epsilon_{\mathbf{k+q}}-\mathrm{i}\nu}. \tag{4.77}$$

Of course, this is already the desired result!

Case $\mathrm{i}\nu=0\wedge\epsilon_{\mathbf{k}}=\epsilon_{\mathbf{k+q}}$ In this case, things change slightly and we are now confronted with the complex line integral

$$\oint_{C_\infty}\mathrm{d}z\,\frac{1}{1+\mathrm{e}^{\beta z}}\frac{1}{(z-\epsilon_{\mathbf{k}})^2}=0. \tag{4.78}$$

Now, two poles fall together and form a second order pole at $\epsilon_{\mathbf{k}}$. The residues can be calculated and yield

$$\mathrm{Res}_{\mathrm{i}\omega_n}\frac{1}{1+\mathrm{e}^{\beta z}}\frac{1}{(z-\epsilon_{\mathbf{k}})^2}=-\frac{1}{\beta}\frac{1}{(\mathrm{i}\omega_n-\epsilon_{\mathbf{k}})^2}. \tag{4.79}$$

$$\mathrm{Res}_{\epsilon_{\mathbf{k}}}\frac{1}{1+\mathrm{e}^{\beta z}}\frac{1}{(z-\epsilon_{\mathbf{k}})^2}=-\frac{\beta\mathrm{e}^{\beta\epsilon_{\mathbf{k}}}}{(1+\mathrm{e}^{\beta\epsilon_{\mathbf{k}}})^2}. \tag{4.80}$$

and therefore

$$\frac{1}{\beta}\sum_{\mathrm{i}\omega_n}\frac{1}{(\mathrm{i}\omega_n-\epsilon_{\mathbf{k}})^2}=-\frac{\beta\mathrm{e}^{\beta\epsilon_{\mathbf{k}}}}{(1+\mathrm{e}^{\beta\epsilon_{\mathbf{k}}})^2}. \tag{4.81}$$

In conclusion, we can now write down the final result for the noninteracting spin susceptibility in the form

$$\chi(\mathbf{q},\mathrm{i}\nu)=\begin{cases}-\frac{1}{N_s}\sum\limits_{\mathbf{k}}\frac{n_{\mathrm{F}}(\epsilon_{\mathbf{k}})-n_{\mathrm{F}}(\epsilon_{\mathbf{k+q}})}{\epsilon_{\mathbf{k}}-\epsilon_{\mathbf{k+q}}-\mathrm{i}\nu} & \text{if}\quad \mathrm{i}\nu\neq 0\\ \frac{1}{N_s}\sum\limits_{\substack{\mathbf{k}\\ \epsilon_{\mathbf{k}}=\epsilon_{\mathbf{k+q}}}}\frac{\beta\mathrm{e}^{\beta\epsilon_{\mathbf{k}}}}{(1+\mathrm{e}^{\beta\epsilon_{\mathbf{k}}})^2}-\frac{1}{N_s}\sum\limits_{\substack{\mathbf{k}\\ \epsilon_{\mathbf{k}}\neq\epsilon_{\mathbf{k+q}}}}\frac{n_{\mathrm{F}}(\epsilon_{\mathbf{k}})-n_{\mathrm{F}}(\epsilon_{\mathbf{k+q}})}{\epsilon_{\mathbf{k}}-\epsilon_{\mathbf{k+q}}} & \text{if}\quad \mathrm{i}\nu=0\end{cases} \tag{4.82}$$

As already mentioned, the second case result can be obtained by setting $\mathrm{i}\nu=0$ and performing the limit $\epsilon_{\mathbf{k}}\to\epsilon_{\mathbf{k+q}}$ using L'Hôpital's rule.

Now, we have established two independent methods to calculate $\chi(\mathbf{q},\mathrm{i}\nu)$ for the 2×2 Hubbard model at $U=0$ and we can thus verify the correctness of the computer implementation of the exact diagonalization code by comparing the two results. The comparison is displayed for an example parameter set in figure 4.8. Note that this is a nontrivial test for the exact diagonalization approach and asures us that we can obtain trustworthy results for the interacting 2×2 Hubbard cluster which will bring us one step up the ladder for the verification of our Monte Carlo approach.

4.5.3. Comparison to Monte Carlo results

In order to demonstrate the numerical exactness of our CT-INT approach and the extrapolation to infinite cutoff frequencies ω_c, we calculate $\chi_s^{+-}(Q)$ for the Hubbard model on a 2×2 cluster via $G_4^{\perp}$ and compare the result to the exact solution obtained from exact diagonalization of the Hamiltonian. We also show data obtained from naive frequency summation without any extrapolation to infinite cutoff frequencies. Our data shows clearly that the cutoff error is substantial and should be corrected for in order to eliminate the systematic error.

This is a serious test for the method and gives us enough confidence to proceed to an application of this method to the DCA in the next section as this is the domain for which it is designed. Note that it is of course by several orders of magnitude easier (in terms of memory and CPU time) to calculate $\chi_s^{+-}(Q)$ directly in CT-INT, a procedure that is — hélas — not applicable to the DCA as we will see in the next section.

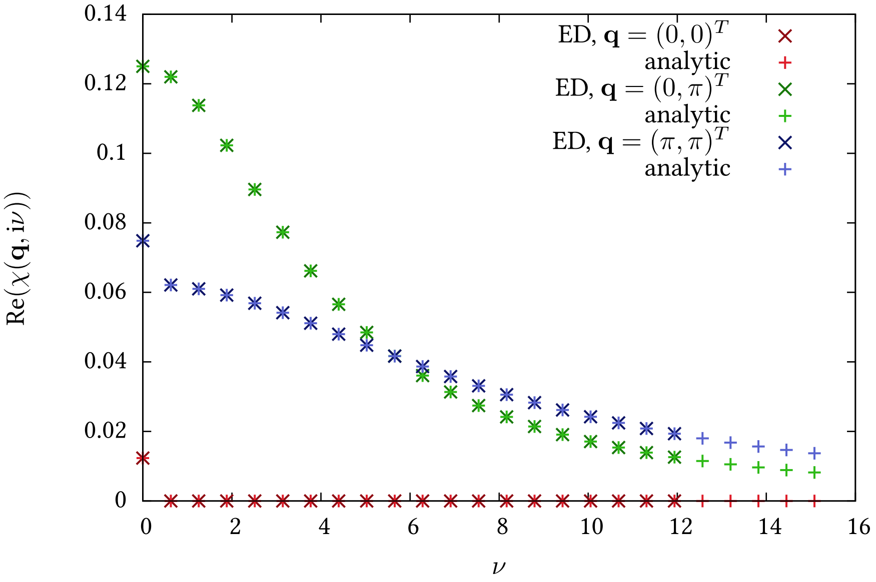

Figure 4.8.: Comparison of the results for $\chi(\mathbf{q}, \mathrm{i}\nu)$ for the noninteracting Hubbard model at $U = 0$, $\beta = 10$, $t = 1$ and $\mu = 0.6$ obtained by our exact diagonalization approach and by the direct analytic evaluation of equation (4.82). The two results agree within numerical rounding errors and the imaginary part of $\chi(\mathbf{q}, \mathrm{i}\nu)$ vanishes for both approaches.

4.6. Spin susceptibility in DCA

4.6.1. DCA

Let us briefly introduce the dynamical cluster approximation (DCA) here. For a detailed and extensive review of DCA and other cluster methods, the reader is referred to reference [16].

The principal idea of DCA is to extend the dynamical mean field theory (DMFT) (cf. e.g. [15]) by relaxing the constraint of the local self energy $\Sigma(\mathrm{i}\omega_n)$ systematically. Whereas the DMFT introduces an effective impurity problem determined through the DMFT self consistency equations for the description of a lattice problem in the thermodynamic limit. The impurity self energy of the impurity problem is then identified with the local self energy of the lattice problem with N sites. In the DCA, nonlocal corrections to the self energy are introduced by replacing the impurity problem by an effective cluster problem with N_c interacting sites. Then, the cluster self energy has a momentum dependence limited to cluster momenta and is identified with the coarse grained self energy of the lattice.

The coarse graining procedure is done in such a way that the Brillouin zone is separated into *patches* associated with the cluster momenta and a sum over lattice momenta in one patch is performed.

We shall denote all quantities on the cluster with an index c and quantities defined on the lattice with the index l. In addition cluster momenta are denoted by capital bold letters and cluster frequency-momenta are given normal capital letters. For lattice momenta we use the same convention but with lower case letters.

The effective cluster model for the description of the lattice problem has to be determined such that the DCA self consistency equations are fulfilled:

$$G_c(K) = G_{l,\mathrm{cg}}(K) = \frac{N_c}{N} \sum_{\mathbf{k}\in\mathbf{K}} \frac{1}{(G_{0,l}(k))^{-1} - \Sigma(K)}. \tag{4.83}$$

Here, the notation $\mathbf{k} \in \mathbf{K}$ refers to all lattice momenta $\mathbf{k}$ that lie on the patch associated with the cluster

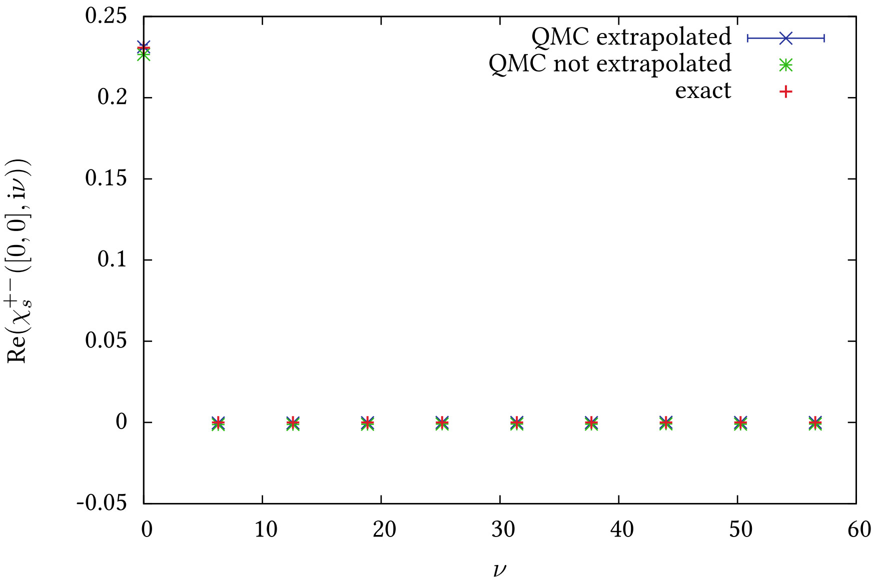

Figure 4.9.: Comparison of different methods for the determination of the real part of $\chi_s^{+-}(\mathbf{Q} = [0,0], \mathrm{i}\nu)$ for the Hubbard model at $U = 8$, $t = 1$, $\beta = 1$ and $\mu = 0$.

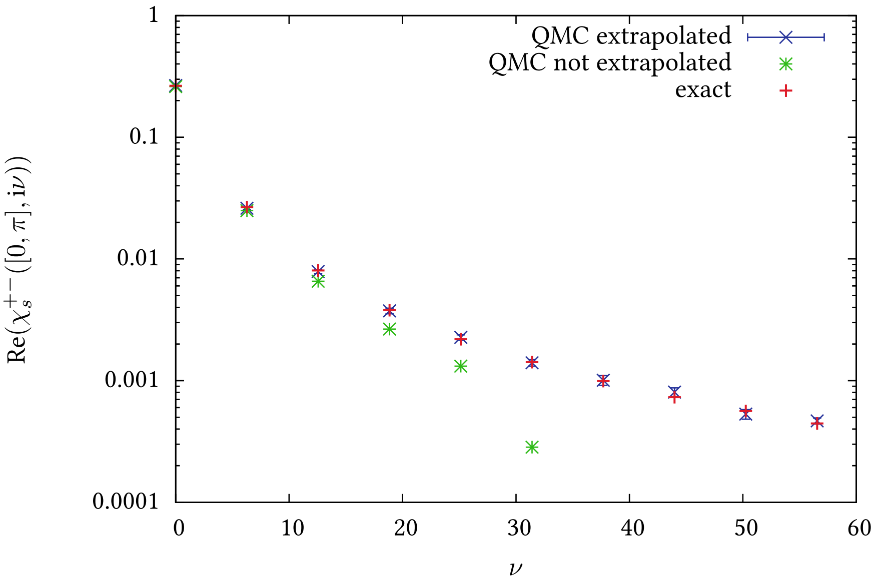

Figure 4.10.: Comparison of different methods for the determination of the real part of $\chi_s^{+-}(\mathbf{Q} = [0,\pi], \mathrm{i}\nu)$ for the Hubbard model at $U = 8$, $t = 1$, $\beta = 1$ and $\mu = 0$. We use a semilogarithmic scale to demonstrate that the asymptotic behaviour as a function of $\mathrm{i}\nu$ is only reproduced correctly if the Matsubara sums (4.54) are summed up completely without truncation.

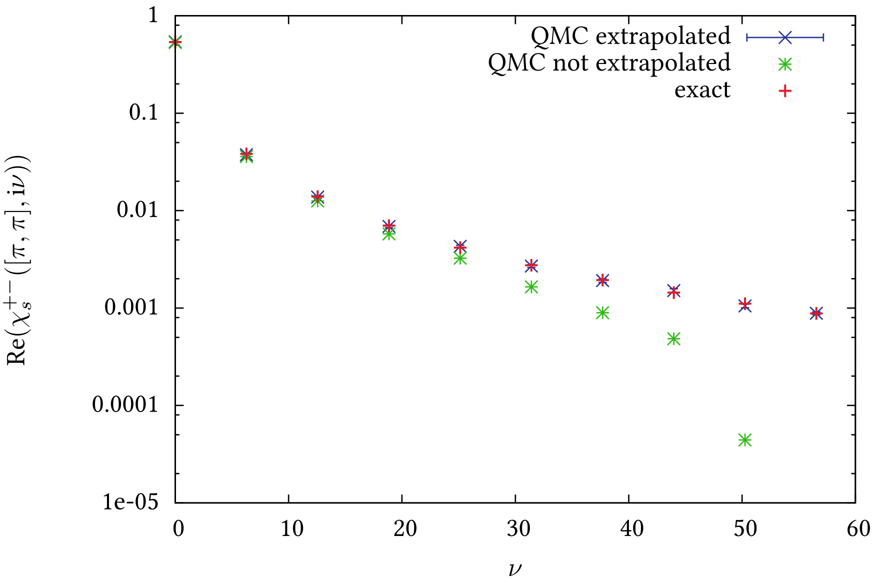

Figure 4.11.: Comparison of different methods for the determination of the real part of $\chi_s^{+-}(\mathbf{Q} = [\pi, \pi], \mathrm{i}\nu)$ for the Hubbard model at $U = 8$, $t = 1$, $\beta = 1$ and $\mu = 0$. We use a semilogarithmic scale to demonstrate that the asymptotic behaviour as a function of $\mathrm{i}\nu$ is only reproduced correctly if the Matsubara sums (4.54) are summed up completely without truncation.

momentum $\mathbf{K}$. The effective model is then described by the noninteracting cluster Green's function

$$G_{c,0}(K) = \frac{1}{(G_c(K))^{-1} + \Sigma(K)} \tag{4.84}$$

together with the local interacting Hamiltonian for every cluster site.

Self consistency is usually reached by iteration, starting with a vanishing self energy and thus using the coarse grained noninteracting lattice Green's function as a starting point. The resulting interacting cluster problem is solved using a cluster solver (e.g. CT-INT) and from the result, the self energy is extracted:

$$\Sigma(K) = \frac{1}{G_{c,0}(K)} - \frac{1}{G_c(K)}. \tag{4.85}$$

$\Sigma(K)$ is plugged into the coarse graining equation (4.83) and from the resulting coarse grained lattice Green's function, a new noninteracting cluster Green's function is determined:

$$G_{c,0}(K) = \frac{1}{(G_{l,\mathrm{cg}}(K))^{-1} + \Sigma(K)}. \tag{4.86}$$

This procedure is repeated until $\Sigma(K)$ converges and does not change any more with new iterations.

As the DCA is a self consistent theory formulated only on the one particle level, the way of calculation of two particle quantities is a priori ambiguous. However, Mark Jarrell et. al. argue in reference [43] that the thermodynamically consistent way to determine two particle quantities in the DCA is given by identifying the irreducible two particle vertex $\Gamma(Q; K, P)$ in the appropriate channel on the DCA cluster with its coarse grained version on the lattice. The reason for this is that susceptibilities obtained this way are identical to second derivatives of the DCA approximation of the grand canonical potential – a property which ensures thermodynamic consistency (cf. [43]).

This is the reason why we have been pursuing the study of two particle quantities given in terms of the two particle Green's function up to this point. This quantity gives us unique access to the irreducible vertex $\Gamma^{\perp}(Q;K,P)$ through the Bethe Salpeter equation (also referred to as two particle Dyson equation for example in [43]):

$$G_4^{\perp}(Q;K,P) = G_4^{\perp,0}(Q;K,P) + \sum_{K',P'} G_4^{\perp,0}(Q;K,K')\Gamma^{\perp}(Q;K',P')G_4^{\perp}(Q;P',P). \tag{4.87}$$

In the DCA, we now have two relevant Bethe salpeter equations, one for the effective model on the cluster and one for the lattice on which we want to calculate susceptibilities:

$$G_{4,c}^{\perp}(Q;K,P) = G_{4,c}^{\perp,0}(Q;K,P) + \sum_{K',P'} G_{4,c}^{\perp,0}(Q;K,K')\Gamma_c^{\perp}(Q;K',P')G_{4,c}^{\perp}(Q;P',P). \tag{4.88}$$

$$G_{4,l}^{\perp}(q;k,p) = G_{4,l}^{\perp,0}(q;k,p) + \sum_{k',p'} G_{4,l}^{\perp,0}(q;k,k')\Gamma_l^{\perp}(q;k',p')G_{4,l}^{\perp}(q;p',p). \tag{4.89}$$

The method of calculating $G_{4,l}^{\perp}(q;k,p)$ can be broken up in the following steps:

- Perform a full DCA cycle until convergence for the calculation of the self energy $\Sigma_c(K)$.
- In the last DCA iteration, calculate $G_{4,c}^{\perp}(Q;K,P)$ (in our case using CT-INT).
- Using
  $$G_{4,c}^{\perp,0}(Q;K,P) = -\frac{1}{\beta N_c}\delta_{K,P-Q}G_c(K)G_c(P) \tag{4.90}$$
  and equation (4.88) calculate $\Gamma_c^{\perp}(Q;K,P)$.
- Identify
  $$\Gamma_l^{\perp}(q;k,p) = \Gamma_c^{\perp}(Q;K,P) \tag{4.91}$$
  by a coarse graining procedure. This means that $\Gamma_l^{\perp}(q;k,p)$ will be constant for all momenta $\mathbf{q}$ lying on the same patch in momentum space as $\mathbf{Q}$ and so on for $\mathbf{k}$ and $\mathbf{p}$.
- Using a patchwise constant irreducible vertex $\Gamma_l^{\perp}(q;k,p)$ together with equation (4.89), using
  $$G_{4,l}^{\perp,0}(q;k,p) = -\frac{1}{\beta N}\delta_{k,p-q}G_l(k)G_l(p), \tag{4.92}$$
  calculate $G_{4,l}^{\perp}(q;k,p)$, where the single particle Green's functions G_l may be obtained from the noninteracting version in addition to the coarse grained self energy $\sigma(K)$ identical to the cluster self energy by virtue of Dyson's equation.

In the very end, the DCA result for the lattice susciptibility $\chi_s^{+-}(q)$ is obtained by summing over the inner Matsubara frequencies and momenta,

$$\chi_{s,l}^{+-}(q) = \sum_{k,p} G_{4,l}^{\perp}(q;k,p). \tag{4.93}$$

Note that this result may be obtained in principle for *any* lattice momentum $\mathbf{q}$ and is not restricted to cluster momenta. Momentum dependence is thus introduced at two levels: Firstly by the noninteracting one particle Green's function on the lattice on a fine momentum grid and secondly by the effect of the interaction communicated by the coarse grained self energy and the coarse grained irreducible vertex. Note that this procedure is constructed in a way as to yield the exact result in infinite dimensions as well as in the limit of infinite cluster size while providing thermodynamic consistency within the DCA at any cluster size.

As noted in reference [43], the Bethe Salpeter equation on the lattice may be completely coarse grained (index cg) to cluster momenta, as the DCA approximation of the irreducible vertex is constant on patches in momentum space corresponding to the cluster momenta:

$$\begin{aligned} G^{\perp,\mathrm{cg}}_{4,l}(q;K,P) = \sum_{\mathbf{k}\in\mathbf{K},\mathbf{p}\in\mathbf{P}} G^{\perp}_{4,l}(q;k,p) = \\ \sum_{\mathbf{k}\in\mathbf{K},\mathbf{p}\in\mathbf{P}} G^{\perp,0}_{4,l}(q;k,p) + \sum_{\mathbf{k}\in\mathbf{K},\mathbf{p}\in\mathbf{P}} \sum_{K',P'} \sum_{\mathbf{k}'\in\mathbf{K}',\mathbf{p}'\in\mathbf{P}'} G^{\perp,0}_{4,l}(q;k,k')\Gamma^{\perp}_{l}(Q;K',P')G^{\perp}_{4,l}(q;p',p), \end{aligned} \tag{4.94}$$

leading to

$$G^{\perp,\mathrm{cg}}_{4,l}(q;K,P) = G^{\perp,0,\mathrm{cg}}_{4,l}(q;K,P) + \sum_{K',P'} G^{\perp,0,\mathrm{cg}}_{4,l}(q;K,K')\Gamma^{\perp}_{l}(Q;K',P')G^{\perp,\mathrm{cg}}_{4,l}(q;P',P). \tag{4.95}$$

Here $G^{\perp,0,\mathrm{cg}}_{4,l}(q;K,P) = \sum_{\mathbf{k}\in\mathbf{K},\mathbf{p}\in\mathbf{P}} G^{\perp,0,}_{4,l}(q;k,p)$ is the coarse grained bubble part of the two particle Green's function[20].

Note that the external transfer momentum $\mathbf{q}$ is not affected by the coarse graining procedure, as the Bethe Salpeter equation is diagonal in the multiindex q. The main reason why this is beneficial is of course the fact that the sum in equation (4.93) may be split into

$$\sum_{k,p} = \sum_{K,P} \sum_{\mathbf{k}\in\mathbf{K},\mathbf{p}\in\mathbf{P}} \tag{4.96}$$

and the inner sum is carried out directly to yield $G^{\perp,\mathrm{cg}}_{4,l}(q;K,P)$. The number of relevant momenta is thus substantially reduced and all quantities depend on the same number of momenta, i.e. the number of cluster momenta.

4.6.2. Truncation of the Bethe-Salpeter equation

As discussed in the previous section, the central equation describing the influence of the irreducible vertex $\Gamma(Q;K,P)$ on two particle quantities $G_4(Q;K,P)$ is the *Bethe-Salpeter equation* [21] (cf. for example [25]):

$$G^{\perp}_{4}(Q;K,P) = G^{\perp,0}_{4}(Q;K,P) + \sum_{K',P'} G^{\perp,0}_{4}(Q;K,K')\Gamma^{\perp}(Q;K',P')G^{\perp}_{4}(Q;P',P). \tag{4.97}$$

For fixed Q, this tensor equation can be formally understood as a matrix equation with a matrix-matrix-matrix product in the second term. Unfortunately, we deal with infinitely sized matrices here and for any numerical calculation the matrices have to be truncated. In the present work, we always deal with a finite set of lattice momenta (on the DCA cluster), therefore no truncation in $\mathbf{K}$ is required. However, Matsubara frequencies have to be cut at some cutoff frequency.

Even though we have already provided many arguments why the frequency window on which $G^{\perp}_{4}$ has to be calculated must be shifted at finite transfer frequencies $\mathrm{i}\nu$, let us illustrate this issue even further in the context of the Bethe Salpeter equation in the following section.

Shift of the frequency window

A naive cutoff scheme consists of choosing the frequency window $\mathrm{i}\omega_1, \mathrm{i}\omega_2 \in \{-\mathrm{i}\omega_c, \dots, \mathrm{i}\omega_c\}$. This, however, leads to the problem of singular matrices:

$$G^{\perp,0}_{4}(Q;K,P) = -\frac{1}{\beta N} G(K)G(P)\delta_{K,P-Q}. \tag{4.98}$$

Obviously, this matrix is singular, if we cut it to the naive frequency window, as it does not have the full rank, which is illustrated in Figure 4.12.

---

[20] Note that our definition of $G^{\perp}_{4}$ implies that no factors of $\frac{N}{N_c}$ occur here.

[21] Here, we only care for the Bethe-Salpeter equation of the $S^{+}S^{-}$ spin channel with $G^{\perp}_{4}(Q;K,P) = \frac{1}{\beta N}\langle \bar{c}_{\sigma,K} c_{\bar{\sigma},K+Q} \bar{c}_{\downarrow,P} c_{\uparrow,P-Q} \rangle$. For the general case, the Bethe-Salpeter equation aquires additional spin indices.

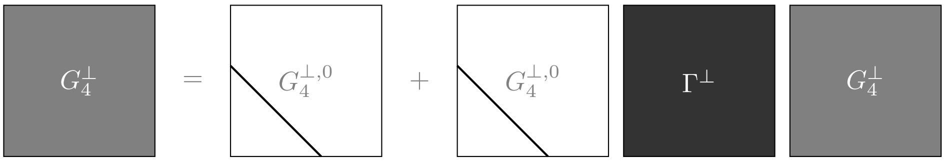

Figure 4.12.: Graphical representation of the naively truncated Bethe Salpeter equation. Vanishing matrix elements are depicted in white. It is obvious that $G_4^{\perp,0}$ is a singular matrix, if truncated in this way. The same is also true for the other matrices but the reduced rank is not as striking in this case.

Even more important, by inspection of actual data (e.g. figure 4.4), one observes that also $G_4^{\perp}(Q)$ may become a (numerically) singular matrix if cut inappropriately. The reason for this is that the matrix has a "center of mass" which shifts away from the central Matsubara frequency point with an increasing external Matsubara frequency $\mathrm{i}\nu$ given by the multiindex Q.

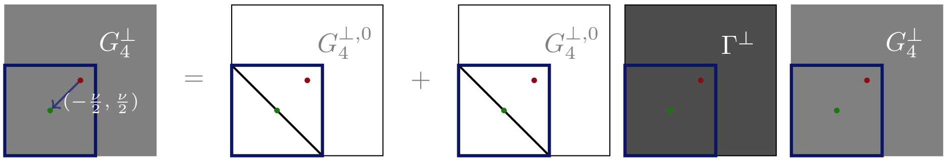

Figure 4.13.: Good truncation scheme. Red dot: Center of the imaginary frequency plane $(\mathrm{i}\omega_1, \mathrm{i}\omega_2)$. Green dot: Center of the shifted frequency window.

It is clear that in the shifted frequency window, $G_4^{\perp,0}(Q)$ is a diagonal matrix and has full rank. We can easily argue that also the other matrices have to be regular matrices[22].

Truncation error

Cutting the high frequency part from all matrices in the Bethe Salpeter equation introduces a systematic error, as the matrix-matrix-matrix product mixes the high and low frequency parts of the matrices.

In a practical calculation, $\Gamma_{\perp}$ is not the final result but used together with the lattice Bethe Salpeter equation. This masks the truncation error and makes it much less severe than it might seem here. The actual procedure for a DCA calculation is presented in the next section.

4.6.3. Calculation of $G_{4,l}^{\perp\mathbf{cg}}(q;K,P)$ on the lattice

Keeping in mind the issue of a possible systematic error (which is controllable by increasing the cutoff frequency) stemming from the truncation of the two Bethe Salpeter equations in the frequency domain, let us go one step back and deal with infinitely sized matrices first for the derivation of a compressed form of the quantity $G_{4,l}^{\perp\mathrm{cg}}(q;K,P)$ without an explicit calculation of the vertex $\Gamma^{\perp}(Q;K,P)$ as already proposed by Mark Jarrell in [43].

---

[22] Except for situations where we have a phase transition in the spin channel, as in this case the matrix $G_4^{\perp,0}(Q)\Gamma^{\perp}$ can have eigenvalues of 1, making the matrix $(\mathbf{1} - G_4^{\perp,0}(Q))\Gamma^{\perp}$ singular and destroying the argument.

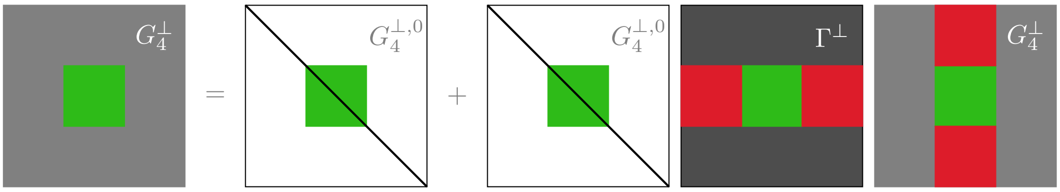

Figure 4.14.: If the Bethe Salpeter equation is truncated to the submatrices marked in green, the red submatrices are neglected. Therefore, in numerical calculations the exact Bethe Salpeter equation is always replaced by an approximate, truncated Bethe Salpeter equation.

It is easy to see that because of the identification $\Gamma_c^\perp(Q;K,P) = \Gamma_l^\perp(Q;K,P) = \Gamma^\perp(Q;K,P)$, the vertex $\Gamma^\perp(Q)$ may be eliminated from equations (4.88) and (4.95) by standard matrix manipulations and we obtain:

$$G_{4,l}^{\perp,\mathrm{cg}}(q) = \left[G_{4,l}^{\perp,0,\mathrm{cg}}(q)^{-1} - G_{4,c}^{\perp,0}(Q)^{-1} + G_{4,c}^{\perp}(Q)^{-1}\right]^{-1}. \tag{4.99}$$

Naturally, this result reduces nicely to the trivial equation $G_{4,l}^{\perp,\mathrm{cg}}(q) = G_{4,c}^{\perp}(Q)$ in the case in which the underlying lattice is identical with the underlying cluster.

Let us first think about the actual *meaning* of the inverse matrix notation. As we know (cf. section 4.4.4) that the diagonal matrix $G_{4,c}^{\perp,0}(Q)$ is transformed into an off diagonal matrix upon the introduction of a nonzero transfer momentum and frequency Q, it may seem that an inverse matrix in this case is not defined. This is indeed a special feature of infinite matrices that this kind of matrices can have an inverse which we can write down easily, adopting a matrix notation:

$$\left(G_{4,c}^{\perp,0}(Q)^{-1}\right)_{K,P} = -\beta N_c \delta_{K,P+Q}\frac{1}{G(K)G(P)}. \tag{4.100}$$

This is indeed the correct result, because

$$\begin{aligned}&\sum_{K'}\left(G_{4,c}^{\perp,0}(Q)^{-1}\right)_{K,K'}\left(G_{4,c}^{\perp,0}(Q)\right)_{K',P} = \\ &\sum_{K'} -\beta N_c \delta_{K,K'+Q}\frac{1}{G(K)G(K')}\left(-\frac{1}{\beta N_c}\right)\delta_{K',P-Q}G(K')G(P) = \delta_{K,P}.\end{aligned} \tag{4.101}$$

As already noted in section 4.6.2, all quantities in the Bethe salpeter equation have to be written down in the *shifted frequency window* upon truncation. It is interesting to observe that this means that all inverted quantities will then automatically be cast into an associated frequency window which is obtained by “transposition” of the shifted frequency window, such that the diagonal of the inverse lies on the diagonal of the frequency window, as is obvious from equation (4.100).

In summary, the correct way of dealing with two particle matrix equations at finite transfer frequency and momentum q requires an appropriate shift of the frequency window. Then, it is allowed to perform matrix manipulations and even inversions, even though the truncation error has to be considered. This leads to a form of equation (4.99) truncated to the shifted frequency window while the matrix inversion of the diagonal “bubble” terms $G_{4,l}^{\perp,0,\mathrm{cg}}(q)$ and $G_{4,c}^{\perp,0}(Q)$ can be performed analytically through equation (4.100).

4.7. Analytic continuation of dynamical two particle quantities

4.7.1. Calculation of the covariance matrix

Now, we have on our hands a viable method for the calculation of two particle quantities in the framework of the DCA. We have invested a considerable amount of care into the construction of a reliable method and have eliminated the systematic error stemming from the truncation of the sum over internal Matsubara frequencies. The result of our calculation is the quantity $\chi_s^{+-}(\mathbf{q}, \mathrm{i}\nu)$. Unfortunately, this quantity is only known on the imaginary frequency axis, while experimentally observable dynamical susceptibilities depend on real frequencies. While theory (cf. e.g. [25, 55, 56]) assures us that there exists a meromorphic function $\chi_s^{+-}(z)$ and the experimental quantity of interest is just $\chi_s^{+-}(\omega + \mathrm{i}0^+)$, the Wick rotation of numerical data from the imaginary frequency axis to the real axis is a daunting task. The method of choice for Monte Carlo data is a stochastic procedure using ideas from probability theory: The stochastic maximum entropy method ([42, 57]). We will not expand on this method here but only emphasize that it is crucial to have an accurate estimate of the covariance matrix of the underlying data before the method can be used. The reason for this is that without the knowledge of the covariance matrix, every data point of $\chi_s^{+-}(\mathbf{q}, \mathrm{i}\nu)$ will be considered to contain the same amount of information. This is, however not true given that the Monte Carlo data used for the estimation of χ_s^{+-} at different frequencies $\mathrm{i}\nu$ is strongly correlated as the same X_{C_n} matrices are used. This leads to potential cross correlations between different frequencies and the off diagonal elements of the covariance matrix therefore should be included.

In addition, the convergence to the asymptotic tail of $\chi_s^{+-}(\mathbf{q}, \mathrm{i}\nu)$ for high frequencies reduces the amount of information in the tail which can only appropriately be taken into account by considering the full covariance matrix.

A trustworthy and robust method for the estimation of the covariance matrix[23] is the *bootstrap* method. It makes the assumption that the sampled Monte Carlo bins are a representative approximation for the whole population. The approximated population is then *resampled* to produce *bootstrap samples* from which derived quantities may be calculated which are associated with a covariance matrix. Let us call our Monte Carlo bins Y_i with $i = 1, 2, \ldots N_{\text{bins}}$. Y_i is typically a high dimensional data structure accomodating scalar, vectorial and tensor-type observables, in our case the sign, the one particle Green's function $G(K)$ and the two particle Green's function $G_4^{\perp}(Q; K, P)$. Obviously, for this kind of object, a $+$ operation can be meaningfully defined and we can resample the Monte Carlo bins to obtain bootstrap samples

$$Y_j^{\mathrm{B}} = \frac{1}{N_{\text{bins}}} \sum_{j=1}^{N_{\text{bins}}} Y_{\text{rand}(N_{\text{bins}})}, \quad j \in \left[1, \ldots, N_{\text{bsamples}}\right] \tag{4.102}$$

with a uniformly distributed, natural random number $\text{rand}(N_{\text{bins}}) \in [1, \ldots, N_{\text{bins}}] \subset \mathbb{N}$. This way of generating a bootstrap sample clearly allows multiple pulling of the same Monte Carlo bin.

On every bootstrap sample, we can now apply our whole data analysis toolbox in order to extract the quantity of interest from the raw Monte Carlo data. We will call this operation formally $f(Y)$. We then obtain the estimate for the covariance matrix of our result f by[24]

$$\text{Cov}_{\text{bstrap}}(x, y) = \frac{1}{N_{\text{bsamples}}} \sum_i [f(Y_i^{\mathrm{B}})]_x [f(Y_i^{\mathrm{B}})]_y - \left(\frac{1}{N_{\text{bsamples}}} \sum_i [f(Y_i^{\mathrm{B}})]_x \right) \left(\frac{1}{N_{\text{bsamples}}} \sum_i [f(Y_i^{\mathrm{B}})]_y \right). \tag{4.103}$$

Numerical evaluation of equation (4.103) for huge data In the present context, the evaluation of equation (4.103) is unfortunately not trivial in the case of huge amounts of data. Because the two particle

---

[23] which itself is again an observable calculated from our Monte Carlo data and is in principle affected by a statistical error on its own right

[24] The result f can of course be as simple as a real number, in which case the covariance reduces to the variance of this scalar result, but it may in general be a complicated high dimensional array, in which case the notion of a covariance matrix has to be formally upgraded to a tensor. In order to circumvent this problem, we will always deal with vectorial quantities. This is acchieved by pulling down higher dimensional quantity to a vector by introduction of a generalized stride. For a matrix quantity this would mean rowwise concatenation of the matrix. Here, the x component of the vector valued function $f(Y)$ is notated as $[f(Y)]_x$.

Green's function $G_4^{\downarrow}(Q;K,P)$ requires large amounts of memory (typical sizes are several gigabytes but increase quickly if the number of frequencies or momenta is increased, the totality of the Monte Carlo bins ranging well over 100 GB), it can easily happen that we can only accomodate a small number N_{mem} bootstrap samples in the memory of the machine on which we perform the data analysis.

Typically, the Monte Carlo bins are stored on a mass storage device, today consisting of hard disk drives (HDD). While HDDs allow for massive data storage, the random access time is very long and reading the Monte Carlo bins from disk for the construction of bootstrap samples uses most of the time of the data analysis code. As the actual application of the function f to the data can usually be parallelized[25] the cost of reading data from disk dominates the total computational cost of the data analysis code.

Naturally, read access should therefore be limited to the absolutely neccessary amount. We notice that this can be acchieved by several measures:

- Generate the array of indices before actually reading the bins Y_i from disk. If for the construction of the bootstrap sample Y_j^{B} a bin is used multiple times, it only has to be read once.
- Generate the array of indices for *all* bootstrap samples before reading any bin from disk. This is beneficial if more than one bootstrap sample can be kept in memory as will be argued in the remaining part of this paragraph.
- Reorder the bootstrap samples in blocks to minimize the total number of Monte Carlo bins read from disk.

One step that might be advantageous with today's hardware possibilities is employing a solid state disk (SSD). SSDs have random access times that are orders of magnitude faster than HDDs and can be employed easily for this task[26].

If more than one bootstrap sample $N_{\text{mem}} > 1$ fit in memory, the total number of bins read from this can be reduced by roughly a factor N_{mem}. The reason for this is that on average every bin read from disk can be reused for the generation of N_{mem} bootstrap samples instead of only one.

As we already know in advance, which bins will be neccessary for which bootstrap samples, we can even optimize the order of the bootstrap samples such that the total number of disk reads is reduced. This process, however, has only turned out to be useful if the number N_{mem} is very small (typically $2\ldots 5$).

Let us illustrate the procedure in an example. For 20 Monte Carlo bins, we wish to generate 20 Bootstrap samples. Naively, one would generate each bootstrap sample at a time and pull a new random number after reading the previous Monte Carlo bin. This is linked to a read cost of 400 as 400 Monte Carlo bins have to be read from disk in total.

However, we can generate the indices to be read for each bootstrap sample beforehand. The result is shown in the upper part of table 4.1. Every line corresponds to a bootstrap sample and the numbers show how many times the Monte Carlo bin of the corresponding column has to be read. For example, bin number 16 is used 5 times to generate the bootstrap sample number 4. Naturally, if we know this before the calculation, we will only read it once from disk and multiply it with its number of occurrences, saving expensive read operations. This procedure brings down the total read cost to 251 in the present example.

Further economy of read operations is achieved by trying to use a bin once read from disk as often as possible before reading the next bin. This can be done by keeping as many bootstrap samples in memory, as possible, 2 in the present example. Now, if we read bin number 1 from disk for the generation of bootstrap sample number 1, we keep it in memory and use it also for the generation of bootstrap sample number 2. This gives us another spectacular reduction of read processes down to only 171. Obviously the lower limit of read processes is 20 which can only be reached if all bootstrap samples fit in memory.

We observe that a further reduction of read processes might be possible by finding the optimal order of bootstrap samples that are generated in parallel. Apparently, we have to block together bootstrap samples

---

[25] In the case of calculating the DCA approximation of $\chi_s^{+-}(Q)$ this can be trivially obtained by exploiting the fact that the Bethe Salpeter equations are diagonal in terms of the bosonic transfer momentum and frequency Q and thus each Q sector can be distributed to a different CPU.

[26] Using a RAID can also speed up the disk reads, but does not reduce the random acces time as SSDs do.

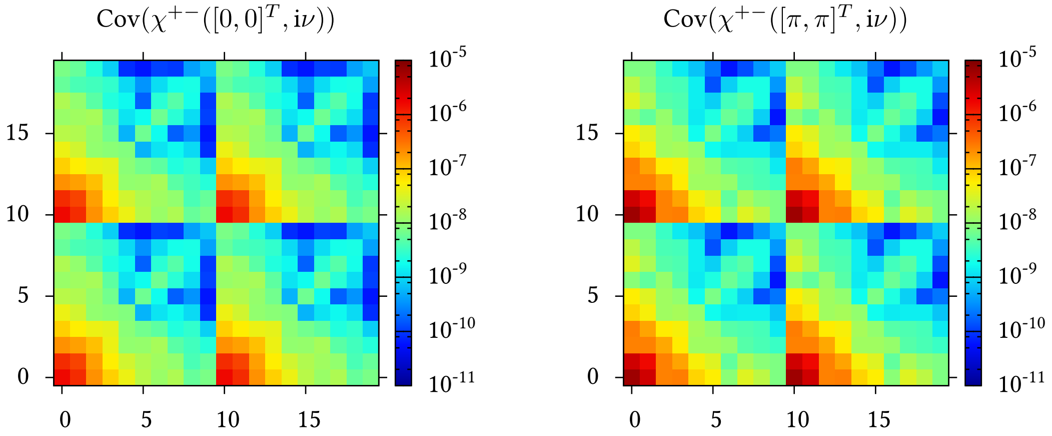

Figure 4.15.: Covariance matrix of $\chi^{+-}(\mathbf{Q}, \mathrm{i}\nu)$ for the same parameters as in figures 4.9 and 4.11. We use a logarithmic color scale and therefore show the absolute value of matrix elements. Note that the indices 0 through 9 correspond to the real part of χ^{+-}, while indices 10 to 19 denote the imaginary part. Thus, the diagonal blocks depict the covariance matrices of $\mathrm{Re}(\chi^{+-})$ and $\mathrm{Im}(\chi^{+-})$ respectively.

which have as many “holes”[27] in common as possible. This is a global optimization problem which grows difficult very quickly. We use a small simulated annealing Monte Carlo algorithm to at least bring down the read cost by some extent without being so ambitious as to really find the global minimum. For this, a *cost function* $\xi(\pi)$ associated with a permutation $\pi \in S(n)$ of the bootstrap samples is introduced. $\xi(\pi)$ is then just the number of read operations associated with a specific order π of bootstrap samples. The optimization process is thus mapped to finding the global minimum of $\xi(\pi)$. It is of course impossible to just check every permutation as their number is already for this small example $20! \approx 2.4 \cdot 10^{18}$.

For the simulated annealing, we introduce a Monte Carlo move $\pi \rightarrow \pi'$ by adding a *transposition* of two elements of the permutation π, i.e. in a given order π we exchange two bootstrap samples. Ergodicity is guaranteed by this procedure as every permutation may be written as a product of transpositions. We exclude swapping two bootstrap samples in the same memory block as this operation leaves the cost function invariant. Introducing an artificial inverse temperature β, we accept a swap with probability

$$P_{\pi \rightarrow \pi'} = \min \left[1, \mathrm{e}^{-\beta\left(\xi(\pi') - \xi(\pi)\right)}\right] . \tag{4.104}$$

The finite temperature allows for temporary increases of the cost function to overcome energy barriers. During the Monte Carlo run, the inverse temperature is slowly decreased until the cost function does not change any more (on a supportable time scale). This procedure allows for bringing down the read cost in the present example to 152. Note that unfortunately the benefit is strongly reduced when N_{mem} is increased, a step that is nevertheless preferable if affordable as the total read cost can be reduced by roughly a factor of N_{mem} until the limit N_{bins} is reached for $N_{\text{mem}} = N_{\text{bsamples}}$.

4.7.2. Importance of the full covariance matrix

The covariance matrices of $\chi^{+-}(\mathbf{Q}, \mathrm{i}\nu)$ for the same data as displayed in figures 4.9 and 4.11 are shown in figure 4.15. The covariance matrix respects the whole data analysis procedure including the extrapolation to infinite cutoff frequency of the frequency sum. It is apparent from the data that the approximation of a diagonal covariance matrix is *not* valid in general. The reason for the correlations between different frequencies

---

[27] i.e. Monte Carlo bins that are not used for the specific bootstrap sample.

is twofold: On the one hand, the asymptotic behaviour for high frequencies is reflected in the covariance matrix and on the other hand, data for different frequencies $\mathrm{i}\nu$ stems originally from the same $X^{\sigma}_{C_n}$ matrices introduced earlier and is therefore correlated.

Ignoring these correlations might introduce spurious behaviour after analytic continuation to the real axis and is therefore not acceptable.

4.7.3. Analytic continuation of the spin susceptibility

Ultimately, we are interested in the spin susceptibility on the real axis

$$\chi''(\mathbf{q},\omega) = \frac{\pi}{Z}\sum_{n,m} \mathrm{e}^{-\beta E_n} \left|\langle n\,|\,S_+(\mathbf{q})\,|\,m\rangle\right|^2 \delta(\omega + E_n - E_m)(1-\mathrm{e}^{-\beta\omega}). \tag{4.105}$$

Here we also understand that $S^+(\mathbf{q}) = \frac{1}{\sqrt{N}}\sum_{\mathbf{k}} c^\dagger_{\uparrow,\mathbf{k}} c_{\downarrow,\mathbf{k}+\mathbf{q}}$ and therefore $(S^+(\mathbf{q}))^\dagger = S^-(\mathbf{q})$. From the DCA code, we obtain the coarse grained lattice 2 particle Green's function

$$\begin{aligned} G_4(k,p,q) = \left(\frac{1}{\beta N}\right)^3 \sum_{r_1,r_2,r_3,r_4} \int_0^\beta \mathrm{d}(1234)\, \mathrm{e}^{\mathrm{i}\omega_n\tau_1 - (\mathrm{i}\omega_n + \mathrm{i}\nu)\tau_2 + \mathrm{i}\omega'_n\tau_3 - (\mathrm{i}\omega'_n - \mathrm{i}\nu)\tau_4} \\ \mathrm{e}^{-\mathrm{i}\mathbf{k}r_1 + \mathrm{i}(\mathbf{k}+\mathbf{q})r_2 - \mathrm{i}\mathbf{p}r_3 + \mathrm{i}(\mathbf{p}-\mathbf{q})r_4} \left\langle T c^\dagger_{\uparrow,r_1}(\tau_1) c_{\downarrow,r_2}(\tau_2) c^\dagger_{\downarrow,r_3}(\tau_3) c_{\uparrow,r_4}(\tau_4)\right\rangle . \end{aligned} \tag{4.106}$$

We obtain the spin susceptibility on the imaginary axis by summing over the internal momenta $\mathbf{k}$ and $\mathbf{p}$ and over the internal frequencies $\mathrm{i}\omega_n$ and $\mathrm{i}\omega'_n$:

$$\chi(\mathbf{q},\mathrm{i}\nu) = \sum_{\mathrm{i}\omega_n,\mathrm{i}\omega'_n,\mathbf{k},\mathbf{p}} G_4(k,p,q). \tag{4.107}$$

This gives us the Lehmann representation

$$\chi(\mathbf{q},\mathrm{i}\nu) = \frac{1}{Z}\sum_{n,m} \left|\langle n\,|\,S_+(\mathbf{q})\,|\,m\rangle\right|^2 \frac{\mathrm{e}^{-\beta E_m} - \mathrm{e}^{-\beta E_n}}{E_n - E_m - \mathrm{i}\nu}. \tag{4.108}$$

Comparing the Lehmann representations on the real and imaginary axis, we obtain the basic equation needed for the analytic continuation:

$$\chi(\mathbf{q},\mathrm{i}\nu) = \frac{1}{\pi}\int_{-\infty}^{\infty} \mathrm{d}\omega\, \frac{1}{\omega + \mathrm{i}\nu}\,\chi''(\mathbf{q},\omega). \tag{4.109}$$

Unfortunately, this cannot be used, as we do not know the sum rule

$$\int_{-\infty}^{\infty} \mathrm{d}\omega\, \chi''(\mathbf{q},\omega). \tag{4.110}$$

We can, however, rewrite the expression such that a sum rule is known, which is crucial for the application of the stochastic maximum entropy method:

$$\chi(\mathbf{q},\mathrm{i}\nu) = \frac{1}{\pi}\int_{-\infty}^{\infty} \mathrm{d}\omega\, \frac{\omega}{\omega+\mathrm{i}\nu}\,\frac{\chi''(\mathbf{q},\omega)}{\omega} = \int_{-\infty}^{\infty} \mathrm{d}\omega\, K(\mathrm{i}\nu,\omega)A(\omega). \tag{4.111}$$

For the "spectral function" $A(\omega)$, a sum rule can be easily found, namely:

$$\int_{-\infty}^{\infty} \mathrm{d}\omega\, A(\omega) = \int_{-\infty}^{\infty} \mathrm{d}\omega\, \frac{\chi''(\mathbf{q},\omega)}{\omega} = \pi\chi(\mathbf{q},\mathrm{i}\nu=0). \tag{4.112}$$

The kernel used in the stochastic maximum entropy method is given by

$$K(\mathrm{i}\nu,\omega) = \frac{\omega}{\pi(\omega+\mathrm{i}\nu)}. \tag{4.113}$$

The maximum entropy method calculates $A(\omega)$, which then has to be transformed back to $\chi''(\mathbf{q},\omega)$.

Note that this procedure has the drawback that the maximum entropy method needs to be fed with a sum rule bearing a statistical error. It is therefore advisable to divide $\chi(\mathbf{q},\mathrm{i}\nu)$ by the sum rule — exploiting the idea discussed in section A.2 — already on the level of bootstrap samples. This leads to the incorporation of statistical uncertainties in the covariance matrix and the exactly known sum rule of 1 can be used.

4.8. Conclusion

We have developed a method for the calculation of the dynamical spin susceptibility in DCA on the real frequency axis. The whole procedure is very involved and requires many intermediate steps that have to be controlled:

- Before starting the two particle calculation, the DCA cycle has to be checked to converge, yielding the cluster self energy $\Sigma(\mathbf{K},\mathrm{i}\omega_n)$. This step can be handeled pretty well as a lot of experience is available and CT-INT is a reliable cluster solver.
- In the second step, for the converged DCA bath Green's function, a final CT-INT calculation is performed, in which $G^{\perp}_{4,c}(Q;K,P)$ is calculated. Appropriate cutoff frequencies have to be chosen. This step is computationally extremely demanding and enormous amounts of CPU time and memory are required.
- For the determination of the lattice two particle Green's function, the cluster $G^{\perp}_{4,c}(Q;K,P)$ matrix has to be inverted for every frequency-momentum combination Q, corrected for the DCA lattice bubble part $G^{\perp,0,cg}_{4,l}(q)$ and inverted back as discussed in section 4.6.3.
- In order to obtain $\chi^{+-}(\mathbf{q},\mathrm{i}\nu)$, the sum over internal frequencies and momenta K and P has to be performed for $G^{\perp}_{4,l}$ for different cutoff frequencies and extrapolated to infinite cutoff frequency.
- The last two steps have to be repeated for every bootstrap sample in order to obtain a reliable estimate of the covariance matrix of $\chi^{+-}(\mathbf{q},\mathrm{i}\nu)$.
- Analytic continuation to the real frequency axis has to be performed for every $\mathbf{q}$ that is requested.

Note that frequency cutoff errors can in principle be eliminated completely by moving the matrix inversion step into the loop for different cutoff frequencies, as the extrapolation procedure will eliminate a potential cutoff error stemming from this step. This comes, however, at the price of an increase of the computational cost for the calculation of $\chi^{+-}(\mathbf{q},\mathrm{i}\nu)$ for every bootstrap sample. Data for the dynamic susceptibility $\chi^{+-}(\mathbf{q},\omega)$ calculated in DCA by using this method of full elimination of the cutoff error will be presented in an upcoming publication [58].

Raw indices for 20 bootstrap samples of 20 Monte Carlo bins.

$\#_{\text{bin}}$ mod 10 =	1	2	3	4	5	6	7	8	9	0	1	2	3	4	5	6	7	8	9	0
$\#_B$ =1	1		1		1		3		2	1	1		3	2	1				2	2
2	3			2		1	1	1	3		2		1	2	1	1	1		1	
3	1	1	1		1	1					3	4	1	2		3		2		
4	1	2			1	1	2		1		1		1	1	1	5			3	
5	2	2	2			3		1		1		2		3					2	2
6		2		1	2	1			4	1	1	1	2	2	1		1	1		
7	2			2	3		1	1	3	1	1		1		1	1	1			2
8	1	2	1	3		2	2			2	3	1					2		1	
9					1		1	3			1	2	3	2	3	2		1		1
10		2		1		1	1	1	1	2	3		1		2	1	1		1	2
11	3	1		3				1		1		1	3	2		3	1			1
12	2		1	1	2			1	1	3		2	1	1		1		3		1
13		1	3		1	1	1	1	1			1	2	1	1	2			2	2
14	1	2	2	1	2	3			2			1		1	1	1		1	1	1
15	1	2	1	2		2	1	1		1	2		1		1	1	1	1	1	1
16		1	1	2		4	1	1	2		1		1			1	1	2	2	
17	1	1	2		1		1		1	3	2		3		2	1			1	1
18	1	1	3		2	1		1	3					2		1		2		3
19		1	1	3	2		1	1	1		1		1			2		1	5	
20	1		1	1		2	2	1		1	2		1	1	2	3	1			1

Naive: 400 reads. Repeat economy: 251 reads. With 2 bins in memory: 171 reads.

Optimized index array for the same bootstrap samples as above.

$\#_{\text{bin}}$ mod 10 =	1	2	3	4	5	6	7	8	9	0	1	2	3	4	5	6	7	8	9	0
$\#_B$ =3	1	1	1		1	1					3	4	1	2		3		2		
6		2		1	2	1			4	1	1	1	2	2	1		1	1		
20	1		1	1		2	2	1		1	2		1	1	2	3	1			1
15	1	2	1	2		2	1	1		1	2		1		1	1	1	1	1	1
13		1	3		1	1	1	1	1			1	2	1	1	2			2	2
9					1		1	3			1	2	3	2	3	2		1		1
7	2			2	3		1	1	3	1	1		1		1	1	1			2
10		2		1		1	1	1	1	2	3		1		2	1	1		1	2
16		1	1	2		4	1	1	2		1		1			1	1	2	2	
19		1	1	3	2		1	1	1		1		1			2		1	5	
14	1	2	2	1	2	3			2			1		1	1	1		1	1	1
18	1	1	3		2	1		1	3					2		1		2		3
12	2		1	1	2			1	1	3		2	1	1		1		3		1
11	3	1		3				1		1		1	3	2		3	1			1
1	1		1		1		3		2	1	1		3	2	1				2	2
17	1	1	2		1		1		1	3	2		3		2	1			1	1
8	1	2	1	3		2	2			2	3	1					2		1	
5	2	2	2			3		1		1		2		3					2	2
2	3			2		1	1	1	3		2		1	2	1	1	1		1	
4	1	2			1	1	2		1		1		1	1	1	5			3	

Optimized bootstrap sample order:152 reads.

Table 4.1.: Example showing a bootstrap sample index array for 20 Monte Carlo bins (columns) before (top) and after the minimization of the bin reads with 2 bins in memory.

5. Josephson current

5.1. Introduction

Magnetic degrees of freedom in superconducting environments have attracted considerable interest due to the underlying competing effects. Already a classical spin oriented along the z-axis [59, 60] embedded in a superconducting host generates a localized state within the superconducting gap. As a function of the interaction strength this excitation crosses the Fermi energy thereby triggering a first order transition between a ground state with vanishing total electronic spin and a ground state with nonzero total electronic spin.

In the case of a quantum spin, things become even more interesting and hybrid superconductor-quantum dot devices have recently attracted much attention [61] due to their peculiar physical behavior determined by the interplay of superconductivity of the leads and the level characteristics of the dot. Applications in nanoelectronics or quantum-information processing are envisaged. Among other properties, DC Josephson transport [62–67] was intensively studied. Similar to the Josephson effect of ordinary tunnel junctions [68] a difference $\phi \neq 0, \pi$ of the order parameter phases of the two superconductors with gap Δ leads to an equilibrium Josephson current J running through the system [62–67]. The focus was on carbon nanotube dots [62, 64–67] with well separated single-particle levels, i.e., level broadening Γ and temperature T much smaller than the level spacings, simplifying the modeling as a single-level dot with energy ϵ can be considered.

It is well established both theoretically [69] as well as experimentally [63–67] that the local Coulomb interaction, i.e. the dot charging energy U, can lead to a 0-π transition of the quantum dot Josephson junction, associated to a first order (level-crossing) quantum phase transition from a singlet (0) to a doublet (π) ground state [70]. In fact, a variation of any of the system parameters U, ϵ, Δ, ϕ, as well as the tunnel couplings $\Gamma_{L/R}$ (with $\Gamma = \Gamma_L + \Gamma_R$) can be used to tune the system across the phase boundary, if the others are taken from appropriate ranges. At $T = 0$ the transition leads to a jump in J from a large and positive (0-phase) to a small and negative value (π-phase) as Cooper pair tunneling through the junction necessarily accumulates a phase π if a local magnetic moment is formed on the quantum dot [71–74]. At finite temperatures, it is smeared out and significantly diminished, yet the sign change of J is clearly observed in SQUID setups [63, 64, 67]. The experimental challenge in observing the true magnitude of the Josephson current to be compared with theoretical predictions consists in suppressing uncontrolled phase fluctuations, which can be achieved by using designed on-chip circuits [65, 66]. In such experiments J is tuned by a variation of a gate voltage V_{g} which translates into a rather controlled change of ϵ[1], inducing a change of the electron number on the impurity. The effect of the changing electron number on the behavior of such systems has also been extensively studied[75–78] and the theoretical expectation of the collapse of the Kondo effect if the superconducting gap Δ exceeds the Kondo temperature T_K has been confirmed by experiments of Buitelaar et al.[79].

The physics becomes particularly interesting if the dot is tuned to a parameter regime in which Kondo correlations [1] become relevant for suppressed superconductivity. It is characterized by the appearance of the Kondo scale (at odd dot filling) $k_{\mathrm{B}}T_{\mathrm{K}} = \sqrt{\Gamma U/2}\exp(-\pi U/8\Gamma)$ [1]. Kondo physics is important if $k_{\mathrm{B}}T \lesssim k_{\mathrm{B}}T_{\mathrm{K}} \ll \Gamma$, with k_{B} denoting the Boltzmann constant. In this regime perturbative methods in either U, such as self-consistent Hartree-Fock (HF) [80], or Γ [69] become uncontrolled. Even for $\Delta \gg k_{\mathrm{B}}T_{\mathrm{K}}$, at which superconductivity prevails, one expects Kondo correlations to have a significant impact on J. These were partly incorporated using a method developed for large Δ [3]. Other techniques successfully used for Kondo correlated quantum dots with normal leads, such as the noncrossing approximation (NCA) [81, 82], numerical renormalization group (NRG) [83–87], (Hirsch-Fye) quantum Monte Carlo (QMC) [88–90], and

---

[1] The gate voltage variation may simultaneously slightly change the level broadening Γ by changing Schottky barriers at the contacts (cf. reference [67]).

functional renormalization group (fRG) [84] were extended to the present setup. With superconducting leads they suffer from significant conceptual or practical limitations such as, e.g. half filling of the dot level (NRG) and high (NCA, QMC) or zero (fRG) temperature and, therefore, cannot be used for a quantitative comparison to experiments performed at temperatures of the order of a few tens of mK and with a wide span of gate voltages [65, 66]. The regime of the strongest competition between superconductivity and Kondo correlations is reached for $\Delta \approx k_{\mathrm{B}}T_{\mathrm{K}}$. For typical experimental gap sizes of $\Delta \approx 0.1\,\mathrm{meV}$ [65–67], in this regime $k_{\mathrm{B}}T_{\mathrm{K}} \ll \Gamma$ is no longer fulfilled. Still, even for $k_{\mathrm{B}}T_{\mathrm{K}} \lesssim \Gamma$ a precursor of Kondo correlations is expected to stabilize the singlet phase and perturbative methods become unreliable.

Most numerical works present in the literature, however, only present either the study of the Josephson current [83, 84, 88, 89] or the study of the spectral properties of the Quantum dot [86].

In addition to numerical efforts, many analytical approximations have been introduced to tackle different aspects of the physics of the problem. The non crossing approximation has been used to show that Andreev bound states crossing the Fermi energy are connected to the 0 to π transition of the Josephson current[81]. Perturbative methods as well as mean field theory have brought a quite complete understanding of the phase diagram featuring the 0 and π phases as well as the intermediate phases $0'$ and π'[3, 91, 92]. Another method employed by several authors is the introduction of different analytically solvable effective models, which are valid in different limits [3, 86, 92]. These models are very useful to acquire an intuitive understanding of the physics. We will present the study of an effective Hamiltonian for the limit of a superconducting gap Δ much larger than the bandwidth to support the interpretation of the CT-INT data.

In this chapter[2] we demonstrate how to use the weak coupling CT-INT method [9] to compute the Josephson current as well as the spectral functions for the same parameter set in order to present a comprehensive study of the 0 to π transition of a Josephson quantum dot. Our numerically exact data clearly confirms the picture of a first order phase transition from a singlet phase linked to the 0-junction regime of the Josephson current J to a doublet phase corresponding to the π-junction regime.

We further exploit the exceptional flexibility and accuracy of this approach and compute J in combination with the normal-state linear conductance G for the parameters of the experiment of Ref. [65]. Our simultaneous analysis of J and G reveals that the dot shows significant Kondo correlations, but superconductivity prevails as $\Delta \approx 10T_{\mathrm{K}}$. In the normal state it lies in the interesting and theoretically challenging parameter regime with $k_{\mathrm{B}}T \approx k_{\mathrm{B}}T_{\mathrm{K}} \approx \mu_{\mathrm{B}}h$, where $\mu_{\mathrm{B}}h$ (with the Bohr magneton μ_{B}) denotes the scale associated to the applied Zeeman field h used to destroy superconductivity. Compared to previous approaches, we are now able to quantitatively study this experimentally relevant parameter regime with a numerically exact method, and find excellent agreement between the experimentally measured critical current J_{c} and the numerically computed one for both the 0- and π-phases (see Fig. 5.16). We show that due to the fairly large left-right asymmetry of the tunnel couplings and the finite temperature the current-phase relation $J(\phi)$ is rather sinusoidal even close to the 0-π transition (see Fig. 5.17), providing an a-posteriori justification of the extraction of J_{c} from the measured current-voltage characteristics of the on-chip circuits applying the extended RSJ model [65, 66]. Finally, using the parameters of the experiment, but increasing Γ such that $\Delta \approx k_{\mathrm{B}}T_{\mathrm{K}}$ we compute the gate voltage dependence of the current in the regime of the strongest competition between superconductivity and (precursors of) Kondo correlations (see Fig. 5.18).

A somewhat related topic — explored out of curiosity — is the study within dynamical mean field theory (DMFT) [15] of the periodic Anderson model with an s-wave BCS-conduction band (BCS-PAM). Within this approximation, the BCS-PAM maps onto the single impurity Anderson model with superconducting baths supplemented with a self-consistency condition. We will show that the physics of the impurity model can be taken over to the lattice case. In particular the first order transition observed in the impurity model is reproduced in the BCS-PAM and is signalized by the crossing of the low energy excitations in the local density of states. The momentum resolved single particle spectral function in the singlet phase reveals the coherent, Bloch-like, superposition of Andreev bound states. In the doublet or local moment phase the single particle spectral function is characterized by incoherent quasiparticle excitations. We provide an understanding of this in terms of models of disorder.

---

[2] The content of this chapter has been published in nearly identical form in references [24] and [28]. Additional technical details are provided here to explain the method for the calculation of the conductance in a more profound way.

5.2. Model

The physics of a quantum dot coupled to two superconducting leads with N lattice sites (L=left, R=right) via a hybridization term is captured by the single impurity Anderson model with the leads described by the BCS mean-field Hamiltonian:

$$\tilde{H} = \sum_{\alpha=L}^{R} \tilde{H}_{0,\alpha} + \tilde{H}_d + \tilde{H}_V, \tag{5.1}$$

with

$$\begin{aligned}
\tilde{H}_{0,\alpha} &= \sum_{k,\sigma} \xi_k \tilde{c}^\dagger_{k,\sigma,\alpha} \tilde{c}_{k,\sigma,\alpha} \\
&\quad - \sum_k \left(\Delta \mathrm{e}^{i\phi_\alpha} \tilde{c}^\dagger_{k,\uparrow,\alpha} \tilde{c}^\dagger_{-k,\downarrow,\alpha} + \text{h.c.} \right), \\
\tilde{H}_d &= \sum_\sigma \xi_d \tilde{d}^\dagger_\sigma \tilde{d}_\sigma + U \left(\tilde{d}^\dagger_\uparrow \tilde{d}_\uparrow - \frac{1}{2} \right) \left(\tilde{d}^\dagger_\downarrow \tilde{d}_\downarrow - \frac{1}{2} \right), \\
\tilde{H}_V &= -\frac{V}{\sqrt{N}} \sum_{\alpha=L}^{R} \sum_{\sigma,k} \left(\tilde{c}^\dagger_{k,\sigma,\alpha} \tilde{d}_\sigma + \tilde{d}^\dagger_\sigma \tilde{c}_{k,\sigma,\alpha} \right).
\end{aligned} \tag{5.2}$$

The operators $\tilde{c}^\dagger_{k,\sigma,\alpha}$ are creation operators for electrons with a z-component of the spin σ and momentum k in lead α, $\tilde{d}^\dagger_\sigma$ is a creation operator of an electron with a z-component of the spin σ on the quantum dot. $\xi_k = \epsilon(k) - \mu = -2t\cos(k) - \mu$ is the dispersion relation for the electrons in the leads, where we assume, that the dispersion is independent of the lead index α, and $\xi_d = \epsilon_d - \mu$ is the position of the dot level. Throughout this chapter, we will express all quantities in units of $t = 1$. The superconducting order parameter has a modulus Δ and a phase ϕ_α. The parameter V characterizes the strength of the hybridization, and U corresponds to the Coulomb blockade.

Since the Hamiltonian does not conserve the electron number as a consequence of the BCS-term, we use the standard trick of rewriting the Hamiltonian in terms of creation and annihilation operators of quasiparticles, which for spin up are identical to the electrons, but correspond to holes in the spin down sector. This can also be expressed as a canonical transformation:

$$\tilde{d}^\dagger_\uparrow \to d^\dagger_\uparrow,\ \tilde{d}^\dagger_\downarrow \to d_\downarrow,\ \tilde{c}^\dagger_{k,\uparrow,\alpha} \to c^\dagger_{k,\uparrow,\alpha},\ \tilde{c}^\dagger_{-k,\downarrow,\alpha} \to c_{k,\downarrow,\alpha}. \tag{5.3}$$

Using the new operators, the Hamiltonian can be written in a Nambu notation:

$$\begin{aligned}
H = H_0 + H_U &= \sum_{k,\alpha} \mathbf{c}^\dagger_{k,\alpha} \mathbf{E}_\alpha(k) \mathbf{c}_{k,\alpha} + \mathbf{d}^\dagger \boldsymbol{\epsilon}_d \mathbf{d} \\
&\quad - \frac{V}{\sqrt{N}} \sum_{k,\alpha} \left(\mathbf{c}^\dagger_{k,\alpha} \boldsymbol{\sigma}_z \mathbf{d} + \mathbf{d}^\dagger \boldsymbol{\sigma}_z \mathbf{c}_{k,\alpha} \right) + H_U
\end{aligned} \tag{5.4}$$

with $H_U = -U(d^\dagger_\uparrow d_\uparrow - \frac{1}{2})(d^\dagger_\downarrow d_\downarrow - \frac{1}{2})$, the Nambu spinors

$$\mathbf{d} = \begin{pmatrix} d_\uparrow \\ d_\downarrow \end{pmatrix}, \quad \mathbf{c}_{k,\alpha} = \begin{pmatrix} c_{k,\uparrow,\alpha} \\ c_{k,\downarrow,\alpha} \end{pmatrix}, \tag{5.5}$$

the matrices

$$\mathbf{E}_\alpha(k) = \begin{pmatrix} \xi_k & -\Delta \mathrm{e}^{i\phi_\alpha} \\ -\Delta \mathrm{e}^{-i\phi_\alpha} & -\xi_k \end{pmatrix}, \quad \boldsymbol{\epsilon}_d = \begin{pmatrix} \xi_d & 0 \\ 0 & -\xi_d \end{pmatrix} \tag{5.6}$$

and the Pauli matrix

$$\boldsymbol{\sigma}_z = \begin{pmatrix} 1 & 0 \\ 0 & -1 \end{pmatrix}. \tag{5.7}$$

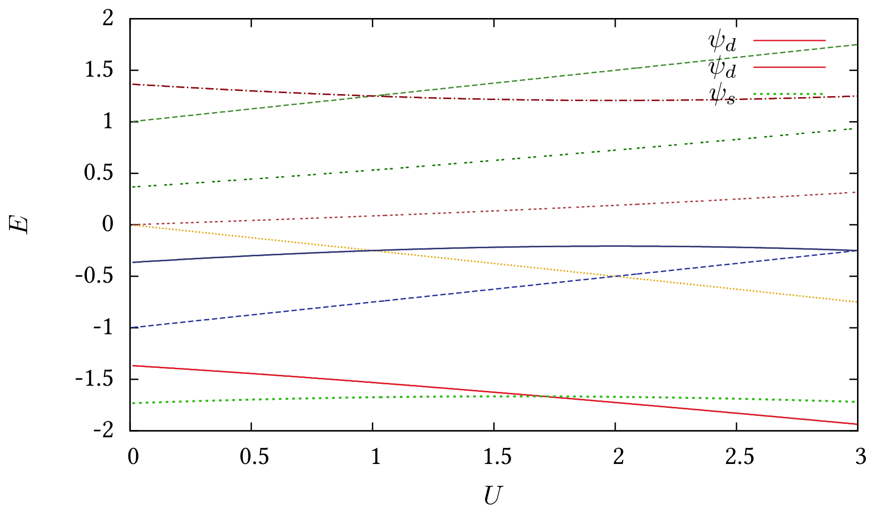

Figure 5.1.: Eigenenergies of the effective Hamiltonian (5.15) for varying U. The fixed parameters are given by $V = 0.5$ and $\Delta = 1$. The crossing of the two lowest levels is clearly seen at $U \approx 1.7$. The ground state for $U < 1.7$ is a singlet state. For larger values of U, the twofold degenerate doublet state becomes energetically more favorable.

For practical reasons, we use the following definition for the single particle Green's function throughout Sec. 5.2 to Sec. 5.5 as already used before:

$$G_{dd}^{\sigma\sigma'}(i\omega_m) = \int_0^\beta \mathrm{d}\tau \, \exp(i\omega_m \tau) \, \langle T d_\sigma^\dagger(\tau) d_{\sigma'} \rangle \,. \tag{5.8}$$

With this definition, the resolvent operator $\mathbf{G}^0(i\omega_m) = \left(-i\omega_m \mathbf{1} - \mathbf{H}_0^T\right)^{-1}$ can be used to obtain the Green's function of the noninteracting system:

$$\begin{aligned} \mathbf{G}_{dd}^0(i\omega_n)^{-1} &= (-i\omega_n \mathbf{1} - \boldsymbol{\epsilon}_d) \\ &\quad + \frac{V^2}{N} \sum_{\alpha,k} \boldsymbol{\sigma}_z \left(i\omega_n \mathbf{1} + \mathbf{E}_\alpha^T(k)\right)^{-1} \boldsymbol{\sigma}_z. \end{aligned} \tag{5.9}$$

From this equation, we obtain $\mathbf{G}_{dd}^0(\tau)$, which is the basic ingredient for the application of CT-INT to this problem as we already detailed in chapter 3.

For the Josephson current, we will also need the Green's function $\mathbf{G}_{kd}^{0,\alpha}$:

$$\mathbf{G}_{kd}^{0,\alpha} = \frac{V_\alpha}{\sqrt{N}} \left(i\omega_n \mathbf{1} + \mathbf{E}_\alpha^T(k)\right)^{-1} \boldsymbol{\sigma}_z \mathbf{G}_{dd}^0(i\omega_n). \tag{5.10}$$

5.3. Effective Hamiltonian in the limit $\Delta/W \to \infty$

To gain a deeper understanding of the physics on the quantum dot, it is useful to search for analytically solvable toy models. We will study an effective model, which reproduces the physics of the Hamiltonian (5.1) in the limit $\Delta/W \to \infty$, where W is the band width. To derive the effective model, we look at the limit $\Delta \to \infty$ of the Green's function in Eq. (5.9). The superconducting order parameter Δ appears only in the

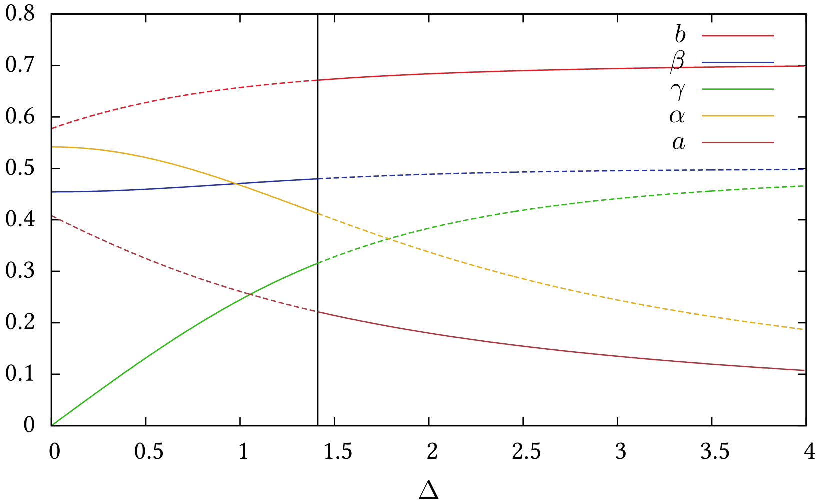

Figure 5.2.: For $\Delta < 1.412$ the ground state is the singlet state from Eq. (5.16). If Δ is increased, the weight α of the single occupied states $|\tilde{\uparrow},\tilde{\downarrow}\rangle$ and $|\tilde{\downarrow},\tilde{\uparrow}\rangle$ decreases in favor of the states with a double occupied quantum dot, corresponding to the weights β and γ. At $\Delta = 1.412$ the ground state changes to the twofold degenerate doublet state given in (5.19) and the weight of the states with a single occupied quantum dot b increases with Δ. The parameters in this plot are $V = 0.5$ and $U = 1.0$.

matrix $\mathbf{E}_\alpha(k)$, thus we examine the behavior of this matrix for large values of Δ. This can easily be done by diagonalizing $\mathbf{E}_\alpha(k)$ for $\phi_\alpha = 0$:

$$\mathbf{E}_\alpha(k) = \mathbf{U}_\Delta^{-1} \begin{pmatrix} -\sqrt{\Delta^2+\xi_k^2} & 0 \\ 0 & \sqrt{\Delta^2+\xi_k^2} \end{pmatrix} \mathbf{U}_\Delta. \tag{5.11}$$

Let us first look at the limit $\Delta \to \infty$ of the transformation matrix U_Δ, which for brevity is not a unitary matrix.

$$\mathbf{U}_\Delta = \begin{pmatrix} -\frac{\xi_k - \sqrt{\Delta^2+\xi_k^2}}{\Delta} & 1 \\ -\frac{\xi_k + \sqrt{\Delta^2+\xi_k^2}}{\Delta} & 1 \end{pmatrix} \Rightarrow \mathbf{U}_\infty = \begin{pmatrix} 1 & 1 \\ -1 & 1 \end{pmatrix}. \tag{5.12}$$

The diagonal matrix in Eq. (5.11) can be considered in a similar manner and we obtain for $\lim_{\Delta\to\infty} \mathbf{E}_\alpha(k) = \mathbf{E}_\infty$:

$$\mathbf{E}_\infty = \mathbf{U}_\infty^{-1} \begin{pmatrix} -\Delta & 0 \\ 0 & \Delta \end{pmatrix} \mathbf{U}_\infty = \begin{pmatrix} 0 & -\Delta \\ -\Delta & 0 \end{pmatrix}. \tag{5.13}$$

Using this result, for large values of Δ the sum over k and α in Eq. (5.9) can be carried out yielding

$$\mathbf{G}_{dd}^{0,\infty}(i\omega_n)^{-1} = (-i\omega_n \mathbf{1} - \epsilon_d) + 2V^2 \boldsymbol{\sigma}_z \left(i\omega_n \mathbf{1} + \mathbf{E}_\infty\right)^{-1} \boldsymbol{\sigma}_z. \tag{5.14}$$

This is exactly the free Green's function obtained from a Hamiltonian of the form:

$$H_{\text{eff}} = -\sqrt{2}V(\mathbf{c}^\dagger \boldsymbol{\sigma}_z \mathbf{d} + \mathbf{d}^\dagger \boldsymbol{\sigma}_z \mathbf{c}) + \mathbf{c}^\dagger \mathbf{E}_\infty \mathbf{c} + \mathbf{d}^\dagger \boldsymbol{\epsilon}_d \mathbf{d} + H_U. \tag{5.15}$$

H_{eff} describes a system consisting of one bath site c connected by a hybridization term to the correlated quantum dot d. The dispersion of the bath has completely vanished, as the superconducting band gap becomes much larger than the bandwidth.

We chose a basis of the 16 dimensional Hilbert space and write the Hamiltonian as a matrix, which subsequently can be diagonalized. As we have restricted the parameter space for the Monte Carlo simulations to $\epsilon_d = 0$ and $\mu = 0$ in the original Hamiltonian of Eq. (5.1), we will use the same parameters for the exact diagonalization results.

Note, that the effective Hamiltonian in the limit Δ/W is not unique. In the case of real Δ, the Green's function (5.9) for $N = 1$, $\mu = -2t$ and $\epsilon_d = \mu$ reduces exactly to (5.14), as $\mathbf{E}_L = \mathbf{E}_R = \mathbf{E}_\infty$. This case corresponds to the effective Hamiltonian in the zero bandwidth limit studied by Vecino et al. [92].

5.3.1. Ground state of the effective model

The ground state of the system (5.15) can be determined by diagonalizing the Hamiltonian H_{eff}. As depicted in Fig. 5.1, the energy levels cross at a critical value of $U = U_c$ and a similar behavior can be observed by varying Δ with a corresponding critical value Δ_c. For $U < U_c$ and $\Delta < \Delta_c$, the ground state is given by $|\,\psi_s\,\rangle = -\alpha\,(|\uparrow\downarrow, 0\rangle - |0, \uparrow\downarrow\,\rangle) - \beta\,(|\uparrow, \downarrow\,\rangle + |\downarrow, \uparrow\,\rangle) - \gamma\,(|\downarrow, \downarrow\,\rangle + |\uparrow, \uparrow\,\rangle)$, with the notation $c^\dagger_\sigma\,|0, 0\rangle = |\,\sigma, 0\rangle$ and $d^\dagger_\sigma\,|0, 0\rangle = |0, \sigma\,\rangle$. Note, that we are using the unphysical basis introduced in Eq. (5.3). To interpret this ground state it is better to return to the physical basis by inverting the canonical transformation in Eq. (5.3) and transforming the vacuum state $|0, 0\rangle \rightarrow |\tilde{\downarrow}, \tilde{\downarrow}\rangle$. The ground state can then be rewritten in the physical basis as:

$$
\begin{aligned}
|\,\psi_s\,\rangle = \alpha &\left(|\tilde{\downarrow}, \tilde{\uparrow}\rangle - |\tilde{\uparrow}, \tilde{\downarrow}\rangle\right) \\
&+ \beta\left(|\tilde{0}, \tilde{\uparrow}\tilde{\downarrow}\rangle + |\tilde{\uparrow}\tilde{\downarrow}, \tilde{0}\rangle\right) + \gamma\left(|\tilde{0}, \tilde{0}\rangle + |\tilde{\uparrow}\tilde{\downarrow}, \tilde{\uparrow}\tilde{\downarrow}\rangle\right).
\end{aligned}
\tag{5.16}
$$

This state is clearly a singlet state, corresponding to a Kondo singlet between the quantum dot and the bath with the dominant weight α. The states representing a pairing on the quantum dot or in the bath have the suppressed weights β and γ for small values of Δ but grow more important if Δ is increased as is shown in Fig. 5.2.

At $U > U_c$, the ground state changes and we get the twofold degenerate ground states

$$
|\,\psi_{d,\uparrow}\,\rangle = a\,(|\uparrow\downarrow, \uparrow\,\rangle - |\uparrow\downarrow, \downarrow\,\rangle) + b\,(|\uparrow, \uparrow\downarrow\,\rangle + |\downarrow, \uparrow\downarrow\,\rangle) \tag{5.17}
$$

and

$$
|\,\psi_{d,\downarrow}\,\rangle = a\,(|0, \uparrow\,\rangle - |0, \downarrow\,\rangle) + b\,(|\downarrow, 0\rangle + |\uparrow, 0\rangle)\,, \tag{5.18}
$$

rewritten in the physical basis:

$$
\begin{aligned}
|\,\psi_{d,\uparrow}\,\rangle &= a\left(|\tilde{\uparrow}, \tilde{0}\rangle - |\tilde{\uparrow}, \tilde{\uparrow}\tilde{\downarrow}\rangle\right) + b\left(|\tilde{0}, \tilde{\uparrow}\rangle + |\tilde{\uparrow}\tilde{\downarrow}, \tilde{\uparrow}\rangle\right) \\
|\,\psi_{d,\downarrow}\,\rangle &= a\left(|\tilde{\downarrow}, \tilde{0}\rangle - |\tilde{\downarrow}, \tilde{\uparrow}\tilde{\downarrow}\rangle\right) + b\left(|\tilde{0}, \tilde{\downarrow}\rangle + |\tilde{\uparrow}\tilde{\downarrow}, \tilde{\downarrow}\rangle\right).
\end{aligned}
\tag{5.19}
$$

This two-fold degenerate ground state has a z-component of the total spin $\pm 1/2$ and hence corresponds to a local moment.

5.3.2. Phase diagram

To further illustrate the phase transition between the singlet state $|\,\psi_s\,\rangle$ and the doublet states $|\,\psi_{d,\uparrow\downarrow}\,\rangle$, the double occupancy $\langle\,\tilde{d}^\dagger_\uparrow \tilde{d}_\uparrow \tilde{d}^\dagger_\downarrow \tilde{d}_\downarrow\,\rangle$ of the quantum dot in the effective model is shown in Fig. 5.3. At low temperature a very sharp drop of the double occupancy on the phase boundary can be observed, which evolves to a jump at $T = 0$. Here the larger values of the double occupancy are connected to the singlet phase, while the lower values belong to the doublet phase, where single occupancy is favored. This can be understood by studying the expectation value of the double occupancy in the ground state. In the singlet phase, we obtain

$$
\langle\,\psi_s\,|\,\tilde{d}^\dagger_\uparrow \tilde{d}_\uparrow \tilde{d}^\dagger_\downarrow \tilde{d}_\downarrow\,|\,\psi_s\,\rangle = |\beta|^2 + |\gamma|^2\,, \tag{5.20}
$$

and for the doublet phase:

$$
\langle\,\psi_{d,\uparrow\downarrow}\,|\,\tilde{d}^\dagger_\uparrow \tilde{d}_\uparrow \tilde{d}^\dagger_\downarrow \tilde{d}_\downarrow\,|\,\psi_{d,\uparrow\downarrow}\,\rangle = |a|^2\,. \tag{5.21}
$$

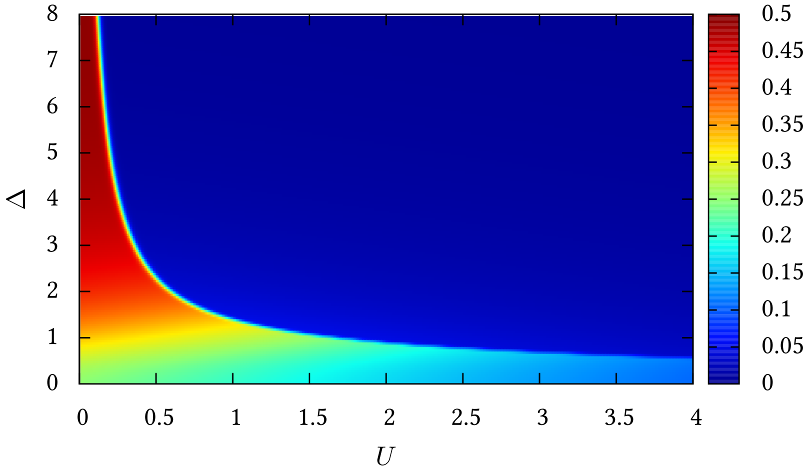

Figure 5.3.: Double occupancy $\langle \tilde{d}_\uparrow^\dagger \tilde{d}_\uparrow \tilde{d}_\downarrow^\dagger \tilde{d}_\downarrow \rangle$ of the quantum dot in the effective model at $\beta = 200$ and $V = 0.5$. This plot can be understood as a phase diagram of the effective model, as the phase boundary is accompanied by a sharp decay of the double occupancy.

From the behavior of the weights β, γ and a shown in Fig. 5.2 it is clear that the double occupancy increases with Δ in the singlet phase and decreases in the doublet phase.

Note, that many of the results presented here can be observed either at fixed U or Δ as can be conjectured from Fig. 5.3.

5.3.3. Proximity effect

To gain further insight in the sign change of the local pair correlations $\langle \tilde{d}_\uparrow^\dagger \tilde{d}_\downarrow^\dagger \rangle$ [83, 93, 94], we calculate the ground state expectation value of the local pair correlations in the effective model (5.15). For the singlet phase, we obtain

$$\begin{aligned} \langle \psi_s | \tilde{d}_\uparrow^\dagger \tilde{d}_\downarrow^\dagger | \psi_s \rangle &= \langle \psi_s | \Big(\beta \, | \tilde{\uparrow}\tilde{\downarrow}, \tilde{\uparrow}\tilde{\downarrow} \rangle + \gamma \, | \tilde{\uparrow}\tilde{\downarrow}, \tilde{0} \rangle \Big) \\ &= 2\mathrm{Re}(\beta^* \gamma) \geq 0. \end{aligned} \tag{5.22}$$

Clearly, only terms describing the pairing on the quantum dot contribute to the pair correlations, whereas the Kondo singlet of electrons on the quantum dot and in the bath does not. From Fig. 5.2, it is obvious that the resulting pairing correlation is positive and increases with Δ. This illustrates the proximity effect, as a pair field in the bath induces a pair field on the quantum dot.

On the other hand, in the doublet phase, we obtain

$$\langle \psi_{d,\downarrow} | \tilde{d}_\uparrow^\dagger \tilde{d}_\downarrow^\dagger | \psi_{d,\downarrow} \rangle = \langle \psi_{d,\downarrow} | \, a \, | \tilde{\downarrow}, \tilde{\uparrow}\tilde{\downarrow} \rangle = - |a|^2 < 0. \tag{5.23}$$

As in the singlet phase, only the states corresponding to a pairing on the quantum dot contribute to the pair correlations. The local moment part of the ground state does not generate pair correlations. As the weight a in the doublet phase ground state is positive and decreases with Δ (see Fig. 5.2), the local pair correlations have a negative sign in contrast to the positive sign in the singlet phase and decrease with Δ.

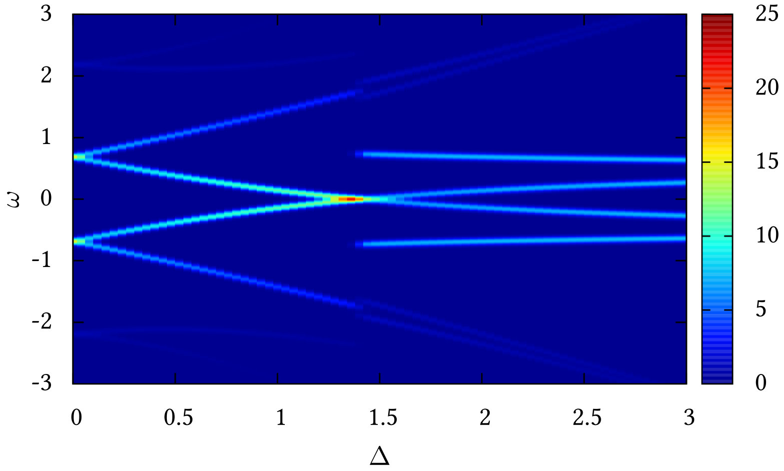

Figure 5.4.: Spectral function $A_{\uparrow\uparrow}(\omega)$ of the effective model for different values of Δ at $\beta = 200$, $U = 1$ and $V = 0.5$. The δ-peaks have been broadened by a Gaussian function of width $\sigma = 0.04$ for better visibility.

5.3.4. Spectral function

Using the Lehmann representation, the spectral function $A_{\uparrow\uparrow}(\omega)$ of the effective model is easily calculated. It is defined by

$$A_{\uparrow\uparrow}(\omega) = \frac{\pi}{Z}\sum_{n,m} M_{nm}\left(\mathrm{e}^{-\beta E_m}+\mathrm{e}^{-\beta E_n}\right)\delta(\omega+E_n-E_m), \tag{5.24}$$

with the matrix elements $M_{nm} = \left|\langle n|\,\tilde{d}^\dagger_\uparrow\,|m\rangle\right|^2$. The spectral function is shown in Fig. 5.4. Comparing this plot to the numerical solution of the full model as depicted in Fig. 5.13, we observe, that the simple model already shows the important feature of an excitation at the position $\omega = 0$ at the critical value of Δ. Even though for very small values of Δ, the Kondo resonance at $\omega = 0$ can not be seen in the simple model, we see a precursor of the Kondo resonance as a pole of the Green's function, which develops into a resonance if we increase the number of sites in the bath[95].

A careful analysis reveals, that the low frequency signature of the spectral function reflects the excitation between the two lowest lying states of the spectrum. These states are the ground states of the singlet and the doublet phase and therefore, the position ω of the excitation marks precisely the energy difference of the two ground states. At the critical value of $\Delta = 1.412$, the level crossing occurs and leads to a vanishing energy difference of the two ground states, meaning that the excitation between the two states lies now precisely at $\omega = 0$.

5.3.5. Dynamical spin structure

Like the spectral function, the dynamical spin structure factor $S(\omega)$ can be calculated using the Lehmann representation:

$$S(\omega) = \frac{\pi}{Z}\sum_{n,m}\mathrm{e}^{-\beta E_n}\left|\langle n|\,\tilde{S}_+\,|m\rangle\right|^2\delta(\omega+E_n-E_m). \tag{5.25}$$

In the Monte Carlo simulation, a numerically more stable quantity is obtained by replacing S_+ by S_z in the above equation. This quantity is completely equivalent to $S(\omega)$, as we only make use of the $SU(2)$-symmetry of the problem, and is therefore used in the following.

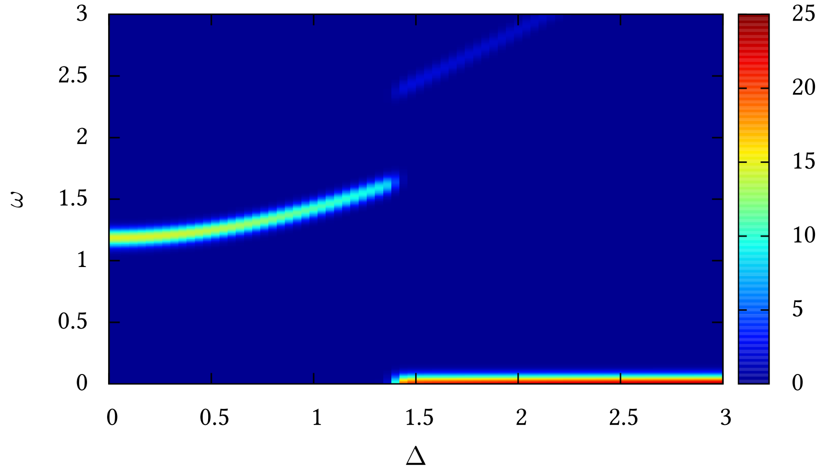

Figure 5.5.: Dynamical spin structure factor $S(\omega)$ of the effective model at $\beta = 200$. The phase transition from the singlet-phase to the doublet-phase for $U = 1$ and $V = 0.5$ occurs at $\Delta \approx 1.412$. At this point a transition from a gapped excitation to a peak at $\omega = 0$ corresponding to a local magnetic moment in the doublet phase is observed. To visualize the δ-functions, a Gaussian broadening of width $\sigma = 0.05$ has been applied.

In the representation (5.25) of $S(\omega)$, it is clear that the dynamical spin structure factor will show excitations at frequencies corresponding to the energy needed to flip the spin on the quantum dot. Therefore, the dynamical spin structure factor is very well suited to determine whether the system is in the singlet or in the doublet regime.

In Fig. 5.5 the phase transition from the singlet phase to the doublet phase is reflected by the fact, that in the singlet phase, a gapped excitation can be observed, whereas in the doublet phase, a peak at $\omega = 0$ emerges, which corresponds to a local magnetic moment.

5.3.6. Dynamical charge structure

The dynamical charge structure factor $N(\omega)$ can be defined by the Lehman representation

$$N(\omega) = -\frac{\pi}{Z} \sum_{n,m} \left| \langle n \,|\, \tilde{n} - \delta_{n,m} \,|\, m \rangle \right|^2 \mathrm{e}^{-\beta E_m} \delta(\omega + E_n - E_m). \tag{5.26}$$

As for the other spectral functions, the charge structure factor $N(\omega)$ shown in Fig. 5.6, exhibits a sharp change of its behavior at the phase transition for the critical value of the superconducting gap Δ. We observe, that the charge structure shows a finite gap for all values of Δ and that for large values of Δ, the gap increases in a slightly nonlinear manner.

A more detailed study of the matrix elements contributing to the charge structure factor reveals, that because of correlation we have completely different excitations than for the spectral function. In fact, the most prominent excitations are excitations from the respective ground states in the two different phases to higher energy states with structure similar to that of the ground states.

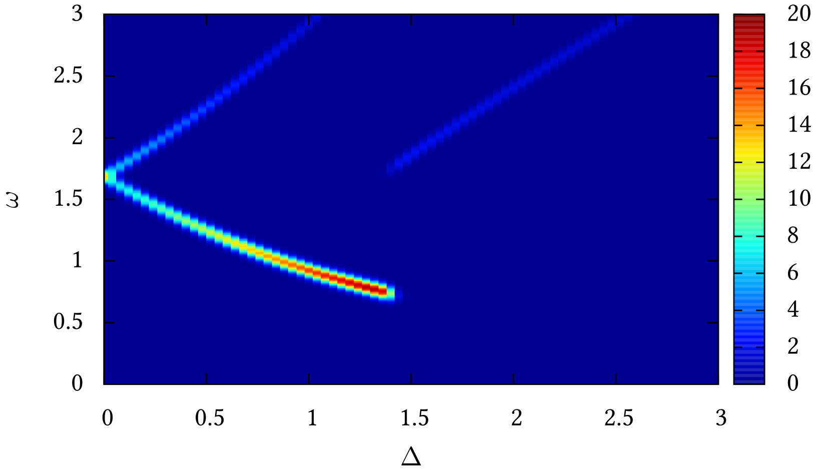

Figure 5.6.: Dynamical charge structure factor $N(\omega)$ of the effective model at $\beta = 200$. We have used the same parameters as for Fig. 5.4

5.4. CT-INT

5.5. Numerical results

In this section, we present the results obtained by CT-INT simulations for the model (5.1). We restrict ourselves to the case of half filling, $\epsilon_d = 0$ and $\mu = 0$. In the first part of this section, we will discuss the results for static quantities including the Josephson current, double occupancy and pair correlations on the quantum dot. We then proceed to dynamical quantities such as the single particle spectral function and the dynamical spin structure factor.

5.5.1. Josephson current

The Josephson current flowing through the Quantum dot can be calculated directly within the CT-INT method, as it is given by an equal time Green's function:

$$\langle j_\alpha \rangle = i \frac{V}{\sqrt{N}} \sum_{k,\sigma} \langle \tilde{c}^\dagger_{k,\sigma,\alpha} \tilde{d}_\sigma - \tilde{d}^\dagger_\sigma \tilde{c}_{k,\sigma,\alpha} \rangle \tag{5.27}$$

We show here our results for the Josephson current at an inverse temperature of $\beta = 50$ as a function of the superconducting gap Δ. For small values of Δ, we observe a sinusoidal form of the Josephson current as a function of the phase difference ϕ with increasing amplitude, as Δ increases (see Fig. 5.7).

This parameter regime is known as the 0-Junction regime, because the Josephson current $I_j(\phi) = \frac{\partial \Omega}{\partial \phi}$ has a zero with positive slope at $\phi = 0$, corresponding to a minimum in the grand potential Ω at $\phi = 0$ (see Fig. 5 in reference [84]).

If the value of Δ is further increased, the behavior of the Josephson current changes, as in the region $\Delta \approx 0.15 \ldots 0.35$ the Josephson current shows a zero between $\phi = 0$ and $\phi = \pi$. (see Fig. 5.7). This leads to a minimum in the grand potential at π and the parameter regime is called $0'$ or π' regime depending on which minimum of the grand potential is the global one [96]. The behavior of the Josephson current is in accordance with the behavior of the double occupancy seen in Fig. 5.11, as in the same parameter region, where we observe the $0'$ to π' transition, the drop of the double occupancy as a function of ϕ can be observed, which is linked to the change of the curvature of the current-phase relation of the Josephson current.

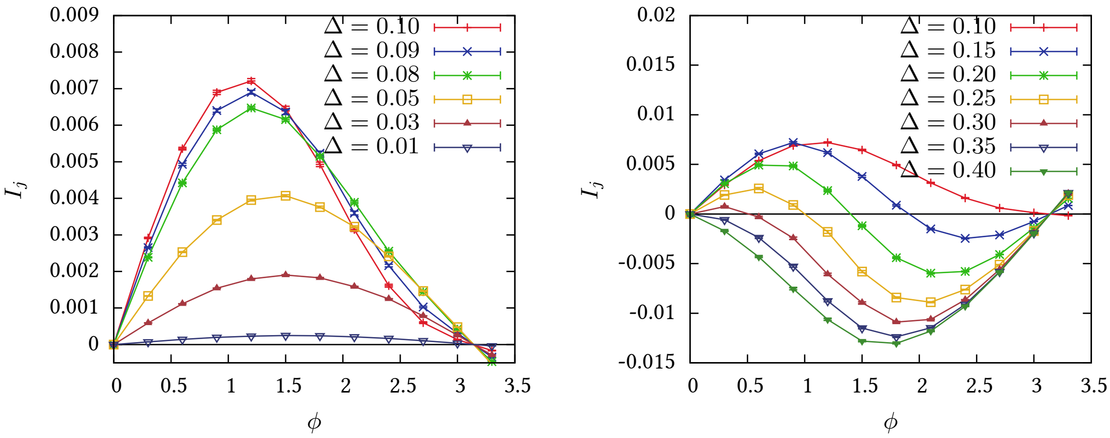

Figure 5.7.: Josephson current in the 0 junction regime (left panel) and in the $0'$ and π' regime (right panel) for the parameter set β =50, $U = 1$, V =0.5, μ =0 and ϵ_d =0.

For larger values of Δ, the sign of the Josephson current changes and the grand potential shows now a single minimum at $\phi = \pi$, this regime is therefore called the π regime (see Fig. 5.8).

The picture for the behavior of the grand potential as a function of ϕ that we get from the current phase relation of the Josephson current agrees very nicely with the results presented by Benjamin et al.[97].

The current phase relations for the different phases presented here were also extensively studied by Karrasch et al. using the fRG and NRG methods [84], Choi et al. using the NRG method [83], as well as by Siano and Egger using the Hirsch-Fye QMC method [88–90]. Even though the numerical exactness of certain results has been debated, the results of all numerical works show very good qualitative agreement and are confirmed by the present results.

In the literature[84, 90], the temperature dependence of the current phase relation of the Josephson current has been discussed. We show CT-INT results in Fig. 5.9 which look very similar to the Siano and Egger result[90]. As CT-INT is numerically exact, our result suggests that the crossing of all curves in one single point[84] at $I_j = 0$ found in the approximate finite temperature NRG is not universal.

5.5.2. Double occupancy

We learned from the toy model described in Sec. 5.3 that the system exhibits a phase transition from the singlet phase to the doublet phase as U is increased. This picture is consistent with the NRG results of Bauer et al. [86]. The phase transition can be observed in the double occupancy $\langle \hat{n}_\uparrow \hat{n}_\downarrow \rangle$ of the quantum dot, which is proportional to $\frac{\partial \Omega}{\partial U}$, where Ω is the grand potential. At $T = 0$, a sharp step function of the double occupancy is expected in the case of a first order phase transition. The reason for this is illustrated easily as in the limit of $T \to 0$ we have[3] $\Omega = -\frac{1}{\beta} \ln Z = E_0$. Clearly, if we have a level crossing associated with the change of the ground state, the slope of $E_0(U)$ changes as illustrated in figure 5.1 and therefore, its derivative shows a sharp jump. While the $T = 0$ regime is not directly accessible to quantum Monte Carlo calculations, we calculated the double occupancy for different temperatures using the CT-INT-method. The results are shown in Fig. 5.10. From the data, it is obvious that with decreasing temperature the curves converge to the step function of the limit $T = 0$, which is a clear sign for a first order phase transition, reflecting a level crossing of the two ground states. This is in complete accordance with the results for the toy model.

It is interesting to correlate the Josephson current as a function of the phase difference $\phi = \phi_L - \phi_R$ for various values of Δ (see Sec. 5.5.1), with the double occupancy on the dot. As depicted in Fig. 5.11, for very small values of Δ as well as for $\Delta >\approx 0.4$, we see that the double occupancy is a constant function of ϕ. This corresponds to a current-phase-relation for the Josephson current fixed in either the π- or the 0-junction regime. For intermediate values of Δ, we observe a far more interesting behavior of the double occupancy:

---

[3] Here, for simplicity, we look at the case $\mu = 0$.

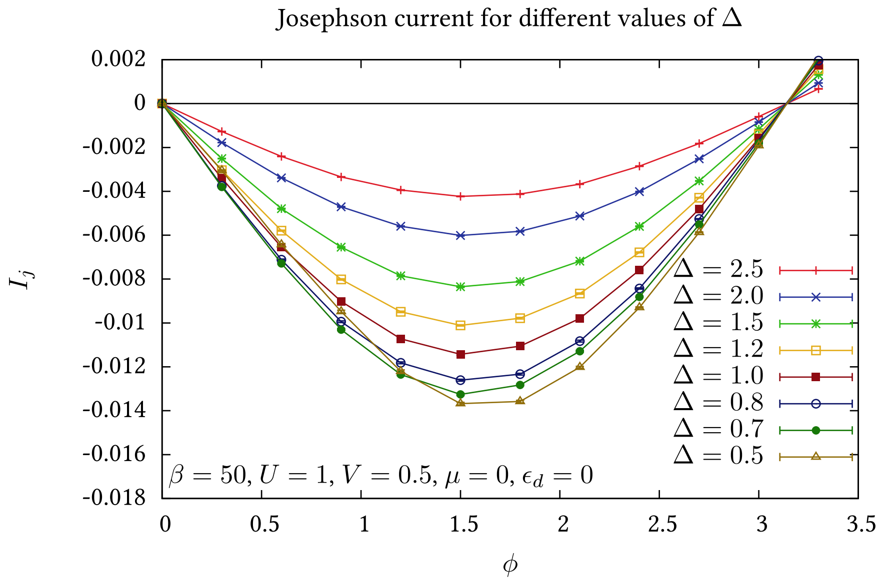

Figure 5.8.: Josephson current in the π junction regime.

At a certain value of ϕ, the double occupancy drops to a smaller value. This drop is of course smeared out by the finite temperature, but can be understood as a way to drive the phase transition from the 0- to the π-junction regime by the phase difference ϕ.

5.5.3. Pair correlation

In agreement with the NRG result of Choi et al. [83] as well as with the mean field results by Salkola et. al. [93], we obtain the local pair correlation on the quantum dot shown in Fig. 5.12. For small Δ, the local pair correlation increases because of the proximity effect, as an increasing magnitude of the pair field Δ in the leads induces a growing pair correlation on the quantum dot. The sharp sign change at the critical value of Δ observed at zero temperature is smeared out at finite temperatures, but the qualitative behavior is exactly the same as for the effective model discussed in Sec. 5.3.3. We therefore conclude, that the sign change of the pair correlation is due to residual pairing on the quantum dot in the doublet phase which decreases with Δ.

The same qualitative behavior of the local pair correlation is also observed, if U is changed instead of Δ as discussed in [86, 93]. The sign change of the local pair correlation Δ_d is traditionally expressed as a π-phase shift in Δ_d.

5.5.4. Spectral function

All quantities studied so far suggest that a first order phase transition occurs when we tune the system from the 0-Junction to the π-Junction regime. This can be confirmed by studying dynamical quantities such as the spectral function.

In Fig. 5.13 we show the spectral function $A(\omega)$ of the quantum dot as a function of Δ. The data has been calculated from the CT-INT data for the Green's function $G_{dd}^{\uparrow\uparrow}(\tau)$ using stochastic analytic continuation[42, 57]. This method works especially well for the low energy spectrum and sharp excitations while the high energy spectrum and excitation continua are more difficult to resolve. Inside the gap, the formation of Andreev bound states can be seen very well.

In the region of $\Delta \approx 0$ we see the Kondo-resonance. As a function of growing values of Δ and as a consequence of the opening of the quasiparticle gap at the Fermi level, the Kondo resonance evolves to Andreev bound state. Note that at the mean-field level, the Kondo resonance merely corresponds to a virtual

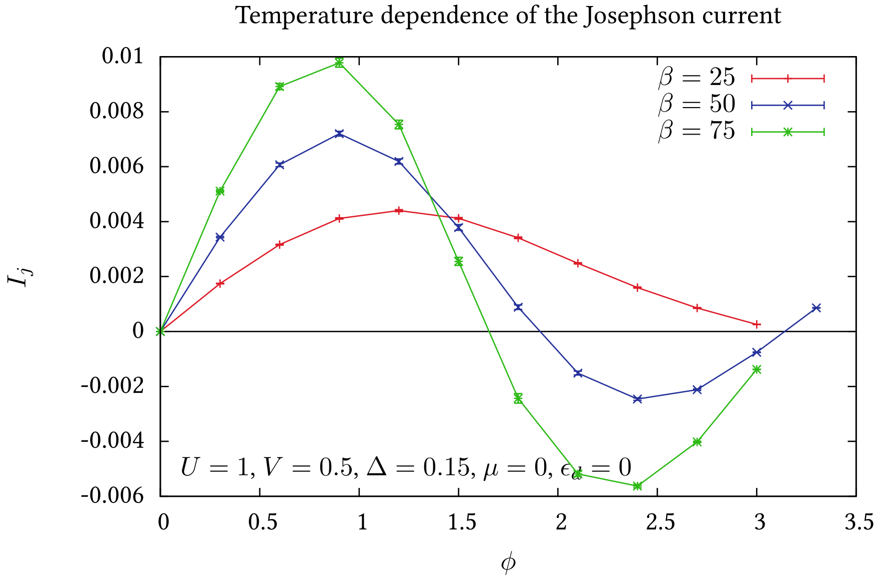

Figure 5.9.: Josephson current for different temperatures $1/\beta$. The current phase relations do not intersect at one single point as suggested by the NRG results of Karrasch et al.[84].

bound state. Opening a quasiparticle gap at the Fermi level drives the lifetime of this virtual bound state to infinity. In the parameter region which corresponds to the 0-Junction regime of the Josephson current ($\Delta \approx 0 \ldots 0.1$), we observe Andreev bound states with excitation energies approaching $\omega = 0$. This corresponds to the crossing point in Fig. 5.13 and has also been observed by Bauer et al. for fixed Δ and increasing U in [86].

The comparison of the Quantum Monte Carlo data shown in Fig. 5.13 with the result obtained from the effective model discussed in Sec. 5.3.4 is particularly insightful. The spectral signature is very similar except for the lack of the Kondo resonance due to the finite size of the effective model. In the effective model, the Andreev bound state excitation corresponds to the energy difference between the ground states of the singlet and the doublet phase. The position Δ at which the Andreev bound states cross at $\omega = 0$ has been identified as a clear sign for the crossing of the ground states of the singlet and doublet phases. Hence, we interpret the crossing of the Andreev bound states in the CT-INT data as a very strong sign for a level crossing and hence a first order phase transition from the singlet to the doublet phase in the full model.

5.5.5. Dynamical spin structure factor

In addition to the spectral function, the dynamical spin structure factor $S(\omega)$ defined in Eq. 5.25, provides a way of characterizing the phases of the system. For $\Delta = 0$, we clearly see a suppressed spectral weight at $\omega = 0$ and a peak which corresponds to the characteristic energy scale of the Kondo temperature T_K. From the peak position, we obtain a rough estimate for the Kondo temperature of $T_K \approx 0.06$.

From $\Delta \approx 0.05$ onwards, spectral weight is accumulated at $\omega = 0$ ultimately forming a pronounced sharp local moment peak for large values of Δ. As the Kondo temperature is a measure for the energy required to break the Kondo singlet, we expect the Kondo effect to break down at a value of $\Delta \approx T_K$. This is indeed observed in Fig. 5.14.

The signature of the breakdown of the Kondo resonance also shows up in the spectral function plotted Fig. 5.13. Since the Kondo resonance stems from a screening of the magnetic moment by conduction electrons in an energy window T_K around the Fermi level, the opening of a single particle gap of order T_K destroys the Kondo resonance giving way to an Andreev bound state.

The breakdown of the Kondo resonance is accompanied by a change of the curvature in the current-phase-

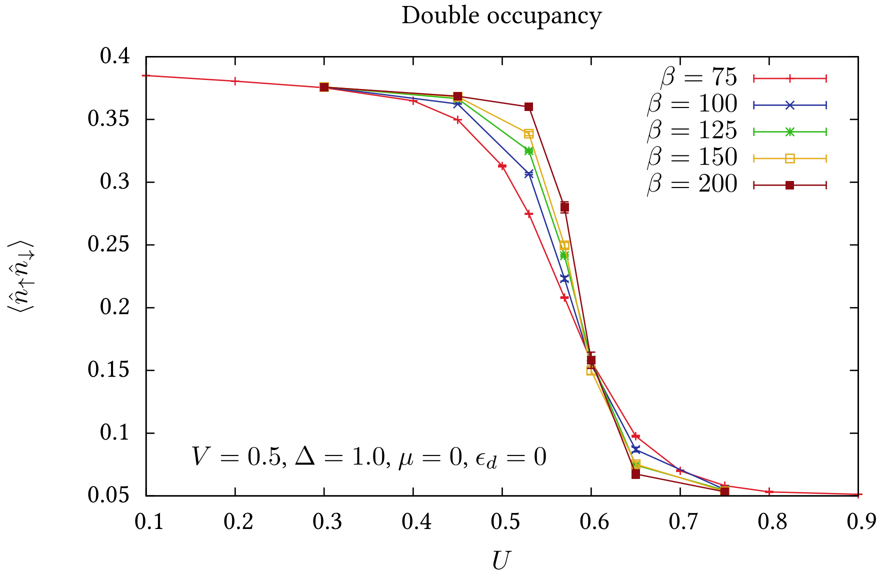

Figure 5.10.: Double occupancy $\langle \hat{n}_\uparrow \hat{n}_\downarrow \rangle$ of the quantum dot at $\Delta = 1.0$. The data shows a jump in the double occupancy becoming sharper with decreasing temperature.

relation of the Josephson current which is a precursor for the transition to the $0'$ phase (see the curves for $\Delta = 0.05$ and $\Delta = 0.08$ in Fig. 5.7). We also observe that after the transition from the π'- to the π- regime has occurred (see the current-phase-relation of the Josephson current of Fig. 5.7) the peak at finite ω vanishes and all the spectral weight is accumulated in the very sharp local moment peak at $\omega = 0$.

5.5.6. Charge gap

From the dynamical charge structure factor, we can determine the gap Δ_c to local charge fluctuations on the dot with two different methods [4]. One way to extract the charge gap is to read off the peak position of the lowest lying excitation in the dynamical charge structure factor obtained from the charge correlation function $C_c(\tau) = \langle \tilde{n}(\tau)\tilde{n} \rangle - \langle \tilde{n} \rangle \langle \tilde{n} \rangle$ via stochastic analytic continuation. The other way of extracting the charge gap from $C_c(\tau)$ is based on the fact, that the charge structure factor $N(\omega)$ is linked to $C_c(\tau)$ via

$$C_c(\tau) \propto \int_{-\infty}^{\infty} \mathrm{d}\omega \, \mathrm{e}^{-\tau\omega} N(\omega). \tag{5.28}$$

If $N(\omega)$ is sharply peaked around a certain value ω_p, we can approximate $N(\omega)$ by $N(\omega) \approx \delta(\omega - \omega_p)$. This corresponds to $C_c(\tau) \approx \mathrm{e}^{-\tau\omega_p}$. Therefore, a least squares fit of an exponential function $\mathrm{e}^{-\tau\omega_p}$ to $C_c(\tau)$ in a region where only one single mode dominates, can reveal the frequency ω_p at which $N(\omega)$ is peaked. The applicability of the method can be seen in the half logarithmic plot of $C_c(\tau)$, where a sharply peaked charge structure factor $N(\omega)$ is reflected by a region, in which $C_c(\tau)$ can be well approximated by a straight line.

The data obtained using these methods is shown in Fig. 5.15. In the context of the effective model discussed in Sec. 5.3.6, we observe, that the behavior of the charge gap of the full model clearly differs from that of the effective model. Especially, we do not see any signature of the phase transition in the behavior of the charge gap.

---

[4] The dynamical charge structure factor itself can in principle be calculated from the CT-INT result for the charge correlation function $C_c(\tau) = \langle \tilde{n}(\tau)\tilde{n} \rangle - \langle \tilde{n} \rangle \langle \tilde{n} \rangle$ using stochastic analytic continuation. This, however is numerically demanding and requires a very high quality of data. In the present case, we were unable to extract more than the lowest lying excitation of the dynamical charge structure factor, which is directly connected to the charge gap. The higher energy spectrum showed an extremely complex structure which is difficult to capture with stochastic analytic continuation.

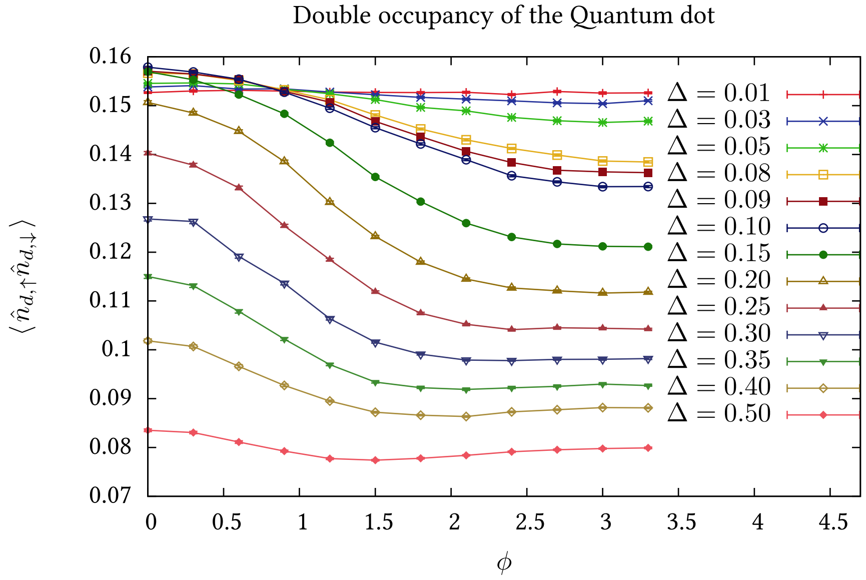

Figure 5.11.: Double occupancy of the quantum dot as a function of the phase difference $\phi = \phi_L - \phi_R$ for different values of Δ.

The charge gap opens approximately linearly with Δ. It is very hard to extract the charge gap from the numerical data at small Δ, therefore we can only extrapolate to $\Delta = 0$. Here, it appears, that we have a finite charge gap even in the absence of superconductivity.

The fact that the local charge fluctuations remain gapped confirms the picture that the 0 to π transition occurs only in the spin sector.

5.6. Quantitative understanding of the Josephson current

After the discussion of the fundamental physics of a strongly correlated Josephson junction in the previous chapter, we will make the connection to a system realized in an experimental sample here[5]. For this, we will make the transition from the model Hamiltonian (5.1) to an implicit action representation by adopting the *wide band limit*. We will also discuss some amount of technical details required for the calculation of experimentally observable quantities, such as the linear conductance.

5.6.1. Model and method.

For the description of an experimentally realizable single level quantum dot with superconducting leads we use again the Anderson impurity model with Hamiltonian $H = H^{\text{dot}} + \sum_{s=L,R} H_s^{\text{lead}} + \sum_{s=L,R} H_s^{\text{coup}}$ as already introduced in slightly different notation in (5.1). The dot part reads

$$H^{\text{dot}} = \sum_{\sigma} \epsilon_\sigma d_\sigma^\dagger d_\sigma + U \left(d_\uparrow^\dagger d_\uparrow - \frac{1}{2} \right) \left(d_\downarrow^\dagger d_\downarrow - \frac{1}{2} \right), \tag{5.29}$$

in standard second quantized notation. In the presence of a Zeeman field h the single-particle energies depend on the orientation of the spin $\epsilon_\sigma = \epsilon + g\mu_{\text{B}} h\sigma/2$, with the Landé g-factor $g = 2$ [98] and $\sigma = \pm 1$. The energy is shifted such that for $h = 0$, $\epsilon = 0$ corresponds to the point of half-filling of the dot. The left

---

[5] This work has been published in [28].

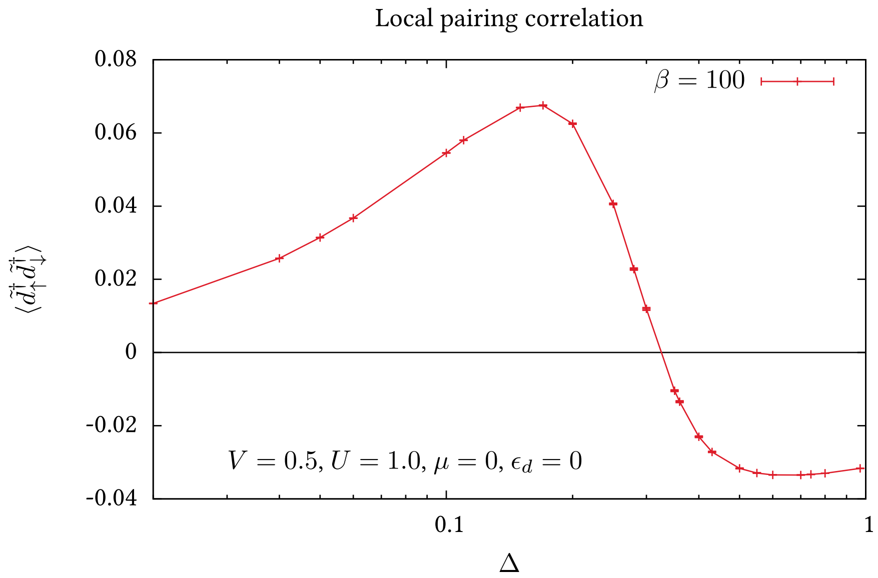

Figure 5.12.: Local pair correlation $\Delta_d = \langle \tilde{d}_\uparrow^\dagger \tilde{d}_\downarrow^\dagger \rangle$ as a function of Δ. We observe the same behavior as Choi et al. [83], which is also in very good agreement with the pair correlation expected for the effective model discussed in 5.3.3.

($s = L$) and right ($s = R$) superconducting leads are modeled by BCS Hamiltonians

$$H_s^{\text{lead}} = \sum_{k\sigma} \epsilon_{sk} c_{sk\sigma}^\dagger c_{sk\sigma} - \Delta \sum_k \left(e^{i\phi_s} c_{sk\uparrow}^\dagger c_{s-k\downarrow}^\dagger + \text{H.c.} \right), \tag{5.30}$$

where (without loss of generality) $\phi_L = -\phi_R = \phi/2$. The quantum dot is coupled to the leads by $H_s^{\text{coup}} = \sum_{k,\sigma} \left(t_{sk} c_{sk\sigma}^\dagger d_\sigma + \text{H.c.} \right)$.

Wide band limit

In the following, we will adopt the wide band limit as the "standard model" of impurity systems, as it has the advantage of eliminating the details of the host material. Our results will prove later that this approximation is indeed valid. The wide band limit is derived for the noninteracting Green's function along the lines of [86].

Starting from equation (5.9), we need to replace the k-sum by an integration over the density of states $\rho(\omega)$. To do that, we first calculate the lead Green's function $\mathbf{g}_k(i\omega_n)$ with

$$\mathbf{g}_k(i\omega_n) = (i\omega_n \mathbf{1} + \mathbf{E}_\alpha^T(k))^{-1} \tag{5.31}$$

directly:

$$\begin{aligned} \mathbf{g}_k(i\omega_n) &= \begin{pmatrix} i\omega_n + \xi_k & -\Delta e^{-i\phi_\alpha} \\ -\Delta e^{i\phi_\alpha} & i\omega_n - \xi_k \end{pmatrix}^{-1} = \\ &= \frac{1}{(i\omega_n + \xi_k)(i\omega_n - \xi_k) - \Delta^2} \begin{pmatrix} i\omega_n - \xi_k & \Delta e^{-i\phi_\alpha} \\ \Delta e^{i\phi_\alpha} & i\omega_n + \xi_k \end{pmatrix} = \\ &= \frac{1}{(i\omega_n)^2 - (\Delta^2 + \xi_k^2)} \begin{pmatrix} i\omega_n - \xi_k & \Delta e^{-i\phi_\alpha} \\ \Delta e^{i\phi_\alpha} & i\omega_n + \xi_k \end{pmatrix}. \end{aligned} \tag{5.32}$$

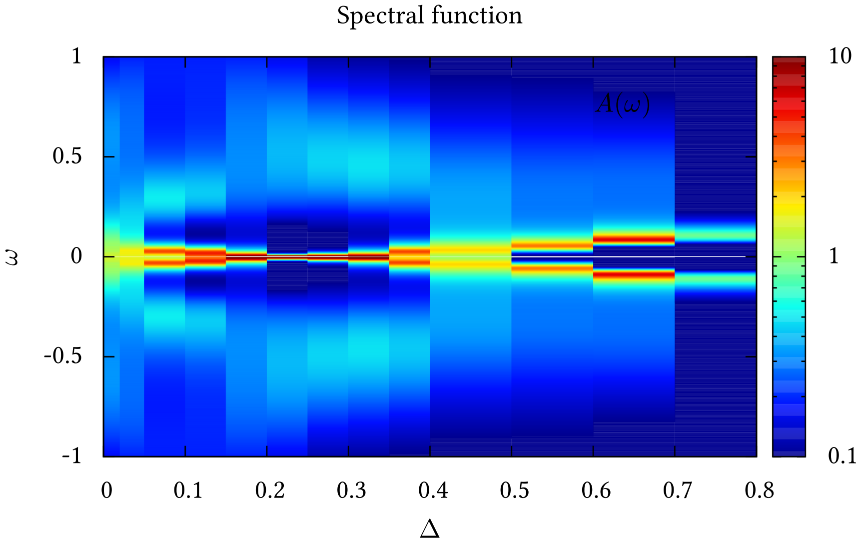

Figure 5.13.: Spectral function $A(\omega)$ as a function of Δ for the parameters $\beta = 100$, $U = 1.0$ and $V = 0.5$ at half filling and zero phase difference between the two superconductors.

Let us now sum over momenta and transform to the energy integral:

$$\begin{aligned}\frac{1}{N}\sum_k \mathbf{g}_k(\mathrm{i}\omega_n) &= \frac{1}{N}\sum_k \frac{1}{(\mathrm{i}\omega_n)^2-(\Delta^2+\xi_k^2)}\begin{pmatrix}\mathrm{i}\omega_n-\xi_k & \Delta \mathrm{e}^{-\mathrm{i}\phi_\alpha}\\ \Delta \mathrm{e}^{\mathrm{i}\phi_\alpha} & \mathrm{i}\omega_n+\xi_k\end{pmatrix} = \\ &= \int_{-\frac{W}{2}}^{\frac{W}{2}} \mathrm{d}\epsilon\, \rho(\epsilon)\frac{1}{(\mathrm{i}\omega_n)^2-(\Delta^2+(\epsilon-\mu)^2)}\begin{pmatrix}\mathrm{i}\omega_n-(\epsilon-\mu) & \Delta \mathrm{e}^{-\mathrm{i}\phi_\alpha}\\ \Delta \mathrm{e}^{\mathrm{i}\phi_\alpha} & \mathrm{i}\omega_n+(\epsilon-\mu)\end{pmatrix} = \\ &= \int_{-\frac{W}{2}-\mu}^{\frac{W}{2}-\mu} \mathrm{d}\epsilon\, \rho(\epsilon-\mu)\frac{1}{(\mathrm{i}\omega_n)^2-(\Delta^2+\epsilon^2)}\begin{pmatrix}\mathrm{i}\omega_n-\epsilon & \Delta \mathrm{e}^{-\mathrm{i}\phi_\alpha}\\ \Delta \mathrm{e}^{\mathrm{i}\phi_\alpha} & \mathrm{i}\omega_n+\epsilon\end{pmatrix} = \end{aligned} \tag{5.33}$$

Making the approximation of a flat band with constant density of states $\rho(\epsilon) = \frac{1}{W}$, we get

$$\frac{1}{N}\sum_k \mathbf{g}_k(\mathrm{i}\omega_n) = \int_{-\frac{W}{2}-\mu}^{\frac{W}{2}-\mu} \mathrm{d}\epsilon\, \frac{1}{W}\frac{1}{(\mathrm{i}\omega_n)^2-(\Delta^2+\epsilon^2)}\begin{pmatrix}\mathrm{i}\omega_n-\epsilon & \Delta \mathrm{e}^{-\mathrm{i}\phi_\alpha}\\ \Delta \mathrm{e}^{\mathrm{i}\phi_\alpha} & \mathrm{i}\omega_n+\epsilon\end{pmatrix}. \tag{5.34}$$

In the limit of $W \to \infty$, the integrals of the form $\int_{-\infty}^{\infty} \mathrm{d}\epsilon \frac{\epsilon}{(\mathrm{i}\omega_n)^2-(\Delta^2+\epsilon^2)}$ will disappear for symmetry reasons, which leaves us with the remaining integral

$$\int_{-\frac{W}{2}-\mu}^{\frac{W}{2}-\mu} \mathrm{d}\epsilon\, \frac{1}{W}\frac{1}{(\mathrm{i}\omega_n)^2-(\Delta^2+\epsilon^2)} = \int_{-\frac{W}{2}-\mu}^{\frac{W}{2}-\mu} \mathrm{d}\epsilon\, \frac{1}{W}\frac{1}{-\omega_n^2-\Delta^2-\epsilon^2}. \tag{5.35}$$

The anti derivative needed in this case is

$$\frac{\mathrm{d}}{\mathrm{d}z}\left(-\frac{1}{2a}\log\left(\frac{a-z}{a+z}\right)\right) = \frac{1}{a^2-z^2}. \tag{5.36}$$

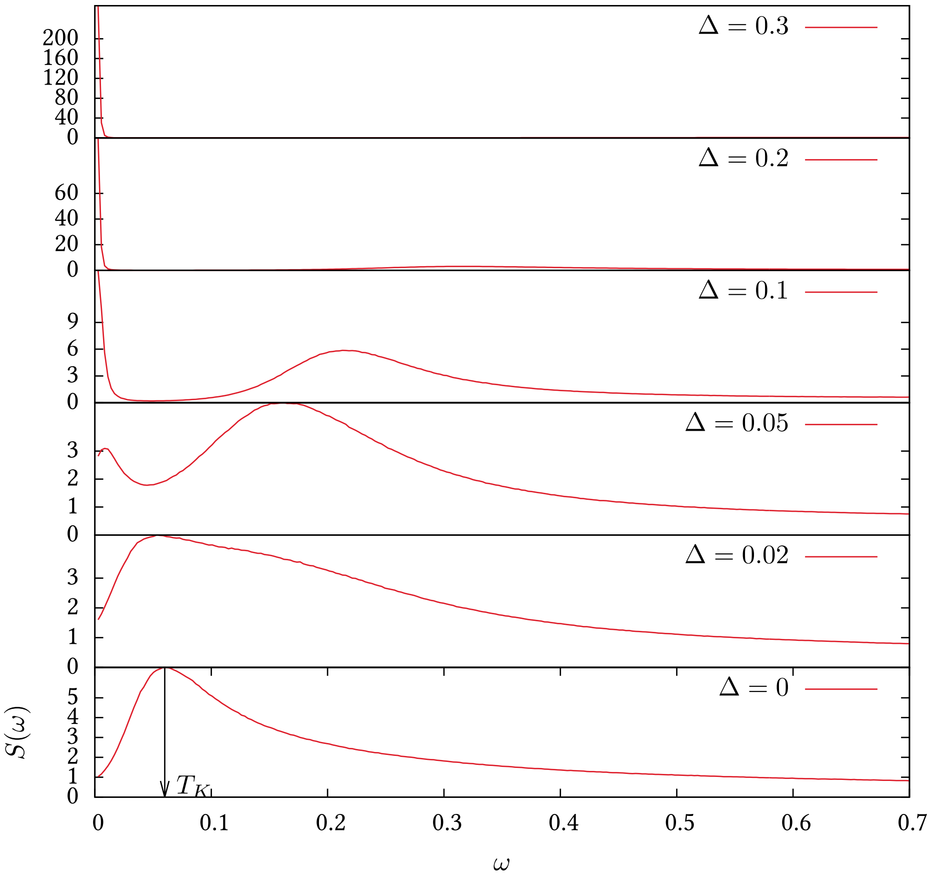

Figure 5.14.: Dynamical spin structure factor $S(\omega)$ as a function of Δ for the parameters $\beta = 100$, $U = 1.0$ and $V = 0.5$ at half filling and zero phase difference between the two superconductors. For $\Delta = 0$ we can roughly estimate the Kondo-Temperature $T_K \approx 0.06$ from the peak position of $S(\omega)$.

This gives us

$$\begin{aligned} \int\limits_{-\frac{W}{2}-\mu}^{\frac{W}{2}-\mu} \mathrm{d}z \frac{1}{(-\Delta^2 - \omega_n^2) - z^2} &= \left[-\frac{1}{2\sqrt{-\Delta^2 - \omega_n^2}} \log\left(\frac{\sqrt{-\Delta^2 - \omega_n^2} - z}{\sqrt{-\Delta^2 - \omega_n^2} + z} \right) \right]_{-\frac{W}{2}-\mu}^{\frac{W}{2}-\mu} = \\ &\overset{W\to\infty}{=} -\frac{1}{2\sqrt{-\Delta^2 - \omega_n^2}} 2 \log(-1) = -\frac{\pi}{\sqrt{\Delta^2 + \omega_n^2}}. \end{aligned} \tag{5.37}$$

This gives us the final result

$$\frac{V_\alpha^2}{N} \sum_k \mathbf{g}_k(\mathrm{i}\omega_n) = -\begin{pmatrix} \mathrm{i}\omega_n & \Delta \mathrm{e}^{-\mathrm{i}\phi_\alpha} \\ \Delta \mathrm{e}^{\mathrm{i}\phi_\alpha} & \mathrm{i}\omega_n \end{pmatrix} \frac{\pi V_\alpha^2 \rho_0}{\sqrt{\Delta^2 + \omega_n^2}} \tag{5.38}$$

Here ρ_0 is the density of states of the flat band. Note that we have to rescale V_α properly while performing the limit $W \to \infty$ so that $\pi V_\alpha^2 \rho_0$ remains finite. We now define

$$\Gamma_\alpha = \pi V_\alpha^2 \rho_0. \tag{5.39}$$

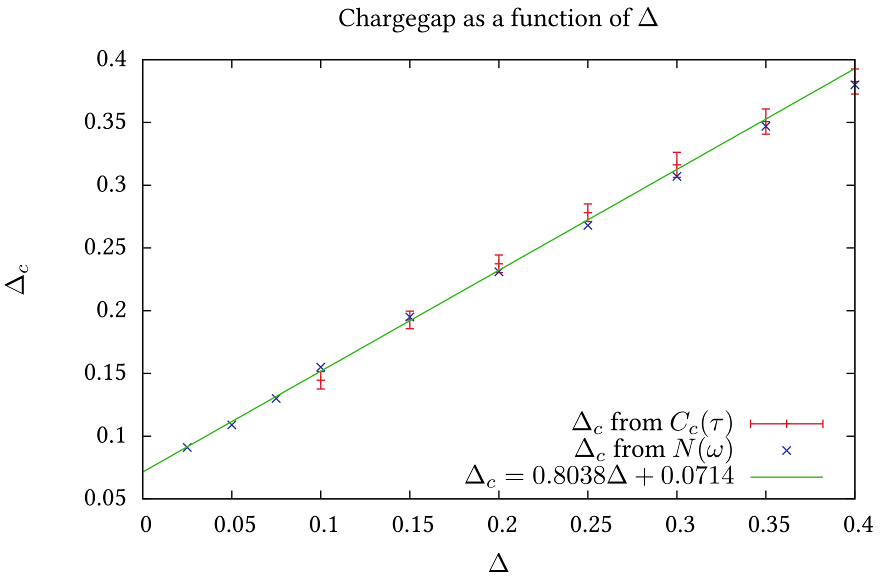

Figure 5.15.: Charge gap Δ_c as a function of Δ. We calculated the dynamical charge structure factor from the charge-charge correlation function $C_c(\tau)$ using stochastic analytic continuation and extracted the charge gap using two different methods. First, we read off the charge gap directly from the stochastic analytic continuation data, secondly, we calculated the charge gap from the charge-charge correlation function. The straight line is a linear fit through the numerical data.

Finally, we have the wide band limit result for the dot Green's function:

$$\begin{aligned}\mathbf{G}_{0,dd}^{-1} &= (-\mathrm{i}\omega_n \mathbf{1} - \boldsymbol{\epsilon}_d) - \sum_\alpha \boldsymbol{\sigma}_z \begin{pmatrix} \mathrm{i}\omega_n & \Delta \mathrm{e}^{-\mathrm{i}\phi_\alpha} \\ \Delta \mathrm{e}^{\mathrm{i}\phi_\alpha} & \mathrm{i}\omega_n \end{pmatrix} \frac{\pi V_\alpha^2 \rho_0}{\sqrt{\Delta^2 + \omega_n^2}} \boldsymbol{\sigma}_z = \\ &= (-\mathrm{i}\omega_n \mathbf{1} - \boldsymbol{\epsilon}_d) - \sum_\alpha \frac{\Gamma_\alpha}{\sqrt{\Delta^2 + \omega_n^2}} \begin{pmatrix} \mathrm{i}\omega_n & -\Delta \mathrm{e}^{-\mathrm{i}\phi_\alpha} \\ -\Delta \mathrm{e}^{\mathrm{i}\phi_\alpha} & \mathrm{i}\omega_n \end{pmatrix}.\end{aligned} \tag{5.40}$$

We will now use this result as the input of the CT-INT calculation in the following and therefore describe the system in terms of an effective action containing only d Grassmann numbers as seen in chapter 3.

Josephson current in the wide band limit

The CT-INT is based on an interaction expansion of the partition function in which *all* diagrams are summed up stochastically. The method is numerically exact and allows the calculation of thermodynamic observables with any required precision σ_{MC} (indicated by errorbars in the figures) with the practical limitation that the computing time grows as $1/\sigma_{\mathrm{MC}}^2$. Details can be found in Ref. [24]. Here we go far beyond the proof-of-principle study of Ref. [24] by considering $\epsilon \neq 0$, larger U/Γ as well as left-right coupling asymmetries. Furthermore, we compute the normal-state linear conductance in the challenging regime $k_{\mathrm{B}}T \approx k_{\mathrm{B}}T_{\mathrm{K}} \approx \mu_{\mathrm{B}}h$.

The Josephson current is computed as the expectation value of the left (or right) current operator $J = \mathrm{i}e/\hbar \sum_{k\sigma} \left\langle t_{Lk} c_{Lk\sigma}^\dagger d_\sigma - \mathrm{H.c.} \right\rangle$. The noninteracting lead degrees of freedom are integrated out and one arrives at a formula for the Josephson current in terms of the imaginary-frequency Nambu-Green function $\mathcal{G}(\mathrm{i}\omega_n)$ of the dot only (directly accessible in CT-INT) [24] which is applicable in the wide band limit:

Performing the canonical transformation, this we can write

$$\begin{aligned} J &= -\frac{2V_\alpha}{\sqrt{N}} \sum_k \Im \left(G^{\alpha\uparrow\uparrow}_{kd}(\tau = 0) + G^{\alpha\downarrow\downarrow}_{kd}(\tau = 0) \right) \\ &= -\frac{2V_\alpha}{\sqrt{N}} \operatorname{Tr} \Im \left(\sum_k \mathbf{G}^{\alpha}_{kd}(\tau = 0) \right) = \\ &= -\frac{2V_\alpha}{\sqrt{N}} \frac{1}{\beta} \operatorname{Tr} \Im \left(\sum_{\mathrm{i}\omega_n} \sum_k \mathbf{G}^{\alpha}_{kd}(\mathrm{i}\omega_n) \right) \end{aligned} \tag{5.41}$$

Of course, in the wide band limit $\mathbf{G}^{\alpha}_{kd}(\mathrm{i}\omega_n)$ does not even exist. We hence make use of the fact that the irreducible self energy $\mathbf{\Sigma}_{\text{full}}(\mathrm{i}\omega_n)$ is only non-zero in the 2×2 block $\mathbf{\Sigma}(\mathrm{i}\omega_n)$ corresponding to $\mathbf{G}_{dd}(\mathrm{i}\omega_n)$. This gives us the 2×2 Dyson equation:

$$\mathbf{G}^{\alpha}_{kd}(\mathrm{i}\omega_n) = \mathbf{G}^{0,\alpha}_{kd}(\mathrm{i}\omega_n) + \mathbf{G}^{0,\alpha}_{kd}(\mathrm{i}\omega_n)\mathbf{\Sigma}(\mathrm{i}\omega_n)\mathbf{G}_{dd}(\mathrm{i}\omega_n). \tag{5.42}$$

Using the expression (5.10) and using (5.31) as in [86], we obtain:

$$\begin{aligned} \mathbf{G}^{\alpha}_{kd}(\mathrm{i}\omega_n) &= \frac{V_\alpha}{\sqrt{N}} \mathbf{g}_k(\mathrm{i}\omega_n)\boldsymbol{\sigma}_{\mathbf{z}}\mathbf{G}^{0}_{dd}(\mathrm{i}\omega_n) \left(\mathbf{1} + \mathbf{\Sigma}(\mathrm{i}\omega_n)\mathbf{G}_{dd}(\mathrm{i}\omega_n)\right) \\ &= \frac{V_\alpha}{\sqrt{N}} \mathbf{g}_k(\mathrm{i}\omega_n)\boldsymbol{\sigma}_{\mathbf{z}}\mathbf{G}_{dd}(\mathrm{i}\omega_n) \end{aligned} \tag{5.43}$$

Now, we can obtain an expression which can be translated to the wide band limit:

$$\frac{V_\alpha}{\sqrt{N}} \sum_k \mathbf{G}^{\alpha}_{kd}(\mathrm{i}\omega_n) = \left(\frac{V_\alpha^2}{N} \sum_k \mathbf{g}_k(\mathrm{i}\omega_n) \right) \boldsymbol{\sigma}_{\mathbf{z}}\mathbf{G}_{dd}(\mathrm{i}\omega_n) \tag{5.44}$$

We obtain for the Josephson current

$$J = -2 \operatorname{Tr} \Im \left(\frac{1}{\beta} \sum_{\mathrm{i}\omega_n} \left[\frac{V_\alpha^2}{N} \sum_k \mathbf{g}_k(\mathrm{i}\omega_n) \right] \boldsymbol{\sigma}_z \mathbf{G}_{dd}(\mathrm{i}\omega_n) \right) \tag{5.45}$$

The frequency sum converges quickly enough for a numerical calculation without further tricks, as we are dealing with the off-diagonal Green's function $\mathbf{G}^{\alpha}_{kd}$, which has an asymptotic form proportional to $\frac{1}{\mathrm{i}\omega_n^2}$. After adopting the wide band limit, this result can be transformed to

$$J = 2\Im\mathrm{Tr} \left[\frac{1}{\beta} \sum_{\mathrm{i}\omega_n} \frac{\Gamma_L}{\sqrt{\Delta^2 + \omega_n^2}} \begin{pmatrix} \mathrm{i}\omega_n & -\Delta \mathrm{e}^{-\mathrm{i}\frac{\phi}{2}} \\ \Delta \mathrm{e}^{\mathrm{i}\frac{\phi}{2}} & -\mathrm{i}\omega_n \end{pmatrix} \mathcal{G}(\mathrm{i}\omega_n) \right]. \tag{5.46}$$

Conductance

As our second observable we investigate the normal-state linear conductance $G = \sum_\sigma G_\sigma$ with

$$G_\sigma = \frac{e^2}{\hbar} \frac{2\Gamma_L\Gamma_R}{\Gamma_L + \Gamma_R} \int_{-\infty}^{\infty} A_\sigma(\omega) \left(-\frac{\mathrm{d}f(\omega)}{\mathrm{d}\omega} \right) \mathrm{d}\omega, \tag{5.47}$$

where A_σ denotes the normal-state dot spectral function and f the Fermi function. The computation of A_σ from the (normal-state) imaginary frequency Green function $\mathcal{G}_\sigma(\mathrm{i}\omega_n)$ obtained numerically by CT-INT is based on analytical continuation. It is found that the calculation of G_σ is much more reliable if the method detailed in Ref. [99] is used. As shown there the conductance can be written as

$$G_\sigma = \frac{e^2}{\hbar} \frac{2\Gamma_L\Gamma_R}{\Gamma_L + \Gamma_R} \frac{2}{\beta} \sum_{\alpha > 0} R_\alpha \Im \frac{\mathrm{d}\mathcal{G}_\sigma(\mathrm{i}\tilde{\omega}_\alpha)}{\mathrm{d}\tilde{\omega}_\alpha}, \tag{5.48}$$

where the frequency derivative of the Green function has to be evaluated at imaginary frequencies $\mathrm{i}\tilde{\omega}_\alpha$ which can differ from the Matsubara ones [6] given together with the weights R_α in Ref. [99]. Within CT-INT $\mathcal{G}_\sigma$ is accessible only at the Matsubara frequencies. Therefore, we introduce a (real) Padé approximant $\mathcal{G}_\mathrm{P}(\omega) = \sum_{j=0}^{M-1} a_j\omega^j \Big/ \sum_{j=0}^{M} b_j\omega^j$ of degree $(M, M+1)$ and minimize the function

$$\begin{aligned}\chi^2(\{a_i\},\{b_i\}) &= \sum_{n,m} \{\mathcal{G}_\mathrm{P}(\omega_n) - \Im[\mathcal{G}_\sigma(\mathrm{i}\omega_n)]\} \\ &\quad \times C^{-1}_{n,m} \{\mathcal{G}_\mathrm{P}(\omega_m) - \Im[\mathcal{G}_\sigma(\mathrm{i}\omega_m)]\},\end{aligned}$$

where C is the carefully bootstrapped estimate of the covariance matrix of the QMC data $\Im\big[\mathcal{G}_\sigma(\mathrm{i}\omega_n)\big]$. The degree of the Padé approximant $(M, M+1)$ is chosen such that the minimal χ^2 is not smaller than the number of degrees of freedom to obtain a statistically consistent fit and is found to be surprisingly small with $M = 3, \ldots, 6$. The Padé approximant may now be safely evaluated at the positions $\mathrm{i}\tilde{\omega}_\alpha$ and Eq. (5.48) can be used.

5.6.2. Comparison to the experiment.

In experiments the charging energy U can be determined accurately from the height of the Coulomb blockade diamonds obtained by bias spectroscopy in the normal state. The same type of measurement in the superconducting state reveals sharp features at the gap position from which Δ can be extracted [65, 66]. In addition, T and h are known within tight bounds. The parameters which are most delicate to determine but strongly affect J are the level width Γ and the asymmetry Γ_L/Γ_R. Based on this insight, we proceed as follows: (i) The parameters Δ, U, T and h are taken directly from the experiment. Those and the comparison of theoretical curves for the normal-state conductance $G(\epsilon)$ with the experimental ones are used for obtaining accurate estimates of Γ, Γ_L/Γ_R, and the gate conversion factor α which relates the change of ϵ to a variation of the gate voltage V_g according to $V_\mathrm{g} = \alpha\epsilon$ [7]. (ii) For the complete parameter set determined this way, we compute the Josephson current and compare to the measured J_c.

We focus on the most symmetric conductance double peak presented in Fig. 4d) of Ref. [65]. The experimental parameter estimates with errors of approximately 10% are $U \approx 3\,\mathrm{meV}$, $\Delta \approx 0.1\,\mathrm{meV}$, $T \approx 75\,\mathrm{mK}$, and $h \approx 150\,\mathrm{mT}$. In Fig. 5.16 a) we show our best fit of $G(\epsilon)$ to the experimental result from which we extract $\Gamma = 0.27\,\mathrm{meV}$, $\Gamma_L/\Gamma_R = 9.3$, and $\alpha = 0.011\,\mathrm{V/meV}$. At fixed U the peak separation and the peak to valley ratio are determined by Γ while the overall height is given by Γ_L/Γ_R, as can be inferred from Eq. (5.48) (in $\mathcal{G}_\sigma$ only $\Gamma = \Gamma_L + \Gamma_R$ enters). Note that Γ turns out to be significantly smaller and Γ_L/Γ_R significantly larger than the values extracted in Ref. [65] based on the assumption that the dot is in the Coulomb blockade regime. However, our analysis allowing for Kondo correlations clearly reveals that those are relevant for $U/\Gamma \approx 11.15$ and the Kondo scale $k_\mathrm{B}T_\mathrm{K} \approx 8\,\mu\mathrm{eV}$. It is roughly an order of magnitude smaller than Γ and of the order of the temperature ($k_\mathrm{B}T = 6.5\,\mu\mathrm{eV}$) as well as the Zeeman energy ($\mu_\mathrm{B}h = 8.7\,\mu\mathrm{eV}$). Therefore neither T nor h can be neglected when considering the normal state; the conductance is characterized by a split Kondo plateau (ridge) [101], not to be mistaken with the Coulomb blockade peaks which would be located at larger energies $\epsilon \approx \pm U/2 \approx \pm 1.5\,\mathrm{meV}$. As an inset we show, for illustration, the normal-state spectral function at $\epsilon = 0$ for the extracted parameters obtained from analytic continuation of CT-INT data onto the real frequency axis by the maximum entropy method [42]. The appearance of a sharp zero energy resonance is a hallmark of Kondo correlations [1]. The splitting of the Kondo resonance by the Zeeman field is too small to be observable on the scale of the plot (but present in the data).

In the experiments [65, 66] J_c, defined as the maximum of $|J(\phi)|$ over $\phi \in [0, \pi]$, is extracted from current-voltage characteristics of the on-chip circuits using an extension of the standard RSJ model [102]. In this analysis it is assumed that $J(\phi)$ is purely sinusoidal with its maximum at $\phi = \frac{\pi}{2}$. At first glance this appears to be at odds with what is known theoretically for the current-phase relation of a Josephson quantum dot

---

[6] The choice of the frequency grid is not unique, an optimal one being proposed by H. Monien [49, 100]. For the problem at hand however, the additional computational effort is minor if the slightly less efficient method of Ref. [99] is used instead of the optimal version, as the (real) Padé approximant of $\Im[\mathcal{G}_\sigma(\mathrm{i}\omega_n)]$ may be evaluated at any frequency at virtually no cost.

[7] Often α is extracted from the ratio of the width and the height of the Coulomb blockade diamonds [65] — a procedure which is not applicable in the Kondo regime as the separation of the linear conductance peaks is less than U [101].

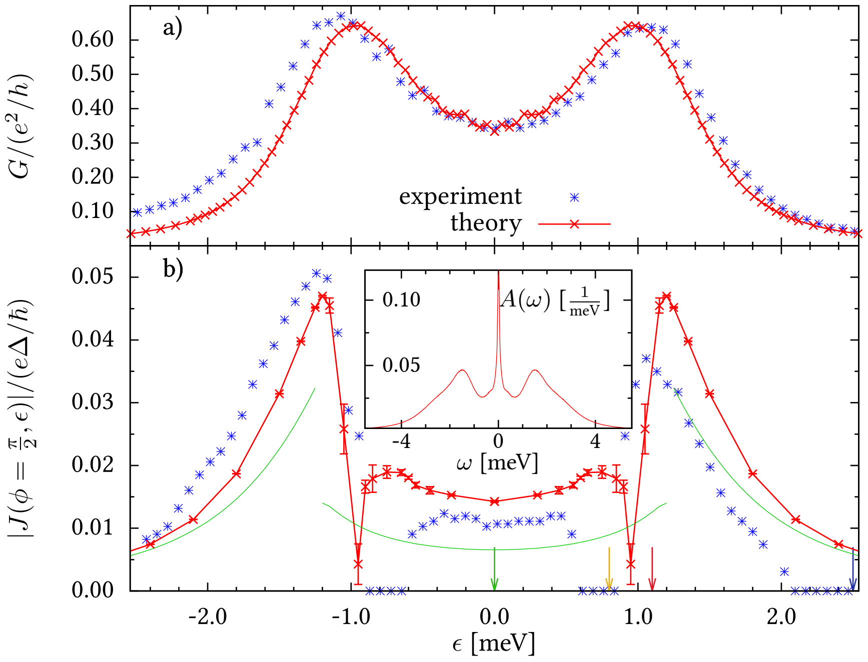

Figure 5.16.: Comparison of experimental data [65] with the numerically exact solution of the superconducting Anderson model. a) Best fit of the normal-state linear conductance with applied magnetic field used for extracting values of Γ and Γ_L/Γ_R (for details see the main text). b) Measured critical current vs. theoretically calculated Josephson current at $\phi = \frac{\pi}{2}$ (CT-INT: symbols with line; self-consistent Hartree-Fock: thin lines). The arrows indicate the level positions for which the current phase relation is presented in Fig. 5.17. *Inset:* Normal-state spectral function at $\epsilon = 0$.

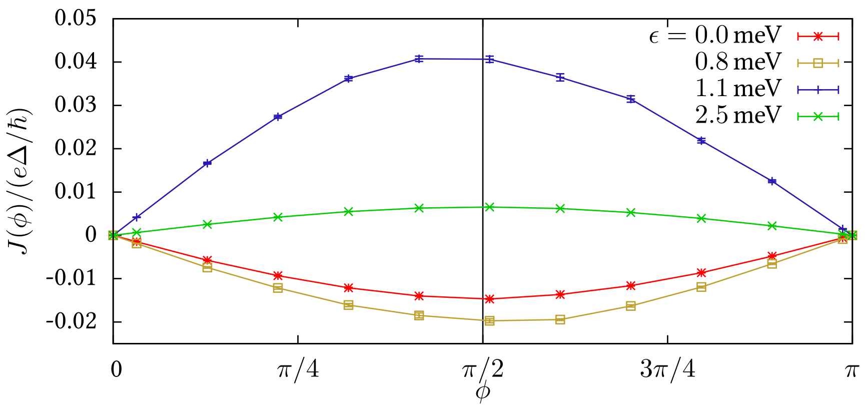

Figure 5.17.: Josephson current-phase relation for the parameters of the experiment [65] at values of ϵ indicated by arrows in Fig. 5.16. It is rather sinusoidal even very close to the critical value of ϵ (1.1 meV and 0.8 meV) and the critical current is thus well approximated by $J(\phi = \frac{\pi}{2})$.

in the 0-phase (half-sinusoidal with maximum at $\phi \to \pi$) and the transition region (jump from $J > 0$ to $J < 0$ at $T = 0$, smeared out by $T > 0$) [3, 82–84, 88]. However, as it was shown already in Ref. [65] for an effective noninteracting model, the sizable left-right asymmetry and the finite temperatures of the experimental setups imply sinusoidal currents in the 0- and π-phase apart from very narrow ranges around the 0-π transitions. This conclusion is confirmed by the numerically exact CT-INT in Fig. 5.17, where we present $J(\phi)$ for the above given parameters at the level positions indicated by the arrows in Fig. 5.16 b) showing $|J(\phi = \frac{\pi}{2}, \epsilon)|$. Apparently only for ϵ very close to the transition the ϕ-position of the maximal current $|J|$ deviates observably from $\frac{\pi}{2}$ and yet the maximal value is still very close to that of $|J(\phi = \frac{\pi}{2})|$. This gives an a-posteriori justification of the extraction of J_c using the extended RSJ model and allows us to focus on the current at $\phi = \frac{\pi}{2}$ when comparing to the gate voltage dependence of the critical current, as done in Fig. 5.16 b). Without any additional fitting parameters we achieve excellent agreement in both the 0- (to the left and right of the peaks) and the π-phase (central region with nearly ϵ-independent J_c). In addition we show $|J(\phi = \frac{\pi}{2}, \epsilon)|$ obtained for the same parameters using the HF approach [80, 84]. Whereas in the empty dot and doubly occupied regime $|\epsilon| \gtrsim 2$ meV this mean-field approximation gives decent agreement with the exact result (CT-INT; see also Fig. 5.18) it apparently fails in the mixed valence regime and for half dot filling ($\epsilon \approx 0$) in which Kondo correlations are crucial. Important features like the smoothing of the phase transition by the finite temperature and the smooth crossing through zero of $J(\frac{\pi}{2})$ cannot even be obtained qualitatively. This emphasizes that Kondo correlations are relevant even in the presence of prevailing superconductivity ($\Delta \approx 10T_{\mathrm{K}}$) [8].

5.6.3. Increasing T_{K}.

Considering $\Gamma = 0.4$ meV and 0.5 meV with all the other parameters fixed at the values given above, we finally investigate the regime $\Delta \approx k_{\mathrm{B}}T_{\mathrm{K}}$ of the strongest competition between superconductivity and (precursors of) Kondo correlations. In Fig. 5.18 $|J(\phi = \frac{\pi}{2}, \epsilon)|$ obtained by CT-INT is compared to HF results. Obviously, the singlet (0) phase is stabilized by the correlations — an effect which HF is unable to describe. For the largest T_{K} (at $\Gamma = 0.5$) $|J(\phi = \frac{\pi}{2}, \epsilon)|$ computed by CT-INT only shows a precursor of the π-phase (the slight suppression close to $\epsilon = 0$) while HF gives a spurious π-phase. It would be very interesting to measure the gate voltage dependence of the critical current for dots falling into this parameter regime, which would confirm the predictive power of our calculations.

---

[8] Besides the failure of HF to quantitatively describe $J(\phi = \frac{\pi}{2}, \epsilon)$ it suffers from the severe artifact that the π phase is produced by a spurious spin-symmetry breaking. We furthermore emphasize that the HF normal-state linear conductance does not capture Kondo physics and thus cannot be used to extract Γ and Γ_L/Γ_R from the measured $G(\epsilon)$ as is done here using CT-INT.

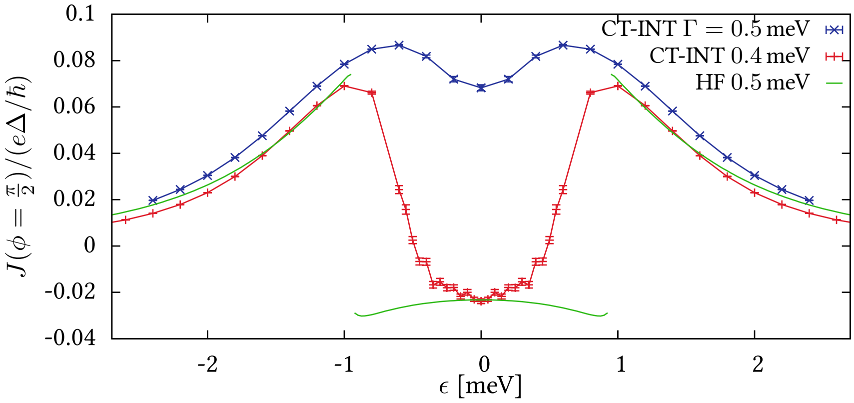

Figure 5.18.: Josephson current at $\phi = \frac{\pi}{2}$ for the parameters of the experiment (see Fig. 5.16) but with increased level broadening $\Gamma = 0.4$ meV and 0.5 meV (instead of 0.27 meV) and thus increased T_{K}. Self-consistent Hartree-Fock is obviously unable to describe the strong competition between superconductivity and Kondo correlations in this parameter regime and leads to a spurious π-phase for parameters for which the numerical exact solution only shows a precursor close to half dot filling $\epsilon = 0$.

5.7. DMFT

5.7.1. Periodic Anderson Model with BCS conduction band

In the previous sections, we have studied the first order phase transition in the impurity model (5.1). As the dynamical mean field theory (DMFT) provides a link between impurity models and lattice models, we can ask the question if the singlet to doublet phase transition observed in the impurity model is also realized in a corresponding lattice model.

An appropriate lattice model will of course include a $U(1)$ symmetry breaking term like the impurity model (5.1) does, and in fact in the framework of the DMFT, a periodic Anderson model extended by the BCS mean field Hamiltonian (BCS-PAM) for the conduction band electrons corresponds to the impurity model presented in the previous sections [9]. The Hamiltonian of the BCS-PAM is given by:

$$H = H_c + H_f + H_V \tag{5.49}$$

with

$$H_c = \sum_{k,\sigma} \xi(k) \tilde{c}^{\dagger}_{k,\sigma} \tilde{c}_{k,\sigma} - \Delta \sum_{k} \left(\tilde{c}^{\dagger}_{k,\uparrow} \tilde{c}^{\dagger}_{-k\downarrow} + \text{h.c.} \right) \tag{5.50}$$

$$H_f = \sum_{k,\sigma} \xi_f \tilde{f}^{\dagger}_{k,\sigma} \tilde{f}_{k,\sigma} + U \sum_{i_f} \left(\tilde{n}_{i_f,\uparrow} - \frac{1}{2} \right) \left(\tilde{n}_{i_f,\downarrow} - \frac{1}{2} \right) \tag{5.51}$$

$$H_V = -V \sum_{k,\sigma} \left(\tilde{c}^{\dagger}_{k,\sigma} \tilde{f}_{k,\sigma} + \text{h.c.} \right) \tag{5.52}$$

We have considered a square lattice with hopping matrix element t between the conduction electrons such that:

$$\xi(k) = -2t \left(\cos(ka_x) + \cos(ka_y) \right). \tag{5.53}$$

---

[9] Strictly speaking, the reference model in the DMFT only has one superconducting bath, while we introduced a left and a right bath in the Hamiltonian (5.1). However, in the CT-INT, the reference model is entirely encoded in the bare Green's function, which can be understood as an action representation in the path integral formalism. The explicit number of the superconducting baths is therefore unimportant.

Note, that the impurity model (5.1) has a large range of applications in the DMFT ranging from the attractive Hubbard model with $U(1)$ symmetry broken solutions studied in references [103, 104] to the BCS-PAM, which is considered here.

The treatment of this model within DMFT involves the same steps as for the impurity model (5.1), introducing a particle-hole transformation for the spin down operators. The Hamiltonian can then be cast in the form $H = H_0 + H_U$ with

$$H_0 = \sum_k \mathbf{c}_k^\dagger \mathbf{E}(k) \mathbf{c}_k - V \sum_k \left(\mathbf{c}_k^\dagger \boldsymbol{\sigma}_z \mathbf{f}_k + \text{h.c.} \right) + \sum_k \mathbf{f}_k^\dagger \boldsymbol{\epsilon}_f \mathbf{f}_k \tag{5.54}$$

and $H_U = -U \sum_{i_f} \left(n_{i_f,\uparrow} - \frac{1}{2} \right) \left(n_{i_f,\downarrow} - \frac{1}{2} \right)$. Here, we have used the same Nambu-spinor notation as in Sec. 5.2 with the exception, that d operators have been renamed f to be consistent with the literature [15, 95].

5.7.2. DMFT with superconducting medium

The standard DMFT can be easily adapted to a superconducting bath using the Nambu formalism [15]. We obtain the self consistency equation for a finite lattice with N sites expressed by a 2×2 matrix equation:

$$\mathbf{G}^{\mathbf{ff}}(i\omega_n) = \frac{1}{N} \sum_{\mathbf{k}} \left[{\mathbf{G}_{\mathbf{kk}}^{\mathbf{0,ff}}}^{-1}(i\omega_n) - \boldsymbol{\Sigma}^{\mathbf{ff}}(i\omega_n) \right]^{-1} . \tag{5.55}$$

Here, $\mathbf{G}^{\mathbf{ff}}(i\omega_n) = -\int\limits_0^\beta \mathrm{d}\tau \, \mathrm{e}^{-i\omega_n \tau} \, \langle T \mathbf{f}(\tau) \mathbf{f}^\dagger \rangle$ is the full Matsubara Green's function of the reference model, $\mathbf{G}_{\mathbf{kk}}^{\mathbf{0,ff}}(i\omega_n)$ is the Matsubara f-Green's function of the bare lattice model and $\boldsymbol{\Sigma}^{\mathbf{ff}}$ is the self energy. Equation (5.55) can be solved by iteration starting usually at a self energy $\boldsymbol{\Sigma}^{\mathbf{ff}} \equiv 0$. From $\mathbf{G}^{\mathbf{ff}}(i\omega_n)$, the bare Green's function $\boldsymbol{\mathcal{G}}_{\mathbf{0}}^{\mathbf{ff}}(i\omega_n)$ of the reference model, can be calculated using Dyson's equation ${\boldsymbol{\mathcal{G}}_{\mathbf{0}}^{\mathbf{ff}}}^{-1} = {\mathbf{G}^{\mathbf{ff}}}^{-1} + \boldsymbol{\Sigma}^{\mathbf{ff}}$. The reference model, which is now described by $\boldsymbol{\mathcal{G}}_{\mathbf{0}}^{\mathbf{ff}}$ and the interaction part of the Hamiltonian can subsequently be solved using the CT-INT method yielding $\mathbf{G}^{\mathbf{ff}}(i\omega_n)$ for the next DMFT iteration.

5.7.3. Hysteresis

In the DMFT, we can calculate the double occupancy $\langle \tilde{f}_{\uparrow,i}^\dagger \tilde{f}_{\uparrow,i} \tilde{f}_{\downarrow,i}^\dagger \tilde{f}_{\downarrow,i} \rangle$ of the f-sites, which is together with the assumption of a homogeneous system proportional to $\frac{\partial \Omega}{\partial U}$. Therefore, we expect a jump in the double occupancy to appear at a critical value of U, if we have a first order phase transition as in the impurity problem.

Figure 5.19 shows our result for the double occupancy of the f sites as a function of U. Depending on the initial choice of the self energy in the DMFT cycle, we obtain two different solutions. If we start with the local Green's function of the bare lattice model, which corresponds to a self energy $\Sigma \equiv 0$, we obtain the upper branch of the hysteresis. The lower branch is obtained by taking the self energy of the solution in the strong coupling phase at $U = 0.44$ as starting point for the DMFT cycle. The coexistence of two solutions is a strong hint that a first order phase transition occurs.

It should be noted that beginning at a value of $U \approx 0.34$, the upper branch of the hysteresis becomes unstable, i.e. the inherent fluctuations of the Monte Carlo results suffice to drop from the upper branch of the hysteresis to the lower branch after a certain number of iterations. Increasing the number of Monte Carlo measurements delays the drop to the lower branch to a higher number of iterations. This behavior can be understood in the following way: In the coexistence region, the grand potential Ω of the upper and lower branch of the hysteresis cross at a certain value of U. For small values of U, Ω is minimal on the upper branch, while the lower branch is metastable, for larger values of U, however, the stable solution is the lower branch.

In the strong coupling phase and on the lower branch of the hysteresis, the Monte Carlo results suddenly develop a finite magnetization corresponding to a frozen spin. This is due to divergent autocorrelation times in the Monte Carlo simulation and is linked to the physical formation of a local moment.

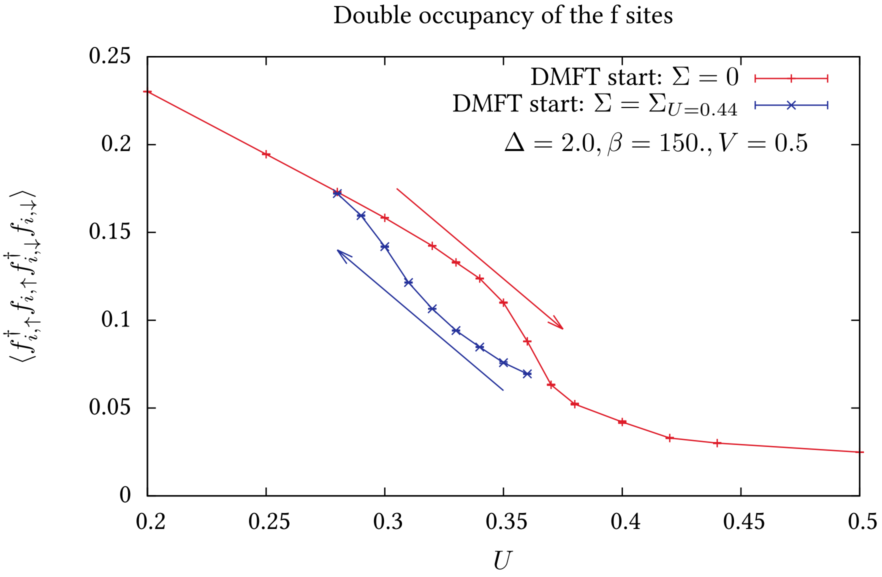

Figure 5.19.: Double occupancy of the f sites in the BCS-PAM. In the proximity of the critical value of U, we observe two different solutions of the DMFT self consistency cycle. The upper (red) branch is generated, if we start the DMFT algorithm with a self energy $\Sigma \equiv 0$, while we obtain the solution shown by the lower (blue) branch if we take the self energy of the data point at $U = 0.44$ as the starting point of the DMFT iterations.

5.7.4. Local dynamical spin structure factor

To further classify the weak and strong coupling phases, we calculate the local dynamical spin structure factor $S(\omega) = \frac{1}{N}\sum_{\mathbf{q}} S(\mathbf{q}, \omega)$. The Lehmann representation for $S(\omega)$ is given by Eq. (5.25), where in this case $S_+ = S_+^{f,i}$.

As in the impurity case, $S(\omega)$ is a measure for the energy needed to flip the spin on an f-site. Figure 5.20 shows the result for the local dynamical spin structure factor on both branches of the hysteresis. The solution corresponding to the upper branch of the hysteresis is linked to the weak coupling regime and shows a characteristic energy scale required for flipping a spin.

The lower branch of the hysteresis represents the strong coupling phase and shows a clear local moment peak in the dynamical spin structure factor at $\omega = 0$.

This behavior reflects exactly the single impurity physics discussed in the previous section where we observed the Kondo effect in the weak coupling phase and the formation of a local moment in the strong coupling phase.

5.7.5. f-Density of states

In order to investigate the behavior of the f-bands at the phase boundary and to be able to compare with the single impurity model, we calculate the density of states for the f-sites ρ_{ff} directly from the local Green's function $G(\tau)$ using the stochastic analytic continuation method for different values of U. From Fig. 5.21, one can recognize the signature of the impurity physics (see Sec. 5.5.4), namely the crossing of Andreev bound states in the vicinity of the first order transition at $U \approx 0.35$. Note, that we have only shown the level crossing for the impurity model if Δ is changed, but for varying U, the crossing of the Andreev bound states in the impurity model (5.1) has been observed by Bauer et al. [86]. Clearly in the lattice model, one expects the Andreev bound states to acquire a dispersion relation which shows up as a finite width in ρ_{ff}.

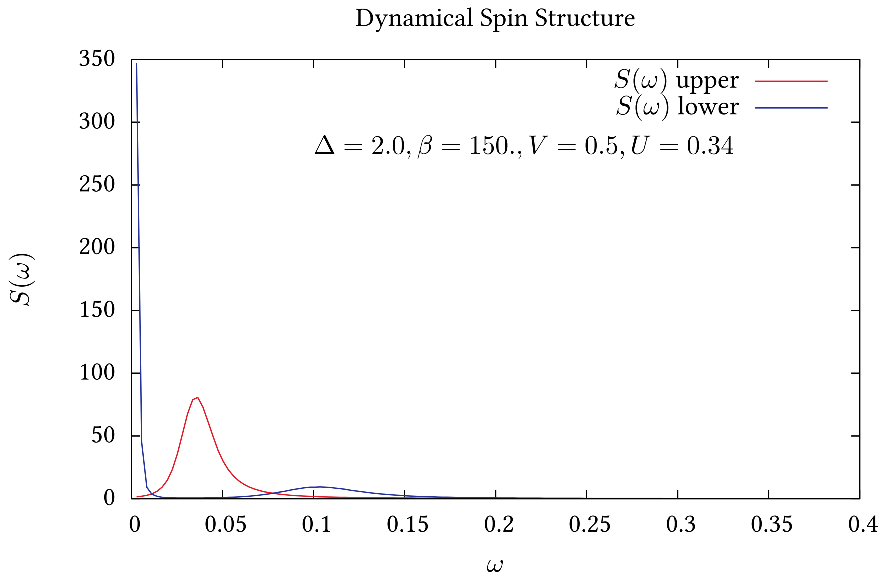

Figure 5.20.: Dynamical spin structure factor for the upper and the lower branch of the hysteresis in Fig. 5.19. Clearly, the upper branch of the hysteresis corresponds to a singlet solution, while the lower branch shows a local moment.

5.7.6. Dispersion relation of Andreev bound states

We have seen in the previous subsections, that the local physics of the single impurity model can be carried over to the lattice case within the DMFT approximation. Here, we concentrate on unique features of the lattice model (5.49), namely the dispersion relation of the f-bands as obtained by analyzing the single particle spectral function.

Using the local self-energy of the DMFT, $\mathbf{\Sigma}^{\mathbf{ff}}(i\omega_n)$, this quantity is extracted from the Green functions

$$\mathbf{G}^{\mathbf{ff}}_{\mathbf{kk}}(i\omega_n) = \left[\mathbf{G}^{\mathbf{0,ff}}_{\mathbf{kk}}(i\omega_n)^{-1} - \mathbf{\Sigma}^{\mathbf{ff}}(i\omega_n)\right]^{-1}. \tag{5.56}$$

and

$$\mathbf{G}^{\mathbf{cc}}_{\mathbf{kk}}(i\omega_n) = \mathbf{G}^{\mathbf{0,cc}}_{\mathbf{kk}}(i\omega_n) - \mathbf{G}^{\mathbf{0,cf}}_{\mathbf{kk}}(i\omega_n)\mathbf{G}^{\mathbf{ff}}_{\mathbf{kk}}(i\omega_n)\mathbf{G}^{\mathbf{0,fc}}_{\mathbf{kk}}(i\omega_n). \tag{5.57}$$

where $\mathbf{G}^{\mathbf{0,cc}}_{\mathbf{kk}}(i\omega_n)$, $\mathbf{G}^{\mathbf{0,ff}}_{\mathbf{kk}}(i\omega_n)$, $\mathbf{G}^{\mathbf{0,cf}}_{\mathbf{kk}}(i\omega_n)$, $\mathbf{G}^{\mathbf{0,fc}}_{\mathbf{kk}}(i\omega_n)$ denote the noninteracting Green functions for the corresponding orbitals in the unit cell.

Using the stochastic analytic continuation, these Green's functions can be rotated to real frequencies, yielding in principle the spectral function $\mathbf{A}(\mathbf{k}, \omega)$. For each $\mathbf{k}$-point and real frequency this quantity is a 4×4 matrix since we have a 2×2 Nambu spectral function for each combination of f and c orbitals. Our analysis of the spectral function is based on the basis independent quantity $A(\mathbf{k}, \omega) = \mathrm{Tr}\, \mathbf{A}(\mathbf{k}, \omega)$.

Fig. 5.22 plots this quantity in the singlet phase. The overall structure of the spectral function is similar to the structure observed for the bare BCS-PAM characterized by the four bands:

$$E_{\pm,\pm}(\mathbf{k}) = \pm\sqrt{V^2 + E^2(\mathbf{k})/2 \pm E(\mathbf{k})\sqrt{V^2 + E^2(\mathbf{k})/4}} \tag{5.58}$$

where $E(\mathbf{k}) = \sqrt{\epsilon^2(\mathbf{k}) + \Delta^2}$. The bands with dominant c-character, $E^c_\pm(\mathbf{k}) \equiv E^{\pm,+}(\mathbf{k})$, at high frequencies are well separated from the bands of dominant f-character at low frequencies, $E^f_\pm(\mathbf{k}) = E_{\pm,-}(\mathbf{k})$. For the considered bare parameters, V is the smallest scale and sets the magnitude of the dispersion relation of the f-band. In particular expanding in V gives:

$$E^f_\pm(\mathbf{k}) = \pm\frac{V^2}{E(\mathbf{k})} + \mathcal{O}\left(\frac{V^4}{E(\mathbf{k})^3}\right) \tag{5.59}$$

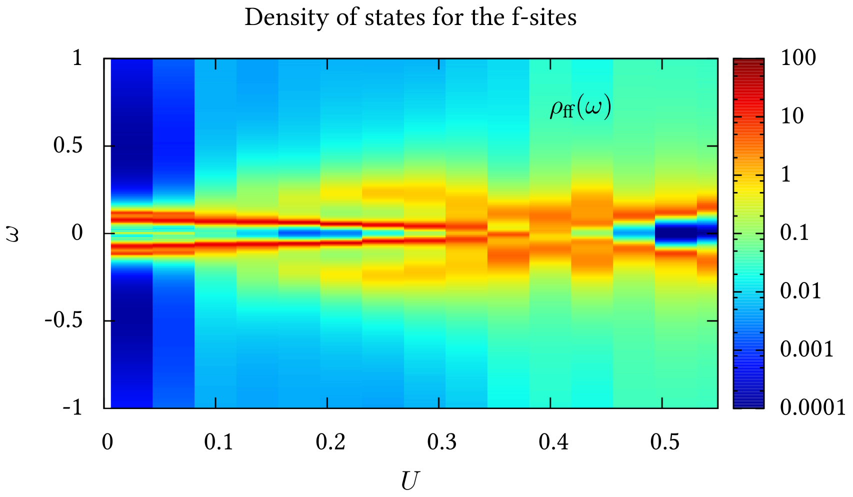

Figure 5.21.: Density of states for the f-electrons as a function of U for the parameters $V = 0.5$, $\Delta = 2$, $\mu = \epsilon_f = 0$ and $\beta = 100$.

Starting from the point of view of the impurity model, which as seen above accounts very well for the overall form of the k-integrated f-spectral function, $E^f_\pm(\mathbf{k})$ may be perceived as the dispersion relation of the Andreev bound states.

The singlet phase is continuously connected to the $U = 0$ point. Starting from this limit, we can account for the Hubbard U within a slave boson approximation [105] which will renormalize the hybridization matrix element to lower values. Owing to Eq. 5.59 this suppresses the dispersion relation of the f-electrons. This aspect is clearly observed in Fig. 5.23.

In the doublet phase, $U > U_c$, the paramagnetic slave-boson mean-field approach fails. In this state, the f-spin is frozen and in the DMFT cycle we have imposed spin symmetric baths thereby inhibiting magnetic ordering. The QMC data of Fig. 5.24 points to a very incoherent f-spectral function. It is therefore tempting to model this state in terms of spin disorder: the spin of the f-electrons on each site is static and points in a random direction. To provide some support for this picture we stay in the dynamical mean field framework but consider a mean-field decomposition of the Hubbard term in the action of the impurity problem:

$$U\left(\tilde{n}_{f,\uparrow} - \frac{1}{2}\right)\left(\tilde{n}_{\downarrow} - \frac{1}{2}\right) \rightarrow -\frac{U m_z}{2}\left(\tilde{n}_{f,\uparrow} - \tilde{n}_{f,\downarrow}\right) \tag{5.60}$$

This mean field approximation, accounts for the local moment formation with z-component of spin m_z. The corresponding mean-field action of the impurity model now reads:

$$\begin{aligned} S_{MF} = & \int_0^\beta \mathrm{d}\tau \int_0^\beta \mathrm{d}\tau' \tilde{\mathbf{f}}^\dagger(\tau) \boldsymbol{\mathcal{G}}^{-1}(\tau - \tau') \tilde{\mathbf{f}}(\tau') \\ & - \frac{U m_z}{2} \int_0^\beta \mathrm{d}\tau \tilde{\mathbf{f}}^\dagger(\tau) \tilde{\mathbf{f}}(\tau) \end{aligned} \tag{5.61}$$

where $\tilde{\mathbf{f}}^\dagger = \left(\tilde{f}^\dagger_\uparrow, \tilde{f}_\downarrow\right)$ and $\boldsymbol{\mathcal{G}}(\tau - \tau')$ corresponds to the bath Green function. To account for disorder, the z-component of the f-spin is sampled from the box distribution $m_z \in [-M_z, M_z]$. Averaging over disorder at each iteration in the DMFT cycle yields the spectral function shown in Fig. 5.25. As apparent, the disorder average generates a finite lifetime.

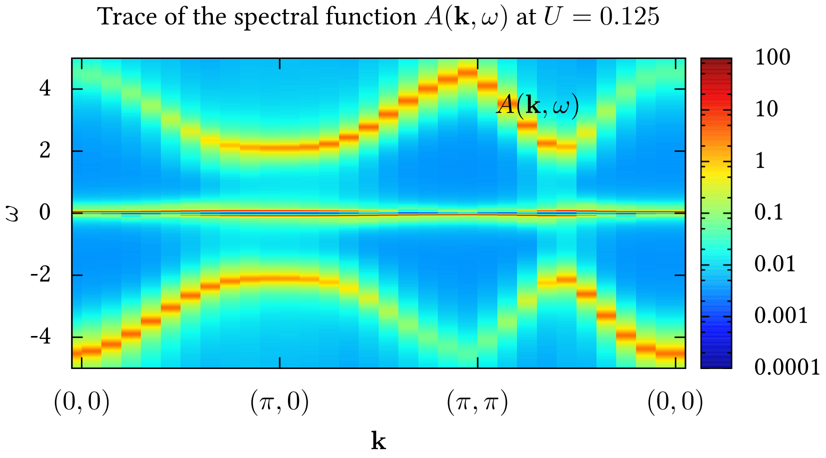

Figure 5.22.: Trace of the spectral function $A(\mathbf{k},\omega)$ at $\beta = 100$ in the singlet regime. The parameters of the simulation were given by $U = 0.125$, $V = 0.5$, $\Delta = 2$ and $\mu = \epsilon_f = 0$.

5.8. Conclusion

We have shown that the weak-coupling CT-INT algorithm is an extremely powerful unbiased tool to compute thermodynamic as well as dynamical quantities of impurity models in superconducting environments. The method can cope very well with a complex phase of the superconducting order parameter thereby allowing for the calculation of the Josephson current. Our detailed results for the impurity problem confirm the picture of a first order phase transition between a single and doublet state. It is accompanied by a π phase shift in the Josephson current.

A quantitative agreement to the measured dependence of the critical current on the gate voltage for a dot with Kondo correlations but prevailing superconductivity was achieved. This shows that our minimal model is sufficient to quantitatively capture the relevant physics and qualifies the CT-INT as a theoretical tool with predictive power for transport properties of correlated quantum dots. We further studied the regime of the strongest competition between superconductivity and Kondo correlations confirming qualitatively that the latter stabilize the singlet state and thus the 0-phase and predicting quantitatively the supercurrent, which can be experimentally verified.

Within DMFT, the physics of the BCS-PAM is mapped onto the single impurity Anderson model supplemented by a self-consistency loop. We have shown that within this approximation, the physics of the impurity model can be carried over to the lattice. In particular at fixed superconducting order parameter Δ the first order transition between a singlet and local moment state as a function of growing values of U shows up in a hysteresis behavior of the double occupancy. Furthermore, the low energy features of the local f-spectral function are reminiscent of the Andreev bound states with vanishing excitation energy (i.e. a crossing point) at the critical coupling. Within the DMFT approximation, we can look into the single particle spectral function. In the singlet phase, the low energy features can be interpreted in terms of a dispersion relation of Andreev bound states. This state is continuously linked to the $U = 0$ limit. In the doublet state or local moment regime, the low energy features of the spectral functions are incoherent. We propose to understand this in terms of models of disorder. In particular in this state, the spin dynamics of the f-electron is frozen and since we are considering paramagnetic states it points in a random different direction in each unit cell. A simple model of disorder following this picture accounts very well for the observed incoherent spectral function.

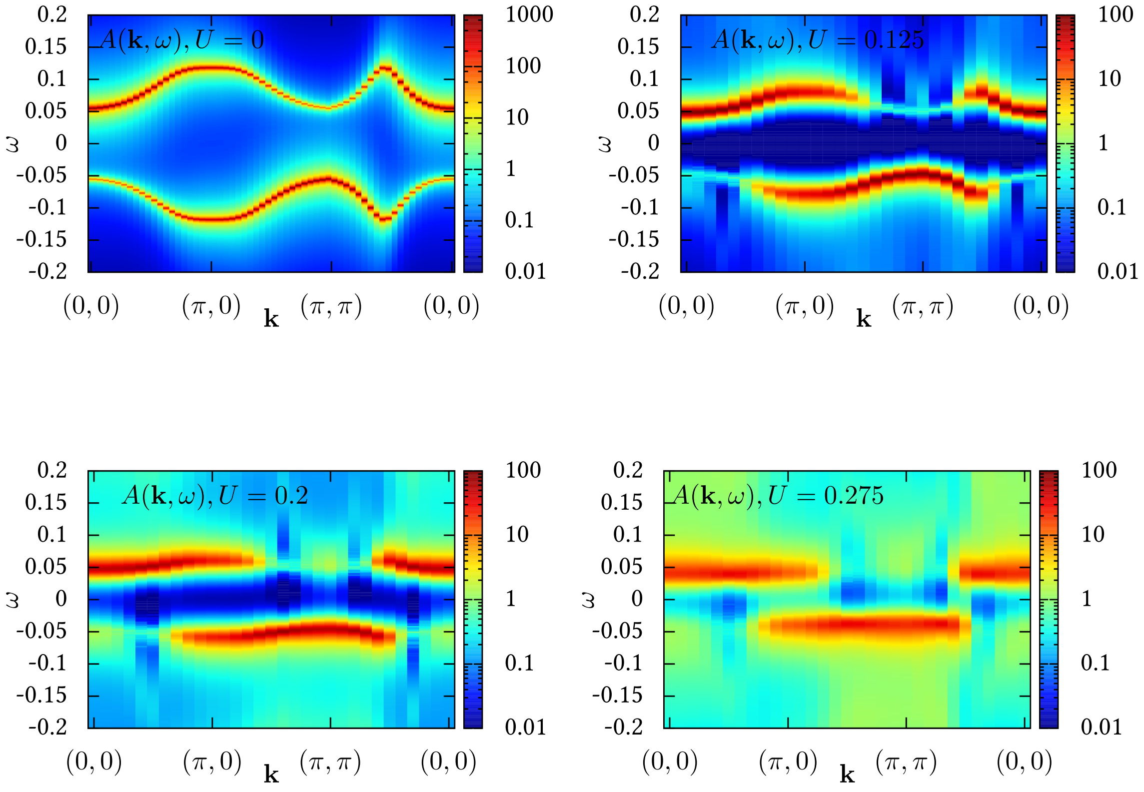

Figure 5.23.: Trace of the spectral function $A(\mathbf{k},\omega)$ at $\beta = 100$ in the singlet regime for increasing interaction U. The width of the f-bands clearly decreases and the dispersion becomes weaker. The parameters of the simulations were given by $V = 0.5$, $\Delta = 2$ and $\mu = \epsilon_f = 0$.

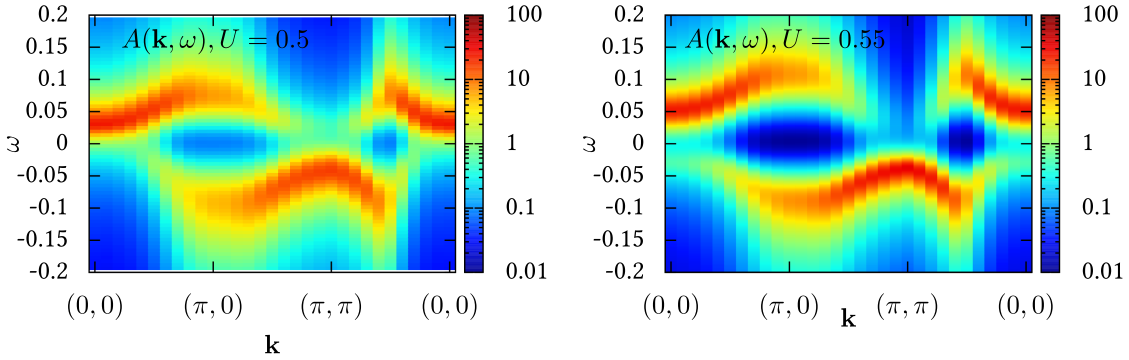

Figure 5.24.: Trace of the spectral function $A(\mathbf{k},\omega)$ at $\beta = 100$ in the doublet regime for different values of U. Here, we only show the f-bands. The parameters of the simulation were given by $V = 0.5$, $\Delta = 2$ and $\mu = \epsilon_f = 0$.

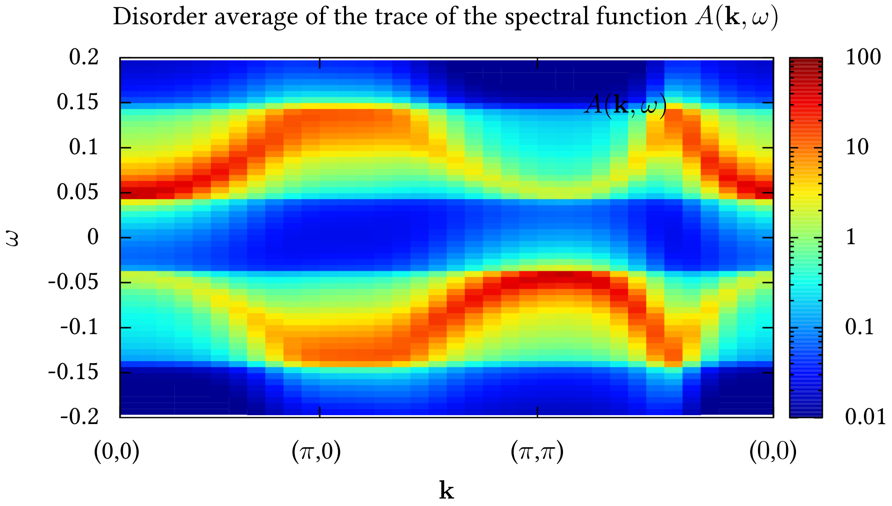

Figure 5.25.: Trace of the spectral function $A(\mathbf{k}, \omega)$ as obtained from using Eq. 5.61 for the impurity action. The z-component of the local moment is sampled from the box distribution $m_z \in [-M_z, M_z]$. The parameters used for this plot were given by $V = 0.5$, $U = 0.5$, $\Delta = 2$ and $M_z = 0.0375$. Here, the calculations are carried out on the real time axis such that no analytical continuation is required.

6. Edge magnetism in graphene

This section is an extended reproduction of work published in reference [106]. This work was done in collaboration with Manuel J. Schmidt and Fakher F. Assaad.

6.1. Introduction

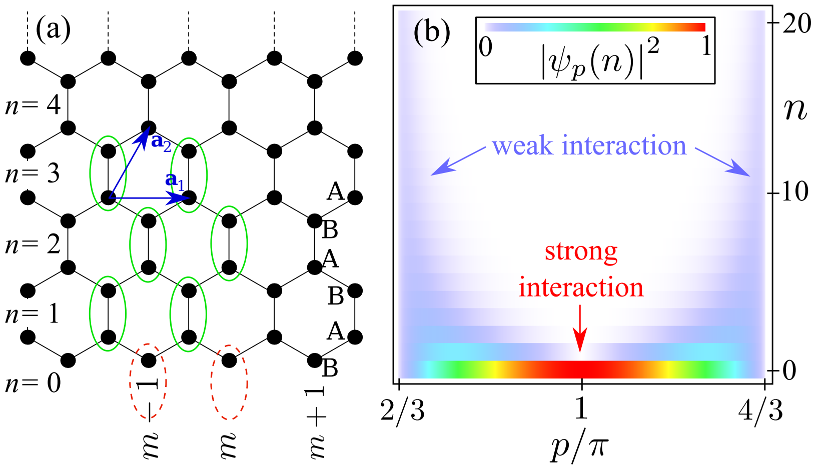

Figure 6.1.: Part (a) shows the half-infinite honeycomb lattice. The solid ellipses (green) are the complete unit cells in the bulk region and the dashed elipses indicate the cut unit cells at the α edge. The n and m directions are indicated as well as the sublattice indices A, B. Part (b) shows the modulus square of the transverse (in n direction) edge state wave function $|\psi_p(n)|^2$ on the B sublattice sites in the reduced Brillouin zone $\frac{2\pi}{3} \leq p \leq \frac{4\pi}{3}$. The extreme momentum dependence of the localization of ψ_p in n direction is crucial for the magnetic properties of edge states.

Since it has first been isolated in the laboratory,[107] graphene, a two-dimensional honeycomb lattice of carbon atoms,[108] attracts much attention. In fact, graphene has multiple amazing properties. To name only a few of them, it ranges among the mechanically strongest materials,[109] it shows a quantum Hall effect at room temperature,[110] and, due to its unusual Dirac band structure, it allows the study of relativistic quantum physics in a solid state environment.[111] Furthermore, its potential application as the basis of the next generation of electronic devices stimulated great efforts to gain experimental control as well as theoretical understanding of this astonishing material.

Usually a strong electron confinement increases the strength of electron-electron interactions by pushing the electrons close together. However, in spite of the extreme electron confinement to only one single layer of atoms, many experiments in graphene may be explained by assuming the electrons to be non-interacting. This is especially true for experiments probing the bulk properties of graphene, as the bulk density of states vanishes at the Fermi level, suppressing the manifestation of interaction effects. On the other hand, the properties of zigzag edges differ greatly from the bulk properties. So-called edge states, i.e. one-dimensional states with very small bandwidth, localized at these edges, give rise to a peak in the local density of states at the Fermi energy.[112] The enhanced density of states allows the electron-electron interaction to drive the zigzag edges to a ferromagnetic state with a magnetic moment localized at the edge.[113–118] This phenomenon is known as edge magnetism.

At normal graphene edges the electron-electron interaction is so strong and the bandwidth of the edge states is so small that the spins of all electrons in the edge states are completely aligned. However, as has been proposed recently, graphene/graphane interfaces provide means to tune the bandwidth of the edge states to regimes in which the edge starts to depolarize and the edge magnetism is gradually suppressed until, for a critical edge state bandwidth, the magnetism disappears.[119]

In Ref. [119] it was argued that this interaction-induced magnetism can be understood on the basis of an effective model, describing the interacting one-dimensional edge states only, while the bulk states are neglected. What at first glance appears to be a contradiction to the Lieb-Mattis theorem,[120] stating that the ground state of interacting electrons in one dimension cannot be spin polarized, can be resolved by noting that the effective edge state model does not fulfill the prerequisites of the Lieb-Mattis theorem.[119] The deeper reasons for the existence of a ferromagnetic ground state in a one-dimensional interacting electron system, however, remained elusive. The present work is devoted to this issue.

In this chapter we present a systematic exact diagonalization analysis of interacting edge states. Two striking features of edge states turn out to be most important for their magnetic properties: (a) the edge states exist only in a restricted part of the Brillouin zone and (b) the transverse edge state wave function has a strong characteristic momentum dependence. These features have consequences for the effective low-energy theory, namely (a) *no umklapp processes are allowed in the interaction Hamiltonian* and (b) *the interaction vertex acquires an unusually strong momentum dependence.* In order to be able to study the consequences of these two features, we introduce a generalized model in which we add an artificial interaction term describing umklapp processes and allow the momentum-dependence of the interaction vertex to be tuned from a momentum-independent vertex, as in usual metals, to the full momentum-dependence, as it is found in edge states. Therefore, the generalized model can be tuned continuously from the limit in which it describes edge states to a limit which corresponds to usual one-dimensional metals such as the Hubbard chain. We solve this generalized model for graphene zigzag edges of finite length $L = 48$ unit cells (i.e. $\sim$12 nm) by exact diagonalization using the Lanczos method for the determination of the ground state of the effective model[1].[22, 121, 122]

The section is organized as follows. In Sec. 6.2 we review the direct model as it has been derived in Ref. [119] and introduce the more versatile generalized model with additional tunability. In Sec. 6.3 the exact diagonalization analysis of the generalized model is presented. Finally, the results are discussed in Sec. 6.6.

6.2. Edge state models

In this section we introduce the models on which our analysis is based. The edge state model obtained from the direct projection of the honeycomb lattice Hubbard model to the Fock space spanned only by the edge states has been discussed in Ref. [119]. This model will be called the *direct model* in the following. We identify two important features of the direct model: (a) the restriction of the Brillouin zone for the edge states and (b) the strong dependence of the transverse localization length on the momentum along the edge. After having analyzed the consequences of these features for the effective interaction vertex, we propose a generalized edge state model in which these features can be tuned. This allows us to investigate the impact of each of these edge state features on the magnetic properties. In particular, the generalized model can be tuned continuously from a Hubbard chain limit, i.e., a usual one-dimensional metal without any ferromagnetic ground state, to the edge state limit with its ferromagnetic ground state.

6.2.1. Direct derivation from the honeycomb model

We start from the simplest possible non-interacting tight-binding model of electrons in graphene zigzag ribbons, taking into account only nearest neighbor hoppings of π electrons $\mathcal{H} = \sum_{\langle i,j\rangle,\sigma} c^{\dagger}_{i\sigma} c_{j\sigma}$, where

---

[1] At $L/3$ filling, and $S_z = 0$, we could access edges of length $L = 48$ with a dimension of the corresponding Hilbert space of 2 594 212 after exploiting all symmetries. For nearly maximal $S_z = L/6 - 2$ and $L/3$ filling, we were able to calculate the groundstate energy of an edge with length $L = 180$ with a Hilbert space dimension of only 26 580. In this case we were limited only by the 64 bit limit of the internal storage of the basis vectors and longer edges are in principle accessible by a modification of our code.

$\langle i,j\rangle$ runs over nearest neighbor sites of a half-infinite honeycomb lattice, $i \equiv (m,n,s)$ is a collective site index for the (m,n)th unit cell and the $s = A, B$ sublattice (see Fig. 6.1), and $c_{i\sigma}$ annihilates an electron at site i with spin σ. Since we are exclusively interested in the zero energy eigenstates of $\mathcal{H}$, the actual energy scale of $\mathcal{H}$ is unimportant so that we may drop it.[2] The zero energy states are created by the fermionic edge state operator

$$e^\dagger_{p\sigma} = \sum_n \psi_p(n) c^\dagger_{pn\sigma}, \qquad \psi_p(n) = \mathcal{N}_p u_p^n \tag{6.1}$$

where $u_p = -1 - e^{ip}$, p is the momentum in m direction (along the edge), and

$$c_{pn\sigma} = L^{-\frac{1}{2}} \sum_m e^{-ipm} c_{(m,n,B)\sigma}, \tag{6.2}$$

with the number of unit cells L in m direction, i.e., along the edge. The p-dependent normalization constant $\mathcal{N}_p = \sqrt{2\cos(p-\pi) - 1}$ can be interpreted as the weight of the edge state wave function right at the edge atoms where $n = 0$. It is easily seen that $\mathcal{H}e^\dagger_{p\sigma} = 0$. As the edge state wave function is only non-zero on the B sublattice we omit the sublattice index, setting it to $s = B$.

The two most important features of the edge state wave function [Eq. (6.1)] are : (a) The edge state only exists for momenta $\frac{2\pi}{3} < p < \frac{4\pi}{3}$. In the rest of the Brillouin zone the edge state wave function is not normalizable, as $|u_p| > 1$ for these momenta. (b) In n direction the edge state is sharply localized at the edge for $p = \pi$, wereas for p close to one of the Dirac points $K = \frac{2\pi}{3}$ and $K' = \frac{4\pi}{3}$, the wave function delocalizes into the bulk [see also Fig. 6.1(b)]. These two edge state properties are stable against adding more details, such as second-nearest neighbor hopping or various edge passivations, to the honeycomb Hamiltonian $\mathcal{H}$.[119, 123] The detailed analysis presented in this chapter will clarify that *the existence of edge magnetism and in particular its tunability are consequences of these two edge state properties.*

The p-dependence of the localization length of ψ_p has consequences for the edge states' self-energy ϵ_0 as well as for their interaction vertex function Γ. Neglecting the bulk state contributions,[119] the self-energy correction due to a perturbation V, which is invariant along the edge, is given by $\epsilon_0(p) = \langle\psi_p|V|\psi_p\rangle$. Due to the delocalization of $\psi_p(n)$ for p near K, K', edge-localized perturbations V lead to self-energy corrections for which $\epsilon_0(K) = \epsilon_0(K') = 0$ while $\epsilon_0(\pi) \sim ||V||$. For sufficiently well behaved perturbations the self-energy correction gives rise to a smooth edge state energy dispersion with a bandwidth $\Delta \sim ||V||$. For a large class of these edge-localized perturbations, the self-energy correction approximately has the form

$$\epsilon_0(p) \simeq \mathcal{N}_p^2 \Delta, \tag{6.3}$$

with $\mathcal{N}_p^2$ the p-dependent weight of the edge state wave function right at the edge. Eq. (6.3) expresses that an edge state which is more localized at the edge experiences a stronger self-energy correction from an edge-localized perturbation than an edge state which is delocalized into the bulk region. Examples of such perturbations are edge passivations, graphane termination,[123] or local interactions with the substrate. Note that the edge state bandwidth Δ is experimentally tunable in various ways so that we consider Δ as a free parameter. Therefore, the noninteracting part of the direct model (dm) edge state Hamiltonian is given by:

$$H_0^{\text{dm}} = -\Delta \sum_\sigma {\sum_p}' \mathcal{N}_p^2 e^\dagger_{p,\sigma} e_{p,\sigma}, \tag{6.4}$$

where the sum is restricted such that only edge state operators $e_{p\sigma}$ with $\frac{2\pi}{3} \le p \le \frac{4\pi}{3}$ appear.

The effective interaction of the edge states, derived by projecting the Hubbard Hamiltonian on the two-dimensional honeycomb lattice $H_U = U\sum_i c^\dagger_{i\uparrow} c_{i\uparrow} c^\dagger_{i\downarrow} c_{i\downarrow}$ to the Fock space spanned by the edge states, reads[119]

$$H_1^{\text{dm}} = \frac{U}{L} {\sum_{p,p',q}}' \Gamma(p,p',q) e^\dagger_{p+q\uparrow} e_{p\uparrow} e^\dagger_{p'-q\downarrow} e_{p'\downarrow}. \tag{6.5}$$

---

[2] It is only important to assume that this energy scale is large enough so that the restriction to the zero energy sector of $\mathcal{H}$ is well justified. The validity of this assumption has been checked in Ref. [119].

Together, we have the effective Hamiltonian $H^{\text{dm}} = H_0^{\text{dm}} + H_1^{\text{dm}}$. The interaction vertex is given by the overlap of the wave functions of all four fermions (with momenta $p+q, p, p'-q, p'$) participating in the interaction

$$\Gamma(p,p',q) = \sum_{n=0}^{\infty} \psi^*_{p+q}(n)\psi_p(n)\psi^*_{p'-q}(n)\psi_{p'}(n) = \frac{\mathcal{N}_{p+q}\mathcal{N}_p\mathcal{N}_{p'-q}\mathcal{N}_{p'}}{1-u^*_{p+q}u_p u^*_{p'-q}u_{p'}}. \tag{6.6}$$

While the denominator, resulting from the geometric series over n, turns out to lead only to unimportant quantitative corrections, the numerator of Γ, which is the product of the wave function weights at the edge $\mathcal{N}_p$ for each of the four fermion operators, leads to the momentum-dependence of the interaction strength which is important for the stability of the weak edge magnetism. Essentially, the effective interaction becomes stronger the more localized the participating fermions are, i.e., the closer their momenta are to $p = \pi$. If one or more of the momenta are close to the Dirac points $\frac{2\pi}{3}, \frac{4\pi}{3}$, where the edge state wave functions delocalize into the bulk, the effective interaction is suppressed (see Fig. 6.1). Note that setting the denominator in Eq. (6.6) to unity corresponds to assuming that the Hubbard interaction is only present at the outermost line of carbon atoms right at the edge. Such an approximation has been used in Ref. [124]. We find that this approximation is inessential for the edge magnetism, leading only to quantitative corrections.

An important consequence of the restriction of the p summation in Eq. (6.5) is the *absence of umklapp processes*. As explained above, edge states only exist in one third of the Brillouin zone, i.e. for $\frac{2\pi}{3} \leq p \leq \frac{4\pi}{3}$, so that no four fermion process with momentum $\pm 2\pi$ exists. Indeed, within the restricted Brillouin zone, the process with the largest possible total momentum p_{tot} is $e^\dagger_{4\pi/3\uparrow}e_{2\pi/3\uparrow}e^\dagger_{4\pi/3\downarrow}e_{2\pi/3\downarrow}$, i.e. $p_{\text{tot}} = \frac{4\pi}{3} < 2\pi$. Processes with larger total momentum leave the restricted Brillouin zone and are therefore suppressed, as they involve the overlap of edge states and bulk states, which is small. Also, most of the bulk states live in a different energy regime than the edge states.[119]

Thus, we have identified two properties of edge states which make them fundamentally different from usual one-dimensional conductors:

(a) Due to the restricted Brillouin zone, umklapp processes are forbidden.

(b) The transverse localization $\mathcal{N}_p$ of the edge state wave function gives rise to a tunable band width $\epsilon_0(p) \simeq \mathcal{N}_p^2\Delta$. Furthermore, the interaction vertex becomes weaker if the momenta of the participating fermions approach a Dirac point, i.e. $\Gamma(p,p',q) \propto \mathcal{N}_{p+q}\mathcal{N}_p\mathcal{N}_{p'-q}\mathcal{N}_{p'}$.

We will show that these properties are the basis for the magnetism at graphene edges.

6.2.2. Generalized model

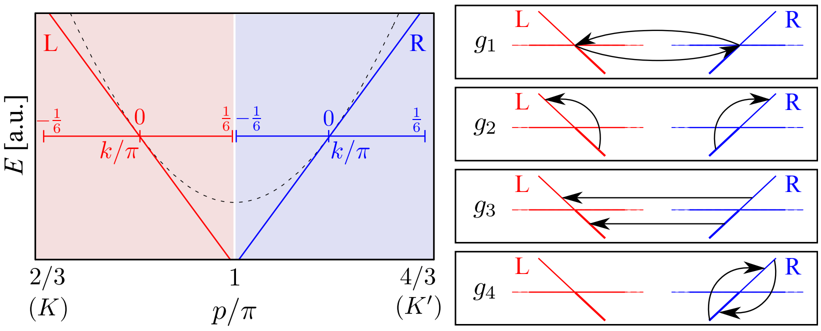

Figure 6.2.: Left: The self-energy $\sim \mathcal{N}_p^2$ of the direct model (dashed line) and the linearized self-energy (solid lines). Right: The four possible interaction processes. The g_3 process is not allowed for graphene edge states.

We now introduce a generalized model in which the different aspects of the effective electron-electron interaction, found in the previous subsection, may be tuned independently. For this, we map the edge state operators $e_{p,\sigma}$ which correspond to right (left) moving modes for $\pi < p < \frac{4\pi}{3}$ ($\frac{2\pi}{3} < p < \pi$), to fermionic operators $c_{kr\sigma}$ in which $r = R, L$ specifies the direction of motion and $-\frac{\pi}{6} \leq k \leq \frac{\pi}{6}$, i.e. $c_{kr\sigma} = e_{k+\pi+r\pi/6,\sigma}$ and $p = k + \pi + r\pi/6$. The direction of motion $r = R, L$ corresponds to $r = \pm 1$ when used in formulas. Note that the zero point of k has been shifted so that $k = 0$ corresponds to $p = \pi \pm \pi/6$ for right and left movers, respectively (see Fig. 6.2).

For the non-interacting part of the generalized edge state model we assume a linear spectrum with slope $\pm v_F$

$$H_0 = v_F \sum_{\substack{r=R,L \\ \sigma=\uparrow,\downarrow}} \sum_{k=-\pi/6}^{\pi/6} (rk) c^\dagger_{kr\sigma} c_{kr\sigma}. \tag{6.7}$$

This linearization of the self-energy [Eq. (6.3)] only leads to inessential quantitative corrections (see also Appendix 6.5). The partitioning into left- and right-movers always gives rise to four terms in the interaction part H_1 of the Hamiltonian involving different combinations of left- and right-moving modes. Conventionally, these terms are called g_1, g_2, g_3, g_4 processes (see Fig. 6.2 and Ref. [125]). g_2, g_4 correspond to forward scattering, involving processes that scatter only between modes with the same direction of motion, g_1 refers to backward scattering, and g_3 are the umklapp terms which are forbidden in edge states. Note that, unlike in usual g-ology,[125] we may not assume that the coupling constants for the individual g_i processes are constant. The momentum-dependence of the g_i must be taken into account.

The two forward scattering processes g_2 and g_4 may be merged together into one Hamiltonian[3]

$$H_1^{\text{fs}} = \frac{U}{L} \sum_{r,r'} \sum_{k,k',q}{}' S^r_{k+q} S^r_k S^{r'}_{k'-q} S^{r'}_{k'} : c^\dagger_{k+qr\uparrow} c_{kr\uparrow} c^\dagger_{k'-qr'\downarrow} c_{k'r'\downarrow} :, \tag{6.8}$$

where $: A :$ enforces the normal order[125] of the operator A. The primed sum is restricted such that $|k| < \pi/6$ for all momentum arguments k in the electron operators. In order to be able to change the amplitude of the momentum-dependence of the interaction vertex $\Gamma(p, p', q)$ [see Eq. (6.6)], we introduce the factors

$$S^r_k = \sqrt{1 - r\Gamma_1 k}, \tag{6.9}$$

from which we build the interaction vertex for the generalized model. The factor $\Gamma_1 \in [0, 6/\pi]$ quantifies the momentum-dependence. For $\Gamma_1 = 0$ the interaction is momentum-independent. This limit corresponds to usual one-dimensional Hubbard chains. For $\Gamma_1 = 6/\pi$ the interaction goes to zero if at least one of the fermions is close to the upper band edge ($k = r\pi/6$). This corresponds to the direct model, where the trigonometric term under the square root in $\mathcal{N}_p$ has been replaced by a linear approximation. The differences between the generalized model in the edge state limit and the direct model only lead to quantitative renormalizations of the critical point, as shown in Appendix 6.5. The essential property of the interaction vertex is that it approaches zero if one of the fermion momenta gets close to the Dirac points. This feature is present in the direct and in the generalized model with $\Gamma_1 = 6/\pi$.

The form of the backscattering (g_1) Hamiltonian H_1^{bs} is similar to H_1^{fs}. However the scattering takes place between left- and right-movers

$$H_1^{\text{bs}} = \lambda_{\text{bs}} \frac{U}{L} \sum_r \sum_{k,k',q} S^r_{k+q} S^{-r}_k S^{-r}_{k'-q} S^r_{k'} c^\dagger_{k+q,r,\uparrow} c_{k,-r,\uparrow} c^\dagger_{k'-q,-r,\downarrow} c_{k',r,\downarrow}. \tag{6.10}$$

We have introduced the additional parameter λ_{bs} which allows us to tune the overall strength of the g_1 processes relative to the g_2, g_4 processes. $\lambda_{\text{bs}} = 1$ corresponds to the physical backscattering strength which is required by SU(2) invariance.[125] Nevertheless, we will investigate the consequences of a suppression of backscattering since this will be important for a bosonization analysis of the generalized model which will be presented in an upcoming paper.[126]

As already pointed out, an important feature of edge states is the absence of umklapp processes in the effective electron-electron interaction. However, in order to be able to compare the edge state model to a

---

[3] The equal strength of the g_2 and g_4 processes is due to the symmetry property $\Gamma(-k_F, k_F, 2k_F) = \Gamma(\pm k_F, \pm k_F, 0)$, which is a consequence of the origin of Γ in the 2D honeycomb Hubbard model (see Ref. [119]).

Hubbard chain, we add an artificial umklapp process with relative strength λ_{us} to the Hamiltonian of the generalized model

$$H_1^{\text{us}} = \lambda_{\text{us}} \frac{U}{L} \sum_r \sum_{k,k',q} S_{k+q}^r S_k^{-r} S_{k'-q}^r S_{k'}^{-r} c_{k+q,r,\uparrow}^\dagger c_{k,-r,\uparrow} c_{k'-q,r,\downarrow}^\dagger c_{k',-r,\downarrow}. \tag{6.11}$$

Varying λ_{us} between 1 (Hubbard chain limit) and 0 (edge state limit) allows us to investigate the consequences of the presence of umklapp processes for one-dimensional ferromagnetism.

Alltogether, the four parameters v_F/U, λ_{bs}, λ_{us}, and Γ_1 define the phase space of the generalized model

$$H = H_0 + H_1^{\text{fs}} + H_1^{\text{bs}} + H_1^{\text{us}}. \tag{6.12}$$

The following limits of this model may be identified:

1. Edge state limit: the generalized model with the parameters $\lambda_{\text{bs}} = 1$, $\lambda_{\text{us}} = 0$, and $\Gamma_1 = 6/\pi$, is a good approximation of the direct model.
2. Hubbard chain limit: for $\lambda_{\text{bs}} = 1$, $\lambda_{\text{us}} = 1$, and $\Gamma_1 = 0$, the generalized model essentially describes a one-dimensional Hubbard chain. The only difference is the assumption of a linearized single-particle spectrum instead of the $2\cos(k)$ dispersion.

Note that it is important to work in the k-space formulation because it is difficult to control the umklapp scattering or the momentum dependence of the interaction vertex in a real space formulation. One reason for this is that an interaction vertex $\Gamma(p, p', q)$ with a nontrivial p, p' dependence does not transform to a real space interaction of the form $V(x - x')$ but to a complicated non-local interaction. This also hampers the application of DMRG methods to this problem.

6.3. Exact diagonalization

The exact ground state of the generalized model is calculated numerically for finite sized zigzag edges up to $L = 48$ by the Lanczos exact diagonalization method,[4][22, 121, 122, 127] which relies on the projection of the Hamiltonian H to an orthonormal basis of the Krylov subspace

$$K = \text{span}\{|\,\phi_s\,\rangle, H\,|\,\phi_s\,\rangle, H^2\,|\,\phi_s\,\rangle, \dots, H^{m-1}\,|\,\phi_s\,\rangle\} \tag{6.13}$$

with a random start vector $|\,\phi_s\,\rangle$ of nonzero overlap with the true groundstate. The groundstate energy of the projected Hamiltonian in this basis converges very quickly to the groundstate energy in the complete Hilbert space with increasing dimension of the Krylov space m, typically a size of $m \approx 10^2 \dots 10^3$ was found to be sufficient for this work. Computationally, the operation $H\,|\,\phi\rangle$ for a state vector $|\,\phi\rangle$ is the most expensive one. We store $|\,\phi\rangle$ in an occupation number basis $\{|\,n\,\rangle\}$ of the full Hilbert space in k space and are then confronted with calculating $H\,|\,\phi\rangle = \sum_n \langle\, n\,|\phi\,\rangle\, H\,|\,n\,\rangle$, where the outcome of $H\,|\,n\,\rangle$ is calculated on the fly.

Separating left and right movers as well as the two spin sectors, the many body basis states can be written in the form

$$|\,\psi\,\rangle = |\,n_{k_1} \dots n_{k_N}\,\rangle_{R,\uparrow} |\,n_{k_1} \dots n_{k_N}\,\rangle_{R,\downarrow} |\,n_{k_1} \dots n_{k_N}\,\rangle_{L,\uparrow} |\,n_{k_1} \dots n_{k_N}\,\rangle_{L,\downarrow}. \tag{6.14}$$

For the generalized model, neither the number of left/rightmovers, nor the total momentum is conserved, thus leaving only

$$N_\sigma = \sum_{k,r} c_{kr,\sigma}^\dagger c_{kr,\sigma} \tag{6.15}$$

as a conserved quantity, making the Hamiltonian block diagonal. We encode one basis state as a pair of 64 bit integer numbers $(i_\uparrow, i_\downarrow)$. Here, we use the $N/2$ lowest bits to encode the momenta of the right movers

---

[4] An edge with L unit cells in length corresponds to only $L/3$ k-space points in the reduced Brillouin zone in which the edge states are defined.

and the next $N/2$ bits to encode the momenta of the left movers. Thus, we can easily keep the number of set bits constant while generating the basis states and therefore stay in the same block of the Hamiltonian.

The application of the Hamiltonian to a basis state can be performed implicitly without the knowledge of its matrix form. However, we will only obtain a set of resulting basis states represented by the integer pairs $(i_\uparrow, i_\downarrow)$. This is inconvenient for the calculation of the actual resulting state $H\left|\psi\right\rangle$ and we need to find the indices of the basis states contained in $H\left|n\right\rangle$ in the basis state array. This reverse search is an expensive operation, slowing down the code substantially. A huge performance gain can be obtained by the introduction of a hash table which allows the quick deduction of the index of a basis state $(i_\uparrow, i_\downarrow)$.

The magnetic properties of the ground state depend on the ratio between the kinetic energy and the potential energy $v_F\pi/U$, which is experimentally tunable at graphene/graphane interfaces.[119] Three additional tuning parameters $\Gamma_1, \lambda_{\text{us}}, \lambda_{\text{bs}}$, which are not accessible experimentally, have been added in order to be able to study the significance of the momentum dependence of the interaction vertex (Γ_1), the influence of the absence of umklapp scattering (λ_{us}) in edge states, and also the importance of backscattering (λ_{bs}). With those artificial parameters, the generalized model may be tuned continuously from a Hubbard chain limit to the edge state limit. In both limits the model describes an interacting one-dimensional metal. The magnetic properties in these two limits, however, differ strongly: while the usual Hubbard chain (with umklapp scattering and without momentum dependence) does not give rise to a ferromagnetic ground state, the edge states (without umklapp scattering and with momentum-dependent interactions) show two magnetic phases in addition to the non-magnetic Luttinger liquid phase: for strong interactions the saturated edge magnetism[113–115] is recovered, while for intermediate interaction strengths, a ferromagnetic Luttinger liquid appears.

The Hamiltonian H [Eq. (6.12)] conserves the numbers $N_\uparrow, N_\downarrow$ of up-spin and down-spin electrons, so that H is block diagonal in the S_z subspaces, which we define by the total spin-polarization in z direction

$$S_z = \frac{1}{2}(N_\uparrow - N_\downarrow) = 0, 1, 2, ..., N/2. \tag{6.16}$$

The total number of electrons $N = N_\uparrow + N_\downarrow = L/3$ is kept constant. This corresponds to half-filling. Note, however, that the filling is physically relevant only if umklapp scattering is present (i.e. $\lambda_{\text{us}} > 0$). For the edge states in which we are finally interested, umklapp scattering is forbidden so that the filling is irrelevant as it only leads to quantitative renormalizations of the interaction strength and the Fermi velocity. In the following, we determine the ground state of H in each S_z subspace separately.

Note that by the definition of the S_z subspaces we have chosen a spin quantization axis. The Hamiltonian H, however, is SU(2) symmetric if the backscattering is at its physical strength $\lambda_{\text{bs}} = 1$. Furthermore, since we are dealing with finite systems, there will be no spontaneous rotational symmetry breaking. Thus, edge magnetism will become manifest in a $(2S+1)$-fold ground state degeneracy, corresponding to a high spin (S) state. For instance, if in a system with $N = 2$ electrons the lowest energy states in the subspaces $S_z = -1, 0, 1$ are the degenerate ground states, then the $\frac{1}{2}$ spins of two electrons point into the same direction, building an $S = 1$ super spin. Because the SU(2) symmetry of the individual electron spins is not broken, also this composite super spin has full rotational symmetry. The S_z quantum numbers of the degenerate S_z subspaces then correspond to the magnetization of this composite spin system. Note that the spin-orbit interaction lowers the symmetry of the super spin, as it breaks the SU(2) invariance of the individual electron spins which form the super spin.

For practical reasons, we extract the total spin quantum number S of the ground state from its ground state degeneracy $(2S+1)$, which is obtained from the S_z subspace ground state energies. We have checked that this is equivalent to calculating the total spin S of the ground state directly.

6.3.1. Hubbard chain vs. edge states

First we study the crossover from a usual Hubbard chain to interacting edge states. As explained above, the generalized model can be tuned continuously between these two limiting cases by means of the parameters λ_{us} and Γ_1. We postpone the analysis of backscattering to the next subsection and set $\lambda_{\text{bs}} = 1$ here.

It is most instructive to begin with the Hubbard chain limit of the generalized model, which is characterized by the full umklapp process strength $\lambda_{\text{us}} = 1$ and a suppressed momentum dependence of the interaction

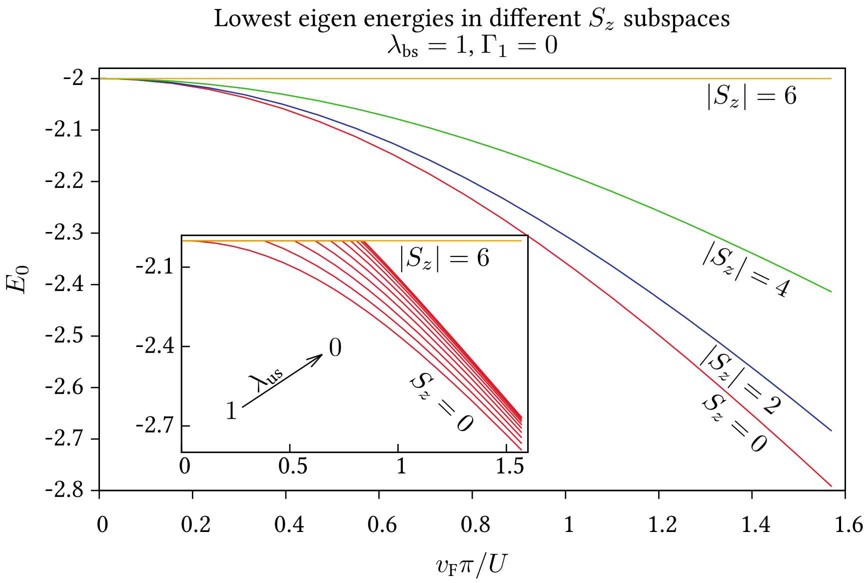

Figure 6.3.: Lowest eigen energies in different S_z subspaces for $N = 12$ in the Hubbard limit with $\lambda_{\text{bs}} = 1$, $\lambda_{\text{us}} = 1$, $\Gamma_1 = 0$, and $U = 1$. The inset shows the lowest eigen energies of the $S_z = 0, 6$ subspaces (zero and full spin-polarization) as the umklapp scattering is suppressed. The lower lines correspond to $\lambda_{\text{us}} = 1$ and the higher lines to $\lambda_{\text{us}} = 0$. For the lines in between, λ_{us} decreases in steps of 0.2.

$\Gamma_1 = 0$. With this parameter set the direct model resembles a one-dimensional metal with a linear single particle dispersion instead of a cos-dispersion. [5] The lowest eigen energies in the different S_z subspaces for the parameter set described above are shown in Fig. 6.3. Obviously, the ground state is non-degenerate and resides in the $S_z = 0$ subspace for arbitrary $v_F\pi/U$, except for the limit of infinitely large U. Thus, as expected, no ferromagnetic phase transition exists for the Hubbard chain limit of the generalized model at finite $v_F\pi/U$, in consistence with the Lieb-Mattis theorem[120] which states that the ground state of a system of one-dimensional interacting electrons has zero total spin and is non-degenerate with higher spin subspaces. [6]

Next, the generalized model is tuned away from the Hubbard chain limit by suppressing the umklapp scattering $\lambda_{\text{us}} < 1$. Suppressed umklapp scattering is one of the properties of edge states which makes them fundamentally different from usual one-dimensional metals. In the inset of Fig. 6.3, the lowest eigen energies of the $S_z = 0$ and the $S_z = \pm N/2$ (full spin-polarization) subspaces are shown as λ_{us} is reduced from 1 to 0 in steps of 0.2. For any $\lambda_{\text{us}} < 1$ there is a nonzero critical value for $v_F\pi/U$ below which the lowest energy states of these two subspaces and also for all S_z in between (not shown in the inset of Fig. 6.3) are equal. This corresponds to a high spin state of size $S = 6$ in which the spins of all electrons point into the same direction. The critical point at which the transition between $S = 0$ and $S = N/2$ takes place depends on the umklapp scattering strength

$$\left[\frac{v_F\pi}{U}\right]^{(\Gamma_1=0)}_{\text{crit.}} \propto (1 - \lambda_{\text{us}})^y \,. \tag{6.17}$$

For $N = 12$ we find for the exponent $y \simeq 0.5 \pm 0.02$. Obviously, the absence of umklapp scattering allows a high spin ground state. However, for $\lambda_{\text{us}} < 1$ and $\Gamma_1 = 0$, the system instantly jumps from zero polarization $S = 0$ to the maximal possible polarization $S = N/2$ at the critical point $[v_F\pi/U]^{(\Gamma_1=0)}_{\text{crit.}}$. This is a first order phase transition. For the case of completely suppressed umklapp scattering $\lambda_{\text{us}} = 0$ this is shown in

---

[5] We have checked that the linearization of the single particle spectrum does not change the results qualitatively.

[6] The point $v_F\pi/U = 0$ corresponds to a *pathologic potential* in Ref. [120], as it can be reached by $U \to \infty$. At this point, all sectors with total spin $0 \leq S \leq S_{\text{max}}$ are degenerate.

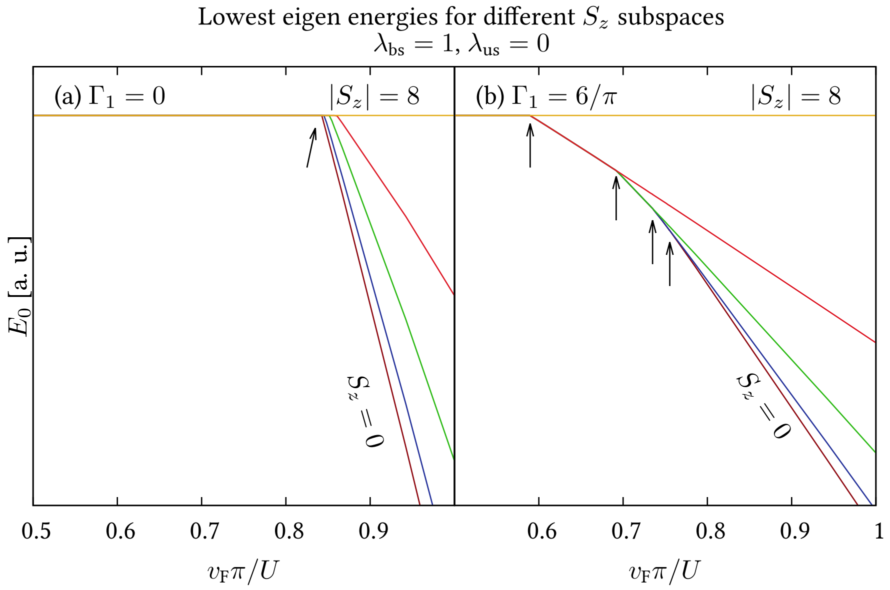

Figure 6.4.: Lowest eigen energies with completely suppressed umklapp scattering $\lambda_{\mathrm{us}} = 0$ and different momentum-dependencies Γ_1. Furthermore, $N = 16$, $\lambda_{\mathrm{bs}} = 1$, and $U = 1$. Part (a) shows the case of a momentum-independent interaction vertex ($\Gamma_1 = 0$), where the ground state degeneracy jumps from 17 ($= 2S_{\mathrm{max}} + 1$) directly to 1 at the position indicated by the arrow. Part (b) shows the case of an interaction vertex with maximal momentum-dependence $\Gamma_1 = 6/\pi$. The arrows indicate a change in the ground state degeneracy.

Fig. 6.4 (a), where the lowest eigen energies of all subspaces are plotted as a function of $v_F\pi/U$: the $S_z = 0$ subspace contains the non-degenerate ground state until at the critical point the lowest energy eigenstates of *all* subspaces form the degenerate ground state; no intermediate regime of $v_F\pi/U$ exists in which there is only a degeneracy between some of the S_z subspaces.

The reason for the instant jump in the total spin is as follows: once the Stoner criterion $v_F\pi/U > [v_F\pi/U]^{(\Gamma_1=0)}_{\text{crit.}}$ is met, the interaction energy gain $\delta E_U(S)$ associated with developing a certain spin polarization S is larger than the corresponding kinetic energy penalty $\delta E_{\mathrm{kin}}(S)$. Unlike in two or three dimensions, however, for one-dimensional systems with momentum-independent interactions, $\delta E(S) = \delta E_U(S) + \delta E_{\mathrm{kin}}(S)$ has no minimum, i.e. $\delta E(S+1) < \delta E(S)$, for all $S < S_{\mathrm{max}}$. Thus, the system instantly 'flows' to the highest possible polarization S_{max}, once the Stoner criterion is met. This is a rather common feature of one-dimensional systems with a constant interaction vertex (such as the Hubbard interaction) and can easily be observed in a variational calculation of the ground state properties (see Appendix 6.4).

The momentum-dependence of the interaction vertex ($\Gamma_1 > 0$) reduces the interaction energy gain as the spin-polarization S becomes larger. This is because for larger S, the Fermi level of the spin-up right-movers is shifted to higher momenta where the interaction is suppressed by the $S_k^{r=R}$ factors [see Eq. (6.8)]. Similarly, for the spin-up left-movers, the Fermi level is then shifted to smaller momenta, where the $S_k^{r=L}$ suppress the interaction.[7] As a result, $\delta E(S)$ develops a minimum at $S = S_{\mathrm{min}} < S_{\mathrm{max}}$, and the system is stable there. Intuitively, this may be understood on the basis of a variational calculation (see Appendix 6.4). Within exact diagonalization one finds that with $\Gamma_1 = 6/\pi$, the ground state degeneracy increases successively from 0 to $2S_{\mathrm{max}} + 1$ by first adding the lowest energy eigenstates of the $S_z = \pm 1$ subspaces to the ground space, and then the $S_z = \pm 2$ subspaces and so forth. This is shown in Fig. 6.4 (b).

If the total spin S is plotted as a function of $v_F\pi/U$, S decreases from S_{max} to 0 in steps. These steps

---

[7] Note that the increase in the interaction vertex for the spin-down electrons with lowered Fermi level is overcompensated by the suppression due to the higher Fermi level of the spin-up electrons, so that in total the interaction is reduced as S grows.

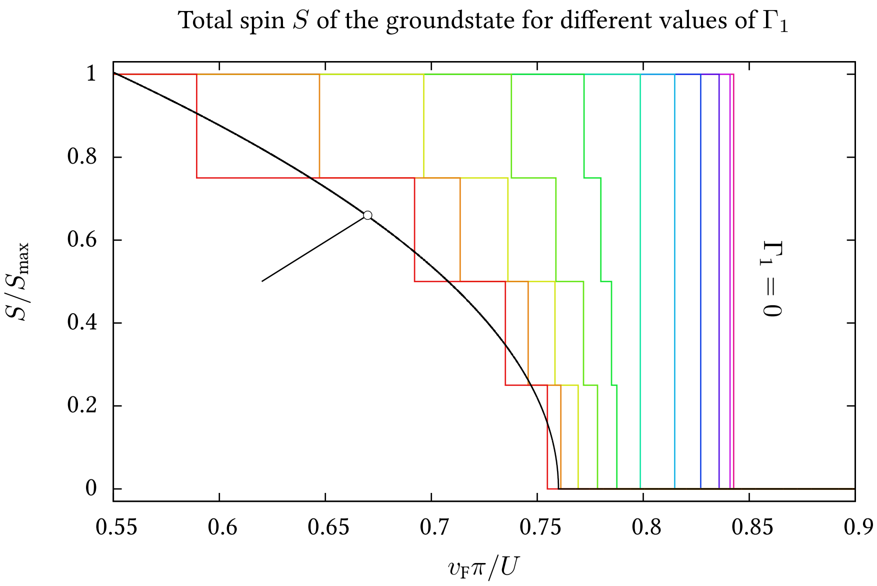

Figure 6.5.: Dependence of the spin-polarization S on $v_F\pi/U$ for different strengths of the momentum-dependence Γ_1 from $\Gamma_1 = 0$ (rightmost curve) to $\Gamma_1 = \frac{6}{\pi}$ (leftmost curve) in steps of $\Delta\Gamma_1 = \frac{6}{10\pi}$. The length of the edge is $L = 48$, $\lambda_{\text{bs}} = 1$ and $\lambda_{\text{us}} = 0$. The smooth curve is a power law fit to the plateau centers of the $\Gamma_1 = \frac{6}{\pi}$ steps with exponent $\beta = 0.5$ (see text).

correspond to the positions $v_F\pi/U$, where the degree of the ground state degeneracy changes, indicated by arrows in Fig. 6.4. For $\Gamma_1 = 0$, there is one step where the spin-polarization jumps from $S = S_{\text{max}} = N/2$ to $S = 0$, while for the maximal $\Gamma_1 = 6/\pi$, there are $N/4$ steps at each of which the spin-polarization is decreased by $\Delta S = 2$.[8] Fig. 6.5 shows these two limiting cases and how the steps evolve as Γ_1 is varied from 0 to $6/\pi$. The momentum-dependence must have a minimum strength $\Gamma_1 > \Gamma_1^c \simeq 1$, in order to break the one big spin- polarization step of height $N/2$ into many small steps of height 2. Thus, for $\Gamma_1 > \Gamma_1^c$ there is a regime of weak edge magnetism, meaning that the total spin S of the ground state is smaller than the maximal spin S_{max}, in addition to the usual saturated edge magnetism for small $v_F\pi/U$ (i.e. $S = S_{\text{max}}$) and the Luttinger liquid regime for large $v_F\pi/U$ with $S = 0$. Figure 6.6 shows a diagram in which the phase boundaries between the Luttinger liquid (LL), the saturated edge magnetism (SEM) and the novel weak edge magnetism (WEM) are shown for different system sizes $N = 8, 12, 16$.

Note that the non-zero Γ_1^c found in the exact diagonalization reveals a weakness of the fermionic mean-field theory in which this minimum momentum dependence, above which a WEM regime appears, is zero (see Appendix 6.4). A non-zero Γ_1^c means that the small momentum-dependencies which always follow from a dependence of the Bloch wave functions in usual one-dimensional conductors on the momentum are not necessarily sufficient to stabilize the weak edge magnetism; the momentum-dependence of the interaction vertex must be sufficiently strong for this.

In the limit $L \to \infty$, which cannot be accessed within exact diagonalization, of course, S/S_{max} becomes a smooth function of $v_F\pi/U$. We approximate this smooth function by a power law

$$S/S_{\text{max}} \sim \left[\left(\frac{v_F\pi}{U}\right)_{\text{crit.}} - \frac{v_F\pi}{U}\right]^{\beta}. \tag{6.18}$$

Fermionic mean-field theory (see Appendix 6.4) predicts $\beta = 0.5$. Because the exact diagonalization study is limited to small systems $N \leq 16$, it is difficult to obtain a decent estimate of the exact exponent β within this work. Fitting the edge state limit of the generalized model to the center of the plateaus of the $N = 16$ results

---

[8] This decrease of 2 in S is due to the contribution of the left- and right-moving branch to the spin-polarization: each branch contributes one spin flip.

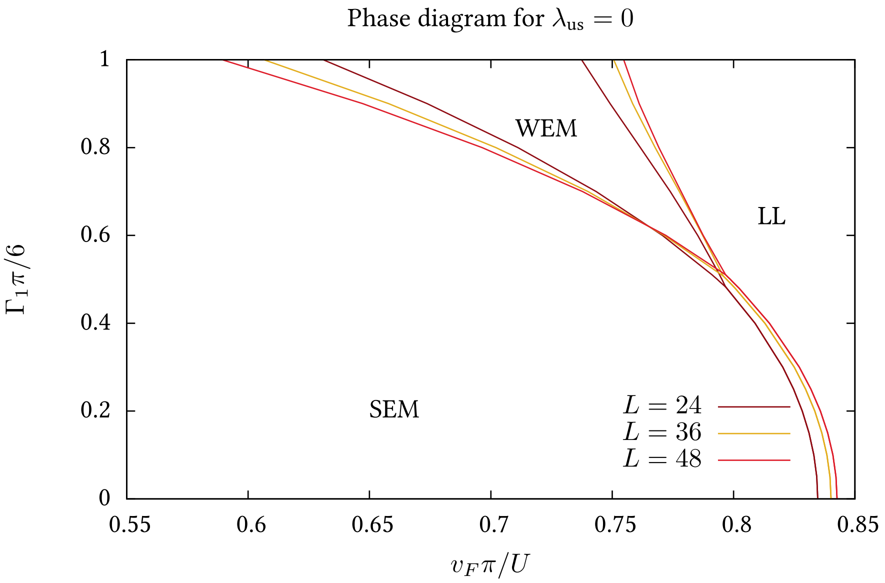

Figure 6.6.: Phase diagram for lengths $L = 24$, $L = 36$ and $L = 48$. For small velocity dependence Γ_1 of the interaction, only the Luttinger liquid (LL) phase and the saturated edge magnetism (SEM) phase exist, whereas above the critical value of $\Gamma_1 = \Gamma_1^c$ the weak edge magnetism (WEM) phase appears.

of the exact diagonalization, we obtain $0.44 < \beta < 0.61$, dependent on how many plateaus are included in the fit. The critical point $\left(\frac{v_F\pi}{U}\right)_{\text{crit.}} \simeq 0.760$ for this fit is obtained by extrapolating the rightmost step from the data sets $N = 4, 8, 12, 16$ to $N = \infty$.

Interestingly, Γ_1 not only affects the order of the transition but also the critical $v_F\pi/U$. This is also not correctly predicted by the mean-field approach (see Appendix 6.4), which, independently of Γ_1, finds $v_F\pi/U = 1$ to be the critical point. For small Γ_1 and $N = 16$ the exact diagonalization gives

$$\left[\frac{v_F\pi}{U}\right]_{\text{crit.}} \simeq 0.84 - 0.17\Gamma_1^2. \tag{6.19}$$

For the maximal $\Gamma_1 = 6/\pi$, the position of the leftmost step can be calculated by exact diagonalization for very large systems.[127] We performed calculations for system sizes up to $L = 180$ in order to extrapolate this step position. Within the limits of the accuracy of this extrapolation, the critical point $v_F\pi/U = 0.5 \pm 0.001$ between the SEM and the WEM regime coincides with the mean-field prediction (see Appendix 6.4). This extrapolation to the thermodynamic limit, in combination with the extrapolation of the critical point between the WEM and the LL regime, is a strong evidence for the existence of the WEM phase for $0.5 \leq v_F\pi/U \leq 0.760$ in the thermodynamic limit.

For completeness we note that our exact diagonalization analysis shows that a SEM phase also exists in the general model with umklapp scattering $\lambda_{\text{us}} = 1$ if $\Gamma_1 > 0$. However even for $\Gamma_1 = 6/\pi$ there is no weak edge magnetism phase between the Luttinger liquid and the saturated edge magnetism as long as $\lambda_{\text{us}} = 1$.

6.3.2. The relevance of backscattering

The backscattering Hamiltonian H_1^{bs} is important for the SU(2) invariance of the Hamiltonian. It is easily seen that only for $\lambda_{\text{bs}} = 1$ the SU(2) symmetry is preserved. At real graphene edges, of course, the backscattering cannot be tuned experimentally. Nevertheless it is interesting to study the consequences of a suppression of H_1^{bs} since in a bosonization treatment of the generalized model H_1^{bs} translates to a sine-Gordon term which is difficult to analyze. Therefore, some insight into the relevance of H_1^{bs} is helpful from a theoretical point of

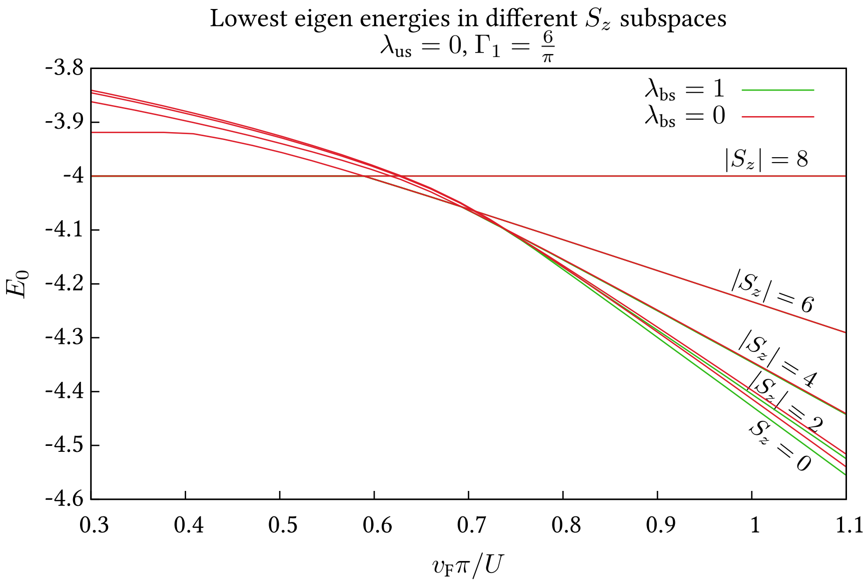

Figure 6.7.: The lowest eigen energies of different S_z subspaces with (blue) and without (green) backscattering calculated for an edge of length $L = 48$. The broken SU(2) symmetry in the case of $\lambda_{\text{bs}} \neq 1$ lifts the degeneracy of the ground states in the different S_z subspaces.

view. Following the philosophy of the previous subsection, we restrict the discussion to the spin polarization properties of the ground state. The analysis of more complicated observables such as spin-spin correlation functions is beyond the scope of this work and will be discussed in another paper.

Fig. 6.7 compares the lowest eigen energies of the S_z subspaces from calculations with and without backscattering. The most striking feature of the suppression of backscattering is the lifting of the ground state degeneracy in the SEM regime. This effect is easily understood by noting that the very reason for the ground state degeneracy in the $\lambda_{\text{bs}} = 1$ case was the SU(2) symmetry, which, however, is broken for $\lambda_{\text{bs}} < 1$. Interestingly, the lifting of the degeneracy is such that the lowest energy states of the subspaces with highest $|S_z|$, in the ground space for $\lambda_{\text{bs}} = 1$, form the ground state for $\lambda_{\text{bs}} < 1$. This means that suppressing backscattering introduces an Ising anisotropy along the spin quantization axis chosen in the definition of the model.

Apart from this degeneracy lifting, the evolution of the ground state properties with $v_F\pi/U$ is very similar for calculations with and without backscattering. The positions of the highest spin-polarization steps are practically unchanged. Only at the steps close to the phase transition between the LL and the WEM regime, a deviation of the $\lambda_{\text{bs}} = 0$ results from the $\lambda_{\text{bs}} = 1$ results can be observed. A handwaving explanation of this behavior can be given in terms of the bosonization analysis of the WEM regime in Ref. [119]. As soon as the Fermi levels for the up-spin electrons and the down-spin electrons are split, the backscattering process for electrons right at the Fermi surface is forbidden because it is not momentum-conserving. Thus, in order to conserve momentum, the electrons are forced to scatter to higher energies if there is a non-zero spin-polarization. This mechanism suppresses the backscattering. In the bosonization language the backscattering Hamiltonian acquires a spatially oscillating phase which makes the corresponding operator irrelevant in the renormalization group. Thus in the WEM regime, not too close to the critical point, H_1^{bs} is suppressed and does not give an important contribution.

Close to the critical point, however, Fig. 6.7 indicates that H_1^{bs} becomes more important. This observation is consistent with the qualitative bosonization argument: Close to the critical point the phase oscillations in the bosonic backscattering Hamiltonian get slower until they completely disappear at the critical point.

6.4. Variational analysis of the generalized model

We calculate the magnetic ground state properties of the generalized model within a fermionic mean-field approximation. It is assumed that only the averages $\left\langle c^\dagger_{kr\sigma} c_{kr\sigma} \right\rangle$ are non-zero, so that the umklapp Hamiltonian H_1^{us} and the backscattering Hamiltonian H_1^{bs} drop out of the mean-field treatment. The resulting non-interacting Hamiltonian is diagonal in the momentum k, in the direction of motion r and in the z-spin projection, so that the mean-field theory is equivalent to a variational ansatz based on the trial wave function

$$|M\rangle = \prod_{\sigma} \left[\prod_{k<k_{F\sigma}} c^\dagger_{kR\sigma} \right] \left[\prod_{k>-k_{F\sigma}} c^\dagger_{kL\sigma} \right] |0\rangle \tag{6.20}$$

with an asymmetric occupation of spin-up and spin-down states. The variational parameter $M \in [0,1]$ is related to the spin-dependent Fermi levels by

$$k_{F\sigma} = \sigma \frac{\pi}{6} M, \tag{6.21}$$

and to the spin-polarization S, used in Sect. 6.3, by $M = S/S_{\text{max}}$. For finite size systems, as discussed in the main part of this chapter, the Fermi level cannot be varied continuously so that also M is a discrete variable in this case. However, within mean-field theory it is easy to perform the calculations in the thermodynamic limit, so that we will consider M to be a continuous variable and interpret it as the magnetization order parameter.

The variational energy $E(M)$ is easily calculated from the Hamiltonian H in Eq. (6.12)

$$E(M) = \langle M| H |M\rangle = \frac{1}{36}(\pi v_F - U)M^2 + \Gamma_1^2 \frac{U\pi^2}{5184} M^4. \tag{6.22}$$

For $U < \pi v_F$, the minimum of $E(M)$ is at $M = 0$, while for $U > \pi v_F$ the mean-field ground state has a finite magnetization

$$M = \min \left[\frac{\sqrt{72}}{\pi \Gamma_1} \sqrt{1 - \frac{v_F \pi}{U}}, 1 \right] \tag{6.23}$$

Note that by definition the magnetization cannot become larger than 1. From Eq. (6.23) it becomes obvious that a non-zero momentum-dependence Γ_1 is required to stabilize the regime of weak edge magnetism. For $\Gamma_1 = 0$, the magnetization would jump from 0 to 1 at the critical point $U = v_F \pi$.

The existence of the weak edge magnetism can be traced back to the M^4 term in Eq. (6.22) which is generated by the momentum-dependence Γ_1 of the interaction vertex. In dimensions higher than one, such M^4 terms emerge also from momentum-independent interactions or directly from the kinetic energy, so that at least on the mean-field level $\Gamma_1 > 0$ is required for the stabilization of weak ferromagnetism only in one dimension.

6.5. Exact diagonalization of the direct model

The direct model Hamiltonian H^{dm} defined by Eqs. (6.4 - 6.5) and the edge state limit of the generalized model Hamiltonian H [Eq. (6.12) with $\lambda_{\text{bs}} = 1$, $\lambda_{\text{us}} = 0$ and $\Gamma_1 = 6/\pi$] are not exactly equal, as the general model linearizes the single particle dispersion and replaces the factors $\mathcal{N}_p$ by the approximation S^r_k. Nevertheless, the most important properties of graphene edge states, i.e. the momentum-dependence of the interaction vertex and the absence of umklapp scattering, are properly described by both, the direct model and the general model in the edge state limit.

In this section, we check that the direct model has qualitatively the same magnetic properties as the general model in the edge state limit. In Fig. 6.8, we present the spin-polarization S as a function of Δ/U, obtained from the exact diagonalization of the direct model. The bandwidth parameter Δ of the direct model corresponds to the Fermi velocity v_F of the general model.

Clearly, for larger Δ/U, which corresponds to the parameter $v_F\pi/U$ in the generalized model, we obtain a Luttinger liquid phase with a ground state of total spin $S = 0$. An intermediate regime with weak edge magnetism exists, where the total spin of the ground state $S < S_{\text{max}}$ is not maximal. As in the exact diagonalization analysis of the general model, only some of the lowest eigen energies in different S_z subspaces are degenerate and form the ground state. For small Δ/U, the saturated edge magnetism phase is reached and the spin of the ground state is maximal, i.e., the lowest eigen energies in *all* S_z subspaces are degenerate.

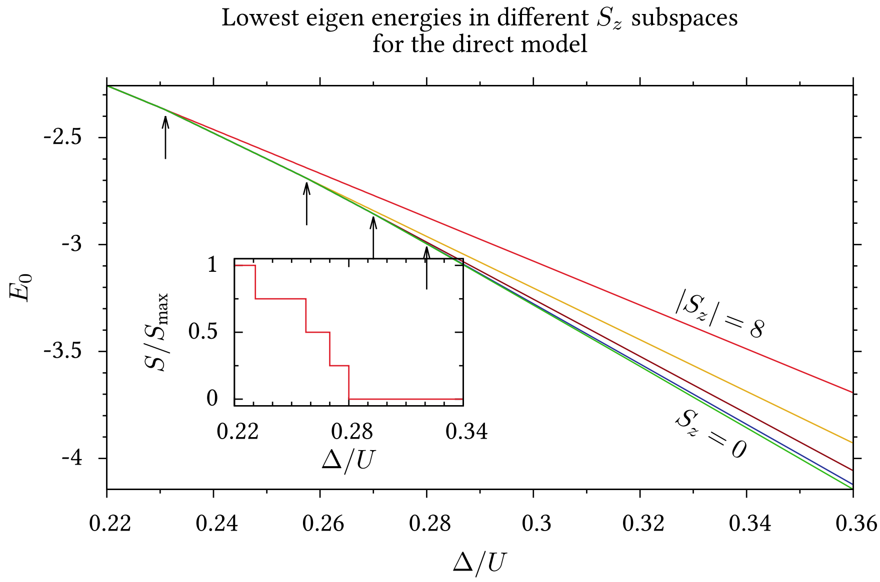

Figure 6.8.: Lowest eigen energies in the $S_z = 0, \pm 2, \pm 4, \pm 6, \pm 8$ subspaces (from bottom to top) for the direct model calculated for an edge of length $L = 48$. The inset shows the dependence of the spin-polarization S as a function of Δ/U determined from the degeneracy of the ground state.

Note that the energy of the fully spin polarized eigenstate of the direct model Hamiltonian has a finite slope (see Fig. 6.8). This is because the direct model lacks a symmetry of H_0 of the generalized model leading to $E_0^{S_{\text{max}}}(v_F) = \text{const}$ (cf. Fig. 6.4). As only the degeneracy of the lowest eigen energies are important, but not their absolute values, this difference does not have any physical consequences.

6.6. Discussion

On the basis of a generalized class of effective models for one-dimensional interacting electrons we have studied the magnetic properties of a graphene zigzag edge. Using exact diagonalization we confirmed the existence of three phases within these models, namely the saturated edge magnetism phase which is present at normal graphene edges, the Luttinger liquid phase which appears for edge states with strongly enhanced bandwidth, and an intermediate regime of weak edge magnetism. The latter phase is a realization of a ferromagnetic Luttinger liquid, a one-dimensional itinerant ferromagnet. We presented evidence that the transition between the Luttinger liquid and the weak edge magnetism phase becomes a second order quantum phase transition in the limit of long edges.

Beyond the identification of the magnetic properties of edge states, we examined the question why electrons in one-dimensional edge states have such a rich phase diagram with two types of ferromagnetic ground states, while usual one-dimensional electrons do not show any ferromagnetism. In view of the Lieb-Mattis theorem,[120] which actually forbids a spin-polarized ground state for interacting electrons in one dimension, this question becomes even more pressing.

A closer inspection of the edge state model, which was derived directly from the graphene crystal structure [119], revealed two unusual features of edge states which cannot be found in other one-dimensional electronic systems, such as quantum wires, for instance. These are (a) the total absence of umklapp processes in the effective electron-electron interaction, independently of the filling factor, and (b) a strong momentum dependence of the effective interaction vertex. Each of these features precludes the applicability of the Lieb-Mattis theorem. The momentum-dependence gives rise to a complicated non-local interaction, which cannot be written as $V(x,y)\hat{n}(x)\hat{n}(y)$, with $\hat{n}(x)$ an electron density operator, as it is required for the Lieb-Mattis theorem. And even in the limit of momentum-independent interactions ($\Gamma_1 = 0$ in the general model) the suppressed umklapp scattering makes the reformulation as a density-density interaction in real space impossible. In order to further track down the particular consequences of these special features for the magnetic properties of graphene edges, we replenished the direct model with a tunable umklapp scattering term and replaced the interaction vertex by a generalized vertex function in which the momentum-dependence can be switched on and off.

The study of this generalized model, which can be tuned continuously between its edge state limit and a regime in which it describes normal one-dimensional metals, revealed the significance of the two edge state features: the absence of umklapp processes is responsible for the existence of a spin-polarized ground state, and the strong momentum dependence of the interaction vertex stabilizes a regime of weak edge magnetism and gives rise to a second order phase transition between the paramagnetic Luttinger liquid and the ferromagnetic Luttinger liquid.

It is interesting to note that the stabilization of the weak edge magnetism phase seems to be very robust against changes in the details of the interaction vertex function. Apparently it is only important that the vertex is suppressed as one of the four momenta of the participating fermions gets close to one of the Dirac points. The exact functional form of this suppression, however, seems to be irrelevant, since the qualitative behavior of the spin-polarization did not depend on whether we used the interaction vertex of the direct model or the interaction vertex of the generalized model with maximal momentum dependence. These two vertex functions have in common that they vanish as one of the momenta approaches a Dirac point. However, their functional forms are very different.

Finally we note that one-dimensional itinerant magnetism has also been studied in Hubbard chains with an additional second neighbor hopping,[128, 129] showing that it is indeed possible to define one-dimensional models which, at first sight, seem to comply with the prerequisites of the Lieb-Mattis theorem, but nevertheless have a high spin ground state. The physical picture behind the model discussed in Refs. [128, 129], however, is much different from the present work. Interestingly, the sign of the hopping amplitude to the nearest neighbor must be different from the sign of the next-nearest neighbor hopping for the system to have a ferromagnetic ground state.

Also, we emphasize that the model discussed here is the low-energy theory of a realistic system which may be studied experimentally. It has been derived in direct line from a two-dimensional lattice model of graphene/graphane interfaces.[119, 123]

7. Conclusion

The present thesis is an attempt of portraying three large projects as examples of computational research in strongly correlated electron systems. For most topics, special care has been taken to provide a pedagogical presentation so that an interested reader is equipped with a sufficient level of detail to actually use the method and further develop it on his own. Furthermore a methodologically intriguing way of tackling problems has always been preferred.

A rather general introduction to the CT-INT method including implementation details, mathematical as well as numerical foundations and tricks has been given in chapter 3 as this method is central to the problems addressed in this thesis.

In chapter 4, the treatment of two particle quantities represented by $G_4^\perp(Q; K, P)$ in CT-INT has been discussed in great detail. The goal was the reliable extraction of dynamical susceptibilities from $G_4^\perp(Q; K, P)$, which is of crucial importance in DCA. We presented a method for summing out the internal momenta and fermionic frequencies K and P without the introduction of a systematic error and show how this method can be carefully checked against exactly known results from exact diagonalization. We argue that it is important to eliminate the cutoff error to avoid an incorrect asymptotic behaviour of dynamical susceptibilities on the imaginary (bosonic) frequency axis. Our data for $G_4^\perp$ show that the frequency structure is reproduced in every momentum sector and differs only by momentum dependent weights of the different features.

In addition to the discussion of lattice calculations, we have used the CT-INT extensively for the study of a correlated Josephson junction in chapter 5. We have shown that the method is extremely well suited for this kind of problem and that the introduction of complex phase factors stemming from superconducting Green's functions do not introduce any further problems. The non spin diagonal Green's functions can be incorporated in the formalism in a natural way. The in depth study of the system leads to a complete picture of the mechanism driving the π phase shift of the Josephson current by means of a first order quantum phase transition from a singlet to a doublet phase reflected by the formation of a local moment on the correlated quantum impurity.

We have been able to develop a strategy for the extraction of experimental model parameters from the Josephson current and normal state conductance measurement of a real experiment and could reproduce experimental data from a model calculation — thus proving the applicability of the model for the description of a single well carbon nanotube coupled to superconducting leads. This allowed us to improve existing data analysis strategies based on the evaluation of Coulomb diamonds — which are strictly speaking not applicable in the presented case as Kondo correlations are important. Furthermore Kondo correlations could be detected by the calculation of the single particle spectral function.

A third project is the study of edge magnetism in graphene. Using the Lanczos method for the calculation of a finite size Hamiltonian in addition to the introduction of a generalized model for the edge states, we discussed the various effects of different terms in the Hamiltonian on the magnetic properties of the ground state.

The variety of different methods applicable for the study of strongly correlated systems should give the reader an idea of different methodological approaches to tackle this class of problems.

A. Appendix

In this appendix, we present fragments of unpublished or yet to be published work. Section A.1 is of particular documentary importance, as it documents the status of work done on the application of the Legendre polynomial basis for two particle Green's functions within the framework of CT-INT. This project has been abandoned in the mean time due to severe performance issues of the approach as will be explained below. If the reader plans to further explore this topic, this section in addition to reference [50] should provide a solid starting point and give an idea of difficulties one might face without having the ambition of being complete.

In section A.2 a pedagogical introduction of the analytical continuation of the self energy is given. While the idea is not novel, the author has found it worthwhile to do the derivation on his own. Details on the application of the method to the Single impurity Kane-Mele model are given and a condensed version of this work will be part of an upcoming article [130].

Finally, some notes on the generation of test data with an analytically known covariance matrix are provided. This has proved useful for sanity tests of data analysis codes in general and the bootstrap code in particular.

A.1. Efficient representation of two particle quantities: Polynomial basis

Whenever we calculate two particle Green's functions $G_4(Q;K,P)$, we realize that the information contained in the huge tensor is not stored in an efficient way. Especially the high frequency part of $G_4(Q;K,P)$ decays arithmetically and the high frequency part has to be partly calculated for a reliable extrapolation to infinite cutoff frequency.

Therefore, we make use of an idea by Lewin Boehnke et al. [50] namely the representation of $G_4(Q;K,P)$ in a mixed basis which is based on the representation of an imaginary time Green's function in terms of Legendre polynomials. Here, we will restrict ourselves to a problem that has all the symmetries of the Hubbard model. This will allow some important simplifications.

The idea is particularly intriguing as Lewin Boehnke argued that two particle quantities in a mixed[1] basis decay exponentially and therefore sums over the internal (Legendre) indices should converge for a finite number of indices without the need of extrapolation as in the case of frequencies discussed in chapter 4.

While Boehnke et al. showed the feasibility of the approach for an impurity problem using the CT-HYB algorithm, it remained unclear how well it can be transported to a cluster problem, for which the application of CT-INT is better suited. The fragment presented here discusses the difficulties we faced during the attempt of adapting the idea for a cluster calculation in CT-INT and tries to provide a conclusion judging the feasability.

A.1.1. Calculating $G_4(Q;L,L')$ in the spin channel in CT-INT directly in the Legendre Basis

We define $Q = \{\mathbf{Q}, \mathrm{i}\nu_m\}$ with a cluster (lattice) momentum $\mathbf{Q}$ indicated by a bold face upper (lower) case letter and a bosonic Matsubara frequency $\mathrm{i}\nu_m$. Analogously, let us define $L = \{\mathbf{K}, l\}$ as well as $L' = \{\mathbf{P}, l'\}$ with cluster momenta $\mathbf{K}$ and $\mathbf{P}$ and Legendre polynomial indices l and l'. Legendre polynomial indices will only replace fermionic Matsubara frequencies $\mathrm{i}\omega_n$ and $\mathrm{i}\omega'_n$.

---

[1] The bosonic transfer frequency is kept, while the two fermionic frequencies are transformed into the basis of Legendre polynomials and thus replaced by Legendre indices l and l'.

The transformation for the single particle Green's function from Matsubara frequencies to the Legendre basis can be written in the following form:

$$G_2(K) = \sum_{l=0}^{\infty} T_{n,l} G_2(L) \quad \text{and} \quad G_2(L) = \sum_{n=-\infty}^{\infty} T^*_{n,l} G_2(K). \tag{A.1}$$

The transformation matrix is given by

$$T_{n,l} = \frac{\sqrt{2l+1}}{\beta} \int\limits_0^\beta \mathrm{d}\tau \, \mathrm{e}^{\mathrm{i}\omega_n \tau} P_l(x(\tau)) = (-1)^n \mathrm{i}^{l+1} \sqrt{2l+1} \, j_l\left(\frac{2n+1}{2}\pi\right). \tag{A.2}$$

Here, $x(\tau) = 2\tau/\beta - 1$ and $j_l(x)$ denotes the spherical Bessel function of order l.
The transformation $T_{n,l}$ is unitary, as

$$\sum_{n=-\infty}^{\infty} T^*_{n,l} T_{n,l'} = \delta_{l,l'} \quad \text{and} \quad \sum_{l=0}^{\infty} T_{n,l} T^*_{n',l} = \delta_{n,n'}. \tag{A.3}$$

The two identities (A.3) can be shown by virtue of the identities[2]

$$\int_{-1}^{1} \mathrm{d}x \, P_l(x) P_{l'}(x) = \frac{2}{2l+1} \delta_{l,l'} \quad \text{and} \quad \sum_{l=0}^{\infty} (2l+1) P_l(x) P_l(y) = 2\delta(x-y). \tag{A.4}$$

We also note the particular property of the transformation matrix element $T_{n,l}$

$$T_{-n-1,l} = T^*_{n,l} = (-1)^{l+1} T_{n,l}. \tag{A.5}$$

Measurement of $G_4^{\perp}(Q; K, P)$ in CT-INT

In order to understand how $G_4^{\perp}(Q; L, L')$ should be calculated most efficiently, let us begin with the equations for the calculation of $G_4^{\perp}(Q; K, P)$ detailed in section 4.4.1.

At this point, one might be inclined to think that a transformation of the accumulation equation (4.42) to the Legendre basis is already possible. Unfortunately, this is not a good idea, as the involved sums over Matsubara frequencies cannot be carried out analytically. Therefore, we have to manipulate the equations in another way. Let us multiply out the accumulation equation to get a better understanding of how this should be done. To keep the equations readable, we define $X_i = (\tau_i, \mathbf{X}_i)^T$ for the vertex i. We also define a scalar product with the metric $g = \mathrm{diag}(1, -\mathbf{1})$ yielding $K \cdot X_i = K^T g X_i = \omega_n \tau_i - \mathbf{K}^T \mathbf{X}_i$. Hence, equation (4.43) reads:

$$\langle\langle \bar{c}_{\sigma,K} c_{\sigma,P} \rangle\rangle_{C_n} = \delta_{K,P} G_2^0(K) - \frac{1}{\beta N} G_2^0(K) G_2^0(P) \sum_{r,s} \mathrm{e}^{\mathrm{i}(K \cdot X_r - P \cdot X_s)} \left(M_\sigma^{-1}\right)_{r,s}. \tag{A.6}$$

Then,

$$\begin{aligned}
\langle\langle \bar{c}_{\uparrow,K} c_{\uparrow,P-Q} \rangle\rangle_{C_n} \langle\langle \bar{c}_{\downarrow,P} c_{\downarrow,K+Q} \rangle\rangle_{C_n} &= \delta_{P,K+Q} G_2^0(K) G_2^0(P) \\
&- \frac{1}{\beta N} \delta_{K,P-Q} G_2^0(K) G_2^0(P) G_2^0(K+Q) \sum_{r,s} \mathrm{e}^{\mathrm{i}(P \cdot X_r - (K+Q) \cdot X_s)} \left(M_\downarrow^{-1}\right)_{r,s} \\
&- \frac{1}{\beta N} \delta_{P,K+Q} G_2^0(P) G_2^0(K) G_2^0(P-Q) \sum_{r,s} \mathrm{e}^{\mathrm{i}(K \cdot X_r - (P-Q) \cdot X_s)} \left(M_\uparrow^{-1}\right)_{r,s} \\
&+ \frac{1}{\beta^2 N^2} G_2^0(K) G_2^0(P-Q) G_2^0(P) G_2^0(K+Q) \times \\
&\times \sum_{r,s,r',s'} \mathrm{e}^{\mathrm{i}(K \cdot X_r - (P-Q) \cdot X_s + P \cdot X_{r'} - (K+Q) \cdot X_{s'})} \left(M_\uparrow^{-1}\right)_{r,s} \left(M_\downarrow^{-1}\right)_{r',s'}.
\end{aligned} \tag{A.7}$$

---

[2] `http://functions.wolfram.com/05.03.21.0006.01` and `http://functions.wolfram.com/05.03.23.0009.01`

Let us now rewrite this equation in the following way:

$$\beta N \langle\langle G_4^{\perp}(Q;K,P)\rangle\rangle_{C_n} = A(Q;K,P) + \sum_{K',K''} B(Q;K,K')C(Q;K',K'')D(Q;K'',P). \tag{A.8}$$

Apparently, we can choose the matrices $A(Q)$, $B(Q)$, $C(Q)$ and $D(Q)$ in the following way:

$$B(Q;K,K') = \frac{1}{\beta N}\delta_{K,K'} G_2^0(K)G_2^0(K+Q). \tag{A.9}$$

$$C(Q;K',K'') = \sum_{r,s,r',s'} \mathrm{e}^{\mathrm{i}(K'\cdot X_r - (K''-Q)\cdot X_s + K''\cdot X_{r'} - (K'+Q)\cdot X_{s'})} \left(M_{\uparrow}^{-1}\right)_{r,s} \left(M_{\downarrow}^{-1}\right)_{r',s'}. \tag{A.10}$$

$$D(Q;K'',P) = \frac{1}{\beta N}\delta_{P,K''} G_2^0(P)G_2^0(P-Q). \tag{A.11}$$

Thus, $A(Q;K,P)$ is uniquely defined by the first three terms of equation (A.7). The transformation to the Legendre basis is now straightforward:

$$T_{K,L} = \delta_{\mathbf{K},\mathbf{P}} T_{n,l}, \text{ with } \sum_L T^*_{K,L} T_{P,L} = \delta_{K,P}. \tag{A.12}$$

Hence, we have

$$\beta N \langle\langle G_4^{\perp}(Q;L,L')\rangle\rangle_{C_n} = A(Q;L,L') + \sum_{L'',L'''} B(Q;L,L'')C(Q;L'',L''')D(Q;L''',L'), \tag{A.13}$$

with $Z(Q;L,L') = \sum_{K,P} T^*_{K,L} Z(Q;K,P) T_{P,L'}$, where $Z \in \{A,B,C,D\}$.

Now, we can treat the transformation of the different terms separately. First, we note that only $C(Q;L,L')$ has to be accumulated during the CTQMC simulation. $B(Q;L,L')$ and $D(Q;L;L')$ do not depend on the QMC configuration and may be calculated in the very end of the Monte Carlo simulation. $A(Q;L,L')$ seems to depend on the configuration of vertices in the Markov chain. This dependence, however, is only on the one particle level, which can be assumed to be known at a stage of the calculation at which we are interested in two particle quantities. Therefore, the Monte Carlo average of $A(Q;K,P)$ can be calculated exactly using the identity

$$\left\langle \frac{1}{\beta N} G_2^0(K)G_2^0(P) \sum_{r,s} \mathrm{e}^{\mathrm{i}(K\cdot X_r - P\cdot X_s)} \left(M_\sigma^{-1}\right)_{r,s} \right\rangle = \delta_{K,P}\left[G^0_{2,\sigma}(K) - G_{2,\sigma}(K)\right]. \tag{A.14}$$

Note again, that we used $G^0_{2,\uparrow}(K) = G^0_{2,\downarrow}(P)$ here to simplify the equations. In situations, where we have a magnetic field which breaks this symmetry, the equations have to be derived including the spin index.

$$\bar{A}(Q;K,P) = \langle A(Q;K,P)\rangle = \delta_{P,K+Q}\left[G_2^0(K)G_2(P) + G_2^0(P)G_2(K) - G_2^0(P)G_2^0(K)\right]. \tag{A.15}$$

In the Legendre basis, we obtain:

$$\begin{aligned}\bar{A}(Q;L,L') &= \sum_{K,P} T^*_{K,L}\delta_{P,K+Q}\left[G_2^0(K)G_2(P) + G_2^0(P)G_2(K) - G_2^0(P)G_2^0(K)\right] T_{P,L'} = \\ &= \sum_K T^*_{K,L} T_{K+Q,L'}\left[G_2^0(K)G_2(K+Q) + G_2^0(K+Q)G_2(K) - G_2^0(K+Q)G_2^0(K)\right].\end{aligned} \tag{A.16}$$

For $B(Q;L,L')$, we have:

$$B(Q;L,L') = \sum_{K,P} T^*_{K,L}\frac{1}{\beta N}\delta_{K,P}G_2^0(K)G_2^0(K+Q)T_{P,L'} = \sum_K \frac{1}{\beta N} T^*_{K,L} T_{K,L'} G_2^0(K)G_2^0(K+Q). \tag{A.17}$$

and for $D(Q;L,L') = B(-Q;L,L')$:

$$D(Q;L,L') = \sum_{K,P} T^*_{K,L} \frac{1}{\beta N} \delta_{P,K''} G^0_2(P) G^0_2(P-Q) T_{P,L'} = \sum_{K} T^*_{K,L} T_{K,L'} \frac{1}{\beta N} G^0_2(K) G^0_2(K-Q). \tag{A.18}$$

Accumulation of $C(Q;L,L')$ Apparently, we only need to calculate $C(Q;L,L')$ during the QMC, similarly to the method we use in the case of the frequency representation discussed in chapter 4. Let us write down the equations in the Legendre basis:

$$C(Q;L,L') = \sum_{K,P} T^*_{K,L} \sum_{r,s,r',s'} \mathrm{e}^{\mathrm{i}(K\cdot X_r - (P-Q)\cdot X_s + P\cdot X_{r'} - (K+Q)\cdot X_{s'})} \left(M^{-1}_{\uparrow}\right)_{r,s} \left(M^{-1}_{\downarrow}\right)_{r',s'} T_{P,L'}. \tag{A.19}$$

We will shortly see that carrying out the sums over K and P is possible but requires the evaluation of $P_l(x(\tau))$ for $\tau \in [-\beta, \beta]$, as this is the codomain of $\tau_s - \tau'_r$. Strictly, this is not allowed and we have to extend the definition of $P_l(x(\tau))$ in a consistent way. Most importantly, we require $G(-\tau) = -G(\beta - \tau)$. Written in terms of Legendre coefficients, this yields:

$$G(-\tau) = \frac{\sqrt{2l+1}}{\beta} \sum_{l\geq 0} \tilde{P}_l(x(-\tau)) G_l \overset{!}{=} -G(\beta-\tau) = -\frac{\sqrt{2l+1}}{\beta} \sum_{l \geq 0} P_l(x(\beta - \tau)) G_l. \tag{A.20}$$

It is clear that the definition

$$\tilde{P}_l(x(\tau)) = \begin{cases} P_l(x(\tau)) & \text{if } \tau \in [0,\beta] \\ -P_l(x(\beta+\tau)) & \text{if } \tau \in [-\beta, 0] \end{cases} \tag{A.21}$$

will fulfill the requirement. We shall use $\tilde{P}_l$ from now on. Note that using this result, we can rewrite $T_{n,l}$ in the following way:

$$T_{n,l} = \frac{\sqrt{2l+1}}{2\beta} \int\limits_{-\beta}^{\beta} \mathrm{d}\tau\, \mathrm{e}^{\mathrm{i}\omega_n \tau} \tilde{P}_l(x(\tau)). \tag{A.22}$$

Let us now reduce equation (A.19) analytically as far as possible, splitting the calculation in two steps:

$$\begin{aligned} \sum_{P} \mathrm{e}^{-\mathrm{i}P(X_s - X_{r'})} T_{PL'} &= \sum_{p,\mathrm{i}\omega_n} \mathrm{e}^{-\mathrm{i}\omega_n(\tau_s - \tau_{r'})} \mathrm{e}^{\mathrm{i}p(\mathbf{x_s}-\mathbf{x_{r'}})} \delta_{\mathbf{p},\mathbf{l'}} \frac{\sqrt{2l'+1}}{2\beta} \int_{-\beta}^{\beta} \mathrm{d}\tau\, \mathrm{e}^{\mathrm{i}\omega_n\tau} \tilde{P}_{l'}(x(\tau)) \\ &= \frac{\sqrt{2l'+1}}{2}\, \mathrm{e}^{\mathrm{i}\mathbf{l'}(\mathbf{x_s}-\mathbf{x_{r'}})}\, \tilde{P}_{l'}(x(\tau_s - \tau_{r'})). \end{aligned} \tag{A.23}$$

Here, we used $\sum\limits_{\mathrm{i}\omega_n} \mathrm{e}^{\mathrm{i}\omega_n\tau} = \beta\delta(\tau)$. Performing the same calculation for the second term of the same form, we get:

$$\sum_{K} T^*_{KL} \mathrm{e}^{\mathrm{i}K(X_r - X'_s)} = \mathrm{e}^{-\mathrm{i}\mathbf{l}(\mathbf{x_r}-\mathbf{x_{s'}})} \frac{\sqrt{2l+1}}{2} \tilde{P}_l(x(\tau_r - \tau_{s'})). \tag{A.24}$$

Consequently, we obtain:

$$\begin{aligned} C(Q;L,L') = \sum_{r,s,r',s'} & \mathrm{e}^{\mathrm{i}Q(X_s - X_{s'})} \left(M^{-1}_{\uparrow}\right)_{r,s} \left(M^{-1}_{\downarrow}\right)_{r',s'} \frac{\sqrt{(2l+1)(2l'+1)}}{4} \times \\ & \times \mathrm{e}^{\mathrm{i}[\mathbf{l'}(\mathbf{x_s}-\mathbf{x_{r'}}) - \mathbf{l}(\mathbf{x_r}-\mathbf{x_{s'}})]} \tilde{P}_l(x(\tau_r - \tau_{s'})) \tilde{P}_{l'}(x(\tau_s - \tau_{r'})) \end{aligned} \tag{A.25}$$

As the imaginary times τ_r and τ_s of the vertices in the CT-INT live on the interval $\tau_r, \tau_s \in [0, \beta]$, we have to evaluate the antisymmetrized Legendre Polynomials $\tilde{P}_l(x(\tau))$ for $\tau \in [-\beta, \beta]$.

In order to efficiently perform these nested loops in a numerical calculation, we rewrite $C(Q;L,L')$ in the following way by first noting that $\tilde{P}_l(x(\tau)) = \mathrm{sgn}(\tau) P_l\left(\frac{2\tau}{\beta} - \mathrm{sgn}(\tau)\right)$:

$$C(Q;L,L') = \frac{\sqrt{(2l+1)(2l'+1)}}{4} \sum_{s,s'} \mathrm{e}^{\mathrm{i}Q(X_s - X'_s)} \mathrm{e}^{\mathbf{il'x_s + ilx_{s'}}} \sum_{r,r'} \mathrm{e}^{\mathbf{-il'x_{r'} - ilx_r}} P_l^{rs'} P_{l'}^{sr'} \left(M_\uparrow^{-1}\right)_{r,s} \left(M_\downarrow^{-1}\right)_{r',s'} . \tag{A.26}$$

Streamlineing inner loops as far as possible yields:

$$\begin{aligned} C(Q;L,L') = \frac{\sqrt{(2l+1)(2l'+1)}}{4} \sum_{s} \mathrm{e}^{\mathrm{i}\nu\tau_s} \mathrm{e}^{\mathbf{il'x_s - iqx_s}} \sum_{s'} \mathrm{e}^{-\mathrm{i}\nu\tau_{s'}} \mathrm{e}^{\mathbf{iqx_{s'} + ilx_{s'}}} \times \\ \times \sum_{r} \mathrm{e}^{\mathbf{-ilx_r}} P_l^{rs'} \left(M_\uparrow^{-1}\right)_{r,s} \sum_{r'} \mathrm{e}^{\mathbf{-il'x_{r'}}} P_{l'}^{sr'} \left(M_\downarrow^{-1}\right)_{r',s'} . \end{aligned} \tag{A.27}$$

Here, the exponentials may be tabelized and the rank 3 tensors P_l^{rs} should also be precalculated. They are given by:

$$P_l^{rs} = \mathrm{sgn}(\tau_r - \tau_s) P_l \left(\frac{2(\tau_r - \tau_s)}{\beta} - \mathrm{sgn}(\tau_r - \tau_s) \right), \tag{A.28}$$

with the obvious symmetry

$$P_l^{sr} = (-1)^{l+1} P_l^{rs}. \tag{A.29}$$

Of course, P_{l+1}^{rs} is related to P_l^{rs} and P_{l-1}^{rs} through the well known Rodriguez Formula. Further, because of $P_l(-1) = (-1)^l$, we have $P_l^{rr} = (-1)^l$, as we use the convention $\mathrm{sgn}(0) = 1$.

Most efficiently, $C(Q;L,L')$ is calculated in the following way:

$$C(Q;L,L') = \frac{\sqrt{(2l+1)(2l'+1)}}{4} \sum_{s} \mathrm{e}^{\mathrm{i}\nu\tau_s - \mathbf{iqx_s}} \sum_{s'} \mathrm{e}^{-\mathrm{i}\nu\tau_{s'} + \mathbf{iqx_{s'}}} h_{\uparrow,L}^{s,s'} h_{\downarrow,L'}^{s,s'}, \tag{A.30}$$

with

$$h_{\uparrow,L}^{s,s'} = \sum_{r} \mathrm{e}^{\mathbf{ilx_{s'}}} \mathrm{e}^{\mathbf{-ilx_r}} P_l^{rs'} \left(M_\uparrow^{-1}\right)_{r,s} \quad \text{and} \quad h_{\downarrow,L'}^{s,s'} = \sum_{r} \mathrm{e}^{\mathbf{il'x_s}} \mathrm{e}^{\mathbf{-il'x_r}} P_{l'}^{sr} \left(M_\uparrow^{-1}\right)_{r,s'} . \tag{A.31}$$

Dealing with the constant in $C(Q;K,P)$ A K and P independent constant in $C(Q;K,P)$ leads to the problem that $C(Q;L,L')$ does not decay as a function of increasing L or L'. This may not be desired, as we have to perform a sum over L and L' and wish the summands to decay, so that the truncation of the sum is valid. The origin of the constant comes from summands where $\tau_r = \tau'_s$ and $\tau'_r = \tau_s$. This part of the sum may be subtracted and transformed separately. Then, T_{nl} matrices will cancel out and we are able to perform some sums analytically.

We know that in the Matsubara frequency representation, $C(Q;K,P)$ has the form (A.10), which can be rewritten as

$$C(Q;K,P) = \sum_{rsr's'} \mathrm{e}^{\mathrm{i}[K\cdot(X_r - X_{s'}) + P\cdot(X_{r'} - X_s) + Q\cdot(X_s - X_{s'})]} \left(M_\uparrow^{-1}\right)_{rs} \left(M_\downarrow^{-1}\right)_{r's'} . \tag{A.32}$$

In this representation, it is obvious that summands with $r = s \vee r' = s'$ yield K- or P-independent contributions to $C(Q;K,P)$. These terms imply the complication of dangling sums over K and P once we transform to the Legendre basis leading to increasing coefficients as a function of l or l'. As an example, take a term $c(Q;P)$ that does not depend on K. The transformation to the Legendre basis looks like:

$$c(Q;L,L') = \sum_{K,P} T_{K,L}^{*} c(Q;P) T_{P,L'} = \left(\sum_{P} c(Q;P) T_{P,L'} \right) \left(\sum_{K} T_{K,L}^{*} \right) . \tag{A.33}$$

The dangling frequency sum yields

$$\sum_{K} T^*_{K,L} = \sum_{\mathbf{K},\mathrm{i}\omega_n} \delta_{\mathbf{K},\mathbf{L}} T^*_{nl} = \sum_{\mathrm{i}\omega_n} \frac{\sqrt{2l+1}}{2\beta} \int\limits_{-\beta}^{\beta} \mathrm{d}\tau \mathrm{e}^{\mathrm{i}\omega_n \tau} \tilde{P}_l(x(\tau)) = \sqrt{2l+1}\tilde{P}_l(-1) = \sqrt{2l+1}(-1)^l. \tag{A.34}$$

A.1.2. Symmetries of $C(Q; L, L')$

In the case of SU(2) symmetry, which will be taken as a prerequisite here, we know that $G_4^{\perp,\uparrow\downarrow\downarrow\uparrow}(Q; K, P) = G_4^{\perp,\downarrow\uparrow\uparrow\downarrow}(Q; K, P)$. Transforming this identity to the Legendre basis, we obtain two quantities playing the role of $C(Q; L, L')$, namely:

$$C^{\sigma\bar{\sigma}}(Q; L, L') = \sum_{K,P} T_{K,L} T^*_{P,L'} \sum_{r,s,r',s'} \mathrm{e}^{\mathrm{i}\left(K\cdot X_r - (P-Q)\cdot X_s + P\cdot X_{r'} - (K+Q)\cdot X'_s\right)} \left(M_\sigma^{-1}\right)_{r,s} \left(M_{\bar{\sigma}}^{-1}\right)_{r',s'}. \tag{A.35}$$

As the other quantities $A(Q; K, P)$ and $B(Q; K, P)$ do not depend on the Monte Carlo configuration nor on the spin index[3], we observe that in the Monte Carlo average $\langle C^{\uparrow\downarrow}(Q; L, L')\rangle_{MC} = \langle C^{\downarrow\uparrow}(Q; L, L')\rangle_{MC}$ must hold. Thus, we can enforce this symmetry already on the level of Monte Carlo configurations by replacing $C^{\uparrow\downarrow}(Q; L, L')$ by $C^{\downarrow\uparrow}(Q; L, L')$ for certain values of L and L'. This has to be done consistently *throughout the whole simulation*, though. With this idea, we can reduce the number of points that have to be calculated roughly by a factor of 2 by using

$$C^{\uparrow\downarrow}(Q; L, L') = (-1)^{l+l'} C^{\downarrow\uparrow}(-Q; L', L) = (-1)^{l+l'} C^{\downarrow\uparrow}(Q; L', L)^*. \tag{A.36}$$

The easiest way to exploit this is to only calculate $C^{\uparrow\downarrow}(Q; L, L')$ for $l' \leq l$ and $\mathrm{index}(\mathbf{l'}) \leq \mathrm{index}(\mathbf{l})$ and reconstruct the full quantity after the simulation by virtue of equation (A.36).

As memory has to be economized, we use a compact linearized storage of $C(Q; L, L')$ in the following way:

$$\begin{aligned} &C(Q; L, L') \rightarrow \\ &\texttt{c\_table}\left[l' + \frac{l(l+1)}{2} + \left(\nu + \mathrm{ind}\left(\mathbf{l'}\right) n_\nu + \frac{\mathrm{ind}\left(\mathbf{l}\right)\left(\mathrm{ind}\left(\mathbf{l}\right)+1\right)}{2} n_\nu + \mathrm{ind}\left(\mathbf{q}\right) n_\nu \frac{N_c(N_c+1)}{2}\right) \frac{n_l(n_l+1)}{2}\right]. \end{aligned} \tag{A.37}$$

This corresponds of course to a triangular storage in the $l - l'$-Hyperplane and in the $\mathbf{l} - \mathbf{l'}$-Hyperplane of the rank 6 tensor. Note that in the C++-valarray `c_table` the indices start at 0. We have $0 \leq l' \leq l < n_l$ and $0 \leq \mathrm{ind}\left(\mathbf{l'}\right) \leq \mathrm{ind}\left(\mathbf{l}\right) < N_c$. The total required storage for one bin of $C(Q; L, L')$ in the compact representation amounts to:

$$\texttt{c\_table.size()} \quad = N_c n_\nu \frac{N_c(N_c+1)}{2} \frac{n_l(n_l+1)}{2}. \tag{A.38}$$

A.1.3. Conclusion

We presented the current status of our attempt to adapt the Legendre polynomial basis to a cluster calculation using CT-INT. Note that this work is not complete so a final answer on the feasibility can not be given as the use of further transformations and tricks might improve the method.

The calculation of the two particle Green's function $G_4(Q; L, L')$ directly in the (mixed) Legendre polynomial basis faces two major difficulties:

---

[3] Because of SU(2) symmetry, $G^\uparrow(K) = G^\downarrow(K) = G(K)$.

- The accumulation formula (A.30) does not factorize in two vertex independent terms and is therefore extremely expensive to calculate. This is a very severe problem and renders the method unusable for practical applications. This can be understood best from equation (A.27), where the matrices $M_\uparrow$ ($M_\downarrow$) connect the unprimed (primed) indices r and s (r' and s'), while primed and unprimed indices are entangled by the Legendre tables P_l^{rs}. This stands in contrast to the situation of a pure frequency basis as used in chapter 4, where the $X_\sigma(K, P)$ matrices have to be calculated only once and are then used for the generation of $\langle\langle T(Q; K, P)\rangle\rangle_{C_n}$.

- Because of the complicated convolution of the original frequency variables, frequency symmetries can hardly be transported to the Legendre basis in a constructive way. Thus a reduction of calculation times from this should not be expected.

Certainly, the first problem is the most severe and renders the present formulation so inefficient that it is not usable. The only way out would be a separation of P_l^{rs} into two terms depending only on l and r or l and s respectively. In any case, performing sums over all vertices in C_n for *every* combination of outer indices $(Q; L, L')$ is illusionary to a degree that we could not obtain satisfactory results using an implementation of equation (A.30).

A.2. Analytic continuation of the self energy

Especially in the context of the dynamical mean field theory or within impurity problems it is convenient to analytically continue the self energy rather than the Green's function to the real frequency axis. The reason for this is that for this kind of problems the only nonzero elements of the self energy correspond to lattice sites with an interaction term which is only one single site in DMFT and impurity problems.

We will follow the lines of reference [23] for the description of the procedure and focus on how the asymptotic behaviour of the self energy may be obtained accurately in a Monte Carlo simulation.

A.2.1. Asymptotic behaviour of the self energy for impurity problems

Let us start with a lattice system described by a Hamiltonian

$$\mathcal{H} = \mathcal{H}_0 + \mathcal{H}_1. \tag{A.39}$$

Here, $\mathcal{H}_0$ does not contain any interaction and $\mathcal{H}_1$ will denote interaction terms acting exclusively on one single lattice site (i.e. the *impurity*). We will denote creation (annihilation) operators for a particle with spin σ on the impurity site with $d_\sigma^\dagger$ (d_σ).

By virtue of Dyson's equation

$$\mathbf{G}(\mathrm{i}\omega_n) = \mathbf{G}_0(\mathrm{i}\omega_n) + \mathbf{G}_0(\mathrm{i}\omega_n)\mathbf{\Sigma}(\mathrm{i}\omega_n)\mathbf{G}(\mathrm{i}\omega_n) \tag{A.40}$$

and using the fact that the self energy matrix is only nonzero in its block $\mathbf{\Sigma}^{\mathrm{dd}}(\mathrm{i}\omega_n)$ corresponding to the impurity lattice site, we obtain trivially Dyson's equation for the impurity site:

$$\mathbf{G}^{\mathrm{dd}}(\mathrm{i}\omega_n) = \mathbf{G}_0^{\mathrm{dd}}(\mathrm{i}\omega_n) + \mathbf{G}_0^{\mathrm{dd}}(\mathrm{i}\omega_n)\mathbf{\Sigma}^{\mathrm{dd}}(\mathrm{i}\omega_n)\mathbf{G}^{\mathrm{dd}}(\mathrm{i}\omega_n) \tag{A.41}$$

and hence

$$\mathbf{\Sigma}^{\mathrm{dd}}(\mathrm{i}\omega_n) = \mathbf{G}_0^{\mathrm{dd}}(\mathrm{i}\omega_n)^{-1} - \mathbf{G}^{\mathrm{dd}}(\mathrm{i}\omega_n)^{-1} \tag{A.42}$$

In the case of a $SU(2)$ invariant problem, the Green's functions are diagonal and spin independent matrices and we are left with the scalar equation

$$\Sigma^{\mathrm{dd}}(\mathrm{i}\omega_n) = \frac{1}{G_0^{\mathrm{dd}}(\mathrm{i}\omega_n)} - \frac{1}{G^{\mathrm{dd}}(\mathrm{i}\omega_n)}. \tag{A.43}$$

From here, it is easy to construct the high frequency expansion for the self energy starting from the asymptotic form of the Green's function[4]:

$$G^{\mathrm{dd}}(\mathrm{i}\omega_n) = \frac{a}{\mathrm{i}\omega_n} + \frac{b}{(\mathrm{i}\omega_n)^2} + \frac{c}{(\mathrm{i}\omega_n)^3} + \mathcal{O}\left(\frac{1}{(\mathrm{i}\omega_n)^4}\right) \text{ and } G_0^{\mathrm{dd}}(\mathrm{i}\omega_n) = \frac{a}{\mathrm{i}\omega_n} + \frac{b_0}{(\mathrm{i}\omega_n)^2} + \frac{c_0}{(\mathrm{i}\omega_n)^3} + \mathcal{O}\left(\frac{1}{(\mathrm{i}\omega_n)^4}\right) \tag{A.44}$$

Inserting this expression in equation (A.43) and expanding in powers of $\frac{1}{\mathrm{i}\omega_n}$ yields[5]:

$$\Sigma^{\mathrm{dd}}(\mathrm{i}\omega_n) = (b - b_0) + \frac{1}{\mathrm{i}\omega_n}\frac{b_0^2 - b^2 + ac - ac_0}{a} + \mathcal{O}\left(\frac{1}{(\mathrm{i}\omega_n)^2}\right). \tag{A.45}$$

It is important to note that the first two terms in this expansion do not change if we take into account more terms in the high frequency expansion of the Green's function.

As a next step, we will see how the coefficients of high frequency expansion of the self energy may be calculated. As a start, we remember the well known fact that the constants a, b, c etc. are given by the *moments* of the spectral function $A(\omega)$ which is obvious, if we perform a high (Matsubara) frequency expansion of the integral kernel $\frac{1}{-\mathrm{i}\omega_n - \omega}$:

$$\frac{1}{-\mathrm{i}\omega_n - \omega} = -\frac{1}{\mathrm{i}\omega_n} + \frac{\omega}{(\mathrm{i}\omega_n)^2} - \frac{\omega^2}{(\mathrm{i}\omega_n)^3} + \mathcal{O}\left(\frac{1}{(\mathrm{i}\omega_n)^4}\right), \tag{A.46}$$

yielding:

$$\begin{aligned} G^{\mathrm{dd}}(\mathrm{i}\omega_n) &= \int\limits_{-\infty}^{\infty} \mathrm{d}\omega \, \frac{A^{\mathrm{dd}}(\omega)}{-\mathrm{i}\omega_n - \omega} = \\ & -\frac{1}{\mathrm{i}\omega_n}\int\limits_{-\infty}^{\infty} \mathrm{d}\omega \, A^{\mathrm{dd}}(\omega) + \frac{1}{(\mathrm{i}\omega_n)^2}\int\limits_{-\infty}^{\infty} \mathrm{d}\omega \, \omega A^{\mathrm{dd}}(\omega) - \frac{1}{(\mathrm{i}\omega_n)^3}\int\limits_{-\infty}^{\infty} \mathrm{d}\omega \, \omega^2 A^{\mathrm{dd}}(\omega) + \mathcal{O}\left(\frac{1}{(\mathrm{i}\omega_n)^4}\right). \end{aligned} \tag{A.47}$$

Apparently,

$$a = -\int\limits_{-\infty}^{\infty} \mathrm{d}\omega \, A^{\mathrm{dd}}(\omega), \qquad b = \int\limits_{-\infty}^{\infty} \mathrm{d}\omega \, \omega A^{\mathrm{dd}}(\omega), \quad \text{and} \quad c = -\int\limits_{-\infty}^{\infty} \mathrm{d}\omega \, \omega^2 A^{\mathrm{dd}}(\omega). \tag{A.48}$$

Moments of the spectral function Similar relations hold for b_0 and c_0. As $A^{\mathrm{dd}}(\omega)$ is usually unknown, we use the Lehmann representation of $A^{\mathrm{dd}}(\omega)$ to obtain an expression accessible in CT-INT:

$$A^{\mathrm{dd}}(\omega) = \frac{1}{Z}\sum_{n,m} \left|\langle\, n\,|\, d_\sigma^\dagger\,|\, m\,\rangle\right|^2 \mathrm{e}^{-\beta E_m}\left(1 + \mathrm{e}^{-\beta\omega}\right)\delta(\omega - E_n + E_m). \tag{A.49}$$

Multiplication by powers of ω and integration yields readily the Lehmann representation for the moments:

$$\int\limits_{-\infty}^{\infty} \mathrm{d}\omega \, \omega^\alpha A^{\mathrm{dd}}(\omega) = \frac{1}{Z}\sum_{n,m}(E_n - E_m)^\alpha\left(\mathrm{e}^{-\beta E_m} + \mathrm{e}^{-\beta E_n}\right)\langle\, n\,|\, d^\dagger\,|\, m\,\rangle\,\langle\, m\,|\, d\,|\, n\,\rangle\,. \tag{A.50}$$

By comparison of the Lehmann representations of right and left hand sides, it is clear that

$$\int\limits_{-\infty}^{\infty} \mathrm{d}\omega \, A^{\mathrm{dd}}(\omega) = \langle\,\left[\, d^\dagger,\, d\,\right]_+\rangle\,. \tag{A.51}$$

---

[4] Note that for generality we keep a as a variable, as depending on the definition of the Green's function, a may be either 1 or -1 but is in any case equal for G and G_0.

[5] exploiting the fact that $a^2 = 1$

$$\int_{-\infty}^{\infty} \mathrm{d}\omega\, \omega A^{\mathrm{dd}}(\omega) = \langle\, [\, [\, d,\, H\,]_-\, ,\, d^\dagger\,]_+ \rangle\, . \tag{A.52}$$

Or in general terms:

$$\int_{-\infty}^{\infty} \mathrm{d}\omega\, \omega^\alpha A^{\mathrm{dd}}(\omega) = \sum_{k=0}^{\alpha} \binom{\alpha}{k} (-1)^{\alpha-k} \langle \left[H^k d^\dagger H^{\alpha-k},\, d \right]_+ \rangle\, . \tag{A.53}$$

This expression can be rewritten as:

$$\int_{-\infty}^{\infty} \mathrm{d}\omega\, \omega^\alpha A^{\mathrm{dd}}(\omega) = (-1)^\alpha \langle \left[\left[\left[\left[d^\dagger,\, H \right]_-\, ,\, H \right]_-\, , \ldots , H \right]_-\, ,\, d \right]_+ \rangle = (-1)^\alpha \langle \left[\left[d^\dagger, H \right]_{-,\alpha}\, ,\, d \right]_+ \rangle \tag{A.54}$$

with the definition

$$[A, B]_{-,\alpha} = \left[[A, B]_{-,\alpha-1}\, ,\, B \right]_- \quad \text{and} \quad [A, B]_{-,1} = [\, A,\, B\,]_-\, . \tag{A.55}$$

Proof of equation (A.54) We demonstrate that

$$\sum_{k=0}^{\alpha} \binom{\alpha}{k} (-1)^{\alpha-k} H^k d^\dagger H^{\alpha-k} = \left[d^\dagger, H \right]_{-,\alpha} \tag{A.56}$$

by induction in α. Starting from $\alpha = 1$, we have trivially

$$d^\dagger H - H d^\dagger = (-1)^\alpha \left[d^\dagger, H \right]_{-,1}\, . \tag{A.57}$$

In the following step, we assume that eq. (A.56) is fullfilled for a given α and prove that this leads to eq. (A.56) for $\alpha + 1$.

$$\begin{aligned}
(-1)^{\alpha+1} \left[d^\dagger, H \right]_{-,\alpha+1} &= (-1) \left[(-1)^\alpha \left[d^\dagger, H \right]_{-,\alpha}\, ,\, H \right]_- = \\
&= -\sum_{k=0}^{\alpha} \binom{\alpha}{k} (-1)^{\alpha-k} H^k d^\dagger H^{\alpha-k+1} - \sum_{k=0}^{\alpha} \binom{\alpha}{k} (-1)^{\alpha-k-1} H^{k+1} d^\dagger H^{\alpha-k} = \\
&= -\sum_{k=0}^{\alpha} \binom{\alpha}{k} (-1)^{\alpha-k} H^k d^\dagger H^{\alpha-k+1} - \sum_{l=1}^{\alpha+1} \binom{\alpha}{l-1} (-1)^{\alpha-l} H^l d^\dagger H^{\alpha-l+1} = \\
&= (-1)^{\alpha+1} d^\dagger H^{\alpha+1} - \sum_{l=1}^{\alpha} \left[\binom{\alpha}{l} - \binom{\alpha}{l-1} \right] (-1)^{\alpha-l} H^l d^\dagger H^{\alpha-l+1} - (-1) H^{\alpha+1} d^\dagger = \\
&= \sum_{l}^{\alpha+1} \binom{\alpha+1}{l} (-1)^{\alpha+1-l} H^l d^\dagger H^{\alpha+1-l}.
\end{aligned} \tag{A.58}$$

A.2.2. Application to the Anderson-Kane-Mele Model

As an application of the general discussion of the asymptotic form presented in section A.2.1 we proceed to a specific form of the Hamiltonian and study the self energy of the Anderson-Kane-Mele model. It is given by fermionic operators a and b acting on the A and B sublattices of a hexagonal lattice and an additional impurity site d which is coupled to the lattice by a hybridization term of strength V:

$$H_{\mathrm{KM}} = H_t - H_\lambda, \tag{A.59}$$

$$H_t = -t \sum_{\mathbf{i}\sigma} a^\dagger_{\mathbf{i}\sigma} (b_{\mathbf{i}\sigma} + b_{\mathbf{i}+\mathbf{a_1}-\mathbf{a_2},\sigma} + b_{\mathbf{i}-\mathbf{a_2},\sigma}) + \text{h.c.} \tag{A.60}$$

$$H_\lambda = \lambda \sum_{\mathbf{i}\sigma} \sigma \left[i a^\dagger_{\mathbf{i}\sigma} \left(a_{\mathbf{i}+\mathbf{a_1},\sigma} + a_{\mathbf{i}-\mathbf{a_2},\sigma} + a_{\mathbf{i}+\mathbf{a_2}-\mathbf{a_1},\sigma} \right) - i b^\dagger_{\mathbf{i}\sigma} \left(b_{\mathbf{i}+\mathbf{a_1},\sigma} + b_{\mathbf{i}-\mathbf{a_2},\sigma} + b_{\mathbf{i}+\mathbf{a_2}-\mathbf{a_1},\sigma} \right) \right] + \text{h.c.} \tag{A.61}$$

$$H_{\text{imp}} = \epsilon_d \sum_\sigma d^\dagger_\sigma d_\sigma + V \sum_\sigma (a^\dagger_{\mathbf{0},\sigma} d_\sigma + d^\dagger_\sigma a_{\mathbf{0},\sigma}) + U \left(n^d_\uparrow - \frac{1}{2} \right) \left(n^d_\downarrow - \frac{1}{2} \right). \tag{A.62}$$

The total Hamiltonian is thus given by $H = H_{\text{KM}} + H_{\text{imp}}$.

Let us now proceed to the calculation of the moments of the spectral function:

$$\int_{-\infty}^{\infty} \mathrm{d}\omega\, A^{\text{dd}}_\sigma(\omega) = \langle \left[d^\dagger_\sigma,\, d_\sigma \right]_+ \rangle = 1. \tag{A.63}$$

For the first moment, we need to calculate $\left[d^\dagger_\sigma,\, H \right]_-$. Using the fact that $\left[d^\dagger_\sigma,\, H_{\text{KM}} \right]_- = 0$, we obtain:

$$\left[d^\dagger_\sigma,\, H \right]_- = -V a^\dagger_{\mathbf{0},\sigma} - \epsilon_d d^\dagger_\sigma + \frac{U}{2} d^\dagger_\sigma + U d^\dagger_{-\sigma} d^\dagger_\sigma d_{-\sigma}. \tag{A.64}$$

Continuing the calculation, we obtain:

$$\int_{-\infty}^{\infty} \mathrm{d}\omega\, \omega A^{\text{dd}}_\sigma(\omega) = -\langle \left[\left[d^\dagger_\sigma,\, H \right]_-,\, d_\sigma \right]_+ \rangle = \epsilon + U \langle d^\dagger_{-\sigma} d_{-\sigma} \rangle - \frac{U}{2}. \tag{A.65}$$

For the second moment, the calculation becomes somewhat more involved but can be partially done using Rok Žitko's `SNEG` [131] after reducing the terms by hand as much as possible. Let us begin with the commutator

$$\left[\left[d^\dagger_\sigma,\, H \right]_-,\, H \right]_- = \left[-V a^\dagger_{\mathbf{0},\sigma} - \epsilon_d d^\dagger_\sigma + \frac{U}{2} d^\dagger_\sigma + U d^\dagger_{-\sigma} d^\dagger_\sigma d_{-\sigma},\, H_{\text{KM}} + H_{\text{imp}} \right]_-. \tag{A.66}$$

Employing the fact, that all d operators commute with H_{KM}, we obtain

$$\left[\left[d^\dagger_\sigma,\, H \right]_-,\, H \right]_- = -V \left(\left[a^\dagger_{\mathbf{0},\sigma},\, H_{\text{KM}} \right]_- + \left[a^\dagger_{\mathbf{0},\sigma},\, H_{\text{imp}} \right]_- \right) + \left[-\epsilon_d d^\dagger_\sigma + \frac{U}{2} d^\dagger_\sigma + U d^\dagger_{-\sigma} d^\dagger_\sigma d_{-\sigma},\, H_{\text{imp}} \right]_-. \tag{A.67}$$

In order to calculate $\left[a^\dagger_{\mathbf{0},\sigma},\, H_{\text{KM}} \right]_-$ we observe that $a^\dagger_{\mathbf{0},\sigma}$ commutes with every term of H_{KM} that does not contain $a_{\mathbf{0},\sigma}$. The remaining terms are

$$\begin{aligned} H_{\text{KM}}(a_{\mathbf{0},\sigma}) = &-t \left(b^\dagger_{\mathbf{0},\sigma} + b^\dagger_{\mathbf{a_1}-\mathbf{a_2},\sigma} + b^\dagger_{-\mathbf{a_2},\sigma} \right) a_{\mathbf{0},\sigma} + \\ &+ \lambda\sigma\mathrm{i} \left(a^\dagger_{-\mathbf{a_1},\sigma} + a^\dagger_{\mathbf{a_2},\sigma} + a^\dagger_{\mathbf{a_1}-\mathbf{a_2},\sigma} - a^\dagger_{\mathbf{a_1},\sigma} - a^\dagger_{-\mathbf{a_2},\sigma} - a^\dagger_{\mathbf{a_2}-\mathbf{a_1},\sigma} \right) a_{\mathbf{0},\sigma}. \end{aligned} \tag{A.68}$$

Thus, we obtain

$$\left[a^\dagger_{\mathbf{0},\sigma},\, H_{\text{KM}} \right]_- = \mathrm{i}\lambda\sigma \left(a^\dagger_{-\mathbf{a_2},\sigma} - a^\dagger_{\mathbf{a_1}-\mathbf{a_2},\sigma} - a^\dagger_{\mathbf{a_2},\sigma} + a^\dagger_{\mathbf{a_2}-\mathbf{a_1},\sigma} \right) + t \left(b^\dagger_{\mathbf{0},\sigma} + b^\dagger_{-\mathbf{a_2},\sigma} + b^\dagger_{\mathbf{a_1}-\mathbf{a_2},\sigma} \right). \tag{A.69}$$

The second term in equation (A.67) yields readily:

$$\left[a^\dagger_{\mathbf{0},\sigma},\, H_{\text{imp}} \right]_- = -V d^\dagger_\sigma. \tag{A.70}$$

The last commutator in (A.67) reduces to the form:

$$\begin{aligned}
&\left[-\epsilon_d d^\dagger_\sigma + \frac{U}{2} d^\dagger_\sigma + U d^\dagger_{-\sigma} d^\dagger_\sigma d_{-\sigma},\, H_{\text{imp}}\right]_- = \\
&= -\frac{UV}{2} a^\dagger_{\mathbf{0},\sigma} + V\epsilon_{\mathrm{d}} a^\dagger_{\mathbf{0},\sigma} + \frac{U^2}{4} d^\dagger_\sigma - U\epsilon_d d^\dagger_\sigma + \epsilon_d^2 d^\dagger_\sigma - UV a^\dagger_{\mathbf{0},-\sigma} d^\dagger_\sigma d_{-\sigma} + \\
&+ UV a_{\mathbf{0},\sigma} d^\dagger_{-\sigma} d_{-\sigma} + UV d^\dagger_{-\sigma} d^\dagger_\sigma a_{\mathbf{0},-\sigma} - 2U\epsilon_d d^\dagger_{-\sigma} d^\dagger_\sigma d_{-\sigma}.
\end{aligned} \tag{A.71}$$

With these intermediate results, we can now move on to calculate the second moment of the spectral function, evaluating the anticommutator

$$\left[\left[\left[d^\dagger_\sigma,\, H\right]_-,\, H\right]_-,\, d_\sigma\right]_+ = V^2 + \frac{U^2}{4} - U\epsilon_d + \epsilon_d^2 + UV a^\dagger_{\mathbf{0},-\sigma} d_{-\sigma} - UV d^\dagger_{-\sigma} a_{\mathbf{0},-\sigma} + 2U\epsilon_d d^\dagger_{-\sigma} d_{-\sigma}. \tag{A.72}$$

We obtain:

$$\begin{aligned}
\int\limits_{-\infty}^{\infty} \mathrm{d}\omega\, \omega^2 A^{\mathrm{dd}}_\sigma(\omega) &= \left\langle \left[\left[\left[d^\dagger_\sigma,\, H\right]_-,\, H\right]_-,\, d_\sigma\right]_+ \right\rangle = \\
&= V^2 + \frac{U^2}{4} - U\epsilon_d + \epsilon_d^2 + UV \left\langle a^\dagger_{\mathbf{0},-\sigma} d_{-\sigma} \right\rangle - UV \left\langle d^\dagger_{-\sigma} a_{\mathbf{0},-\sigma} \right\rangle + 2U\epsilon_d \left\langle d^\dagger_{-\sigma} d_{-\sigma} \right\rangle.
\end{aligned} \tag{A.73}$$

Asymptotic behaviour of the self energy Collecting all the above results, we are finally able to present the asymptotic behaviour of the self energy of the Kane-Mele-Anderson model.

$$b - b_0 = U \left\langle d^\dagger_{-\sigma} d_{-\sigma} \right\rangle - \frac{U}{2}. \tag{A.74}$$

$$\frac{b_0^2 - b^2 + ac - ac_0}{a} = UV \left(\left\langle a^\dagger_{\mathbf{0},-\sigma} d_{-\sigma} \right\rangle - \left\langle d^\dagger_{-\sigma} a_{\mathbf{0},-\sigma} \right\rangle \right) + U^2 \left\langle d^\dagger_{-\sigma} d_{-\sigma} \right\rangle - U^2 \left\langle d^\dagger_{-\sigma} d_{-\sigma} \right\rangle^2. \tag{A.75}$$

A.2.3. Analytic continuation of the self energy

In order to employ the stochastic maximum entropy method for $\Sigma(z)$ directly, we introduce a slightly different quantity as already shown in [23]:

$$\Sigma'(z) = \frac{\left[\Sigma(z) - \left(a_2 - a_2^0\right)\right] a_1}{a_2^2 - \left(a_2^0\right)^2 + a_1 a_3 - a_1 a_3^0}. \tag{A.76}$$

This quantity has exactly the same properties as the Green's function itself, namely that its asymptotic series starts with $\frac{1}{\mathrm{i}\omega_n}$, the corresponding spectral function has a sum rule $\int \mathrm{d}\omega A_\Sigma(\omega) = 1$ and that it does not have a constant term.

In principle, these properties could be corrected for in the maximum entropy procedure but the quantities a_2 and a_3 can only be obtained up to a statistical errorbar and therefore the correct inclusion of these errors is very cumbersome. Performing the transformation A.76 is therefore a very straightforward procedure, as the thoroughly bootstrapped covariance matrix of Σ' will contain all uncertainties stemming from the CT-INT calculation.

A.3. Generation of test data

A.3.1. Data with given covariance

In order to test the maximum entropy code, it might be helpful to generate random data with a given covariance matrix. This can be done in the following way. Let us define a vector $\mathbf{y}_{\text{exact}} \in \mathbb{R}^n$ which contains exact data. We now want to add noise with a given covariance matrix $\mathbf{C} \in \mathbb{R}^{n\times n}$. We make the following ansatz

$$\mathbf{y} = \mathbf{y}_{\text{exact}} + \mathbf{A}\mathbf{r}$$

Here, $\mathbf{y}$ is the data with the noise having a covariance matrix $\mathbf{C}$ as required and $\mathbf{r} \in \mathbb{R}^n$ is a vector of statistically independent gaussian random variables with mean $\mu = \langle r_i \rangle = 0$ and standard deviation $\sigma = \sqrt{\langle r_i r_i \rangle - \mu^2} = 1$. This means that $\langle r_i r_j \rangle = \delta_{ij}$. Our task is now to find an appropriate matrix $\mathbf{A}$. Let us calculate the covariance matrix of the data $\mathbf{y}$: [6]

$$\begin{aligned}\mathbf{C}_{ij} = \text{Cov}(y_i, y_j) &= \langle y_i y_j \rangle - \langle y_i \rangle \langle y_j \rangle = \langle (y_{\text{exact},i} + A_{il} r_l)(y_{\text{exact},j} + A_{jk} r_k) \rangle - y_{\text{exact},i} y_{\text{exact},j} = \\ &= y_{\text{exact},i} y_{\text{exact},j} + A_{il} A_{jk} \langle r_l r_k \rangle - y_{\text{exact},i} y_{\text{exact},j} = \\ &= (\mathbf{A}\mathbf{A}^T)_{ij}\end{aligned}$$

Of course, the covariance matrix $\mathbf{C}$ has to be positive semidefinite and symmetric, so a positive semidefinite and symmetric matrix $\mathbf{A}$ can be determined that obeys the condition $\mathbf{C} = \mathbf{A}\mathbf{A}$. This can be done by diagonalizing $\mathbf{C}$ and taking the square root of the diagonal matrix, then rotating back to the original basis.

A.3.2. Sums of random numbers

The central limit theorem gives an inspiring idea for the generation of well defined test data that may be used for testing the accuracy of data analysis code for the calculation of the covariance matrix. Suppose we have a sequence of statistically independent random variables x_i, $i \in [1, N]$ distributed at the uniform probability density $p(x_i) = \Theta(x_i)\Theta(1 - x_i)$. From this, we can define new random variables

$$X_j = \frac{1}{N - M + 1} \sum_{i=j}^{j+N-M} x_i, \qquad j \in [1, M]\,. \tag{A.77}$$

Clearly, the random variables X_j will not be completely independent from each other, as their values originate partly from the same underlying data x_i. Therefore, the covariance matrix can not be diagonal. Let us calculate its value analytically in the following.

The average value for X_j is independent of j and evaluates to

$$\langle X_j \rangle = \frac{1}{N - M + 1} \sum_{i=j}^{j+N-M} \langle x_i \rangle = \frac{1}{N - M + 1} (N - M + 1) \frac{1}{2} = \frac{1}{2}. \tag{A.78}$$

For the covariance matrix, we find:

$$\text{Cov}(X_i, X_j) = \langle X_i X_j \rangle - \langle X_i \rangle \langle X_j \rangle = \langle X_i X_j \rangle - \frac{1}{4}. \tag{A.79}$$

In order to calculate the correlation term $\langle X_i X_j \rangle$, we have to keep in mind that for statistically independent random variables x_i and x_j — i.e. if $i \neq j$ — the expectation value factorizes: $\langle x_i x_j \rangle = \langle x_i \rangle \langle x_j \rangle = \frac{1}{4}$. On the other hand, if $i = j$, we need to calculate $\langle x_i^2 \rangle = \langle x^2 \rangle$:

$$\langle x^2 \rangle = \int_{-\infty}^{\infty} \mathrm{d}x\, p(x) x^2 = \int_0^1 \mathrm{d}x\, x^2 = \frac{1}{3}. \tag{A.80}$$

Obviously, the calculation of $\langle X_i X_j \rangle$ is now only a matter of counting the occurence of the case $i = j$

$$\langle X_i X_j \rangle = \left(\frac{1}{N - M + 1} \right)^2 \sum_{l=i}^{i+N-M} \sum_{k=j}^{j+N-M} \langle x_l x_k \rangle\,. \tag{A.81}$$

---

[6] Note that we use the Einstein summation convention that repeated indices imply a summation over the index

We already know, that in this expression the summand $\langle x_i x_j \rangle$ can only take the values $\frac{1}{4}$ or $\frac{1}{3}$. Further, the total number of terms is of course $(N-M+1)^2$, while the number of terms for which $l = k$ is given by $\max\left(N-M+1-|i-j|, 0\right)$. Thus, the result for the covariance matrix $\mathrm{Cov}(X_i, X_j)$ is given by

$$\begin{aligned}
&\mathrm{Cov}(X_i, X_j) = \langle X_i X_j \rangle - \langle X_i \rangle \langle X_j \rangle \\
&= \left(\frac{1}{N-M+1}\right)^2 \left\{ \frac{1}{4}\left[(N-M+1)^2 - \max\left(N-M+1-|i-j|, 0\right)\right] + \right. \\
&\left. + \frac{1}{3}\max\left(N-M+1-|i-j|, 0\right) \right\} - \frac{1}{4} \\
&= \left(\frac{1}{N-M+1}\right)^2 \frac{\max\left(N-M+1-|i-j|, 0\right)}{12}.
\end{aligned} \tag{A.82}$$

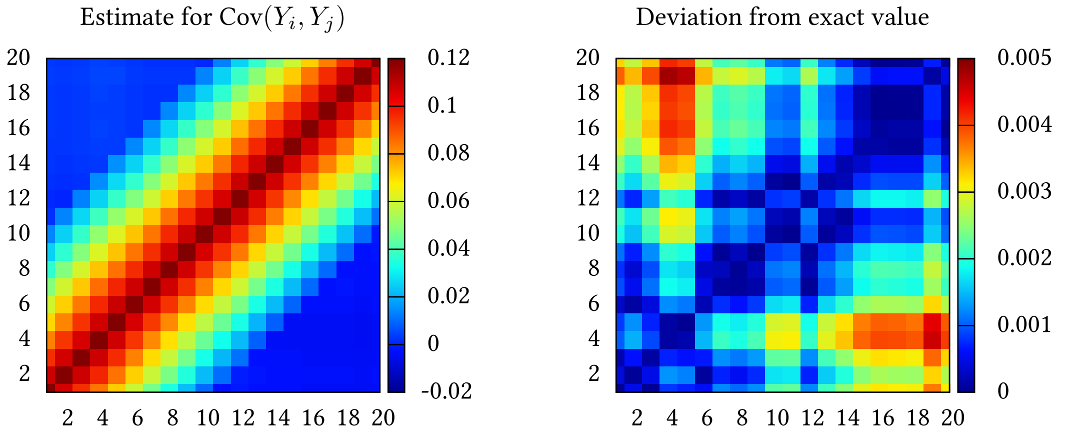
Estimate for $\mathrm{Cov}(Y_i, Y_j)$

Deviation from exact value

Figure A.1.: Graphical representation of the sample covariance as an estimate for $\mathrm{Cov}(Y_i, Y_j)$ [cf. (A.83)] (left panel) together with the difference between the sample covariance and the exact value of $\mathrm{Cov}(Y_i, Y_j)$ given by equation (A.86) (right panel). For this illustration, $L = 7$, $N = 30$ and $M = 20$ was used. Note that the estimate of the covariance matrix is best on the main diagonal and that the quality decreases with the distance from it. Naturally, the overall quality of the sample covariance imporves with the size of the sample, which is $N_{\text{sample}} = 2000000$ in this case.

In order to mimic the work with Monte Carlo bins, we introduce yet another set of random variables Y_i, which consist of the average of L realizations of the random variables X_i:

$$Y_i = \frac{1}{L}\sum_{l=1}^{L} X_i^{(l)}. \tag{A.83}$$

The expectation value of the random variables Y_i is trivial: $\langle Y_i \rangle = \langle X_i \rangle = \frac{1}{2}$. For the covariance matrix, we obtain the following expression:

$$\mathrm{Cov}(Y_i, Y_j) = \langle Y_i Y_j \rangle - \langle Y_i \rangle \langle Y_j \rangle = \frac{1}{L^2}\sum_{l,k=1}^{L} \langle X_i^{(l)} X_j^{(k)} \rangle - \frac{1}{4}. \tag{A.84}$$

As the underlying sequence of random variables x_n is different for $X_i^{(l)}$ and $X_j^{(k)}$ if $l \neq k$, the expectation value factorizes for this case. In the case of $l = k$, we obtain

$$\langle X_i^{(l)} X_j^{(l)} \rangle = \langle X_i X_j \rangle = \mathrm{Cov}(X_i, X_j) + \langle X_i \rangle^2 \,. \tag{A.85}$$

This leads to

$$\begin{aligned}\mathrm{Cov}(Y_i, Y_j) &= \frac{1}{L^2} \left[\sum_{l \neq k}^{L} \langle X_i^{(l)} \rangle \langle X_j^{(k)} \rangle + \sum_{l}^{L} \left(\mathrm{Cov}(X_i, X_j) + \langle X_i \rangle^2 \right) \right] - \langle X_i \rangle \langle X_j \rangle \\ &= \frac{1}{L^2} \left[(L^2 - L) \langle X_i \rangle^2 + L\, \mathrm{Cov}(X_i, X_j) + L \langle X_i \rangle^2 \right] - \langle X_i \rangle^2 = \frac{1}{L} \mathrm{Cov}(X_i, X_j).\end{aligned} \tag{A.86}$$

The result is illustrated by a numerically generated sample covariance matrix in figure A.1.

B. General Mathematical identities

B.1. Block matrix operations

B.1.1. Block matrix inversion

As the inversion of a big $N \times N$ matrix is an expensive $\mathcal{O}(N^3)$ operation, it is often useful to use already known information, such as the inverse matrix of a (large) sub-block. The inverse of a block matrix $\mathbf{M} \in \mathbb{C}^{(n+m)\times(n+m)}$ can be obtained in the following way:

$$\mathbf{M}\mathbf{M}^{-1} = \begin{pmatrix} \mathbf{A} & \mathbf{B} \\ \mathbf{C} & \mathbf{D} \end{pmatrix} \begin{pmatrix} \mathbf{E} & \mathbf{F} \\ \mathbf{G} & \mathbf{H} \end{pmatrix} = \begin{pmatrix} \mathbf{1} & \mathbf{0} \\ \mathbf{0} & \mathbf{1} \end{pmatrix}. \tag{B.1}$$

Multiplying out this equation and solving for the unknown matrices $\mathbf{E}, \mathbf{F}, \mathbf{G}, \mathbf{H}$, we obtain easily:

$$\begin{aligned} \mathbf{E} &= \mathbf{A}^{-1} + \mathbf{A}^{-1}\mathbf{B}\left(\mathbf{D} - \mathbf{C}\mathbf{A}^{-1}\mathbf{B}\right)^{-1}\mathbf{C}\mathbf{A}^{-1}. \\ \mathbf{F} &= -\mathbf{A}^{-1}\mathbf{B}\left(\mathbf{D} - \mathbf{C}\mathbf{A}^{-1}\mathbf{B}\right)^{-1}. \\ \mathbf{G} &= -\left(\mathbf{D} - \mathbf{C}\mathbf{A}^{-1}\mathbf{B}\right)^{-1}\mathbf{C}\mathbf{A}^{-1}. \\ \mathbf{H} &= \left(\mathbf{D} - \mathbf{C}\mathbf{A}^{-1}\mathbf{B}\right)^{-1}. \end{aligned} \tag{B.2}$$

Or in compressed form saving matrix multiplications and inversions:

$$\begin{aligned} \mathbf{H} &= \left(\mathbf{D} - \mathbf{C}\mathbf{A}^{-1}\mathbf{B}\right)^{-1}. \\ \mathbf{G} &= -\mathbf{H}\mathbf{C}\mathbf{A}^{-1}. \\ \mathbf{F} &= -\mathbf{A}^{-1}\mathbf{B}\mathbf{H}. \\ \mathbf{E} &= \mathbf{A}^{-1} - \mathbf{F}\mathbf{C}\mathbf{A}^{-1} \\ &= \mathbf{A}^{-1} - \mathbf{A}^{-1}\mathbf{B}\mathbf{G}. \end{aligned} \tag{B.3}$$

B.1.2. Block determinant

Let $\mathbf{M} \in \mathbb{C}^{n\times n}$, $\mathbf{u}, \mathbf{v} \in \mathbb{C}^{n\times m}$ and $\boldsymbol{\alpha} \in \mathbb{C}^{m\times m}$ be matrices, $\mathbf{M}$ having full rank. Then, the following identity holds:

$$\det \begin{pmatrix} \mathbf{M} & \mathbf{u} \\ \mathbf{v}^T & \boldsymbol{\alpha} \end{pmatrix} = \det \mathbf{M} \det\left(\boldsymbol{\alpha} - \mathbf{v}^T\mathbf{M}^{-1}\mathbf{u}\right). \tag{B.4}$$

The proof can be found easily:

$$\det \begin{pmatrix} \mathbf{M} & \mathbf{u} \\ \mathbf{v}^T & \boldsymbol{\alpha} \end{pmatrix} = \det\left\{ \begin{pmatrix} \mathbf{M} & 0 \\ 0 & \mathbf{1} \end{pmatrix} \left[\mathbf{1} + \begin{pmatrix} \mathbf{M}^{-1} & 0 \\ 0 & \mathbf{1} \end{pmatrix} \begin{pmatrix} \mathbf{u} \\ 0 \end{pmatrix} \begin{pmatrix} 0 & \mathbf{1} \end{pmatrix} + \begin{pmatrix} \mathbf{M}^{-1} & 0 \\ 0 & \mathbf{1} \end{pmatrix} \begin{pmatrix} 0 \\ \mathbf{1} \end{pmatrix} \begin{pmatrix} \mathbf{v}^T & [\boldsymbol{\alpha} - \mathbf{1}] \end{pmatrix} \right] \right\}. \tag{B.5}$$

Next, we make use of the fact that $\det(\mathbf{AB}) = \det \mathbf{A} \det \mathbf{B}$ in addition to

$$\det \begin{pmatrix} \mathbf{M} & 0 \\ 0 & \mathbf{1} \end{pmatrix} = \det \mathbf{M}, \quad \begin{pmatrix} \mathbf{M}^{-1} & 0 \\ 0 & \mathbf{1} \end{pmatrix} \begin{pmatrix} 0 \\ \mathbf{1} \end{pmatrix} = \begin{pmatrix} 0 \\ \mathbf{1} \end{pmatrix} \tag{B.6}$$

and obtain

$$\det \begin{pmatrix} \mathbf{M} & \mathbf{u} \\ \mathbf{v}^T & \boldsymbol{\alpha} \end{pmatrix} = \det \mathbf{M} \det\left[\begin{pmatrix} \mathbf{1} & \mathbf{M}^{-1}\mathbf{u} \\ 0 & \mathbf{1} \end{pmatrix} + \begin{pmatrix} 0 \\ \mathbf{1} \end{pmatrix} \begin{pmatrix} \mathbf{v}^T & [\boldsymbol{\alpha} - \mathbf{1}] \end{pmatrix} \right] \tag{B.7}$$

Using the block matrix inversion technique discussed in B.1.1, it is trivial to obtain

$$\begin{pmatrix} \mathbf{1} & \mathbf{M}^{-1}\mathbf{u} \\ 0 & \mathbf{1} \end{pmatrix}^{-1} = \begin{pmatrix} \mathbf{1} & -\mathbf{M}^{-1}\mathbf{u} \\ 0 & \mathbf{1} \end{pmatrix} \tag{B.8}$$

and therefore

$$\det \begin{pmatrix} \mathbf{M} & \mathbf{u} \\ \mathbf{v}^T & \boldsymbol{\alpha} \end{pmatrix} = \det \mathbf{M} \det \begin{pmatrix} \mathbf{1} & \mathbf{M}^{-1}\mathbf{u} \\ 0 & \mathbf{1} \end{pmatrix} \det \left[\mathbf{1} + \begin{pmatrix} \mathbf{1} & -\mathbf{M}^{-1}\mathbf{u} \\ 0 & \mathbf{1} \end{pmatrix} \begin{pmatrix} 0 \\ \mathbf{1} \end{pmatrix} \begin{pmatrix} \mathbf{v}^T & [\boldsymbol{\alpha} - \mathbf{1}] \end{pmatrix} \right]. \tag{B.9}$$

Noting that

$$\det \begin{pmatrix} \mathbf{1} & \mathbf{M}^{-1}\mathbf{u} \\ 0 & \mathbf{1} \end{pmatrix} = 1 \tag{B.10}$$

and exploiting Sylvester's theorem[1], we can reduce equation (B.9) to

$$\det \begin{pmatrix} \mathbf{M} & \mathbf{u} \\ \mathbf{v}^T & \boldsymbol{\alpha} \end{pmatrix} = \det \mathbf{M} \det \left[\mathbf{1} + \begin{pmatrix} \mathbf{v}^T & [\boldsymbol{\alpha} - \mathbf{1}] \end{pmatrix} \begin{pmatrix} \mathbf{1} & -\mathbf{M}^{-1}\mathbf{u} \\ 0 & \mathbf{1} \end{pmatrix} \begin{pmatrix} 0 \\ \mathbf{1} \end{pmatrix} \right]. \tag{B.12}$$

Multiplying out the block matrix product yields trivially equation (B.4) □.

B.1.3. Determinant lemma

Another well known identity follows directly from Sylvester's theorem mentioned in the previous section: The so called *determinant lemma.* It states that for an invertible matrix $\mathbf{A} \in \mathbb{C}^{n\times n}$ and two rectangular matrices $\mathbf{U}, \mathbf{V} \in \mathbb{C}^{n\times m}$ the following equation holds:

$$\det(\mathbf{A} + \mathbf{U}\mathbf{V}^T) = \det \mathbf{A} \det(\mathbf{1} + \mathbf{V}^T\mathbf{A}^{-1}\mathbf{U}). \tag{B.13}$$

B.1.4. Block matrix determinant identity

In this section a general determinant identity is proven, which can be used to derive Wick's theorem for contributions of a configuration C_n to physical observables. Let us define the vectors $\mathbf{u_i}$, $\mathbf{v_i} \in \mathbb{C}^m$ and the numbers $\alpha_{ij} \in \mathbb{C}$. Further, let $A \in \mathbb{C}^{m\times m}$ be a matrix of rank m. We define the non-singular matrices $\mathbf{M_n} \in \mathbb{C}^{(m+n)\times(m+n)}$ and $\mathbf{A_{ij}} \in \mathbb{C}^{(m+1)\times(m+1)}$ by:

$$\mathbf{M_n} = \begin{pmatrix} \mathbf{A} & \mathbf{u_1} & \dots & \mathbf{u_n} \\ \mathbf{v_1}^T & \alpha_{11} & \dots & \alpha_{1n} \\ \vdots & \vdots & \ddots & \vdots \\ \mathbf{v_n}^T & \alpha_{n1} & \dots & \alpha_{nn} \end{pmatrix}, \quad \mathbf{A_{ij}} = \begin{pmatrix} \mathbf{A} & \mathbf{u_j} \\ \mathbf{v_i}^T & \alpha_{ij} \end{pmatrix}. \tag{B.14}$$

With these definitions, the following determinant identity holds:

$$\det \mathbf{M_n} (\det \mathbf{A})^{n-1} = \det \begin{pmatrix} \det \mathbf{A_{11}} & \dots & \det \mathbf{A_{1n}} \\ \vdots & \ddots & \vdots \\ \det \mathbf{A_{n1}} & \dots & \det \mathbf{A_{nn}} \end{pmatrix}. \tag{B.15}$$

The identity can be proven by induction in n. It is trivial for $n = 1$, so we have to start with $n = 2$, where we have to show

$$\frac{\det \mathbf{M_2}}{\det \mathbf{A}} = \frac{\det \mathbf{A_{11}}}{\det \mathbf{A}} \frac{\det \mathbf{A_{22}}}{\det \mathbf{A}} - \frac{\det \mathbf{A_{12}}}{\det \mathbf{A}} \frac{\det \mathbf{A_{21}}}{\det \mathbf{A}}. \tag{B.16}$$

---

[1] For two appropriately sized matrices A and B, it states

$$\det(\mathbf{1} + \mathbf{AB}) = \det(\mathbf{1} + \mathbf{BA}). \tag{B.11}$$

A collection of proofs is provided in [34].

For the following calculations, we introduce several vectors:

$$\mathbf{u}^{\mathbf{1}}_{\mathbf{ij}} = \begin{pmatrix} \mathbf{u_j} \\ \alpha_{ij} - 1 \end{pmatrix}, \ \mathbf{v}^{\mathbf{2}}_{\mathbf{ij}} = \begin{pmatrix} \mathbf{v_i} \\ 0 \end{pmatrix}, \ \mathbf{u^2} = \mathbf{v^1} = \begin{pmatrix} \mathbf{0} \\ 1 \end{pmatrix} \in \mathbb{C}^{m+1}. \tag{B.17}$$

$$\mathbf{u}^{\mathbf{1}}_{\mathbf{M}} = \begin{pmatrix} \mathbf{u}_2 \\ \alpha_{12} \\ \alpha_{22} - 1 \end{pmatrix}, \mathbf{v}^{\mathbf{2}}_{\mathbf{M}} = \begin{pmatrix} \mathbf{v}_2 \\ \alpha_{21} \\ 0 \end{pmatrix}, \mathbf{u}^{\mathbf{2}}_{\mathbf{M}} = \mathbf{v}^{\mathbf{1}}_{\mathbf{M}} = \begin{pmatrix} \mathbf{0} \\ 1 \end{pmatrix} \in \mathbb{C}^{m+2}. \tag{B.18}$$

Let us define the *expanded* matrix $\mathbf{C}_{\text{ex}}$ of a square matrix $\mathbf{C}$ as the matrix C expanded by one row and one column containing a unit vector:

$$\mathbf{C}_{\text{ex}} = \begin{pmatrix} \mathbf{C} & \mathbf{0} \\ \mathbf{0}^T & 1 \end{pmatrix}. \tag{B.19}$$

As a last definition, we introduce the abbreviation $b_{ij} = \mathbf{v_i}^T \mathbf{A}^{-1} \mathbf{u_j}$. Using these notations, we can write the matrices $\mathbf{A_{ij}}$ as

$$\mathbf{A_{ij}} = \mathbf{A}_{\text{ex}} + \mathbf{u}^{\mathbf{1}}_{\mathbf{ij}} \mathbf{v^1}^T + \mathbf{u^2} \mathbf{v}^{\mathbf{2}}_{\mathbf{ij}}{}^T. \tag{B.20}$$

To calculate the determinant $\det \mathbf{A_{ij}}$, we use the matrix determinant lemma

$$\det(\mathbf{A} + \mathbf{u}\mathbf{v}^T) = (1 + \mathbf{v}^T \mathbf{A}^{-1} \mathbf{u}) \det \mathbf{A} \tag{B.21}$$

(cf. section B.1.3), yielding

$$\frac{\det \mathbf{A_{ij}}}{\det \mathbf{A}_{\text{ex}}} = \left[1 + \mathbf{v}^{\mathbf{2}}_{\mathbf{ij}}{}^T (\mathbf{A}_{\text{ex}} + \mathbf{u}^{\mathbf{1}}_{\mathbf{ij}} \mathbf{v^1}^T)^{-1} \mathbf{u^2} \right] (1 + \mathbf{v^1}^T \mathbf{A}_{\text{ex}}^{-1} \mathbf{u}^{\mathbf{1}}_{\mathbf{ij}}). \tag{B.22}$$

The inverse matrix of $(\mathbf{A}_{\text{ex}} + \mathbf{u}^{\mathbf{1}}_{\mathbf{ij}} \mathbf{v^1}^T)$ can be obtained from the Sherman-Morrison formula and a tedious calculation making use of the special form of the vectors and matrices gives the result

$$\frac{\det \mathbf{A_{ij}}}{\det \mathbf{A}} = \alpha_{ij} - b_{ij}. \tag{B.23}$$

From this, the right hand side of Eq. (B.16) can be easily obtained. For the left hand side, we have to perform an analogous calculation using the decomposition of the matrix $\mathbf{M_2}$:

$$\mathbf{M_2} = \mathbf{A_{11}}_{\text{ex}} + \mathbf{u}^{\mathbf{1}}_{\mathbf{M}} \mathbf{v}^{\mathbf{1}}_{\mathbf{M}}{}^T + \mathbf{u}^{\mathbf{2}}_{\mathbf{M}} \mathbf{v}^{\mathbf{2}}_{\mathbf{M}}{}^T. \tag{B.24}$$

Again, we apply the matrix determinant lemma two times and insert the Sherman-Morrison formula to calculate the inverse matrix of $(\mathbf{A_{11}}_{\text{ex}} + \mathbf{u}^{\mathbf{1}}_{\mathbf{M}} \mathbf{v}^{\mathbf{1}}_{\mathbf{M}}{}^T)$. Simplifying the result as far as possible, we finally arrive at

$$\frac{\det \mathbf{M_2}}{\det \mathbf{A}} = (\alpha_{11} - b_{11})(\alpha_{22} - b_{22}) - (\alpha_{12} - b_{12})(\alpha_{21} - b_{21}). \tag{B.25}$$

If we compare (B.25) with (B.23), it is clear, that Eq. (B.16) holds.

We now assume that for a certain value $n \in \mathbb{N}$ Eq. (B.15) holds. For $n + 1$, we can cast the matrix $\mathbf{M_{n+1}}$ in a form, where we can make use of Eq. (B.15) holding for n:

$$\mathbf{M_{n+1}} = \begin{pmatrix} \tilde{\mathbf{A}} & \tilde{\mathbf{u}}_{\mathbf{2}} & \cdots & \tilde{\mathbf{u}}_{\mathbf{n+1}} \\ \tilde{\mathbf{v}}_{\mathbf{2}}{}^T & \alpha_{2,2} & \cdots & \alpha_{2,n+1} \\ \vdots & \vdots & \ddots & \vdots \\ \tilde{\mathbf{v}}_{\mathbf{n}}{}^T & \alpha_{n,2} & \cdots & \alpha_{n,n+1} \\ \tilde{\mathbf{v}}_{\mathbf{n+1}}{}^T & \alpha_{n+1,2} & \cdots & \alpha_{n+1,n+1} \end{pmatrix}, \tag{B.26}$$

where we have introduced the new matrix $\tilde{\mathbf{A}}$ and the vectors $\tilde{\mathbf{u}}_{\mathbf{i}}$ and $\tilde{\mathbf{u}}_{\mathbf{j}}$ with:

$$\tilde{\mathbf{A}} = \begin{pmatrix} \mathbf{A} & \mathbf{u_1} \\ \mathbf{v_1}^T & \alpha_{11} \end{pmatrix}, \ \tilde{\mathbf{u}}_{\mathbf{i}} = \begin{pmatrix} \mathbf{u_i} \\ \alpha_{1i} \end{pmatrix}, \ \tilde{\mathbf{v}}_{\mathbf{i}} = \begin{pmatrix} \mathbf{v_i} \\ \alpha_{i1} \end{pmatrix}. \tag{B.27}$$

Further, we need the matrices $\mathbf{\tilde{A}_{ij}}$ defined analogously to (B.14):

$$\mathbf{\tilde{A}_{ij}} = \begin{pmatrix} \mathbf{\tilde{A}} & \mathbf{\tilde{u}_j} \\ \mathbf{\tilde{v}_i}^T & \alpha_{ij} \end{pmatrix} = \begin{pmatrix} \mathbf{A} & \mathbf{u_1} & \mathbf{u_j} \\ \mathbf{v_1}^T & \alpha_{11} & \alpha_{1j} \\ \mathbf{v_i}^T & \alpha_{i1} & \alpha_{ij} \end{pmatrix} \tag{B.28}$$

With these definitions, and with the abbreviations $a_{ij} = \det \mathbf{A_{ij}}$ and $\tilde{a}_{ij} = \det \mathbf{\tilde{A}_{ij}}$, we are now able to apply Eq. (B.15) holding for n:

$$\det \mathbf{M_{n+1}} (\det \mathbf{\tilde{A}})^{(n-1)} = \det \begin{pmatrix} \tilde{a}_{2,2} & \dots & \tilde{a}_{2,n+1} \\ \vdots & \ddots & \vdots \\ \tilde{a}_{n+1,2} & \dots & \tilde{a}_{n+1,n+1} \end{pmatrix}. \tag{B.29}$$

For $\tilde{a}_{ij}$, we make use of Eq. (B.15) with $n = 2$, which we have proved above:

$$\tilde{a}_{ij} = \frac{1}{\det \mathbf{A}} \left(a_{11} a_{ij} - a_{i1} a_{1j} \right). \tag{B.30}$$

Inserting this result in (B.29) yields a determinant with entries of the form $a_{11}a_{ij} - a_{i1}a_{1j}$. We make use of the multi linearity of the determinant to decompose this expression and we obtain a sum of determinants with prefactors of the form a_{ij}. Eliminating zero contributions, the resulting expression corresponds precisely to the Laplace-expansion of a larger determinant, and we finally obtain

$$\det \mathbf{M_{n+1}} \det \mathbf{A}^n = \det \begin{pmatrix} a_{1,1} & a_{1,2} & \dots & a_{1,n+1} \\ a_{2,1} & a_{2,2} & \dots & a_{2,n+1} \\ \vdots & \vdots & \ddots & \vdots \\ a_{n+1,1} & a_{n+1,2} & \dots & a_{n+1,n+1} \end{pmatrix}. \tag{B.31}$$

This is the identity (B.15) for $n + 1$. Hence we have derived the determinant identity for $n + 1$ using only the identity for n and $n = 2$. By induction, the identity (B.15) therefore holds for every $n \in \mathbb{N}$, as it is trivial for $n = 1$.

B.2. Matsubara sums

Using the standard summation trick employing complex analysis and the residue theorem, presented in detail in section 4.5.2 by studying the complex contour integral $\oint \mathrm{d}z\, n_F(z) \frac{1}{z}$ for the evaluation of $\sum_{\mathrm{i}\omega_n} \frac{1}{\mathrm{i}\omega_n}$, we obtain[2]:

$$\frac{1}{\beta} \sum_{\mathrm{i}\omega_n} \frac{1}{\mathrm{i}\omega_n} = \frac{1}{2}. \tag{B.33}$$

Using this identity, we can formally write:

$$\frac{1}{\beta} \sum_{\mathrm{i}\omega_n} \mathrm{e}^{-\mathrm{i}\omega_n \tau} = \delta(\tau). \tag{B.34}$$

For the closure of the Fourier transforms for example in equation (2.5), the other direction is obtained trivially as

$$\frac{1}{\beta} \int_0^\beta \mathrm{d}\tau \mathrm{e}^{\mathrm{i}\nu\tau} = \delta_{\nu,0}. \tag{B.35}$$

---

[2] Note that this sum only converges, if we introduce a conversion inducing factor $\mathrm{e}^{\mathrm{i}\omega_n 0^+}$, this is understood implicitly when writing sums of this form, i.e.:

$$\sum_{\mathrm{i}\omega_n} \frac{1}{\mathrm{i}\omega_n} := \sum_{\mathrm{i}\omega_n} \frac{\mathrm{e}^{\mathrm{i}\omega_n 0^+}}{\mathrm{i}\omega_n}. \tag{B.32}$$

Note the use of the *bosonic* Matsubara frequency here, as differences of fermionic Matsubara frequencies are always bosonic and fulfill therefore the identity

$$\mathrm{e}^{\mathrm{i}\nu} = 1. \tag{B.36}$$

B.3. Dirac identity

A very important mathematical identity is the so called *Dirac identity*, which provides the link between Green's functions and spectral functions[3]:

$$\frac{1}{x + \mathrm{i}0^{+}} = -\mathrm{i}\pi\delta(x) + \mathcal{P}\left(\frac{1}{x}\right), \tag{B.37}$$

where $\mathcal{P}$ is the principal value of $\frac{1}{x}$.

---

[3] This is apparent when thought about in terms of Lehmann representations.

Bibliography

[1] A. Hewson. *The Kondo Problem to Heavy Fermions.* Cambridge University Press, Cambridge, England, 1993. ISBN 0521599474.

[2] J.G. Bednorz and K.A. Müller. Possible highTc superconductivity in the Ba–La–Cu–O system. *Zeitschrift für Physik B Condensed Matter*, 64:189–193, 1986. ISSN 0722-3277. doi: 10.1007/BF01303701. URL `http://dx.doi.org/10.1007/BF01303701`.

[3] Tobias Meng, Serge Florens, and Pascal Simon. Self-consistent description of andreev bound states in josephson quantum dot devices. *Physical Review B*, 79(22):224521, 06 2009. URL `http://link.aps.org/doi/10.1103/PhysRevB.79.224521`.

[4] Sandro Sorella, Yuichi Otsuka, and Seiji Yunoki. Absence of a Spin Liquid Phase in the Hubbard Model on the Honeycomb Lattice. *eprint arXiv:1207.1783*, July 2012.

[5] Michael E. Fisher. The renormalization group in the theory of critical behavior. *Rev. Mod. Phys.*, 46: 597–616, Oct 1974. doi: 10.1103/RevModPhys.46.597. URL `http://link.aps.org/doi/10.1103/RevModPhys.46.597`.

[6] R. Shankar. Renormalization-group approach to interacting fermions. *Rev. Mod. Phys.*, 66:129–192, Jan 1994. doi: 10.1103/RevModPhys.66.129. URL `http://link.aps.org/doi/10.1103/RevModPhys.66.129`.

[7] R. Blankenbecler, D. J. Scalapino, and R. L. Sugar. Monte Carlo calculations of coupled boson-fermion systems. I. *Phys. Rev. D*, 24:2278–2286, Oct 1981. doi: 10.1103/PhysRevD.24.2278. URL `http://link.aps.org/doi/10.1103/PhysRevD.24.2278`.

[8] J. E. Hirsch and R. M. Fye. Monte Carlo Method for Magnetic Impurities in Metals. *Phys. Rev. Lett.*, 56:2521–2524, Jun 1986. doi: 10.1103/PhysRevLett.56.2521. URL `http://link.aps.org/doi/10.1103/PhysRevLett.56.2521`.

[9] A. N. Rubtsov, V. V. Savkin, and A. I. Lichtenstein. Continuous-time quantum Monte Carlo method for fermions. *Phys. Rev. B*, 72:035122, Jul 2005. doi: 10.1103/PhysRevB.72.035122. URL `http://link.aps.org/doi/10.1103/PhysRevB.72.035122`.

[10] F. F. Assaad and T. C. Lang. Diagrammatic determinantal quantum Monte Carlo methods: Projective schemes and applications to the Hubbard-Holstein model. *Phys. Rev. B*, 76:035116, Jul 2007. doi: 10.1103/PhysRevB.76.035116. URL `http://link.aps.org/doi/10.1103/PhysRevB.76.035116`.

[11] Gull, E., Werner, P., Parcollet, O., and Troyer, M. Continuous-time auxiliary-field Monte Carlo for quantum impurity models. *EPL*, 82(5):57003, 2008. doi: 10.1209/0295-5075/82/57003. URL `http://dx.doi.org/10.1209/0295-5075/82/57003`.

[12] S. M. A. Rombouts, K. Heyde, and N. Jachowicz. Quantum Monte Carlo Method for Fermions, Free of Discretization Errors. *Phys. Rev. Lett.*, 82:4155–4159, May 1999. doi: 10.1103/PhysRevLett.82.4155. URL `http://link.aps.org/doi/10.1103/PhysRevLett.82.4155`.

[13] Steven R. White. Density matrix formulation for quantum renormalization groups. *Phys. Rev. Lett.*, 69:2863–2866, Nov 1992. doi: 10.1103/PhysRevLett.69.2863. URL `http://link.aps.org/doi/10.1103/PhysRevLett.69.2863`.

[14] F. Verstraete, V. Murg, and J.I. Cirac. Matrix product states, projected entangled pair states, and variational renormalization group methods for quantum spin systems. *Advances in Physics*, 57(2):143–224, 2008. doi: 10.1080/14789940801912366. URL `http://www.tandfonline.com/doi/abs/10.1080/14789940801912366`.

[15] Antoine Georges, Gabriel Kotliar, Werner Krauth, and Marcelo J. Rozenberg. Dynamical mean-field theory of strongly correlated fermion systems and the limit of infinite dimensions. *Rev. Mod. Phys.*, 68 (1):13, Jan 1996. doi: 10.1103/RevModPhys.68.13.

[16] Thomas Maier, Mark Jarrell, Thomas Pruschke, and Matthias H. Hettler. Quantum cluster theories. *Rev. Mod. Phys.*, 77:1027–1080, Oct 2005. doi: 10.1103/RevModPhys.77.1027. URL `http://link.aps.org/doi/10.1103/RevModPhys.77.1027`.

[17] A. N. Rubtsov, M. I. Katsnelson, and A. I. Lichtenstein. Dual fermion approach to nonlocal correlations in the Hubbard model. *Phys. Rev. B*, 77:033101, Jan 2008. doi: 10.1103/PhysRevB.77.033101. URL `http://link.aps.org/doi/10.1103/PhysRevB.77.033101`.

[18] A. Toschi, A. A. Katanin, and K. Held. Dynamical vertex approximation: A step beyond dynamical mean-field theory. *Phys. Rev. B*, 75:045118, Jan 2007. doi: 10.1103/PhysRevB.75.045118. URL `http://link.aps.org/doi/10.1103/PhysRevB.75.045118`.

[19] G. Alvarez, M. S. Summers, D. E. Maxwell, M. Eisenbach, J. S. Meredith, J. M. Larkin, J. Levesque, T. A. Maier, P. R. C. Kent, E. F. D'Azevedo, and T. C. Schulthess. New algorithm to enable 400+ TFlop/s sustained performance in simulations of disorder effects in high-Tc superconductors. In *Proceedings of the 2008 ACM/IEEE conference on Supercomputing*, SC '08, pages 61:1–61:10, Piscataway, NJ, USA, 2008. IEEE Press. ISBN 978-1-4244-2835-9. URL `http://dl.acm.org/citation.cfm?id=1413370.1413433`.

[20] H. G. Evertz. The loop algorithm. *Advances in Physics*, 52(1):1–66, 2003. doi: 10.1080/0001873021000049195. URL `http://www.tandfonline.com/doi/abs/10.1080/0001873021000049195`.

[21] Emanuel Gull, Andrew J. Millis, Alexander I. Lichtenstein, Alexey N. Rubtsov, Matthias Troyer, and Philipp Werner. Continuous-time Monte Carlo methods for quantum impurity models. *Rev. Mod. Phys.*, 83:349–404, May 2011. doi: 10.1103/RevModPhys.83.349. URL `http://link.aps.org/doi/10.1103/RevModPhys.83.349`.

[22] Lanczos, Cornelius. *J. Res. Nat. Bur. Stand.*, 45:255, 1950.

[23] Sebastian Fuchs, Emanuel Gull, Matthias Troyer, Mark Jarrell, and Thomas Pruschke. Spectral properties of the three-dimensional Hubbard model. *Phys. Rev. B*, 83:235113, Jun 2011. doi: 10.1103/PhysRevB.83.235113. URL `http://link.aps.org/doi/10.1103/PhysRevB.83.235113`.

[24] David J. Luitz and Fakher F. Assaad. Weak-coupling continuous-time quantum Monte Carlo study of the single impurity and periodic Anderson models with s-wave superconducting baths. *Phys. Rev. B*, 81:024509, Jan 2010. doi: 10.1103/PhysRevB.81.024509. URL `http://link.aps.org/doi/10.1103/PhysRevB.81.024509`.

[25] Alexander Altland and Ben Simons. *Condensed Matter Field Theory*. Cambridge University Press, 6 2006. ISBN 9780521845083.

[26] John W. Negele and Henri Orland. *Quantum Many-particle Systems (Advanced Books Classics)*. Westview Press, 1998. ISBN 0738200522.

[27] Franz Wegner. *Grassmann Variable*. Universität Heidelberg, 1998. URL `http://www.tphys.uni-heidelberg.de/~wegner/grassmann.ps`.

[28] D. J. Luitz, F. F. Assaad, T. Novotný, C. Karrasch, and V. Meden. Understanding the Josephson Current through a Kondo-Correlated Quantum Dot. *Phys. Rev. Lett.*, 108:227001, May 2012. doi: 10.1103/PhysRevLett.108.227001. URL `http://link.aps.org/doi/10.1103/PhysRevLett.108.227001`.

[29] Z. Y. Meng, T. C. Lang, S. Wessel, F. F. Assaad, and A. Muramatsu. Quantum spin liquid emerging in two-dimensional correlated Dirac fermions. *Nature*, 464:847–851, April 2010. doi: 10.1038/nature08942. URL `http://www.nature.com/nature/journal/v464/n7290/suppinfo/nature08942_S1.html`.

[30] Philipp Werner and Andrew J. Millis. Hybridization expansion impurity solver: General formulation and application to Kondo lattice and two-orbital models. *Phys. Rev. B*, 74:155107, Oct 2006. doi: 10.1103/PhysRevB.74.155107. URL `http://link.aps.org/doi/10.1103/PhysRevB.74.155107`.

[31] Martin Hohenadler, Stefan Wessel, Maria Daghofer, and Fakher F. Assaad. Interaction-range effects for fermions in one dimension. *Phys. Rev. B*, 85:195115, May 2012. doi: 10.1103/PhysRevB.85.195115. URL `http://link.aps.org/doi/10.1103/PhysRevB.85.195115`.

[32] Fakher F. Assaad. Monte Carlo Methods. unpublished, 2006.

[33] Nicholas Metropolis, Arianna W. Rosenbluth, Marshall N. Rosenbluth, Augusta H. Teller, and Edward Teller. Equation of State Calculations by Fast Computing Machines. *The Journal of Chemical Physics*, 21 (6):1087–1092, 1953. doi: 10.1063/1.1699114. URL `http://link.aip.org/link/?JCP/21/1087/1`.

[34] Alkiviadis G. Akritas, Evgenia K. Akritas, and Genadii I. Malaschonok. Various proofs of Sylvester's (determinant) identity. *Mathematics and Computers in Simulation*, 42(4–6):585 – 593, 1996. ISSN 0378-4754. doi: 10.1016/S0378-4754(96)00035-3. URL `http://www.sciencedirect.com/science/article/pii/S0378475496000353`. Symbolic Computation, New Trends and Developments.

[35] Anders W. Sandvik and Juhani Kurkijärvi. Quantum Monte Carlo simulation method for spin systems. *Phys. Rev. B*, 43:5950–5961, Mar 1991. doi: 10.1103/PhysRevB.43.5950. URL `http://link.aps.org/doi/10.1103/PhysRevB.43.5950`.

[36] K. Mikelsons, A. Macridin, and M. Jarrell. Relationship between Hirsch-Fye and weak-coupling diagrammatic quantum Monte Carlo methods. *Phys. Rev. E*, 79:057701, May 2009. doi: 10.1103/PhysRevE.79.057701. URL `http://link.aps.org/doi/10.1103/PhysRevE.79.057701`.

[37] William H. Press, Saul A. Teukolsky, William T. Vetterling, and Brian P. Flannery. *Numerical Recipes 3rd Edition: The Art of Scientific Computing*. Cambridge University Press, New York, NY, USA, 3 edition, 2007. ISBN 0521880688, 9780521880688.

[38] Karlis Mikelsons. *Extensions of Numerical Methods for Strongly Correlated Electron Systems*. PhD thesis, 2009. URL `http://gradworks.umi.com/3389709.pdf`.

[39] Florian Goth and Fakher F. Assaad. Time and spatially resolved quench of the fermionic Hubbard model showing restricted equilibration. *Phys. Rev. B*, 85:085129, Feb 2012. doi: 10.1103/PhysRevB.85.085129. URL `http://link.aps.org/doi/10.1103/PhysRevB.85.085129`.

[40] Cyrano De Dominicis and Paul C. Martin. Stationary Entropy Principle and Renormalization in Normal and Superfluid Systems. I. Algebraic Formulation. *Journal of Mathematical Physics*, 5(1):14–30, 1964. doi: 10.1063/1.1704062. URL `http://link.aip.org/link/?JMP/5/14/1`.

[41] S. X. Yang, H. Fotso, J. Liu, T. A. Maier, K. Tomko, E. F. D'Azevedo, R. T. Scalettar, T. Pruschke, and M. Jarrell. Parquet approximation for the 4×4 Hubbard cluster. *Phys. Rev. E*, 80:046706, Oct 2009. doi: 10.1103/PhysRevE.80.046706. URL `http://link.aps.org/doi/10.1103/PhysRevE.80.046706`.

[42] K. S. D. Beach. Identifying the maximum entropy method as a special limit of stochastic analytic continuation. *eprint arXiv:cond-mat/0403055*, March 2004.

[43] M. Jarrell, Th. Maier, C. Huscroft, and S. Moukouri. Quantum Monte Carlo algorithm for nonlocal corrections to the dynamical mean-field approximation. *Phys. Rev. B*, 64:195130, Oct 2001. doi: 10.1103/PhysRevB.64.195130. URL `http://link.aps.org/doi/10.1103/PhysRevB.64.195130`.

[44] N. E. Bickers. *Self-Consistent Many-Body Theory for Condensed Matter Systems.* CRM Series in Mathematical Physics. Springer New York, 2004. ISBN 978-0-387-21717-8. URL `http://dx.doi.org/10.1007/0-387-21717-7_6`.

[45] Jutta Ortloff. *unpublished.* PhD thesis, Universität Würzburg, 2013.

[46] Andreas Eberlein and Walter Metzner. Parametrization of Nambu Vertex in a Singlet Superconductor. *Progress of Theoretical Physics*, 124(3):471–491, 2010. doi: 10.1143/PTP.124.471. URL `http://ptp.ipap.jp/link?PTP/124/471/`.

[47] G. Rohringer, A. Valli, and A. Toschi. Local electronic correlation at the two-particle level. *Phys. Rev. B*, 86:125114, Sep 2012. doi: 10.1103/PhysRevB.86.125114. URL `http://link.aps.org/doi/10.1103/PhysRevB.86.125114`.

[48] Jan Kuneš. Efficient treatment of two-particle vertices in dynamical mean-field theory. *Phys. Rev. B*, 83:085102, Feb 2011. doi: 10.1103/PhysRevB.83.085102. URL `http://link.aps.org/doi/10.1103/PhysRevB.83.085102`.

[49] Hartmut Monien. *Math. Comp.*, 79:857–869, 2010.

[50] Lewin Boehnke, Hartmut Hafermann, Michel Ferrero, Frank Lechermann, and Olivier Parcollet. Orthogonal Polynomial Representation of Imaginary Time Green Functions . *arXiv:1104.3215v2*, 2011.

[51] Wolfgang Nolting. *Grundkurs Theoretische Physik 7: Viel-Teilchen-Theorie (Springer-Lehrbuch).* Springer Berlin Heidelberg, 7., aktualisierte aufl. edition, September 2009. ISBN 9783642016059.

[52] David Ascher, Paul F. Dubois, Konrad Hinsen, James Hugunin, and Travis Oliphant. *Numerical Python.* Lawrence Livermore National Laboratory, Livermore, CA, ucrl-ma-128569 edition, 1999. URL `http://dsnra.jpl.nasa.gov/software/Python/numpydoc/index.html`.

[53] G. C. Wick. The Evaluation of the Collision Matrix. *Phys. Rev.*, 80:268–272, Oct 1950. doi: 10.1103/PhysRev.80.268. URL `http://link.aps.org/doi/10.1103/PhysRev.80.268`.

[54] Henrik Bruus and Karsten Flensberg. *Many-Body Quantum Theory in Condensed Matter Physics: An Introduction (Oxford Graduate Texts).* Oxford University Press, USA, 2004. ISBN 0198566336.

[55] Gerald D. Mahan. *Many Particle Physics (Physics of Solids and Liquids).* Springer, 2010. ISBN 1441933395.

[56] A. A. Abrikosov. *Methods of Quantum Field Theory in Statistical Physics (Dover Books on Physics).* Dover Publications, 1975. ISBN 0486632288.

[57] Anders W. Sandvik. Stochastic method for analytic continuation of quantum Monte Carlo data. *Phys. Rev. B*, 57:10287–10290, May 1998. doi: 10.1103/PhysRevB.57.10287. URL `http://link.aps.org/doi/10.1103/PhysRevB.57.10287`.

[58] David J. Luitz and Fakher F. Assaad. Calculation of the dynamical spin susceptibility in DCA. in preparation, 2013.

[59] Hiroyuki Shiba. Classical Spins in Superconductors. *Prog. Theor. Phys.*, 40(3):435–451, September 1968.

[60] Akio Sakurai. Comments on Superconductors with Magnetic Impurities . *Prog. Theor. Phys.*, 44(6):1472–1476, December 1970.

[61] Silvano De Franceschi, Leo Kouwenhoven, Christian Schönenberger, and Wolfgang Wernsdorfer. Hybrid superconductor-quantum dot devices. *Nat Nano*, 5(10):703–711, 10 2010. URL `http://dx.doi.org/10.1038/nnano.2010.173`.

[62] A. Yu. Kasumov, R. Deblock, M. Kociak, B. Reulet, H. Bouchiat, I. I. Khodos, Yu. B. Gorbatov, V. T. Volkov, C. Journet, and M. Burghard. Supercurrents through single-walled carbon nanotubes. *Science*, 284(5419):1508–1511, 05 1999. URL `http://www.sciencemag.org/content/284/5419/1508`.

[63] Jorden A. van Dam, Yuli V. Nazarov, Erik P. A. M. Bakkers, Silvano De Franceschi, and Leo P. Kouwenhoven. Supercurrent reversal in quantum dots. *Nature*, 442(7103):667–670, 08 2006. URL `http://dx.doi.org/10.1038/nature05018`.

[64] J. P. Cleuziou, W. Wernsdorfer, V. Bouchiat, T. Ondarcuhu, and M. Monthioux. Carbon nanotube superconducting quantum interference device. *Nat Nano*, 1(1):53–59, 10 2006. URL `http://dx.doi.org/10.1038/nnano.2006.54`.

[65] H. Ingerslev Jørgensen, T. Novotný, K. Grove-Rasmussen, K. Flensberg, and P. E. Lindelof. Critical current 0–π transition in designed josephson quantum dot junctions. *Nano Letters*, 7(8):2441–2445, 2011/11/24 2007. doi: 10.1021/nl071152w. URL `http://dx.doi.org/10.1021/nl071152w`.

[66] A. Eichler, R. Deblock, M. Weiss, C. Karrasch, V. Meden, C. Schönenberger, and H. Bouchiat. Tuning the josephson current in carbon nanotubes with the kondo effect. *Physical Review B*, 79(16):161407, 04 2009. URL `http://link.aps.org/doi/10.1103/PhysRevB.79.161407`.

[67] Romain Maurand, Tobias Meng, Edgar Bonet, Serge Florens, Laëtitia Marty, and Wolfgang Wernsdorfer. First order $0-pi$ quantum phase transition in the kondo regime of a superconducting carbon nanotube quantum dot. 2011. URL `http://arxiv.org/abs/1110.2067`.

[68] M. Tinkham. *Introduction to superconductivity*. McGraw–Hill, New York, 1996. ISBN 0486435032.

[69] L. I. Glazman and K. A. Matveev. Resonant josephson current through kondo impurities in a tunnel barrier. *JETP Lett.*, 49(10):659, May 1989.

[70] T.Matsuura. *Prog. Theor. Phys.*, 57:1823, 1977.

[71] Brian David Josephson. Possible new effects in superconductive tunnelling. *Phys. Lett.*, 1(7):251–253, July 1962.

[72] I. O. Kulik. Magnitude of the critical Josephson tunnel current. *Sov. Phys. JETP*, 22(4):841–843, April 1966.

[73] L. I. Galzman and K. A. Matveev. Resonant Josephson current through Kondo impurities in a tunnel Barrier. *JETP Lett.*, 49(10):659–662, May 1989.

[74] B. I. Spivak and S. A. Kivelson. Negative local superfluid densities: The difference between dirty superconductors and dirty Bose liquids. *Phys. Rev. B*, 43(4):3740–3743, Feb 1991. doi: 10.1103/PhysRevB.43.3740.

[75] K Grove-Rasmussen, H Ingerslev Jørgensen, and P E Lindelof. Kondo resonance enhanced supercurrent in single wall carbon nanotube Josephson junctions. *New Journal of Physics*, 9(5):124, 2007. URL `http://stacks.iop.org/1367-2630/9/124`.

[76] H. I. Jørgensen, K. Grove-Rasmussen, T. Novotný, K. Flensberg, and P. E. Lindelof. Electron Transport in Single-Wall Carbon Nanotube Weak Links in the Fabry-Perot Regime. *Physical Review Letters*, 96 (20):207003, 2006. doi: 10.1103/PhysRevLett.96.207003. URL `http://link.aps.org/abstract/PRL/v96/e207003`.

[77] T. Sand-Jespersen, J. Paaske, B. M. Andersen, K. Grove-Rasmussen, H. I. Jørgensen, M. Aagesen, C. B. Sørensen, P. E. Lindelof, K. Flensberg, and J. Nygård. Kondo-Enhanced Andreev Tunneling in InAs Nanowire Quantum Dots. *Physical Review Letters*, 99(12):126603, 2007. doi: 10.1103/PhysRevLett.99.126603. URL `http://link.aps.org/abstract/PRL/v99/e126603`.

[78] A. Eichler, M. Weiss, S. Oberholzer, C. Schönenberger, A. Levy Yeyati, J. C. Cuevas, and A. Martín-Rodero. Even-Odd Effect in Andreev Transport through a Carbon Nanotube Quantum Dot. *Physical Review Letters*, 99(12):126602, 2007. doi: 10.1103/PhysRevLett.99.126602. URL `http://link.aps.org/abstract/PRL/v99/e126602`.

[79] M. R. Buitelaar, T. Nussbaumer, and C. Schönenberger. Quantum Dot in the Kondo Regime Coupled to Superconductors. *Phys. Rev. Lett.*, 89(25):256801, Dec 2002. doi: 10.1103/PhysRevLett.89.256801.

[80] Hiroyuki Shiba. A hartree-fock theory of transition-metal impurities in a superconductor. *Progress of Theoretical Physics*, 50(1):50–73, 1973. doi: 10.1143/PTP.50.50. URL `http://ptp.ipap.jp/link?PTP/50/50/`.

[81] Aashish A. Clerk and Vinay Ambegaokar. Loss of π-junction behavior in an interacting impurity josephson junction. *Physical Review B*, 61(13):9109–9112, 04 2000. URL `http://link.aps.org/doi/10.1103/PhysRevB.61.9109`.

[82] Gabriel Sellier, Thilo Kopp, Johann Kroha, and Yuri S. Barash. π-junction behavior and Andreev bound states in Kondo quantum dots with superconducting leads. *Physical Review B*, 72(17):174502, 11 2005. URL `http://link.aps.org/doi/10.1103/PhysRevB.72.174502`.

[83] Mahn-Soo Choi, Minchul Lee, Kicheon Kang, and W. Belzig. Kondo effect and josephson current through a quantum dot between two superconductors. *Physical Review B*, 70(2):020502, 07 2004. URL `http://link.aps.org/doi/10.1103/PhysRevB.70.020502`.

[84] C. Karrasch, A. Oguri, and V. Meden. Josephson current through a single Anderson impurity coupled to BCS leads. *Physical Review B*, 77(2):024517, 01 2008. URL `http://link.aps.org/doi/10.1103/PhysRevB.77.024517`.

[85] Akira Oguri, Yoshihide Tanaka, and A. C. Hewson. Quantum Phase Transition in a Minimal Model for the Kondo Effect in a Josephson Junction. *Journal of the Physical Society of Japan*, 73(9):2494–2504, 2004. doi: 10.1143/JPSJ.73.2494. URL `http://jpsj.ipap.jp/link?JPSJ/73/2494/`.

[86] J. Bauer, A. Oguri, and A. C. Hewson. Spectral properties of locally correlated electrons in a Bardeen-Cooper-Schrieffer superconductor. *Journal of Physics: Condensed Matter*, 19(48):486211 (19pp), 2007. URL `http://stacks.iop.org/0953-8984/19/486211`.

[87] T. Hecht, A. Weichselbaum, J. von Delft, and R. Bulla. Numerical renormalization group calculation of near-gap peaks in spectral functions of the Anderson model with superconducting leads. *Journal of Physics: Condensed Matter*, 20(27):275213 (10pp), 2008. URL `http://stacks.iop.org/0953-8984/20/275213`.

[88] F. Siano and R. Egger. Josephson current through a nanoscale magnetic quantum dot. *Physical Review Letters*, 93(4):047002, 07 2004. URL `http://link.aps.org/doi/10.1103/PhysRevLett.93.047002`.

[89] F. Siano and R. Egger. Erratum: Josephson Current through a Nanoscale Magnetic Quantum Dot [Phys. Rev. Lett. 93, 047002 (2004)]. *Physical Review Letters*, 94(3):039902, 01 2005. URL `http://link.aps.org/doi/10.1103/PhysRevLett.94.039902`.

[90] F. Siano and R. Egger. Siano and Egger Reply:. *Physical Review Letters*, 94(22):229702, 06 2005. URL `http://link.aps.org/doi/10.1103/PhysRevLett.94.229702`.

[91] A. V. Rozhkov and Daniel P. Arovas. Interacting-impurity Josephson junction: Variational wave functions and slave-boson mean-field theory. *Phys. Rev. B*, 62(10):6687–6691, Sep 2000. doi: 10.1103/PhysRevB.62.6687.

[92] E. Vecino, A. Martín-Rodero, and A. Levy Yeyati. Josephson current through a correlated quantum level: Andreev states and π junction behavior. *Phys. Rev. B*, 68(3):035105, Jul 2003. doi: 10.1103/PhysRevB.68.035105.

[93] M. I. Salkola, A. V. Balatsky, and J. R. Schrieffer. Spectral properties of quasiparticle excitations induced by magnetic moments in superconductors . *Phys. Rev. B*, 55(18):12648–12661, May 1997. doi: 10.1103/PhysRevB.55.12648.

[94] A. V. Balatsky, I. Vekhter, and Jian-Xin Zhu. Impurity-induced states in conventional and unconventional superconductors. *Reviews of Modern Physics*, 78(2):373, 2006. doi: 10.1103/RevModPhys.78.373. URL `http://link.aps.org/abstract/RMP/v78/p373`.

[95] Alexander Cyril Hewson and David Edwards. *The Kondo Problem to Heavy Fermions (Cambridge Studies in Magnetism)*. Cambridge University Press, 2003. ISBN 0521599474.

[96] A. V. Rozhkov and Daniel P. Arovas. Josephson Coupling through a Magnetic Impurity. *Phys. Rev. Lett.*, 82(13):2788–2791, Mar 1999. doi: 10.1103/PhysRevLett.82.2788. URL `http://prola.aps.org/abstract/PRL/v82/i13/p2788_1`.

[97] C. Benjamin, T. Jonckheere, A. Zazunov, and T. Martin. Controllable π junction in a Josephson quantum-dot device with molecular spin . *Eur. Phys. J. B*, 57:279–289, June 2007.

[98] Sander J. Tans, Michel H. Devoret, Hongjie Dai, Andreas Thess, Richard E. Smalley, L. J. Geerligs, and Cees Dekker. Individual single-wall carbon nanotubes as quantum wires. *Nature*, 386(6624):474–477, 04 1997. URL `http://dx.doi.org/10.1038/386474a0`.

[99] C. Karrasch, V. Meden, and K. Schönhammer. Finite-temperature linear conductance from the matsubara green's function without analytic continuation to the real axis. *Physical Review B*, 82(12):125114, 09 2010. URL `http://link.aps.org/doi/10.1103/PhysRevB.82.125114`.

[100] Hartmut Monien. Gaussian summation: An exponentially converging summation scheme. 2006. URL `http://arxiv.org/abs/math/0611057v1`. eprint arXiv:math/0611057v1.

[101] T. A. Costi. Magnetotransport through a strongly interacting quantum dot. *Physical Review B*, 64(24): 241310, 12 2001. URL `http://link.aps.org/doi/10.1103/PhysRevB.64.241310`.

[102] Y. M. Ivanchenko and L. A. Zil'Berman. The Josephson Effect in Small Tunnel Contacts. *JEPT Lett.*, 28: 1272, 1969.

[103] J. Bauer and A. C. Hewson. Quasiparticle excitations and dynamic susceptibilities in the BCS-BEC crossover. *EPL (Europhysics Letters)*, 85(2):27001 (6pp), 2009. URL `http://stacks.iop.org/0295-5075/85/27001`.

[104] J. Bauer, A. C. Hewson, and N. Dupuis. Dynamical mean-field theory and numerical renormalization group study of superconductivity in the attractive Hubbard model. arXiv:0901.1760v2, May 2009. URL `http://arxiv.org/abs/0901.1760`.

[105] Gabriel Kotliar and Andrei E. Ruckenstein. New Functional Integral Approach to Strongly Correlated Fermi Systems: The Gutzwiller Approximation as a Saddle Point. *Phys. Rev. Lett.*, 57(11):1362–1365, Sep 1986. doi: 10.1103/PhysRevLett.57.1362.

[106] David J. Luitz, Fakher F. Assaad, and Manuel J. Schmidt. Exact diagonalization study of the tunable edge magnetism in graphene. *Phys. Rev. B*, 83:195432, May 2011. doi: 10.1103/PhysRevB.83.195432. URL `http://link.aps.org/doi/10.1103/PhysRevB.83.195432`.

[107] K. S. Novoselov, A. K. Geim, S. V. Morozov, D. Jiang, Y. Zhang, S. V. Dubonos, I. V. Grigorieva, and A. A. Firsov. Electric Field Effect in Atomically Thin Carbon Films. *Science*, 306(5696):666–669, 2004. doi: 10.1126/science.1102896.

[108] A. H. Castro Neto, F. Guinea, N. M. R. Peres, K. S. Novoselov, and A. K. Geim. The electronic properties of graphene. *Rev. Mod. Phys.*, 81(1):109–162, Jan 2009. doi: 10.1103/RevModPhys.81.109.

[109] Changgu Lee, Xiaoding Weil, Jeffrey W. Kysar, and James Hone. Measurement of the Elastic Properties and Intrinsic Strength of Monolayer Graphene. *Science*, 321:385–388, 2008. doi: 10.1126/science.1157996.

[110] Yuanbo Zhang, Yan-Wen Tan, Horst L. Stormer, and Philip Kim. Experimental observation of the quantum Hall effect and Berry's phase in graphene. *Nature*, 438(7065):201–204, Nov 2005. ISSN 0028-0836. doi: 10.1038/nature04235. URL `http://dx.doi.org/10.1038/nature04235`.

[111] K. S. Novoselov, A. K. Geim, S. V. Morozov, D. Jiang, M. I. Katsnelson, I. V. Grigorieva, S. V. Dubonos, and A. A. Firsov. Two-dimensional gas of massless Dirac fermions in graphene. *Nature*, 438(7065): 197–200, Nov 2005. ISSN 0028-0836. doi: 10.1038/nature04233.

[112] Mitsutaka Fujita, Katsunori Wakabayashi, Kyoko Nakada, and Koichi Kusakabe. Peculiar Localized State at Zigzag Graphite Edge. *Journal of the Physical Society of Japan*, 65(7):1920–1923, 1996. doi: 10.1143/JPSJ.65.1920. URL `http://jpsj.ipap.jp/link?JPSJ/65/1920/`.

[113] Young-Woo Son, Marvin L. Cohen, and Steven G. Louie. Energy Gaps in Graphene Nanoribbons. *Phys. Rev. Lett.*, 97(21):216803, Nov 2006. doi: 10.1103/PhysRevLett.97.216803.

[114] Young-Woo Son, Marvin L. Cohen, and Steven G. Louie. *Nature*, 444:347, 2007. doi: 10.1038/nature05180.

[115] J. Jung and A. H. MacDonald. Carrier density and magnetism in graphene zigzag nanoribbons. *Phys. Rev. B*, 79(23):235433, Jun 2009. doi: 10.1103/PhysRevB.79.235433.

[116] Hélène Feldner, Zi Yang Meng, Andreas Honecker, Daniel Cabra, Stefan Wessel, and Fakher F. Assaad. Magnetism of finite graphene samples: Mean-field theory compared with exact diagonalization and quantum Monte Carlo simulations. *Phys. Rev. B*, 81(11):115416, Mar 2010. doi: 10.1103/PhysRevB.81.115416.

[117] Hélène Feldner, Zi Yang Meng, Thomas C. Lang, Fakher F. Assaad, Stefan Wessel, and Andreas Honecker. Dynamical Signatures of Edge-State Magnetism on Graphene Nanoribbons. *Phys. Rev. Lett.*, 106:226401, May 2011. doi: 10.1103/PhysRevLett.106.226401. URL `http://link.aps.org/doi/10.1103/PhysRevLett.106.226401`.

[118] Toshiya Hikihara, Xiao Hu, Hsiu-Hau Lin, and Chung-Yu Mou. Ground-state properties of nanographite systems with zigzag edges. *Phys. Rev. B*, 68(3):035432, Jul 2003. doi: 10.1103/PhysRevB.68.035432.

[119] Manuel J. Schmidt and Daniel Loss. Tunable edge magnetism at graphene/graphane interfaces. *Phys. Rev. B*, 82(8):085422, Aug 2010. doi: 10.1103/PhysRevB.82.085422.

[120] Elliott Lieb and Daniel Mattis. Theory of Ferromagnetism and the Ordering of Electronic Energy Levels. *Phys. Rev.*, 125(1):164–172, Jan 1962. doi: 10.1103/PhysRev.125.164.

[121] Elbio Dagotto. Correlated electrons in high-temperature superconductors. *Rev. Mod. Phys.*, 66(3): 763–840, Jul 1994. doi: 10.1103/RevModPhys.66.763.

[122] David Sénéchal. An introduction to quantum cluster methods. eprint arXiv:0806.2690v2, 2008. URL `http://arxiv.org/abs/0806.2690v2`.

[123] Manuel J. Schmidt and Daniel Loss. Edge states and enhanced spin-orbit interaction at graphene/graphane interfaces. *Phys. Rev. B*, 81(16):165439, Apr 2010. doi: 10.1103/PhysRevB.81.165439.

[124] M. Hohenadler, T. C. Lang, and F. F. Assaad. Correlation Effects in Quantum Spin-Hall Insulators: A Quantum Monte Carlo Study. *Phys. Rev. Lett.*, 106:100403, Mar 2011. doi: 10.1103/PhysRevLett.106.100403. URL `http://link.aps.org/doi/10.1103/PhysRevLett.106.100403`.

[125] T. Giamarchi. *Quantum Physics in One Dimension.* Oxford Univ. Press, 2003. ISBN 0198525001.

[126] Manuel J. Schmidt. Bosonic field theory of tunable edge magnetism in graphene. *Phys. Rev. B*, 86:075458, Aug 2012. doi: 10.1103/PhysRevB.86.075458. URL `http://link.aps.org/doi/10.1103/PhysRevB.86.075458`.

[127] At $L/3$ filling, and $S_z = 0$, we could access edges of length $L = 48$ with a dimension of the corresponding Hilbert space of 2 594 212 after exploiting all symmetries. For nearly maximal $S_z = L/6 - 2$ and $L/3$ filling, we were able to calculate the groundstate energy of an edge with length $L = 180$ with a Hilbert space dimension of only 26 580. In this case we were limited only by the 64 bit limit of the internal storage of the basis vectors and longer edges are in principle accessible by a modification of our code.

[128] S. Daul. *Eur. Phys. J. B*, 14:649, 2000.

[129] S. Daul and R. M. Noack. *Phys. Rev. B*, 58:2635, 1998.

[130] Florian Goth, David J. Luitz, and Fakher F. Assaad. Single magnetic impurities in the Kane-Mele model. eprint arXiv:1302.0856, 2013. URL `http://arxiv.org/abs/1302.0856`.

[131] Rok Žitko. SNEG - Mathematica package for symbolic calculations with second-quantization-operator expressions. *Computer Physics Communications*, 182(10):2259 – 2264, 2011. ISSN 0010-4655. doi: 10.1016/j.cpc.2011.05.013. URL `http://www.sciencedirect.com/science/article/pii/S0010465511001792`.

[132] Pierce Coleman. *Introduction to Many Body Physics.* Rutgers University, 2012. URL `http://www.physics.rutgers.edu/users/coleman/620/mbody/pdf/bk.pdf`.

Acknowledgments

First of all, I wish to thank my advisor Fakher Assaad for giving me the opportunity of working in this extremely interesting field. He has never failed to provide great advice, support and motivation and it was just a privilege to work with him and his group. Thank you for pointing to the fascinating mix of projects and giving me the liberty of working on them all, I definitely enjoyed it and learned a lot!

Many thanks to Manuel Schmidt for his friendship and advice, for uncountable discussions that we had in the far too short time in which we shared our office and for being so pleasant to work with!

Special thanks go to Jutta Ortloff for being a great friend and office mate. Thank you for diving with me into the subject of two particle quantities and for many long discussions sometimes even extending to evenings on the bike!

I am very grateful to Florian Goth for endless discussions about physics, computers and everything. Thank you for teaching me even the finest details about proper C++ metaprogramming and for doing an excellent job in proofreading.

I am also indebted to Thomas Lang for his friendship and inspiring discussions about physics as well as to Martin Bercx who was a great companion over so many years.

Of course the rest of the group has been as important to me, in particular Jan Werner, Marcin Raczkowski, Martin Hohenadler, Michael Seißinger, Max Aulbach, Michael Mützel, Maximilian Kiesel, Christian Platt and Gang Li. You have been great! Alexandra Lösch earns special merit for ironing out administrative wrinkles and being extremely helpful whenever needed.

I am deeply indebted to Mark Jarrell for his advice and interesting discussions during my stays at Louisiana State University as well as during his visits to Germany.

Outstanding guidance and support has been given to me by Volker Meden during our common project on making contact to experimental data for the Josephson current. Thank you Volker, this has been a delightful experience. Equally, I wish to thank Tomáš Novotný for his invaluable contribution to this project.

Thanks go also to Nico Parragh for being a very pleasant friend and office mate during my last year. It was great to have a CTQMC expert in the office!

Extraacademic thanks are due to Monteverdichor Würzburg. It was an pleasure to enjoy music with all of you!

I also wish to thank Thomas, Teresa, Elisabeth and Sonja for being the best friends I could imagine. Thanks for being so much fun and for your extraordinary support during tough times!

It is impossible to thank my family enough for their love, my dear parents, Manuel, Janina, Pascal and Julian, you are the best and I can not imagine how the world would look like without you.

Last but certainly not least, I thank my darling Theresa for her love and for making the writeup period of this thesis a pleasure! You are incomparable!